



UNIVERSITÀ DEL PIEMONTE ORIENTALE

Università del Piemonte Orientale “Amedeo Avogadro”, Alessandria

Dipartimento di Scienze e Innovazione Tecnologica (DiSIT)

Advances in Sensors: The Enabling Roles of Photocatalysis, Polymer Brushes and Exotic Characterization Approaches

Guido Panzarasa

Advisor: Dr. Katia Sparnacci

Ph.D. Thesis in *Chemical Sciences*

XXVIII Cycle

Table of Contents

General Abstract (*p. 5*)

Introduction (*p. 7*)

I. Photocatalytic Lithography: a Powerful Technique for the Patterning of Polymer Brushes and Nanoparticles

1. Patterning of Polymer Brushes Made Easy Using Titanium Dioxide: Direct and Remote Photocatalytic Lithography (*p. 10*)
2. SERS-Active Patterns Obtained by Photocatalytic Shaping of Self-Assembled Silver Nanoprisms (*p. 44*)

II. Polymer Brushes: Advanced Applications and Innovative Characterization

3. Grafted-From Polymer Brushes Make Silicon Wafer Electrochemically Responsive (*p. 61*)
4. Positron Annihilation Spectroscopy: A New Frontier for Understanding Nanoparticle-Loaded Polymer Brushes (*p. 91*)

III. Self-Cleaning Properties in Engineered Sensors for the Electroanalytical Detection of Catecholamine Neurotransmitters

5. Developing an Efficient, Self-Cleaning Device for the Electroanalysis of Catecholamine Neurotransmitters (*p. 125*)
6. Self-Cleaning Electrochemical Sensors, *Part I: Towards Clinical Applications* (*p. 158*)
7. Self-Cleaning Electrochemical Sensors, *Part II: A Proof-of-Concept for On-Field Applications* (*p. 182*)

Conclusion and Perspectives (*p. 200*)

Appendix A - Polymer Brushes (*p. 203*)

Appendix B - Titanium Dioxide and Photocatalysis (*p. 211*)

Appendix C - General Procedures (*p. 215*)

Collaborations (*p. 220*)

Acknowledgments (*p. 221*)

General Abstract

The work described in this Thesis is highly interconnected and related to applied surface science, polymer chemistry and nanotechnology. For the sake of clarity, this work has been divided in three Sections with subsequent division in Chapters.

Section I is dedicated to the application of photocatalytic lithography to the patterning and modification of self-assembled monolayers, polymer brushes and nanoparticles. Here, the first example of polymer brushes patterning based on photocatalytic lithography is reported.

Section II is about the characterization of polymer brushes using exotic techniques such as positron annihilation spectroscopy (PAS) and electrochemistry. The most relevant features described are: the first report about the application of PAS to the study of polymer brushes and of their composites with nanoparticles, and the first report on the electrochemical properties of silicon wafer coated with grafted-from functional polymer brushes.

In **Section III** an innovative self-cleaning electroanalytical sensor for the detection of catecholamine neurotransmitters is presented. The relevance of this work can be best described by referring to the highlights received in *Chemistry World* and *Scientific American*.

There are three Appendices: **Appendix A** introduces polymer brushes and **Appendix B** deals with titanium dioxide photocatalysis, while in **Appendix C** the general synthetic procedures reported throughout this Thesis are described in detail.

Keywords

Surface science, Nanotechnology, Titanium dioxide, Photocatalysis, Self-assembly, Lithography, Patterning, Polymer brushes, Controlled radical polymerization, SI-ATRP, Silver nanoparticles, SERS, Positron Annihilation Spectroscopy, Electrochemistry, Self-cleaning, Catecholamine neurotransmitters, Sensors.

Introduction

Sensing the difference

Sensors are everywhere.

They are not only companions of our daily life: they are essential part of us and, more broadly, of all living beings. The sense of taste, of smell, of touch, of view, of hearing are all products of complex sensing systems shaped by Nature during eons of evolution. Sensors and sensor systems are vital to our awareness of our surroundings and provide safety, security and surveillance as well as enable monitoring of our health and environment.

No mystery that they are so important, after all.

A *sensor* is defined as a device able to give a response, of qualitative and/or quantitative nature, when subjected to a proper stimulus.

A transformative advance in the field of sensor technology has been the development of smart sensor systems. The definition of a smart sensor may vary, but typically, a smart sensor is the combination of a sensing element with processing capabilities provided by a microprocessor. That is, smart sensors are basic sensing elements with embedded intelligence. The sensor signal is fed to the microprocessor, which processes the data and provides an informative output to an external user. The innumerable applications of such systems are apparent. The incorporation of sensors into textiles (wearable sensors) and

eventually into living bodies for *e.g.* real-time monitoring of vital parameters is of special relevance in this context.

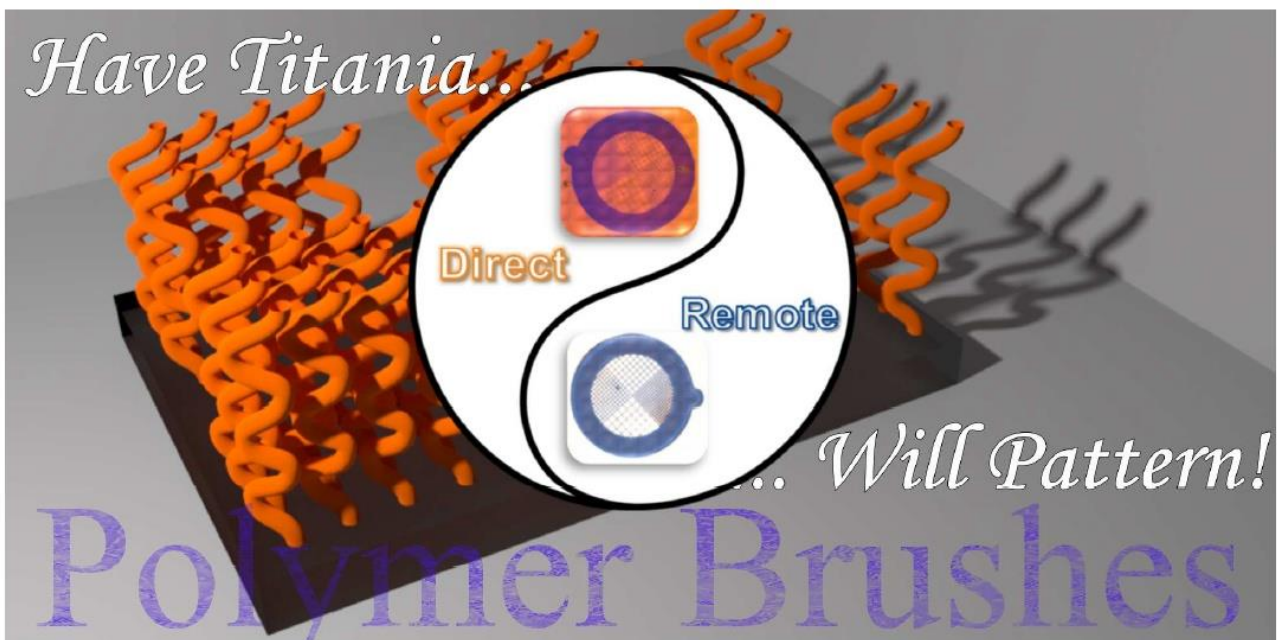
One major implication of smart sensor systems is the use of robust and reliable sensing devices. It could appear to be trivial, but even the most intelligent system is completely useless if its sensing core doesn't work properly. For this reason, it is of paramount importance to develop highly efficient sensing platforms with self-calibrating, self-healing, self-compensating and self-cleaning properties. This is one of the most challenging and actual field of research, which benefited much from the "nanotechnology revolution", generating high promises especially for the development of miniaturized devices. This broad field crosses many different disciplines ranging from chemistry to physics to materials science, with a major role played by surface science.

The scope of this Thesis is to explore three different, although converging, approaches to develop such kind of sensing platforms.

The enabling roles of photocatalysis, polymer brushes and of exotic characterization techniques (such as positron annihilation spectroscopy) to reach this goal are discussed. Theoretical as well as highly applicative results are described, as products of a genuine curiosity-driven approach.

I

Photocatalytic Lithography: a Powerful Technique for the Patterning of Polymer Brushes and Nanoparticles



Chapter 1

Patterning of Polymer Brushes Made Easy Using Titanium Dioxide: Direct and Remote Photocatalytic Lithography

ABSTRACT Photocatalytic lithography is demonstrated for the first time as a convenient technique to achieve patterning of polymer brushes. Both a “direct” and a “remote” approach are studied and both are based on the efficient degradation experienced by organic molecules when exposed to photo-generated reactive oxygen species. In the direct approach, a photoactive titanium dioxide surface, previously functionalized with a suitable initiator of polymerization, is exposed to near-UV light through a contact photomask. On the other hand, in the remote approach irradiation is performed on a generic, initiator-functionalized substrate through a transparent photoactive TiO₂ film and a photomask. Selective degradation of initiator molecules only in the zones not covered by the photomask is observed. The resulting pattern is then amplified as polymer brushes with surface-initiated polymerization technique. Features down to 10 μm can be obtained using simple equipment. The process is intrinsically parallel, high-throughput and scalable to wafer size, does not require photoresists nor high-intensity UV sources, making it relatively safe for the operator and powerful for microfabrication purposes. The possibility to obtain positive and negative patterns has been demonstrated using direct photocatalytic lithography, while remote photocatalytic lithography has been successfully coupled with nanosphere lithography.

1.1 Introduction

Polymer brushes, dense arrays of surface-tethered polymer chains, are perfect tools for surface engineering. They exhibit excellent robustness and well-organized chain conformation, which endow superior control over several surface properties such as morphology, grafting density and chemical composition [1-3]. Patterned polymer brushes [4,5] are versatile building blocks for micro-fabrication and controlled assembly of small particles [6], sensors/biosensors and actuators [7-15], drug delivery systems [16], electronic devices [17], anti-biofouling coatings [18] and biocompatible scaffolds [19]. In general, they are efficient means to confer smart, stimuli-responsive behavior to surfaces and interphases [20-22].

By a combination of lithographic tools and surface-initiated polymerization (“grafting-from”, as opposed to “grafting to” which relies on adsorption of preformed polymer) [23,24], micro- and nanoscale architectures can be obtained from suitable self-assembled monolayers (SAMs) [25-28]. SAMs are ordered arrays of molecules chemisorbed at a surface [29]. If they are composed by polymerization initiators, polymer chains can grow directly from them. Eventually, if the SAMs are patterned, patterned polymer brushes will be obtained.

The expertise to master patterning [30] is crucial in order to realize devices with applications ranging from biotechnology [31] to electronics [32]. An impressive array of patterning strategies is available. To name a few: colloidal lithography [33,34], micro-contact printing [35,36], electron beam lithography [37], scanning probe [38] or near field lithography [39], conventional photolithography (with the use of photoresists [40,41]) and SAM

photolithography [42,43]. The latter typically requires high-intensity UV sources [6,44-46] (*e.g.* deep-UV, vacuum-UV) [47,48] or highly focused beams (UV-lasers) [49].

There is a significant demand for more affordable and facile lithographic techniques, which should update the present technologies [50] to reliably pattern polymer brushes at the wafer scale [51] with high resolution micrometric and sub-micrometric features. Here we are reporting for the first time about how this challenge can be successfully addressed by taking advantage of photocatalytic lithography [52,53].

TiO₂ is one of the major protagonists in nanotechnology. It is inexpensive, non-toxic, its surface is biocompatible and can be functionalized using established chemistries [54]. It is an intrinsic semiconductor whose photochemical and photophysical properties have had great relevance both in fundamental [55,56] and applied research [57,58]. When TiO₂ is irradiated with photons of wavelength in the UV region, electron-hole pairs are produced: holes are powerful oxidants, electrons are good reducing agents and both rapidly react with adsorbates [59]. Titanium dioxide is now playing a central role for the engineering of surfaces [60,61], in particular in the field of lithography [53,62]. Here, we report for the first time an improved access to micro-patterned polymer brushes using near-UV light titanium dioxide photocatalytic lithography.

First, transparent and mechanically robust TiO₂ anatase films with high photoactivity are deposited on glass and silicon wafer from an acidic TiO₂ sol using an electrochemically-assisted technique first reported by the Group of Prof. S. Ardizzone (all the relevant details can be found in Appendix C) [63]. The requirement of common lab instrumentation and the possibility to store and reuse the sol for up to one month makes this process highly appealing, cheap and scalable. In addition, the quality of the TiO₂ film is better in terms of

smoothness (rms 0.563 nm) compared to those commonly obtained by dip-coating or spin-coating (Figure 1.1) [64]. Film thickness can be increased at will by repeating the deposition cycle [63]. The films showed the typical increase in hydrophilicity upon exposure to 365 nm UV radiation due to enhanced hydroxyl surface termination (generally reported as “surface-induced hydrophilicity” [65]). We exploited this phenomenon to improve chemisorption of the atom transfer radical polymerization (ATRP) initiator (3-(2-bromoisobutyramido)propyl)triethoxysilane (BIB-APTES) [66] on TiO₂.

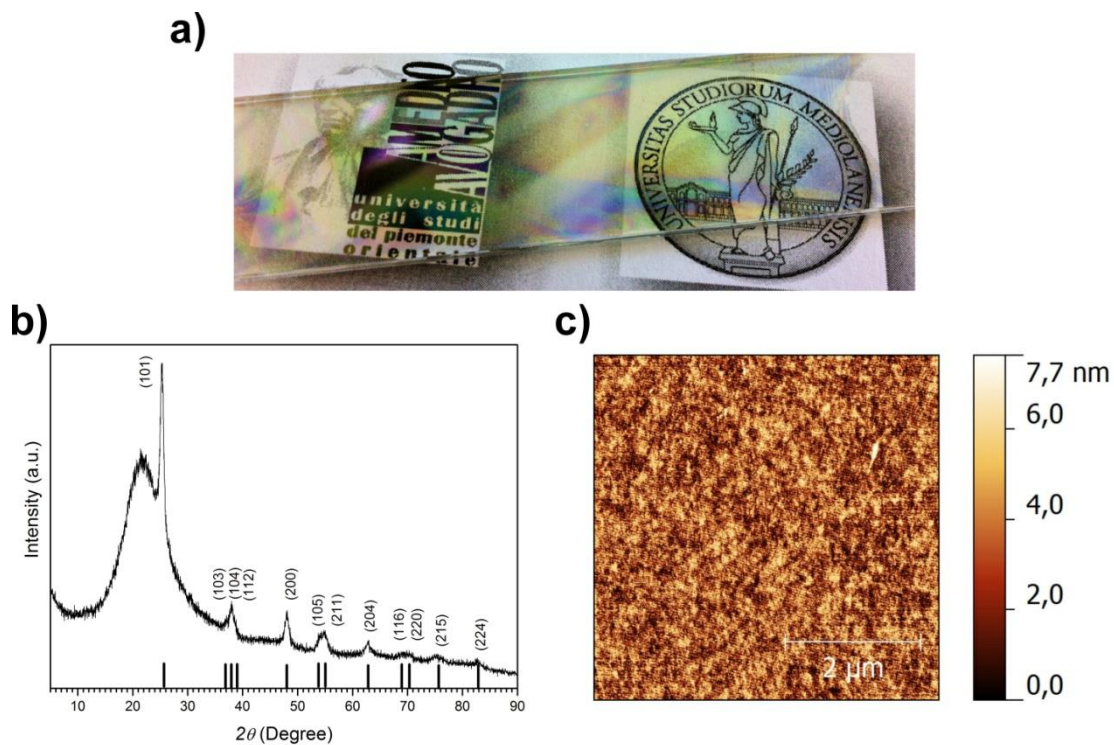


Figure 1.1 Titanium dioxide films deposited on glass: in a) the film high transparency is evident, in b) XRD analysis shows pure anatase polymorph, with crystallite dimension of ~ 17 nm. c) AFM topography picture (tapping mode).

We use then surface-initiated atom transfer radical polymerization (SI-ATRP), a controlled free radical polymerization process, to amplify the obtained initiator pattern into a polymer brushes pattern [67,68]. Compared to other controlled radical polymerization techniques, ATRP allows to adopt very mild conditions (*e.g.* polymerization can be conducted at room

temperature). Both “conventional” and “activators regenerated by electron transfer” (ARGET) ATRP are used in this study. The latter is selected thanks to improved oxygen tolerance and lower concentration of metal catalyst required [69]. Methyl methacrylate (MMA) is chosen as a standard monomer but any other ATRP-friendly monomer can be used.

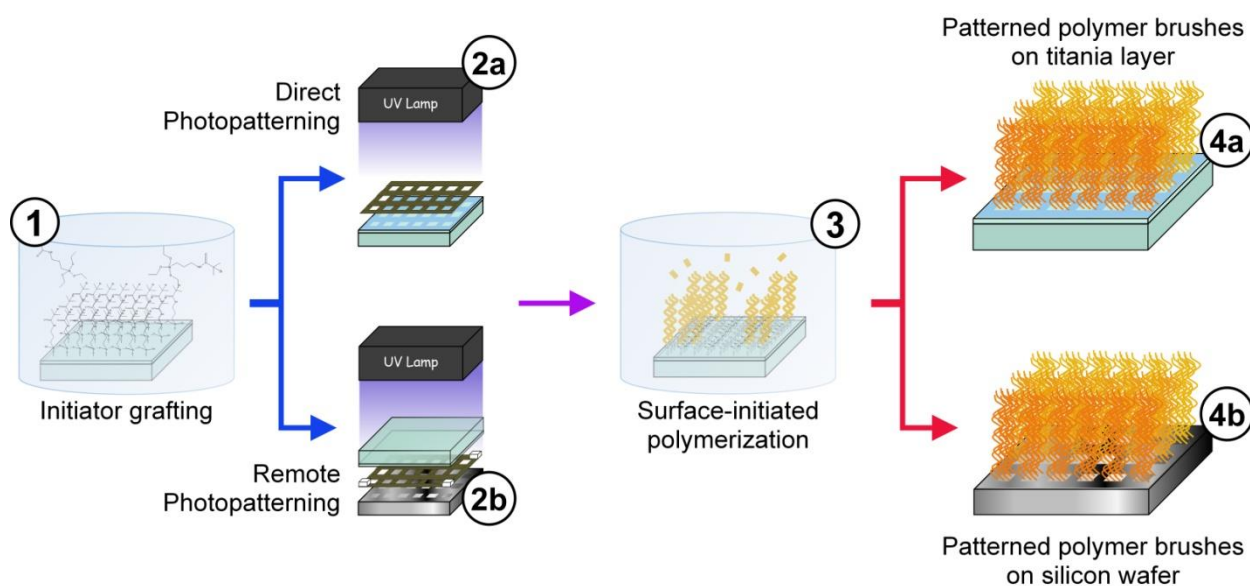


Figure 1.2 Patterned polymer brushes obtained by photocatalytic lithography of initiator-functionalized substrates. Steps: 1) grafting of the ATRP initiator, 2) pattern formation using either direct (2a) or remote (2b) photocatalytic lithography, 3) pattern amplification using SI-ATRP to obtain 4) the corresponding polymer patterns (4a, 4b).

1.2 Results and Discussion

1.2.1 Direct Photocatalytic Lithography

Direct photocatalytic lithography (Figure 1.3) is achieved by irradiating, with 365 nm near-UV light, a self-assembled monolayer (SAM) of ATRP initiators grafted directly on a titanium dioxide film. A metallic TEM grid deposited the substrate performs as a contact photomask. The resulting pattern is then amplified into polymer brushes by surface-initiated polymerization.

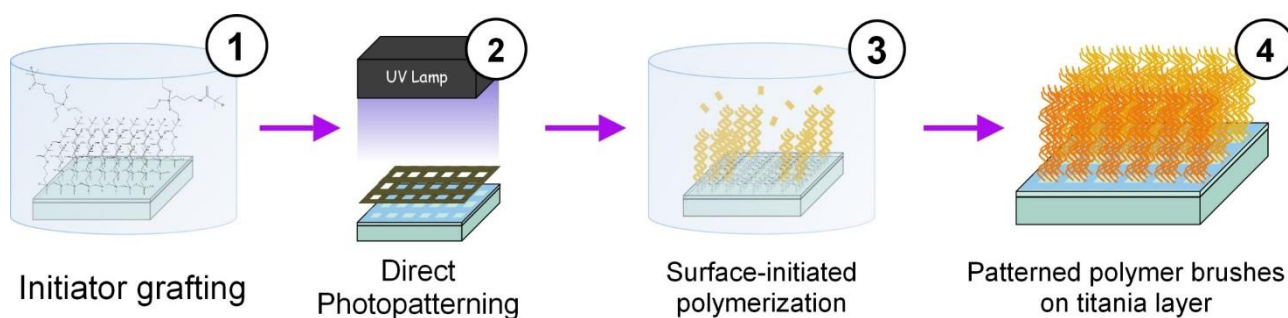


Figure 1.3 Patterning of polymer brushes by direct photocatalytic lithography.

The kinetics of photocatalytic degradation are followed on dedicated substrates by water contact angle measurements (Figure 1.4). The water contact angle for surfaces functionalized with BIB-APTES, stored in the dark, is 75° . After 1 h of irradiation, the θ_w decreases to less than 15° .

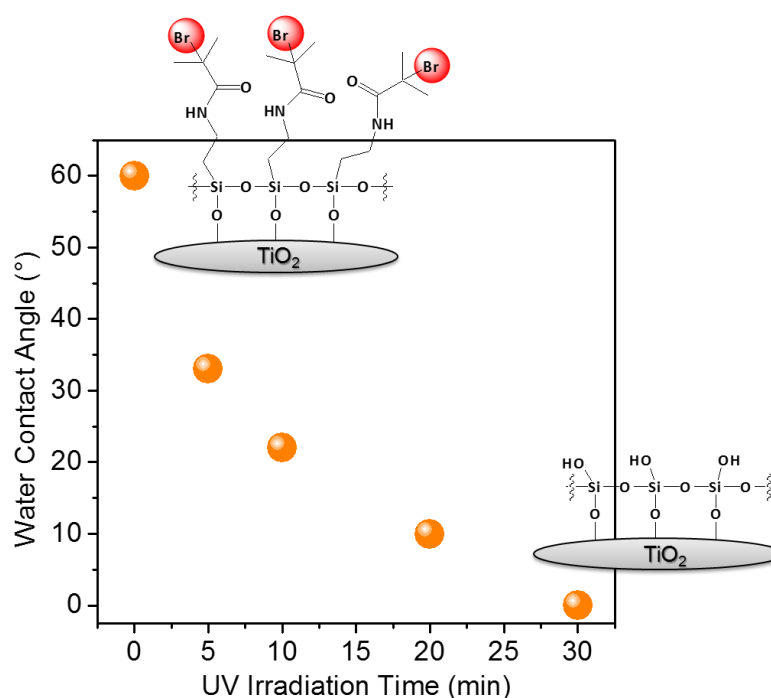


Figure 1.4 Water contact angle kinetics for the photodegradation of BIB-APTES grafted on TiO_2 exposed to 365 nm-UV light. The most probable structures of the initiator SAM before and after 30 min of irradiation are showed.

The disappearance of nitrogen and bromine signals from the XPS spectra gave definitive evidence of complete removal of the initiator molecules (Figure 1.5, Tables 1.1 and 1.2). On the other hand, BIB-APTES grafted on surfaces with no photoactivity such as silicon wafer or glass remains unaffected even after 3 h of UV irradiation as confirmed by the unchanged water contact angle and ability to start the growth of polymer brushes. That demonstrates the critical role of TiO₂ for the photopatterning of initiator.

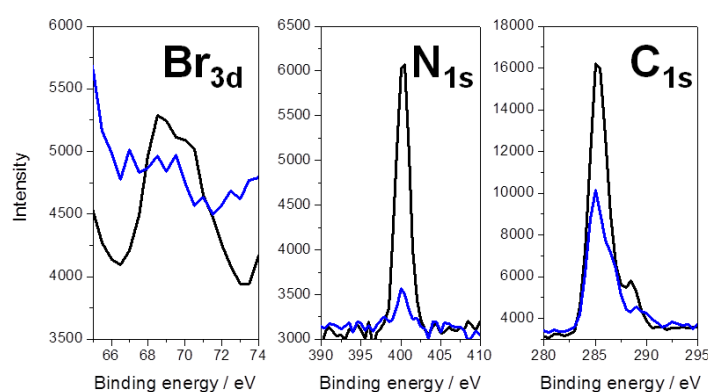


Figure 1.5 XPS confirmation of the photocatalytic degradation of grafted initiator. Black line: before irradiation. Blue line: after 1 h of 365 nm-UV irradiation.

It can be seen, from the relative atomic percentages (Table 1.1), that there is a C:N ratio of about 8:1 for BIB-APTES grafted on TiO₂. These values are in good accordance with the 7:1 C:N ratio expected for a uniform SAM of BIB-APTES with each of its three Si-O groups forming a siloxane bond with the -OH-terminated TiO₂ surface. Although some molecules may retain ethoxy functional groups on their Si-O tails, an ordered monolayer has formed. The Br 3d signal is apparently underestimated, thus preventing its quantification. However, complete disappearance of both nitrogen and bromine signals after direct photocatalytic lithography confirms the successful degradation of the initiator molecules. Table 1.2 reports the energetic positions of principal peaks. For carbon, signals relating to C-C (285.0 eV) and

C=O (288.5) are observed, in accordance with the molecular structure of BIB-APTES. For BIB-APTES on TiO₂ after 1 h of UV irradiation a shoulder appears at 286.5 eV which is attributable to -C-OH groups. The position of N 1s peak at 400 eV was assigned to the O=C-N species. The oxygen peak position is dependent on nature of the surface: in this case, it is 530.5 eV. The position of the silicon peak depends on the number of bonded oxygen atoms: 99.5 eV, no bound oxygen atoms; 102.5 eV, three bound oxygen atoms; 103.5 eV, four bound oxygen atoms.

Table 1.1 Atomic composition of BIB-APTES-functionalized surfaces before and after direct photocatalytic lithography determined by XPS.

Sample	Treatment	O 1s (at.% ± 10%)	Ti 2p (at.% ± 10%)	C 1s (at.% ± 10%)	Si 2p (at.% ± 10%)	N 1s (at.% ± 10%)	Br 3d (at.% ± 10%)
BIB-APTES on TiO ₂	None (as-prepared)	54.9	22.2	17.9	2.1	2.2	0.78
	1 h UV	62.9	26.2	8.9	2.0	--	--

Table 1.2 Binding energy for the principal elements detected by XPS.

Sample	Treatment	O 1s (eV ± 0.5)	Ti 2p ₃ (eV ± 0.5)	C 1s (eV ± 0.5)	Si 2p (eV ± 0.5)	N 1s (eV ± 0.5)	Br 3d (eV ± 0.5)
BIB-APTES on TiO ₂	None (as-prepared)	530.5	459.0	285.0 288.5	102.5	400.0	71.0
	1 h UV	530.5	459.0	285.0 286.5 289.0	102.5	--	--

Polymerization of MMA is carried out at 30 °C in a 4:1 v/v methanol-water mixture using a CuBr₂/tris(2-pyridylmethyl)amine (TPMA) catalyst activated by an excess of ascorbic acid. Water contact angle measurements (68°, which is consistent with previous wetting experiments with water on PMMA brushes [70]) and FTIR analysis confirm the successful grafting of polymer brushes (Figure 1.6b,c, red line).

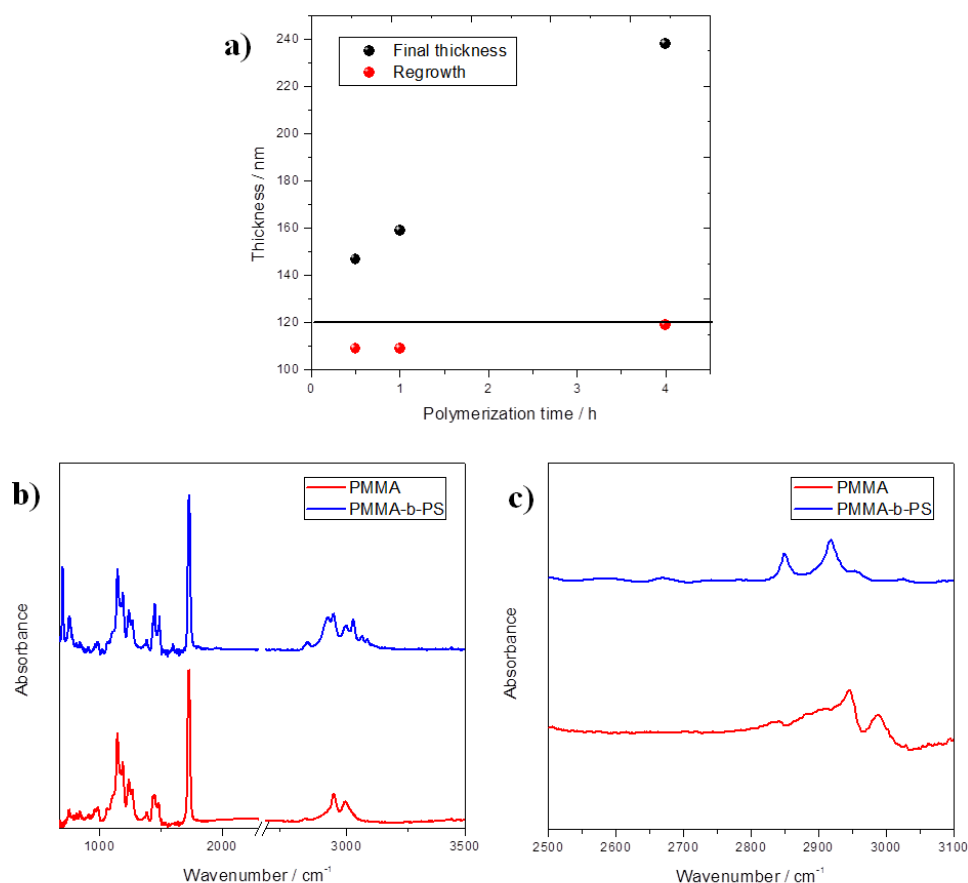


Figure 1.6 a) Demonstration of the reinitiation efficiency for PMMA brushes. The straight line represents the mean thickness h_{4h} for a 4 h-grown PMMA brush. Results indicate very good macroinitiator efficiency ($I \geq 90\%$), *i.e.* the fraction of the original growing chains capable to restart polymerization. That is defined as $I = (\Delta h / h_{4h}) \cdot 100$, where Δh is the thickness increase after restarting polymerization with MMA. (b) Comparison of FTIR spectra for a poly(methyl methacrylate) (PMMA) brush, thickness 106 ± 1 nm, and for a block copolymer brush obtained by restarting polymerization from PMMA brush with styrene (PS thickness 86 ± 2 nm). Substrate: silicon wafer. Both brushes show characteristic IR absorption spectra with the most pronounced differences occurring in the C-H stretching regions. A strong peak due to C=O stretching at 1730 cm^{-1} is visible in both spectra. In the

PMMA spectrum, the main features are at 2951 cm^{-1} (CH_2 asymmetric stretching and CH_3 asymmetric stretching) and at 2996 cm^{-1} (CH_3 of OCH_3 asymmetric stretching). In the PMMA-PS block copolymer spectrum, the diagnostic peaks are at 699 cm^{-1} and 755 cm^{-1} (wagging of the 5 H of the aromatic ring), 2847 cm^{-1} (CH_2 symmetric stretching), 2927 cm^{-1} (CH_2 asymmetric stretching); the peaks at 2998 cm^{-1} , 3026 cm^{-1} , 3060 cm^{-1} , 3083 cm^{-1} are all due to the aromatic C-H stretching). (c) Comparison of FTIR spectra for a poly(methyl methacrylate) (PMMA) brush, thickness $83 \pm 1\text{ nm}$ and for a block copolymer brush obtained by restarting polymerization from PMMA brush with styrene (PS thickness $83 \pm 2\text{ nm}$). Substrate: TiO_2 . Both brushes show characteristic IR absorption spectra with the most pronounced differences occurring in the C-H stretching regions. In the PMMA spectrum, the peaks at 2946 cm^{-1} (CH_2 asymmetric stretching and CH_3 asymmetric stretching) and at 2999 cm^{-1} (CH_3 of OCH_3 asymmetric stretching) are visible. In the PS spectrum, the peaks at 2849 cm^{-1} (CH_2 symmetric stretching) and at 2918 cm^{-1} (CH_2 asymmetric stretching) can be recognized.

Polymerization on BIB-APTES-functionalized substrates proceeds smoothly, leading to PMMA brushes with thicknesses up to 200 nm depending upon the amount of time allowed for polymerization. The brush thickness is linearly correlated with polymerization time (over at least 8 h) suggesting a good control of the polymerization (Figure 1.7).

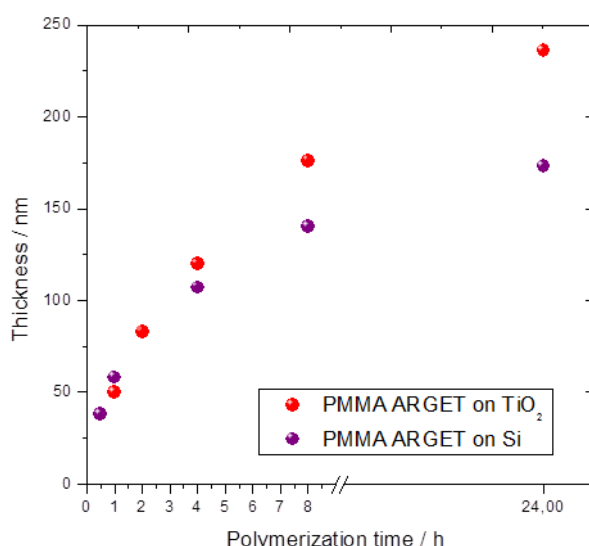


Figure 1.7 Evolution of PMMA brushes thickness as a function of the polymerization time. A deviation from linearity is observed for longer reaction times, which could be explained by increased steric interference to chain growth as polymer brushes grow longer and by the occurrence of irreversible chain termination.

This is confirmed also by the excellent ($\geq 90\%$) re-initiation efficiency showed by the brushes (Figure 1.6a), which allows to perform block-copolymerization. For example, PMMA-b-PS brushes with a poly(styrene) (PS) block up to 80 nm thick are obtained by subsequent polymerization of styrene for 4 h from a PMMA brush as shown by the increase in contact angle (from 68° to 90° , in accordance with literature findings [71]) and FTIR analysis (Figure 1.6, blue line). According to SEM and AFM images, the grid patterns are successfully replicated by polymer brushes onto the TiO_2 surface and 10 μm -wide PMMA lines were obtained with very good resolution (Figure 1.8).

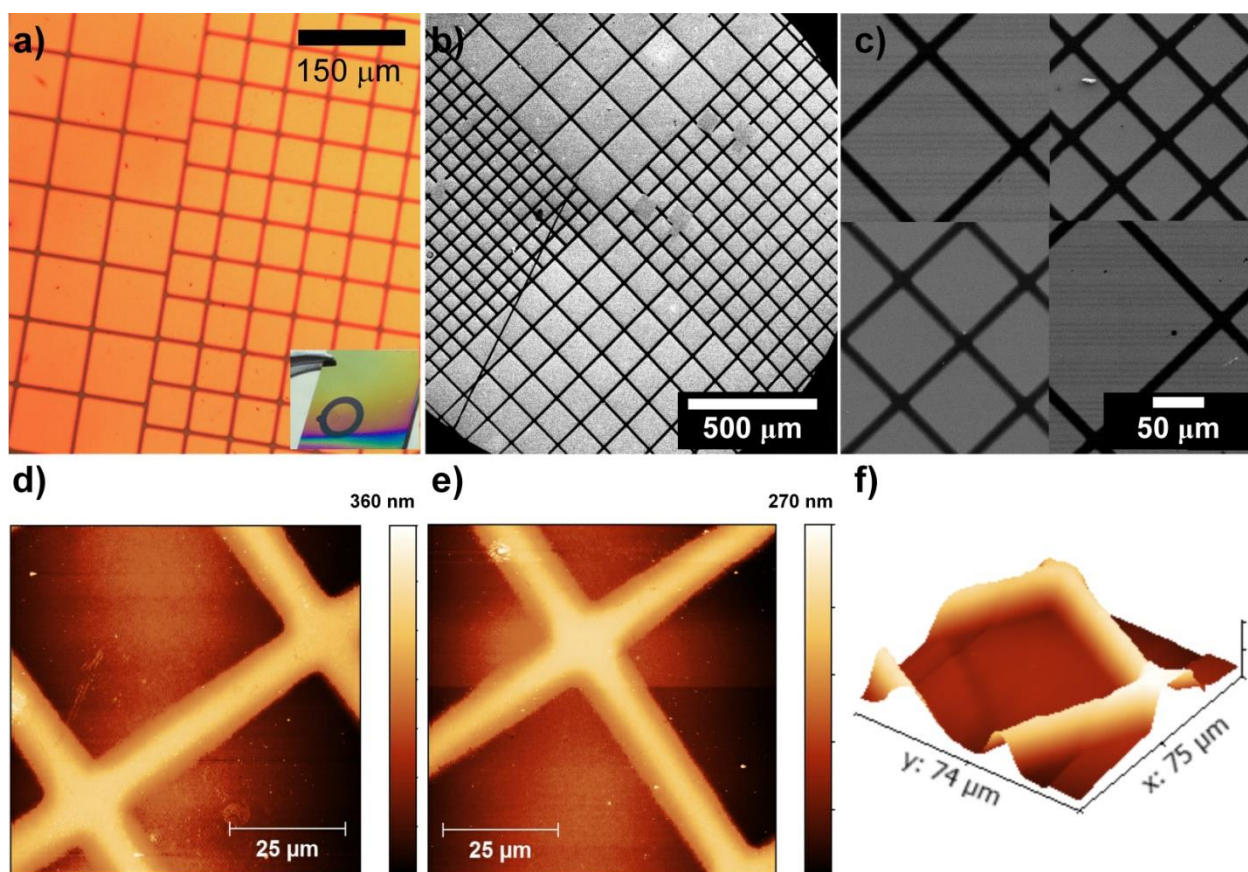


Figure 1.8 Polymer brushes patterns obtained after SI-ATRP of patterned initiators: a) optical microscopy (the inset shows the picture of a typical sample), b,c) scanning electron microscopy, d-f) atomic force microscopy (tapping mode).

Patterning of pH-responsive polymer brushes

As already mentioned, peculiar properties arise from polymer brushes with specific structure, making them powerful tools for surface engineering. Examples are control of phase-segregation in response to external stimuli, wetting control, lubrication, adsorption of molecules and particles (including proteins and cells) [72]. Noteworthy, brushes made of polyelectrolytes are able to respond to a wide range of external stimuli such as pH, temperature and ionic strength, which induce structural (*e.g.* swelling) and chemical (*e.g.* functional group modification) changes in the individual polymer chain leading to a collective, amplified response of the brushes [73-75]. Poly(2-(dimethylamino)ethyl methacrylate) (PDMAEMA) is one of the most studied pH-responsive polymer for the development of smart surfaces, sensors and actuators [76,77] and for this reason it is chosen here to demonstrate the potential of photocatalytic lithography applied to polymer brushes. After direct photocatalytic lithography of a BIB-APTES initiator SAM on titanium dioxide, polymerization of DMAEMA is performed using conventional ATRP in presence of 5 mol% CuBr₂ as added deactivator (see the Specific procedures paragraph for details) [78]. The brushes thickness can be tuned by increasing the polymerization time up to 4 h: the linear increase of thickness as a function of the polymerization time suggests a controlled process (Figure 1.9a).

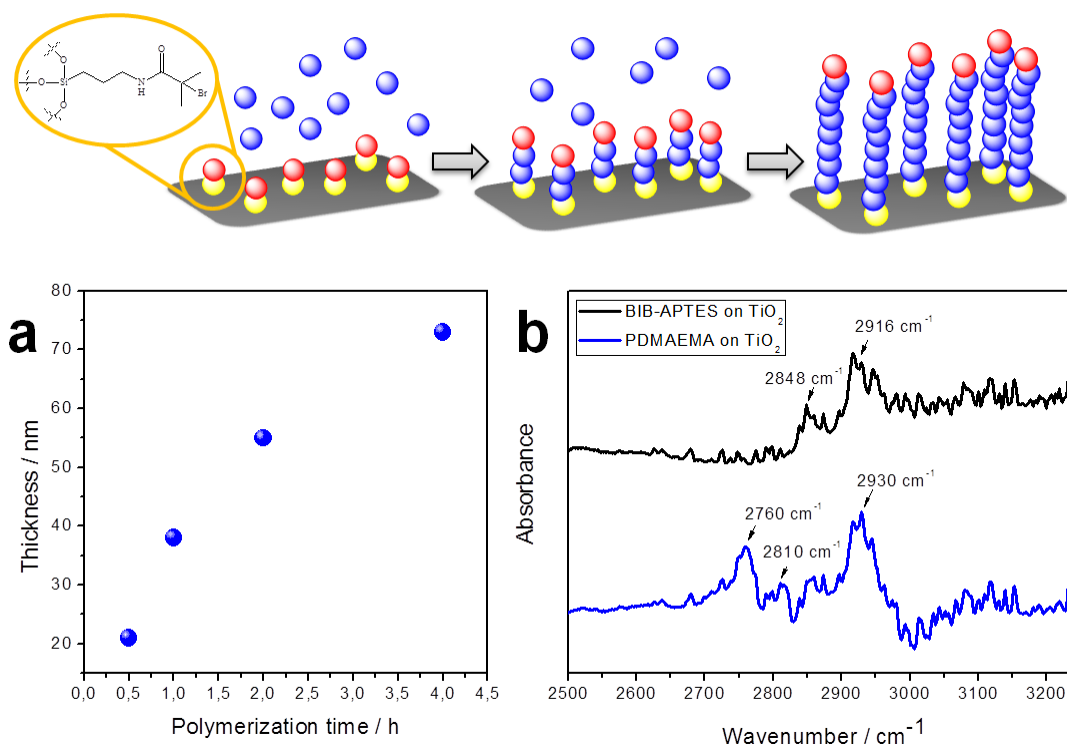


Figure 1.9 Depiction of the polymerization process for PDMAEMA brushes and resulting a) polymerization kinetics, b) FTIR spectra.

Successful formation of PDMAEMA brushes is confirmed also by FTIR spectroscopy (Figure 1.9b). BIB-APTES-functionalized substrates show only peaks from the $-\text{CH}_2-$ groups. Extra peaks are visible after DMAEMA polymerization at 2760 cm^{-1} and 2810 cm^{-1} (symmetric stretching) and a peak at 2930 cm^{-1} , associated with C-H vibration modes of $-\text{CH}_3$ of the tertiary amine groups $-\text{N}(\text{CH}_3)_2$ [79-81].

Optical microscopy and scanning electron microscopy are used to examine the pattern quality of the obtained brushes and the resolution attained: the images reveal well defined patterns (ca. 10 micron-width) exactly as those observed for PMMA brushes, demonstrating the effectiveness of photocatalytic lithography (Figure 1.10).

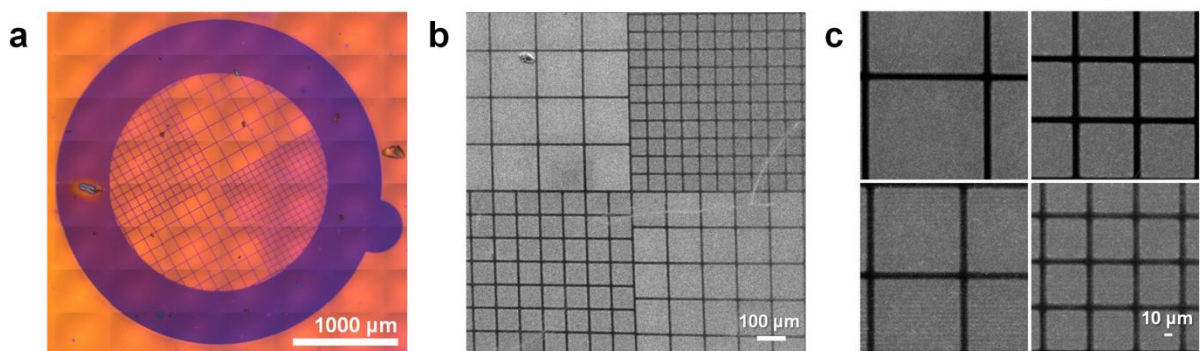


Figure 1.10 a) Optical microscopy and b,c) SEM images of patterned PDMAEMA brushes.

PDMAEMA is a weak polybase with pKa ca. 7, thus its tertiary amine group is protonated at $\text{pH} < 7$ and deprotonated at $\text{pH} > 7$ [82]. Protonation introduces electrostatic charges, which cause the chains to repel each other and swell by absorption of water, so pH changes are accompanied by changes in the brushes hydrophilicity which can be easily followed by water contact angle measurements. The brushes (water contact angle ca. 55°) can be made more hydrophilic (ca. 14°) or less hydrophilic (ca. 60°) by simple immersion in acid or base solutions, respectively. This behavior is completely reversible and can be easily appreciated for micropatterned samples (Figure 1.11).

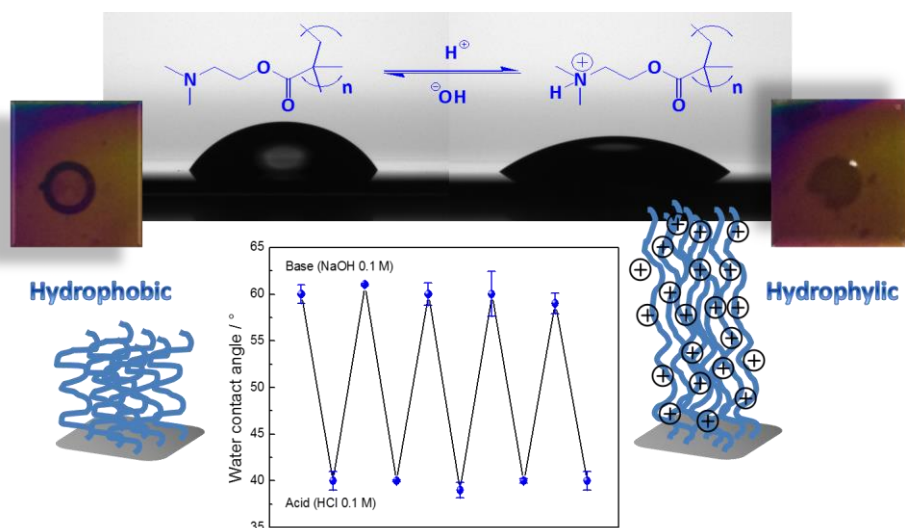


Figure 1.11 The pH-responsive behavior of PDMAEMA brushes is demonstrated by reversible contact angle switching.

Positive *vs* Negative Patterns obtained using sacrificial SAMs

In the previous paragraphs, the described pattern was the positive replica of the photomask. However, here we demonstrate that using a sacrificial SAM it is possible to obtain the negative equivalent pattern.

First of all, an ATRP-inert alkylsilane is used to form a self-assembled monolayer on titanium dioxide. To this end, an optimized chemical vapor deposition (CVD) procedure is used (see Appendix C for details) [83]. Then, the SAM is patterned using direct photocatalytic lithography. As discussed before, the exposed zones are free from contamination and are thus prone to be re-filled with another SAM, in this case of an initiator of polymerization such as BIB-APTES. After SI-ATRP, the corresponding negative pattern made of polymer brushes is successfully achieved, as judged by optical microscopy (Figure 1.12) and atomic force microscopy (Figure 1.13).

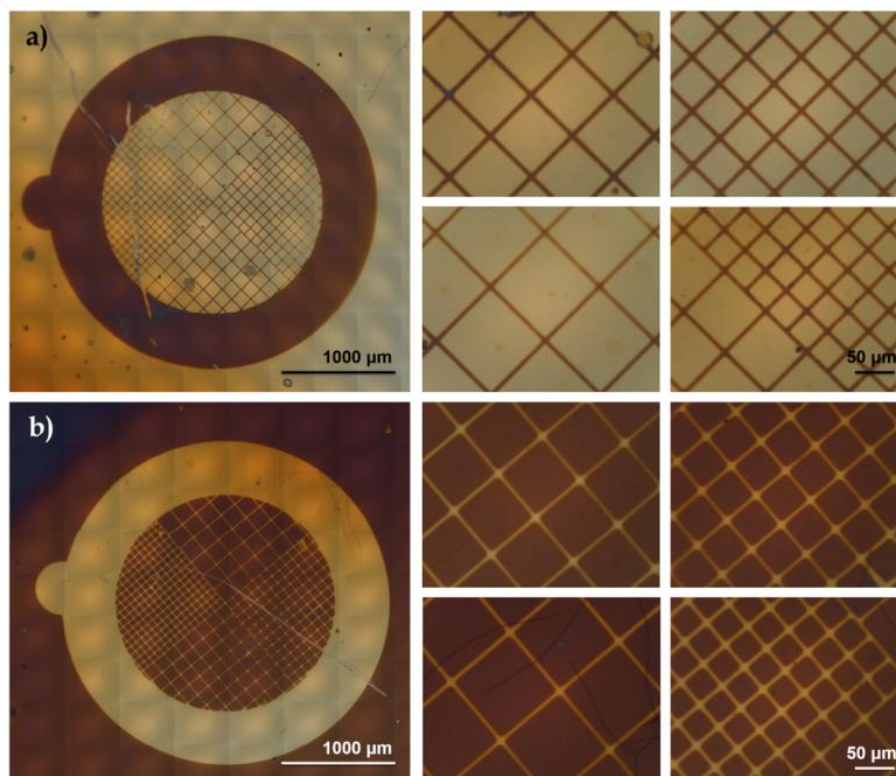


Figure 1.12 Optical microscopy images of a) positive and b) negative patterns of polymer brushes obtained without and with the use of a sacrificial monolayer, respectively.

POSITIVE

NEGATIVE

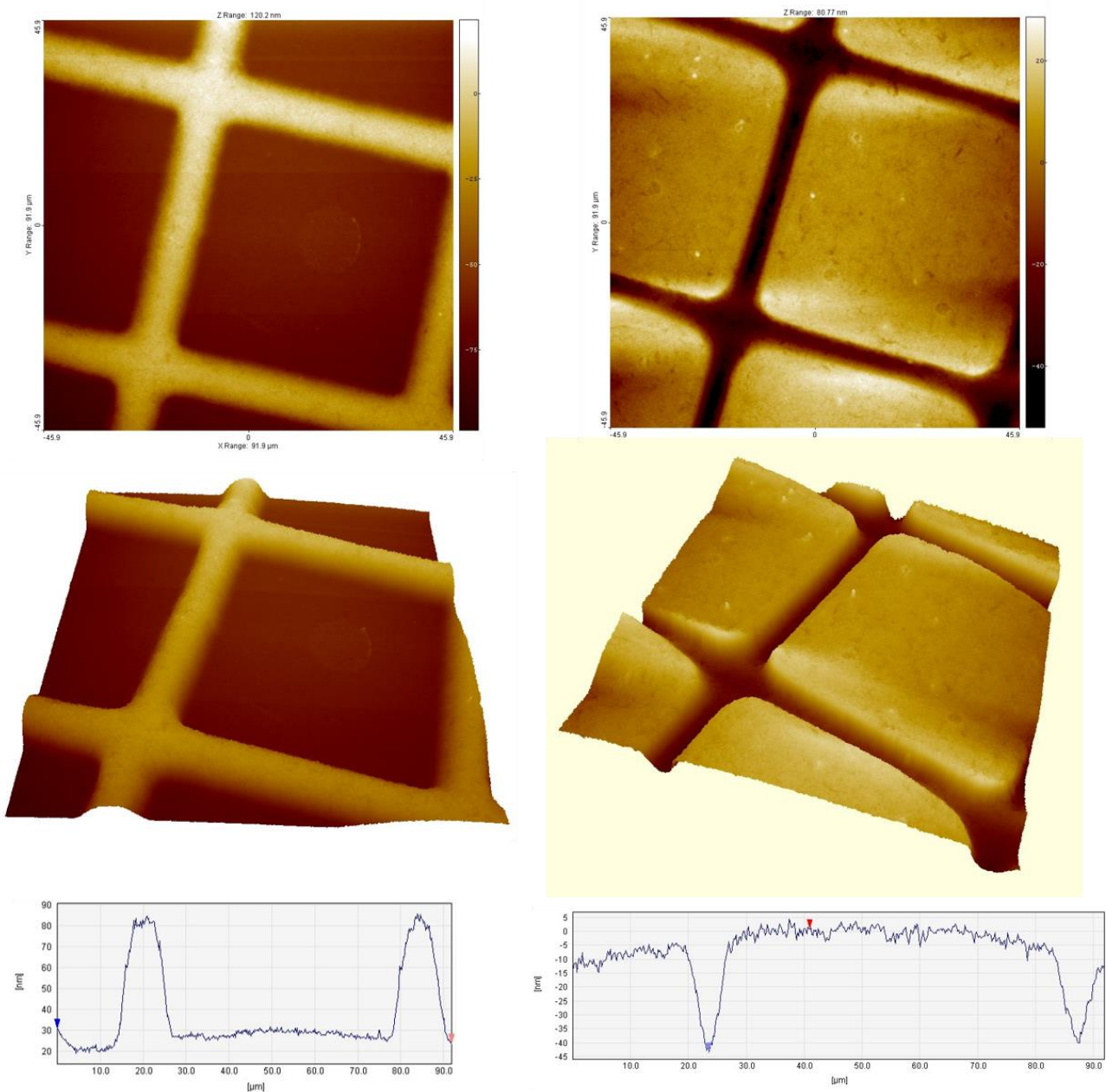
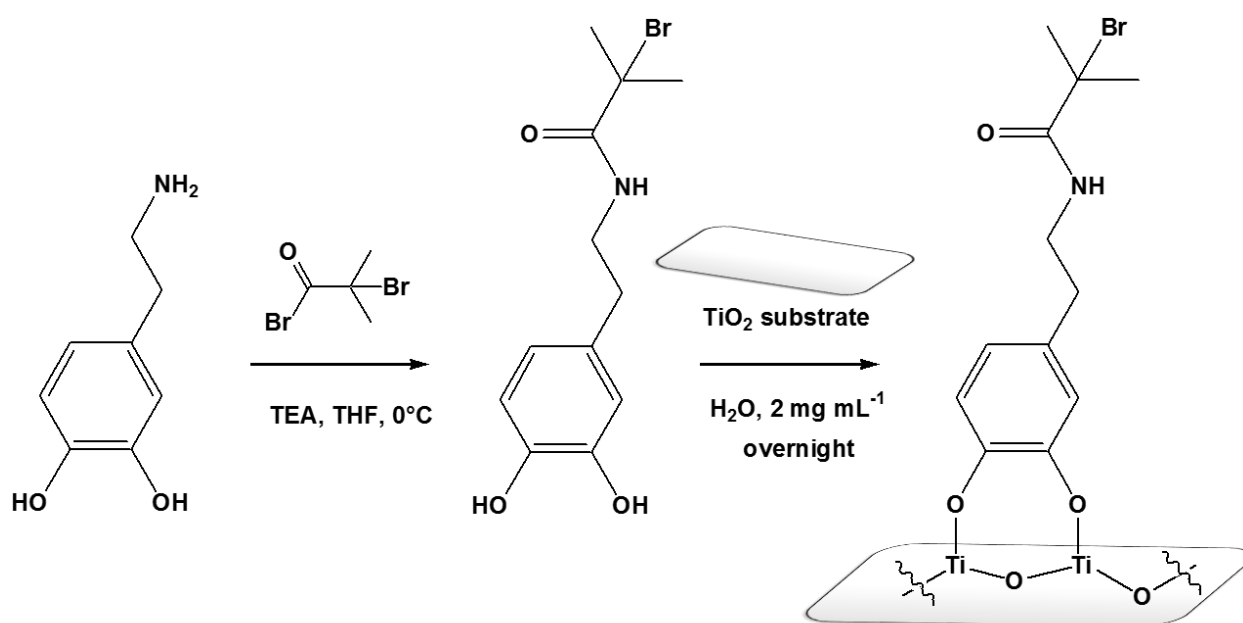


Figure 1.13 AFM images (2D, 3D reconstruction and profiles) of positive and negative patterns (grids *vs* squares) of polymer brushes obtained without and with the use of a sacrificial monolayer, respectively.

The quality of the first SAM is of paramount importance to reduce the risk of spurious polymerization due to the formation of islands during deposition of initiator: the sacrificial SAM must be tightly packed and homogeneous. CVD of Silres 1701 proved to be the most

successful approach to reach this goal. For example, a sacrificial SAM made of octadecyltrimethoxysilane deposited from toluene with the conventional approach was unsuccessful.

This problem could be overcome using catechol-derived initiators (Scheme 1.1), because they not only have high affinity towards the clean oxide surface but also allow the use of solvents such as water (which are orthogonal towards hydrophobic brushes) [84].



Scheme 1.1 Example of a dopamine-derived ATRP initiator and its attachment to a TiO₂ surface through its catechol moiety.

1.2.2 Remote Photocatalytic Lithography

Direct photocatalytic lithography could play a crucial role for innovation in the field of polymer brushes micro-lithography. Nevertheless, the need of a TiO₂ layer or, in general, of a photoactive substrate is limiting for many applications. Notwithstanding the smoothness, the transparency, the hardness and the biocompatibility of the titania layer, its

photocatalytic properties could not be desired for some applications. In addition, it could be necessary to graft the brushes directly onto a specific surface or onto substrates that cannot withstand a high temperature (ca. 500 °C) thermal treatment, which is needed for the development of titania photoactivity. We found in remote photocatalysis (Figure 1.14) a powerful solution for this general problem.

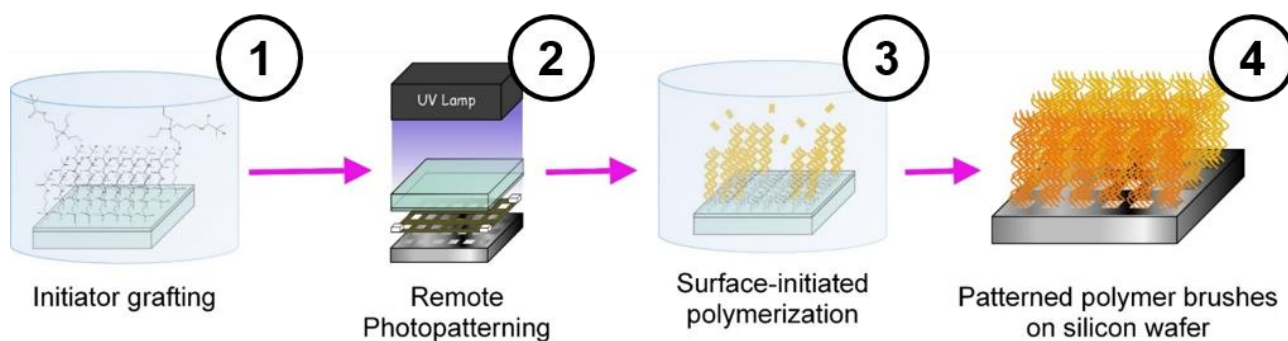


Figure 1.14 Patterning of polymer brushes by remote photocatalytic lithography.

The Group of A. Fujishima first reported that the photooxidation of organic molecules could occur not only on the surface of titanium dioxide but also on substrates placed at considerable distances (up to 500 μm) from it [65,85]. The mechanism of remote photocatalysis has been highly controversial until Kubo *et al.* [86] demonstrated that H_2O_2 molecules, which are generated at the photocatalyst surface from adsorbed water and oxygen molecules, migrate in the surrounding atmosphere and are cleaved to HO^\bullet radicals in the illuminated areas of the target surface (Figure 1.15). Such mechanism is particularly useful to explain the high pattern resolution obtained by us. Highly oxidative radical species form only in the irradiated areas, avoiding lateral oxidation due to migration [87,88].

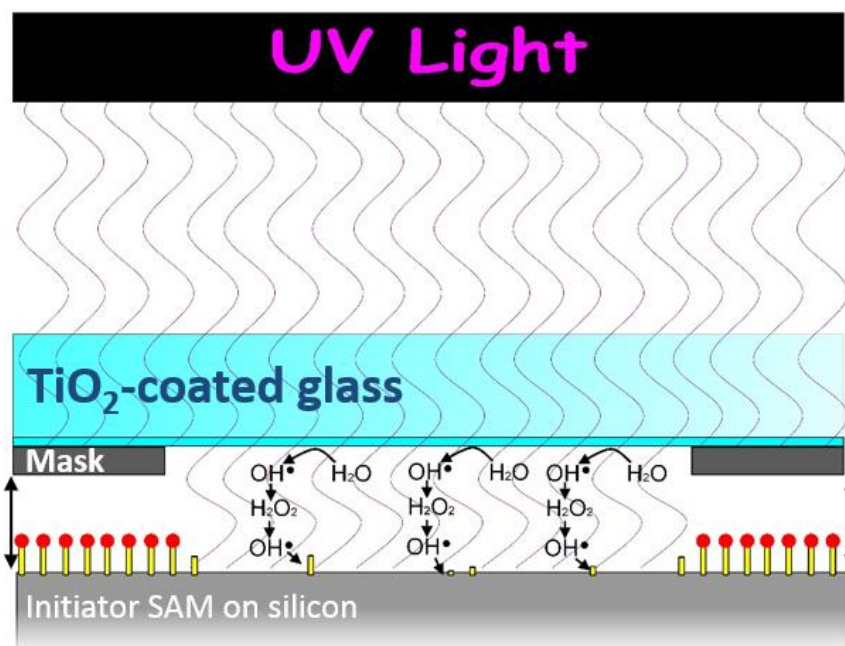


Figure 1.15 Mechanism of remote photocatalytic lithography.

Numerous reports are available on the remote oxidation not only of organic contaminants, alkylsiloxane and thiol SAMs, but also of polymers and metals [89,90]. Here, for the first time, we describe the successful application of remote photocatalytic lithography for the realization of patterned polymer brushes. This is a potentially universal approach, able to generate high resolution patterns on any kind of substrate. In order to obtain a good resolution, avoiding effects connected to the titania substrate morphology and light scattering ability, the quality of the photoactive layer is critical. Again, electrochemically-assisted titania deposition films gave high performance in terms of transparency and smoothness. Remote photocatalytic patterning was performed by irradiating with 365 nm UV light BIB-APTES-functionalized silicon substrates through our titania-coated glass, pre-cleaned by UV irradiation for 1 h, using a 100 μm -thick Teflon spacer. Micropatterning was achieved using a TEM grid and patterns were amplified with PMMA brushes, as already discussed for direct photolithography. Water contact angle decreased from 70° to 33° after

2 h of irradiation of the initiator-functionalized substrate. In addition, as for the direct approach, XPS showed complete disappearance of the bromine signal along with the nitrogen signal (Tables 1.3 and 1.4). The discussion of the XPS data is the same for BIB-APTES-functionalized titania. The C:N ratio of 9:1 is indicative of good SAM quality. The only difference compared to TiO₂ is the position of the oxygen peak, which depends on the surface nature: 530.5 eV for TiO₂, 533.0 eV for SiO₂.

Table 1.3 Atomic composition of BIB-APTES-functionalized surfaces before and after remote photocatalytic lithography determined by XPS.

Sample	Treatment	O 1s (at.% ± 10%)	C 1s (at.% ± 10%)	Si 2p (at.% ± 10%)	N 1s (at.% ± 10%)	Br 3d (at.% ± 10%)
BIB-APTES on Si	None (as- prepared)	38.0	24.6	34.5	2.6	0.33
	5 h remote photocatalysis	49.6	4.9	45.5	--	--

Table 1.4 Binding energy for the principal elements detected by XPS.

Sample	Treatment	O 1s (eV ± 0.5)	C 1s (eV ± 0.5)	Si 2p (eV ± 0.5)	N 1s (eV ± 0.5)	Br 3d (eV ± 0.5)
BIB- APTES on Si	None (as- prepared)	533.0	285.5 288.5	99.5 103.5	400.5	71.0
	5 h remote photocatalysis	533.0	285.0	99.5 103.5	--	--

A kinetic investigation is carried out to determine the optimum time necessary to develop a pattern of good quality (Figure 1.16). Although a well-resolved pattern can be obtained after 3 h of irradiation, the best pattern resolution is achieved with an irradiation time of 5 h (Figure 1.17).

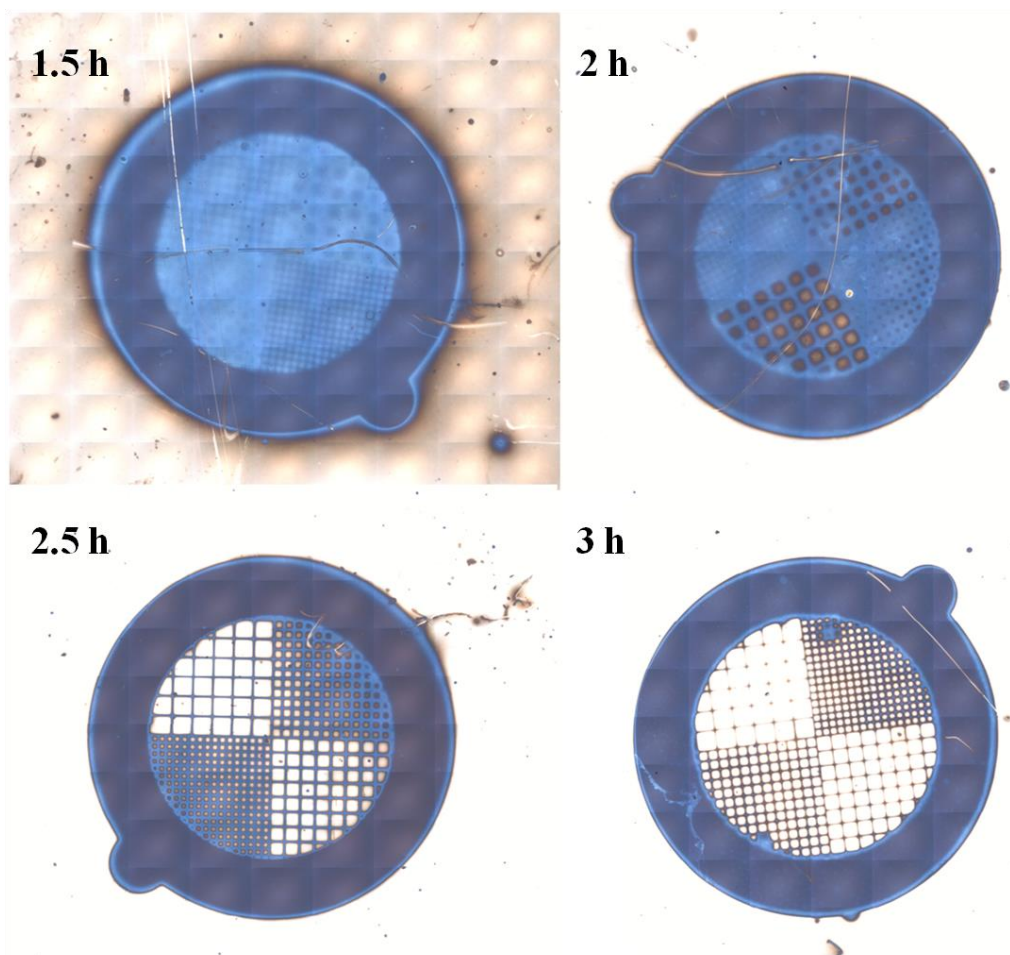


Figure 1.16 Optical microscopy images of the pattern evolution of remote photocatalytic lithography on silicon. For a UV irradiation time of 1.5 h the photomask is clearly replicated with 120 nm-thick PMMA brushes but the internal microstructure is barely visible, also the surrounding surface is heavily stained with polymer (thickness ca. 39 nm). After 2 h, the exposed surface is completely free from polymer and after 2.5 h the pattern replica is completely developed. The resolution of the latter is improved after 3 h of irradiation. The blue color of brushes is due to optical effects.

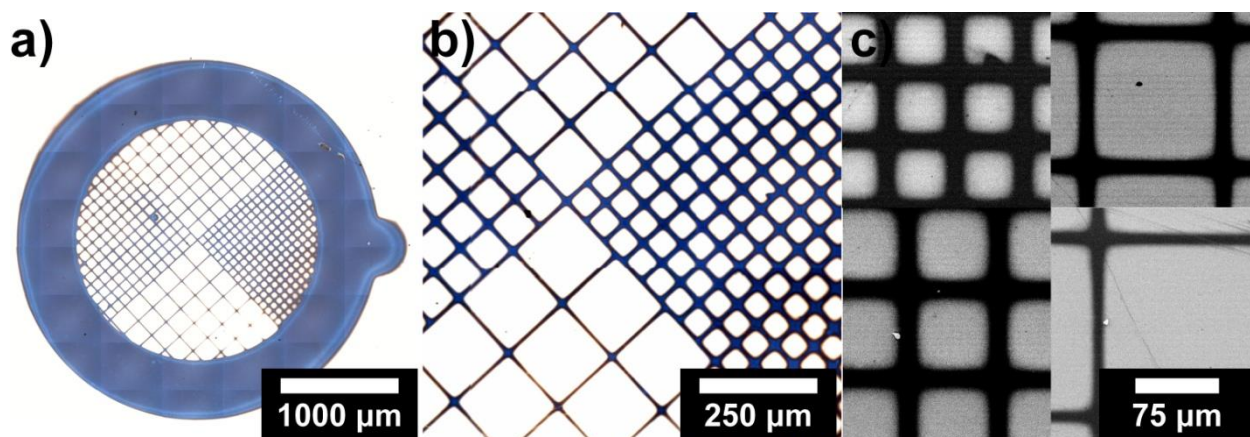


Figure 1.17 Patterning by remote photocatalytic lithography of initiators and subsequent SI-ATRP. a,b) Optical microscopy and c) scanning electron microscopy of the patterned PMMA brushes obtained on silicon.

Patterning of functional polymer brushes for the development of silicon wafer-based electrochemical devices

Remote photocatalytic lithography is successfully applied to modify silicon wafer electrodes with different patterns of polymer brushes to perform electrochemical experiments. This work is described in detail in Chapter 3 (Figure 1.18).

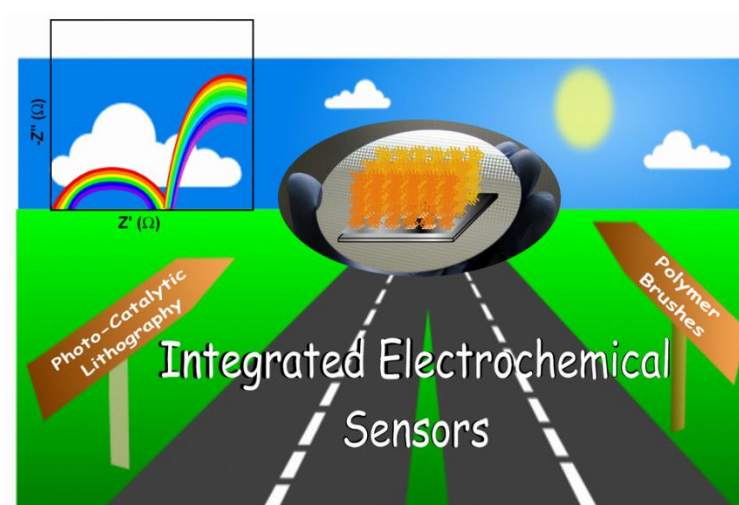


Figure 1.18 Polymer brushes can make silicon wafer electrochemically responsive, making possible to develop integrated electrochemical sensors.

Coupling remote photocatalysis with nanosphere lithography

Nanosphere lithography employs self-assembled arrays of nano- or microspheres, typically made of polymer or silica, as lithographic and/or evaporation masks. Due to the very low size of the particles, nanoscale features such as arrays of dots and other features can be fabricated in an economical way [91].

Here we coupled remote photocatalysis with nanosphere lithography to achieve nanoscale patterning of polymer brushes. First, a 1%_{m/v} ethanol suspension of poly(styrene) particles (mean diameter 1 μm , prepared by dispersion polymerization. For details see the Specific procedures section) is spread on the surface of a BIB-APTES-functionalized silicon substrate. Particle self-assembly is then obtained by means of spin-coating (2000 rpm, 500 rpm s⁻¹, 20 s). A sparse particle array is generated, due to the scarce affinity of the nanoparticles towards the surface (Figure 1.19). Typical protocols for the self-assembly of particles are described for highly hydrophilic surfaces [92], in which surface tension effects can drastically help the formation of ordered arrays. In our case, surfactants such as Triton X-100 have been tried to improve the assembly process but without relevant results.

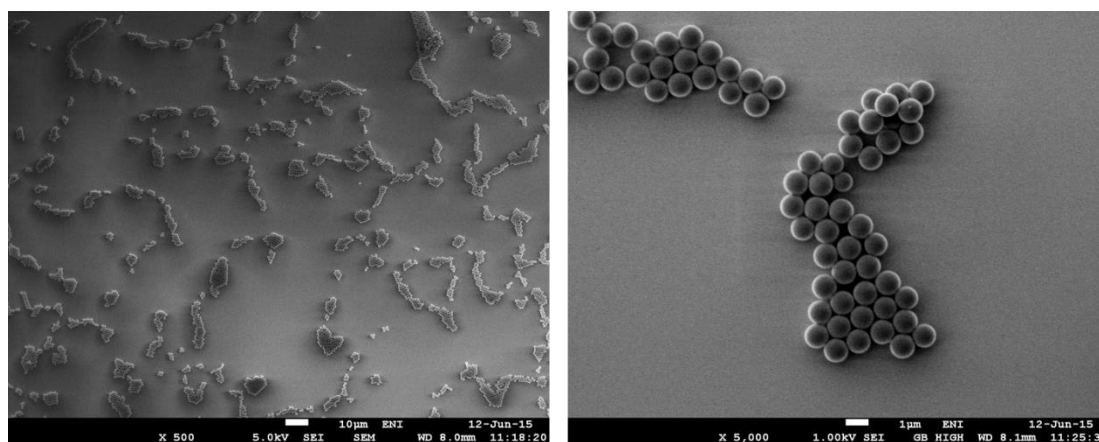


Figure 1.19 Scanning electron microscopy images of the particle arrays generated on BIB-APTES-functionalized silicon wafer.

The resulting particle arrays are subjected to remote photocatalytic lithography for 2.5 h according to the procedure described in the previous paragraph. The particles are then removed simply by sonication in ethanol for 5 minutes and the substrates are dried under nitrogen. The obtained pattern is eventually amplified with PMMA brushes (polymerization time: 4 h) using the SI-ATRP protocol described in the Specific procedures paragraph. Figure 1.20 shows the morphology of the resulting patterns.

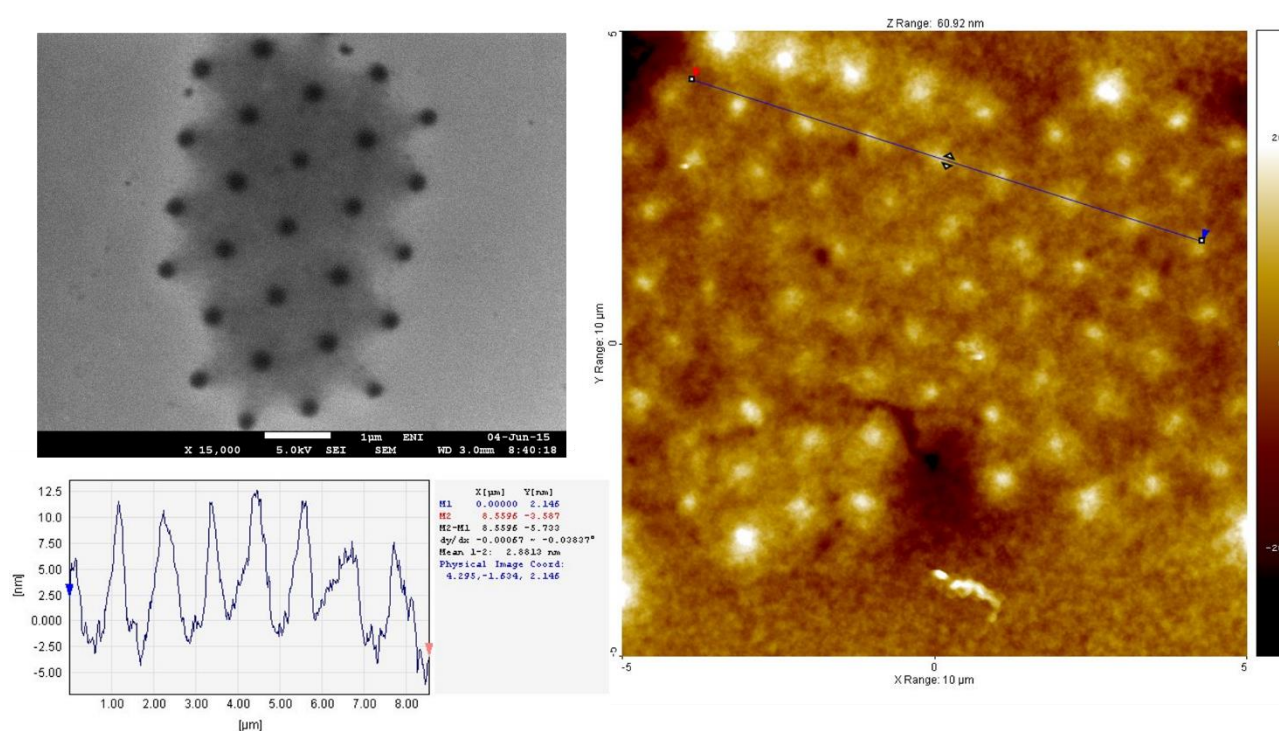
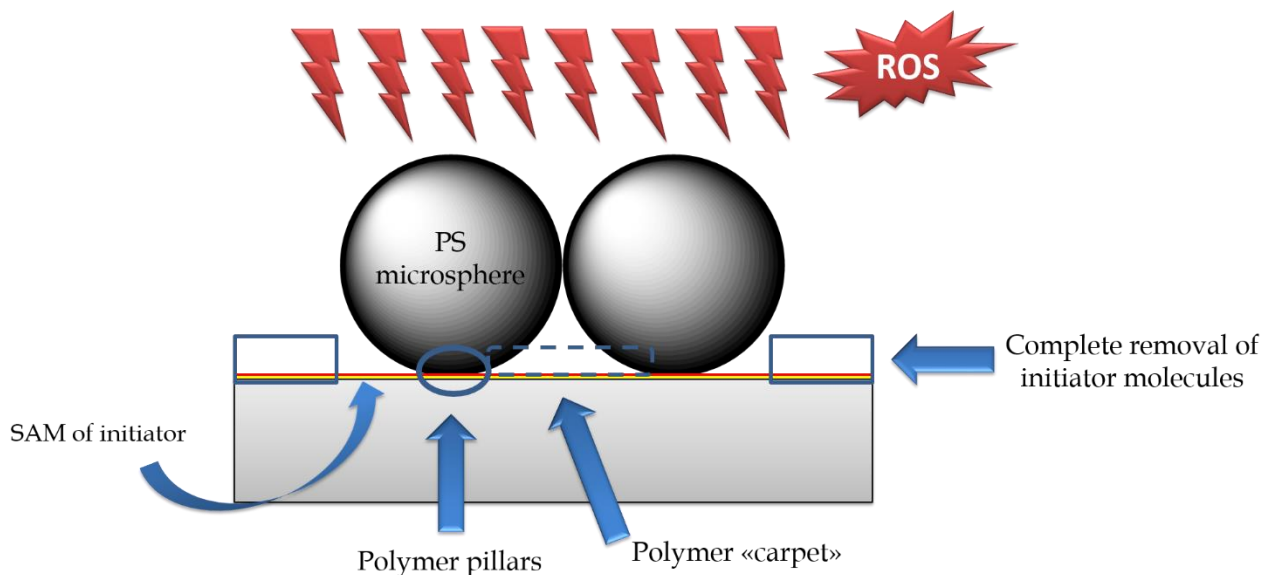


Figure 1.20 SEM and AFM images of the patterns obtained after 2.5 h of remote photocatalytic lithography coupled to nanosphere lithography and amplification by SI-ATRP.

From the morphological analysis it can be deduced that, after SI-ATRP, arrays of polymer brushes shaped as conical pillars emerging from a polymer “carpet” are obtained. We hypothesize that this peculiar morphology would originate from an anisotropic, gradient-like etching due to the diffusion of photocatalytically-generated ROS under the particles.

According to Scheme 1.2, pillars would arise from the zones where the particles actually touch the substrate, efficiently screening the underlying initiator molecules from the etching action of ROS, while the “carpet” would originate from inter-particle spaces.



Scheme 1.2 Proposed etching processes leading to the formation of polymer pillars and carpets as a result of remote photocatalysis coupled to nanosphere lithography.

1.3 Conclusion

The growing excitement in the field of polymer brushes and the proved request for efficient patterning strategies urge the introduction of facile and low-cost methods to develop such architectures. Here, we discussed for the first time the use of photocatalytic lithography for making patterned polymer brushes, clearly showing how innovative this approach could be. Titanium dioxide film with high photoactivity are employed to selectively degrade initiators of polymerization under near-UV irradiation using a simple contact photomask and the obtained patterns were replicated by SI-ATRP. Access to negative patterns was demonstrated through the use of sacrificial SAMs.

While direct photocatalytic lithography could be obtained only on the surface of a titania layer, the remote approach allowed to achieve photocatalytic patterning on virtually any kind of substrate thanks to the migration of oxidizing species from a TiO₂ interface. Both approaches lead to sharp edges and high line resolution. The remote approach is especially relevant being a general, non-invasive and high-throughput lithographic technique. We also demonstrated the successful coupling of remote photocatalysis with nanosphere lithography to obtain arrays of pillars made of polymer brushes. The obtained results are even more relevant considering that even cheap, conventional glass (with a significant inner filter effect towards UV radiation) instead than expensive quartz can be used as a support for titanium dioxide films used to perform photocatalysis experiments.

Our process can be scaled up to the wafer scale, with the future final goal to design controlled areas with different functionalities, useful for applications *e.g.* in microfluidics and for the development of cell-responsive surfaces.

1.4 Specific procedures

Materials: All the chemicals, unless otherwise stated, were reagent grade, purchased from Aldrich and used as received. Monomers were filtered through an inhibitor-remover column and stored at -18 °C until use. Silicon (100) wafers, single-polished, n type, phosphorus doped, 3 – 6 (Ω cm), with a native oxide layer ca. 1.5 nm thick, were purchased from Ultrasil Corporation. Cleaning and activation of TiO₂ films is accomplished using a Spectroline crosslinker equipped with 254 nm UV lamps. Photocatalytic patterning was achieved using a Jelosil HG500 halogen lamp (refer to Appendix C for details).

Characterization methods: Thickness is measured using a Filmetrics F20 reflectometer. Each value is the average of at least three measurements performed on different spots of a same sample. Water contact angle analyses are performed using a Krüss Easy Drop

Standard with DSA1 software. A 3 μ L-drop of HPLC-grade water is deposited and the contact angle measured after 5 s. Each value is the average of at least three measurements performed on different spots of a same sample. Atomic force microscopy (AFM) pictures are acquired on an Ntegra Aura AFM (NT-MDT) device in tapping mode, with NSC35/AIBS tips (μ masch). Scanning electron microscopy (SEM) was performed using a Jeol JSM 7600f Schottky Field Emission Scanning Electron Microscope; to facilitate imaging samples were deposited on conducting carbon tape. X-ray photoelectron spectroscopy (XPS) analyses were performed by a PHI-5500 - Physical Electronics spectrometer, equipped with a monochromatized source with aluminum anode ($K\alpha = 1486.6$ eV) operating at a 200 W of applied power. Samples were placed in UHV (10^{-9} Torr) and irradiated with 200 kV X-rays, survey scans were recorded at a 23.50 eV pass energy, 0.2 s time per step and 0.5 eV energy-step. XPS spectra were collected at takeoff angles of 45° . The analysis area was 0.8 mm² and the depth was within 10 nm. The spectrometer was calibrated assuming the Ag(3d 5/2) binding energy (BE) at 368.3 eV with respect to the Fermi-level and the measured full width half maximum (FWHM) was 0.46 eV. The quantitative analysis data were reported as atomic percentage of elements and the normalization was performed without including hydrogen. Optical microscopy images and high resolution FTIR spectra were acquired using a Nicolet™ iN™10 Infrared Microscope in transmittance (for silicon samples) or reflectance (for titania samples) mode, with a liquid nitrogen-cooled MCT detector (spectral range 4000 - 675 cm⁻¹, resolution 4 cm⁻¹, aperture 150 x 150 μ m). Background (500 scans) was collected before each sample (1000 scans) from cleaned silicon or titanium dioxide. Baseline correction was performed automatically by the acquisition software.

TITANIUM DIOXIDE FILM DEPOSITION

Refer to Appendix C

SYNTHESIS OF THE ATRP INITIATOR (BIB-APTES)

Refer to Appendix C

GRAFTING OF THE BIB-APTES INITIATOR

Refer to Appendix C

SURFACE-INITIATED POLYMERIZATION

SI-ARGET ATRP of methyl methacrylate (MMA)

In a nitrogen-purged Schlenk flask 0.021 g (~ 0.07 mmol) of tris(2-pyridylmethyl)amine (TPMA), 0.002 g (~ 0.01 mmol) of copper(II) bromide and 0.023 g (0.13 mmol) of ascorbic acid are dissolved in 10 mL of a 4:1 v/v methanol-water mixture previously degassed by nitrogen bubbling. 10 mL (94 mmol) of degassed MMA are added and the mixture is stirred under nitrogen. A 5 mL-aliquot of this mixture is poured over the initiator-functionalized substrates placed separately in nitrogen-purged Schlenk flasks which are immersed in an oil bath at 30 °C to allow polymerization. The polymerization time was varied from 0.5 to 8 h to control thickness. Samples are then rinsed extensively with THF, gently sonicated in the same solvent and dried under a nitrogen stream.

SI-ATRP of styrene (S)

In a nitrogen-purged Schlenck flask 0.1 g (0.7 mmol) of copper(I) bromide are dissolved in a degassed solution of 270 μ L (1.3 mmol) of pentamethyldiethylenetriamine (PMDETA) in 10 mL DMSO. Then 30 mL (~ 260 mmol) of degassed styrene are added and the mixture is stirred under nitrogen. A 5 mL-aliquot of this mixture is poured over each initiator-functionalized substrate placed in a nitrogen purged Schlenck flask immersed in an oil bath at 90 °C to allow polymerization. After reaction, the sample is rinsed extensively with THF, gently sonicated in the same solvent and dried under a nitrogen stream.

SI-ATRP of dimethylaminoethyl methacrylate (DMAEMA)

Each initiator-functionalized substrate was placed in a nitrogen-purged Schlenck flask and covered with 5 mL of a polymerization mixture prepared as follow. In a nitrogen-purged Schlenck flask 0.312 g (2.0 mmol) of bipyridyl and 0.144 g (1.0 mmol) of copper(I) bromide were dissolved in 6 mL of a 4:1 v/v methanol-water mixture previously degassed by bubbling nitrogen. 14 mL (83 mmol) of degassed DMAEMA were added and the mixture was stirred under nitrogen to obtain a homogeneous solution. For polymerizations with added deactivator the polymerization mixture contained also 11 mg (0.05 mmol) of copper(II) bromide. Polymerization proceeded at 30 °C for different times to control the brush thickness. After polymerization the samples were rinsed extensively with ethanol, gently sonicated in the same solvent and dried under a nitrogen stream.

SYNTHESIS OF POLY(STYRENE) MICROPARTICLES

The synthesis of poly(styrene) microparticles is accomplished using a simple dispersion polymerization protocol. First, 1.2 g of poly(vinylpyrrolidone) (M_w ca. 360000 g mol⁻¹) are dissolved in 170 g of ethanol in a 500 mL three-necked round bottomed flask equipped with a mechanical stirrer and an Allihn condenser. The mixture is degassed under stirring by bubbling nitrogen for a convenient time (about 30 min), then 30 g of styrene and 0.6 g of azobis(isobutyronitrile) (AIBN) are added and the mixture is degassed again. The homogeneous solution is then heated at 60 °C using an oil bath to start the polymerization. After 24 h the resulting latex is diluted with ethanol, the particles collected by centrifugation (9000 rpm, 15 min) and redispersion in ethanol.

1.5 References

- [1] R. Barbey, L. Lavanant, D. Paripovic, N. Schuwer, C. Sugnaux, S. Tugulu and H.-A. Klok, *Chem. Rev.*, **2009**, *109*, 5437–5527.
- [2] S. G. Boyes, A. M. Granville, M. Baum, B. Akgun, B. K. Mirous and W. J. Brittain, *Surf. Sci.*, **2004**, *570*, 1–12.
- [3] O. Azzaroni, *J. Polym. Sci., Part A: Polym. Chem.*, **2012**, *50*, 3225–3258.
- [4] T. Chen, I. Amin and R. Jordan, *Chem. Soc. Rev.*, **2012**, *41*, 3280–3296.
- [5] M. E. Welch and C. K. Ober, *J. Polym. Sci., Part B: Polym. Phys.*, **2013**, *51*, 1457–1472.
- [6] G. J. Dunderdale, J. R. Howse and J. P. A. Fairclough, *Langmuir*, **2011**, *27*, 11801–11805.
- [7] J. Cui, O. Azzaroni and A. del Campo, *Macromol. Rapid Commun.*, **2011**, *32*, 1699–1703.
- [8] G. J. Dunderdale and J. P. A. Fairclough, *Langmuir*, **2013**, *29*, 3628–3635.
- [9] M. Singh, O. Odusanya, G. M. Wilmes, H. B. Eitouni, E. D. Gomez, A. J. Patel, V. L. Chen, M. J. Park, P. Fragouli, H. Iatrou, N. Hadjichristidis, D. Cookson and N. P. Balsara, *Macromolecules*, **2007**, *40*, 4578–4585.
- [10] C. R. Daniels, L. J. Tausin, E. Foster, R. C. Advincula and C. F. Landes, *J. Phys. Chem. B*, **2013**, *117*, 4284–4290.

- [11] I. Tokareva, I. Tokarev, S. Minko, E. Hutter and J. H. Fendler, *Chem. Commun.*, **2006**, 3343–3345.
- [12] T. Chen, R. Ferris, J. Zhang, R. Ducker and S. Zauscher, *Prog. Polym. Sci.*, **2010**, *35*, 94–112.
- [13] H. Ma, J. He, X. Liu, J. Gan, G. Jin and J. Zhou, *ACS Appl. Mater. Interfaces*, **2010**, *2*, 3223–3230.
- [14] H. C. McCaig, E. Myers, N. S. Lewis and M. L. Roukes, *Nano Lett.*, **2014**, *14*, 3728–3732.
- [15] C. Xu, X. Fu, M. Fryd, S. Xu, B. B. Wayland, K. I. Winey and R. J. Composto, *Nano Lett.*, **2006**, *6*, 282–287.
- [16] S. Kumar, Y. L. Dory, M. Lepage and Y. Zhao, *Macromolecules*, **2011**, *44*, 7385–7393.
- [17] H. J. Snaith, G. L. Whiting, B. Sun, N. C. Greenham, W. T. S. Huck and R. H. Friend, *Nano Lett.*, **2005**, *5*, 1653–1657.
- [18] G. Gunkel, M. Weinhart, T. Becherer, R. Haag and W. T. S. Huck, *Biomacromolecules*, **2011**, *12*, 4169–4172.
- [19] D. Falconnet, G. Csucs, H. M. Grandin and M. Textor, *Biomaterials*, **2006**, *27*, 3044–3063.
- [20] S. Peng and B. Bhushan, *RSC Adv.*, **2012**, *2*, 8557.
- [21] F. Zhou and W. T. S. Huck, *Phys. Chem. Chem. Phys.*, **2006**, *8*, 3815.
- [22] S. Dai, P. Ravi and K. C. Tam, *Soft Matter*, **2008**, *4*, 435.
- [23] A. Olivier, F. Meyer, J. Raquez, P. Damman and P. Dubois, *Prog. Polym. Sci.*, **2012**, *37*, 157–181.
- [24] D. M. Jones and W. T. S. Huck, *Adv. Mater.*, **2001**, *13*, 1256.
- [25] S. Santer, A. Kopyshv, H. Yang and J. R uhe, *Macromolecules*, **2006**, *39*, 3056–3064.
- [26] O. A. Guskova and C. Seidel, *Macromolecules*, **2011**, *44*, 671–682.
- [27] S. Santer, A. Kopyshv, J. Donges, J. R uhe, X. Jiang, B. Zhao and M. M uller, *Langmuir*, **2007**, *23*, 279–285.
- [28] Y.-K. Lai, Z. Chen and C.-J. Lin, *J. Nanoeng. Nanomanuf.*, **2011**, *1*, 18–34.
- [29] A. Ulman, *Chem. Rev.*, **1996**, *96*, 1533–1554.
- [30] M. Geissler and Y. Xia, *Adv. Mater.*, **2004**, *16*, 1249–1269.

- [31] Q. Liu, C. Wu, H. Cai, N. Hu, J. Zhou and P. Wang, *Chem. Rev.*, **2014**, *114*, 6423–6461.
- [32] E. Menard, M. A. Meitl, Y. Sun, J. Park, D. J. Shir, Y. Nam, S. Jeon and J. A. Rogers, *Chem. Rev.*, **2007**, *107*, 1117–1160.
- [33] Y. Li, J. Zhang, L. Fang, L. Jiang, W. Liu, T. Wang, L. Cui, H. Sun and B. Yang, *J. Mater. Chem.*, **2012**, *22*, 25116.
- [34] T. Chen, D. P. Chang, R. Jordan and S. Zauscher, *Beilstein J. Nanotechnol.*, **2012**, *3*, 397–403.
- [35] T. Chen, R. Jordan and S. Zauscher, *Polymer*, **2011**, *52*, 2461–2467.
- [36] Y. Tsujii, M. Ejaz, S. Yamamoto, T. Fukuda, K. Shigeto, K. Mibu and T. Shinjo, *Polymer*, **2002**, *43*, 3837–3841.
- [37] S. J. Ahn, M. Kaholek, W.-K. Lee, B. LaMattina, T. H. LaBean and S. Zauscher, *Adv. Mater.*, **2004**, *16*, 2141–2145.
- [38] M. Kaholek, W. Lee, B. LaMattina, K. C. Caster and S. Zauscher, *Nano Lett.*, **2004**, *4*, 373–376.
- [39] E. ul Haq, Z. Liu, Y. Zhang, S. a. A. Ahmad, L.-S. Wong, S. P. Armes, J. K. Hobbs, G. J. Leggett, J. Micklefield, C. J. Roberts and J. M. R. Weaver, *Nano Lett.*, **2010**, *10*, 4375–4380.
- [40] X. Fan, L. Lin, J. L. Dalsin and P. B. Messersmith, *Polym. Prepr.*, **2005**, *46*, 442–443.
- [41] J.-K. Chen, Z.-Y. Chen, H.-C. Lin, P.-D. Hong and F.-C. Chang, *ACS Appl. Mater. Interfaces*, **2009**, *1*, 1525–1532.
- [42] N. Herzer, S. Hoepfener and U. S. Schubert, *Chem. Commun.*, **2010**, *46*, 5634–5652.
- [43] S. Hoepfener, R. Maoz and J. Sagiv, *Nano Lett.*, **2003**, *3*, 761–767.
- [44] S. A. Ahmad, G. J. Leggett, A. Hucknall and A. Chilkoti, *Biointerphases*, **2011**, *6*, 8–15.
- [45] R. Iwata, P. Suk-In, V. P. Hoven, A. Takahara, K. Akiyoshi and Y. Iwasaki, *Biomacromolecules*, **2004**, *5*, 2308–2314.
- [46] S. Tugulu, M. Harms, M. Fricke, D. Volkmer and H.-A. Klok, *Angew. Chem., Int. Ed.*, **2006**, *45*, 7458–7461.
- [47] O. P. Khatri, H. Sano, K. Murase and H. Sugimura, *Langmuir*, **2008**, *24*, 12077–12084.
- [48] M. Yamaguchi, K. Ikeda, M. Suzuki, A. Kiyohara, S. N. Kudoh, K. Shimizu, T. Taira, D. Ito, T. Uchida and K. Gohara, *Langmuir*, **2011**, *27*, 12521–12532.

- [49] S. Sun and G. J. Leggett, *Nano Lett.*, **2007**, 7, 3753–3758.
- [50] S. Nishimoto, A. Kubo, K. Nohara, X. Zhang, N. Taneichi, T. Okui, Z. Liu, K. Nakata, H. Sakai, T. Murakami, M. Abe, T. Komine and A. Fujishima, *Appl. Surf. Sci.*, **2009**, 255, 6221–6225.
- [51] Z. Xie, C. Chen, X. Zhou, T. Gao, D. Liu, Q. Miao and Z. Zheng, *ACS Appl. Mater. Interfaces*, **2014**, 6, 11955–11964.
- [52] K. Nakata and A. Fujishima, *J. Photochem. Photobiol. C*, **2012**, 13, 169–189.
- [53] K. Liu, M. Cao, A. Fujishima and L. Jiang, *Chem. Rev.*, **2014**, 114, 10044–10094.
- [54] H. Park, Y. Park, W. Kim and W. Choi, *J. Photochem. Photobiol. C*, **2013**, 15, 1–20.
- [55] U. Diebold, *Surf. Sci. Rep.*, **2003**, 48, 53–229.
- [56] C. Marchiori, G. Di Liberto, G. Soliveri, L. Loconte, L. Lo Presti, D. Meroni, M. Ceotto, C. Oliva, S. Cappelli, G. Cappelletti, C. Aieta and S. Ardizzone, *J. Phys. Chem. C*, **2014**, 118, 24152–24164.
- [57] K. Nakata, T. Ochiai, T. Murakami and A. Fujishima, *Electrochim. Acta*, **2012**, 84, 103–111.
- [58] A. Antonello, G. Soliveri, D. Meroni, G. Cappelletti and S. Ardizzone, *Catal. Today*, **2014**, 230, 35–40.
- [59] O. Carp, *Prog. Solid State Chem.*, **2004**, 32, 33–177.
- [60] G. Soliveri, R. Annunziata, S. Ardizzone, G. Cappelletti and D. Meroni, *J. Phys. Chem. C*, **2012**, 116, 26405–26413.
- [61] G. Soliveri, D. Meroni, G. Cappelletti, R. Annunziata, V. Aina, G. Cerrato and S. Ardizzone, *J. Mater. Sci.*, **2014**, 49, 2734–2744.
- [62] Y. Paz, *Beilstein J. Nanotechnol.*, **2011**, 2, 845–861.
- [63] G. Maino, D. Meroni, V. Pifferi, L. Falcicola, G. Soliveri, G. Cappelletti and S. Ardizzone, *J. Nanopart. Res.*, **2013**, 15, 2087.
- [64] Q. Xu, D. V. Wellia, M. A. Sk, K. H. Lim, J. S. C. Loo, D. W. Liao, R. Amal and T. T. Y. Tan, *J. Photochem. Photobiol. A*, **2010**, 210, 181–187.
- [65] A. Fujishima, X. Zhang and D. Tryk, *Surf. Sci. Rep.*, **2008**, 63, 515–582.
- [66] X. He, W. Yang and X. Pei, *Macromolecules*, **2008**, 41, 4615–4621.

- [67] K. Matyjaszewski, P. J. Miller, N. Shukla, B. Immaraporn, A. Gelman, B. B. Luokala, T. M. Siclovan, G. Kickelbick, T. Vallant, H. Hoffmann and T. Pakula, *Macromolecules*, **1999**, *32*, 8716–8724.
- [68] S. Edmondson, V. L. Osborne and W. T. S. Huck, *Chem. Soc. Rev.*, **2004**, *33*, 14–22.
- [69] K. Matyjaszewski, H. Dong, W. Jakubowski, J. Pietrasik and A. Kusumo, *Langmuir*, **2007**, *23*, 4528–4531.
- [70] Y. Ma, X. Cao, X. Feng, Y. Ma and H. Zou, *Polymer*, **2007**, *48*, 7455–7460.
- [71] A. Samadi, S. M. Husson, Y. Liu, I. Luzinov and S. Michael Kilbey, *Macromol. Rapid Commun.*, **2005**, *26*, 1829–1834.
- [72] S. G. Boyes, A. M. Granville, M. Baum, B. Akgun, B. K. Mirous, W. J. Brittain, *Surf. Sci.*, **2004**, *570*, 1–12.
- [73] T. Chen, I. Amin, R. Jordan, *Chem. Soc. Rev.*, **2012**, *41*, 3280–3296.
- [74] T. Chen, R. Ferris, J. Zhang, R. Ducker, S. Zauscher, *Prog. Polym. Sci.*, **2010**, *35*, 94–112.
- [75] S. Kumar, Y. L. Dory, M. Lepage, Y. Zhao, *Macromolecules*, **2011**, *44*, 7385–7393.
- [76] G. J. Dunderdale, J. P. A. Fairclough, *Langmuir*, **2013**, *29*, 3628–3635.
- [77] L. A. Fielding, S. Edmondson, S. P. Armes, *J. Mater. Chem.*, **2011**, *21*, 11773–11780.
- [78] H. Zhang, B. Klumperman, W. Ming, H. Fischer, Rob van der Linde, *Macromolecules*, **2001**, *34*, 6169–6173.
- [79] C. Xu, T. Wu, C. M. Drain, J. D. Batteas, M. J. Fasolka, K. L. Beers, *Macromolecules*, **2006**, *39*, 3359–3364.
- [80] H.-J. Koo, K. V. Waynant, C. Zhang, R. T. Haasch, P. V. Braun, *Chem. Mater.*, **2014**, *26*, 2678–2683.
- [81] S. Sanjuan, P. Perrin, N. Pantoustier, Y. Tran, *Langmuir*, **2007**, *23*, 5769–5778.
- [82] P. van de Wetering, N. J. Zuidam, M. J. van Steenbergen, O. A. G. J. van der Houwen, W. J. M. Underberg, W. E. Hennink, *Macromolecules*, **1998**, *31*, 8063–8068.
- [83] G. Soliveri, D. Meroni, G. Cappelletti, R. Annunziata, V. Aina, G. Cerrato and S. Ardizzone, *J. Mater. Sci.*, **2014**, *49*, 2734–2744.
- [84] X. Fan, L. Lin, J. L. Dalsin, P. B. Messersmith, *J. Am. Chem. Soc.*, **2005**, *127*, 15843–15847.

- [85] T. Tatsuma, S. Tachibana, T. Miwa, D. A. Tryk and A. Fujishima, *J. Phys. Chem. B*, **1999**, *103*, 8033–8035.
- [86] W. Kubo and T. Tatsuma, *J. Am. Chem. Soc.*, **2006**, *128*, 16034–16035.
- [87] T. Tatsuma, W. Kubo and A. Fujishima, *Langmuir*, **2002**, *18*, 9632–9634.
- [88] N. Blondiaux, S. Zürcher, M. Liley and N. D. Spencer, *Langmuir*, **2007**, *23*, 3489–3494.
- [89] T. Tatsuma, S. Tachibana and A. Fujishima, *J. Phys. Chem. B*, **2001**, *105*, 6987–6992.
- [90] W. Kubo, T. Tatsuma, A. Fujishima and H. Kobayashi, *J. Phys. Chem. B*, **2004**, *108*, 3005–3009.
- [91] X. Ye, L. Qi, *Nano Today*, **2011**, *6*, 608–631.
- [92] J. Chen, P. Dong, D. Di, C. Wang, H. Wang, J. Wang, X. Wu, *Appl. Surf. Sci.*, **2013**, *270*, 6–15

Chapter 2

SERS-Active Patterns Obtained by Photocatalytic Shaping of Self-Assembled Silver Nanoprisms

Abstract

Self-assembled triangular silver nanoprisms on the surface of a photocatalytically active titanium dioxide film are shaped into smaller nanospheres by near-UV irradiation. This phenomenon can be applied as a patterning strategy to perform spatially resolved microSERS, since silver nanoprisms and nanospheres display a dramatically different SERS behavior. Interestingly, silver nanoprisms are not affected at all by remote photocatalysis, suggesting that a direct interaction between titania and silver nanoparticles takes place under UV light and is responsible for the observed phenomena.

2.1 Introduction

Surface-enhanced Raman scattering (SERS) is a leading non-destructive technique that can extend the sensitivity of Raman spectroscopy to the single-molecule detection level. In the recent years, researchers have found that metallic nanostructures can give rise to dramatic enhancements of the Raman signals thanks to the surface plasmon-polariton near-fields generated by the interaction of a light source with an active substrate in the form of either nanoparticles, nanostructures, or electrochemically roughened surfaces [1].

For this reason, noble metals such as Au and Ag are most often employed as their surface plasmon resonance is in the visible or near-infrared region of the electromagnetic radiation. It is widely acknowledged that Raman signals are also closely related to the morphology of SERS substrate, therefore metals with different architectures have been widely constructed to get effective SERS active-substrate. Structurally, most SERS substrates are made from pure metallic nanostructures with multiple shapes, such as nanoparticles, nanorods, nanocubes, nanotriangles, and core-shell nanoparticles [2].

Recently, it has been found that TiO_2 can be used as a possible candidate for the fabrication of SERS substrates [3-5] and that depositing silver nanoparticles onto TiO_2 can enhance the Raman scattering effect because of the synergetic contribution of incorporated metal and the semiconductor [6,7].

SERS applications span various fields, including analytical chemistry, life science, medical science, and the characterization of trace chemical species. Its acceptance as

a general analytical tool will be promoted if cheaper and easier to make and handle SERS substrates become available [8].

Fabrication of periodic arrays of nanoparticles can be accomplished by patterning techniques such as photolithography, nanosphere lithography, electron beam lithography, and focused ion beam milling. However, most are too technologically demanding and expensive to be used to fabricate large quantities of substrates for practical applications. In addition, the problem that traditional SERS substrates are single-use has resulted in its availability not being fully explored or recognized by the analytical scientists as a routine analytical technique. Consequently, reducing the cost of preparing SERS-active substrates by developing a cheap technique of preparing SERS-active substrates is a significant topic.

Silver nanoprisms are gaining interest for applications concerning photophysical processes *e.g.* to increase the light harvesting efficiency of photoactive materials with applications from dye-sensitized solar cells (DSSCs) to enhanced photocatalysis to sensing, thanks to their peculiar optical properties arising from their surface plasmon resonance [8,9]. Their usefulness for SERS purposes has also been demonstrated [10]. Assemblies of silver nanoprisms are typically made using nanosphere lithography or are produced by photochemical deposition. Nanosphere lithography, while offering good control over uniformity and spatial distribution of the particles, is not very suitable for large-surface applications and requires special skills and dedicated instrumentation [11]. On the other hand, photochemical deposition could be highly suitable for large-surface applications but does not allow sufficient control on the shape and size distribution of the particles [12].

Self-assembly of pre-made silver nanoprisms could be a good compromise between these two strategies. In the present work, silver nanoprisms previously synthesized with a controlled etching process are self-assembled on 3-aminopropyltriethoxysilane (APTES)-functionalized titanium dioxide films. The presence of APTES is necessary since no adhesion of silver nanoprisms is not observed on the bare surface of titania.

Then, by irradiating with near-UV light the resulting composite in presence of a simple contact photomask (a TEM grid), as described in Chapter 1, we are able to photocatalytically shape nanoprisms into nanospheres. Since these two shapes display different SERS behavior, we are able to obtain a spatial contrast in the SERS signal of the underlying titania.

2.2 Results and Discussion

Triangular silver nanoprisms: synthesis and characterization

Silver nanoprisms are synthesized using an established protocol (see the Specific procedures section for details) [13]. The UV-vis spectrum of the obtained blue nanoprisms suspension features a sharp peak at 333 nm, a shoulder at around 450 nm and an intense band at around 725 nm (Figure 2.1). These three features are, according to theoretical calculations, assigned respectively to the plasmon resonance of out-of-plane quadrupoles, in-plane quadrupoles and in-plane dipoles. The absence of a peak around 400 nm demonstrates the absence of silver nanospheres.

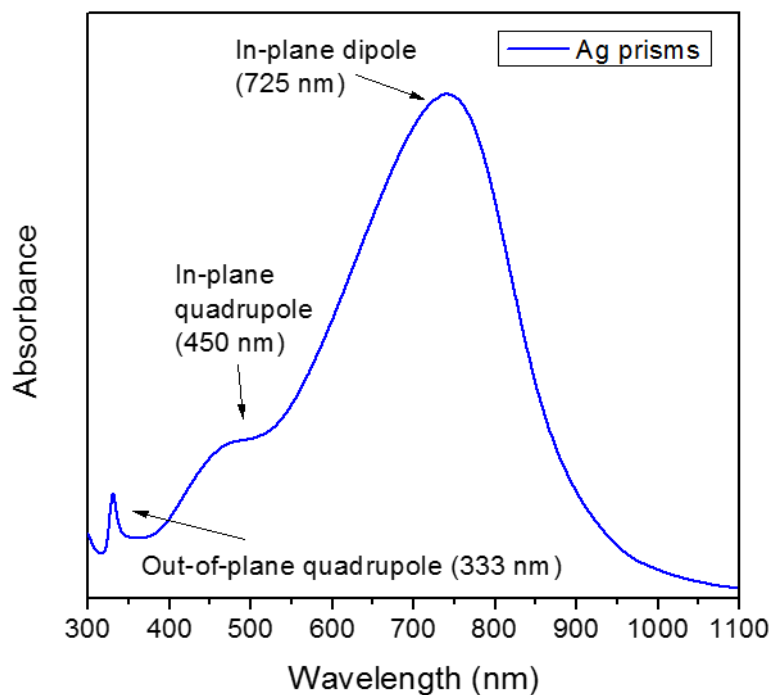


Figure 2.1 UV-vis spectrum of the aqueous suspension of silver nanoprisms.

Successful nanoprisms synthesis is confirmed also by high-resolution transmission electron microscopy (HRTEM) which shows planar particles with triangular shape, mean edge length 34 nm and mean thickness 4 nm. Lattice fringes of ca. 214 pm, corresponding to the (111) orientation, are visible revealing that the nanoprisms are crystalline (Figure 2.2).

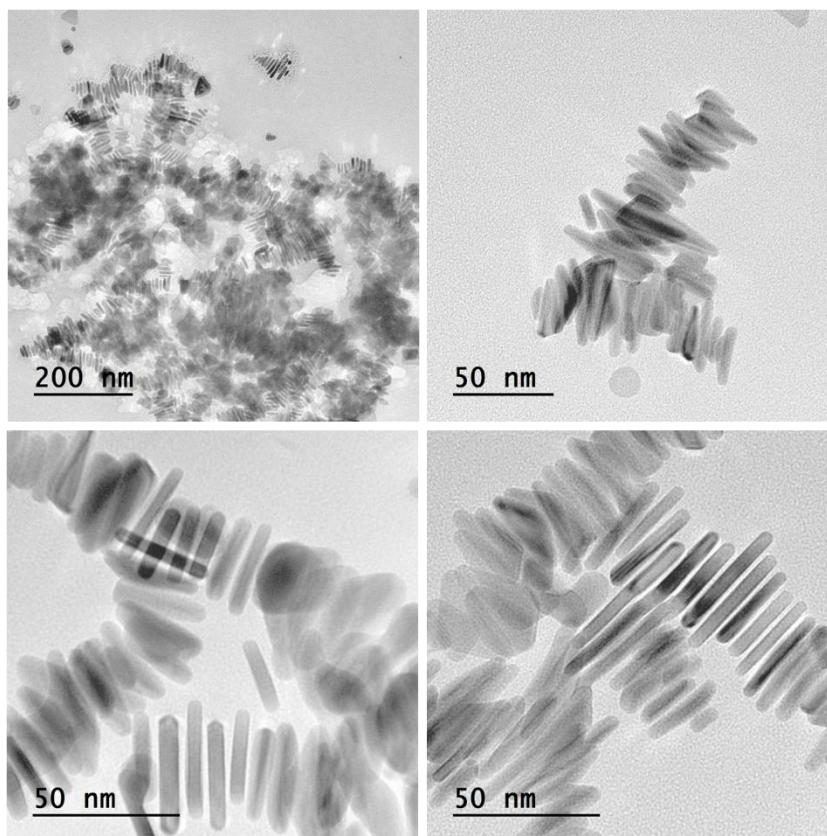


Figure 2.2 HRTEM images of silver triangular nanoprisms. Side stacking is due to their low affinity for the support.

The crystalline nature of silver nanoprisms is definitely proved by the X-ray diffraction pattern obtained for a concentrated film of nanoprisms embedded in a poly(vinyl alcohol) (PVA) matrix (Figure 2.3). The presence of only (111) Ag signal is coherent with the currently accepted mechanism of formation of silver nanoprisms, that is selective growth of (111) facets [14].

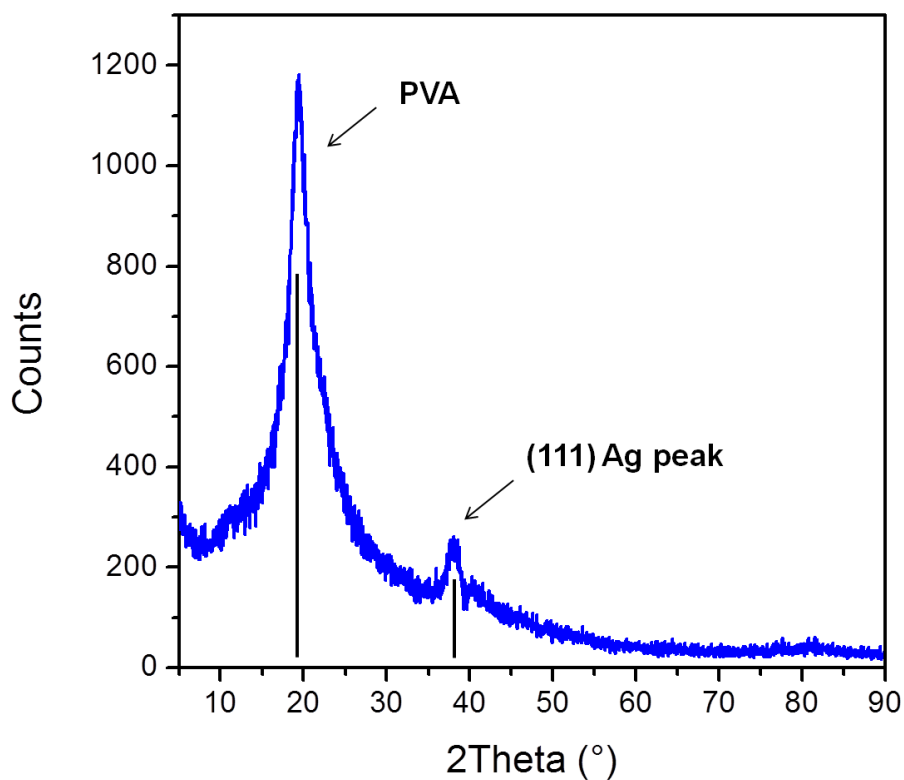


Figure 2.3 XRD pattern of silver nanoprisms showing the (111) peak.

Self-assembly and photocatalytic shaping of silver nanoprisms

Functionalization of titania with APTES is, as previously mentioned, a necessary step to promote self-assembly of silver nanoprisms (see the Specific procedures paragraph for the necessary details). According to SEM images (Figure 2.4), the titania surface is homogeneously covered with silver nanoprisms.

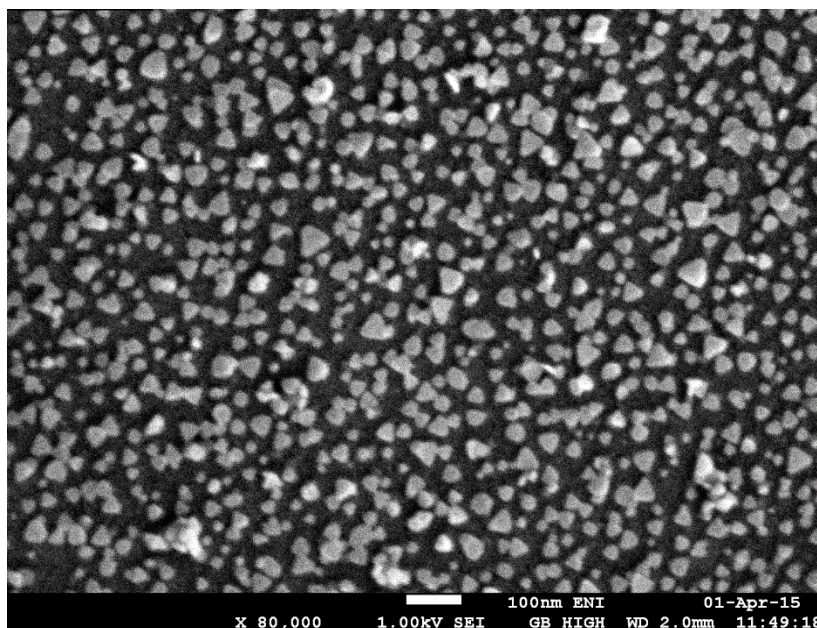


Figure 2.4 SEM image of silver nanoprisms self-assembled on APTES-functionalized titania.

By direct irradiation in air with 365 nm-UV light of a sample, like that shown in Figure 2.4, silver nanoprisms are changed into spherical nanoparticles. A kinetic study, performed by imaging samples irradiated for increasing times, shows that the photoshaping process is quite fast and that it apparently reaches a plateau after 1 h (Figure 2.5). Rounding of corners and even the disappearance of smaller nanoprisms is visible just after 15 min of irradiation. It has been reported for silver nanoparticles that plasmon-induced charge separation (PICS)-based oxidative dissolution of Ag proceeds preferentially at the sites where the plasmonic near field is strongly localized *i.e.*, for silver nanoprisms, the tips (which are also responsible for the enhanced SERS effect, see below).

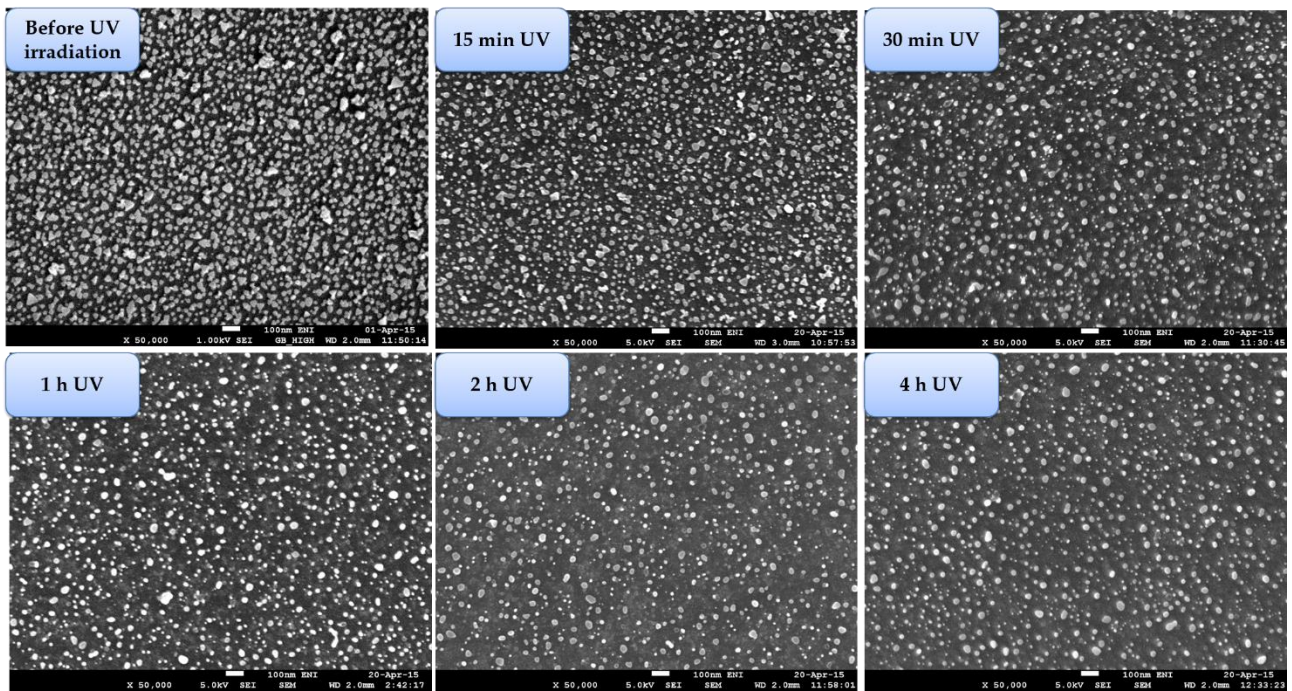


Figure 2.5 Kinetic investigation of the photocatalytic conversion of silver nanoprisms into nanospheres.

Transparent titania-coated glass slides are used as substrates to perform the nanoprism irradiation experiments in order to acquire their UV-vis absorbance spectra (Figure 2.6). The observed variations in the position and intensity of peaks support the conclusion that titania-supported nanoprisms are changed into spherical nanoparticles upon irradiation with UV light.

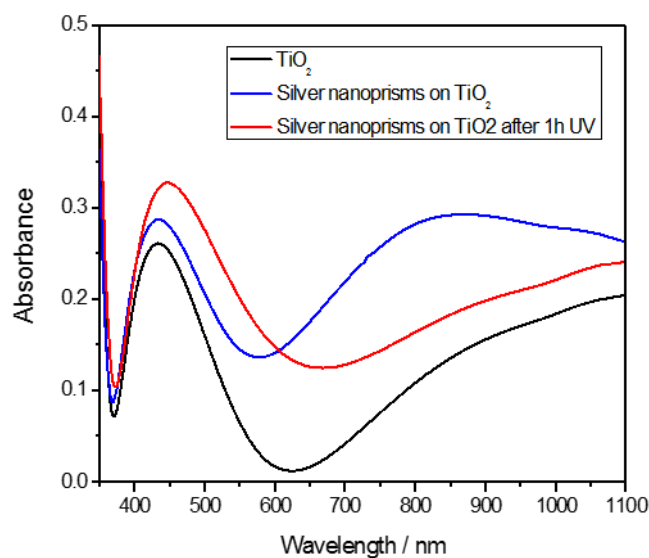


Figure 2.6 UV-vis absorption spectra for samples obtained on transparent glass substrates. Titania films are functionalized with APTES and silver nanoprism suspension is spread only on one face of the substrate. It is apparent that the peak at 850 nm is due to surface-attached silver nanoprisms while the increase in the peak at 450 nm after 1 h of UV irradiation could be ascribed to the presence of smaller, rounded nanoparticles.

Development of patterned SERS scaffolds

The described process opens up new possibilities for the development of patterned SERS-active platforms which would be useful *e.g.* for sensing applications. As a proof-of-concept, we applied the same lithographic approach described in Chapter 1, exposing a nanoprism-decorated titania film to UV light through a photomask for 1 h to obtain the pattern shown in Figure 2.6 and Figure 2.7a,b.

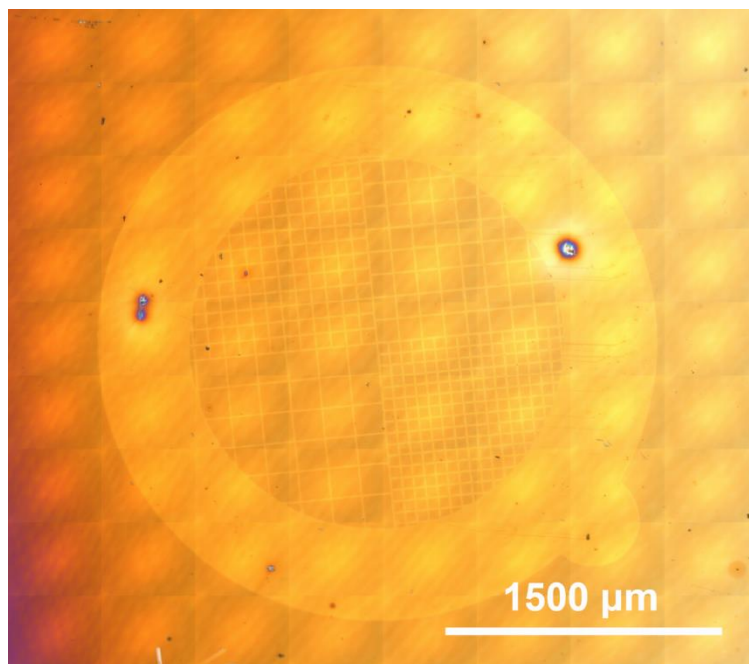


Figure 2.6 Optical microscopy image of the grid replica. The lighter zones are those that were covered with the photomask.

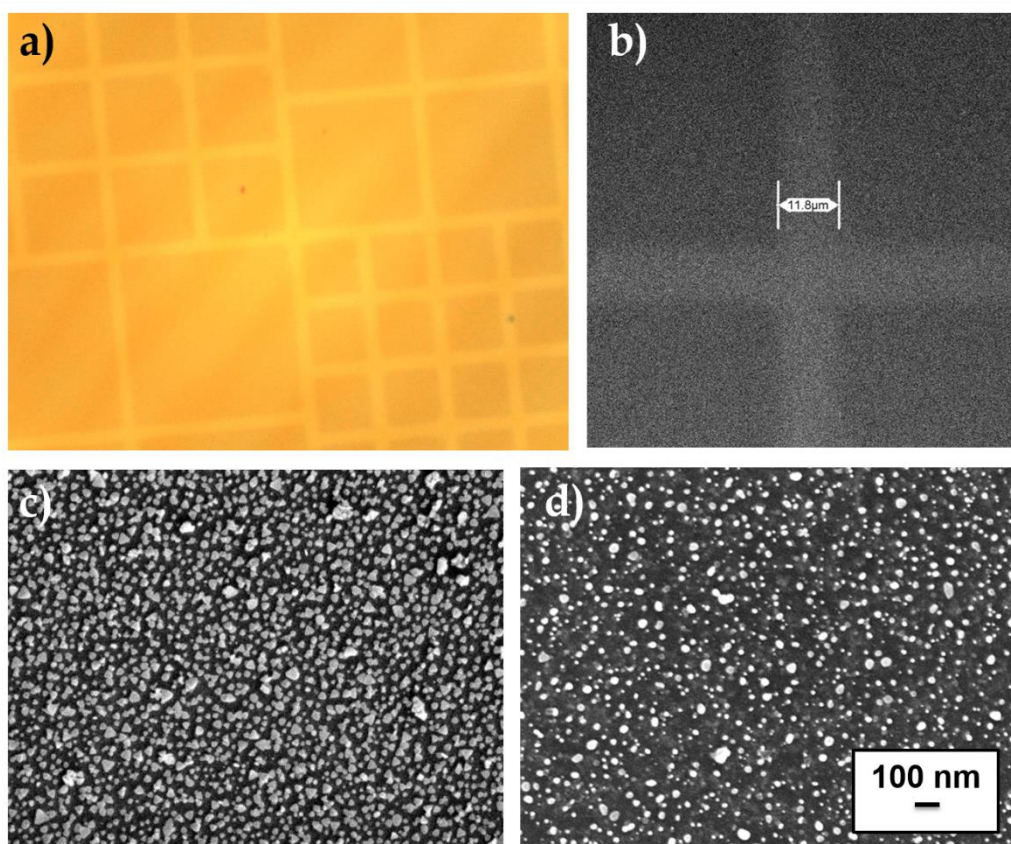


Figure 2.7 a) Optical and b) electron microscopy magnified images of the resulting pattern. c,d) SEM images of the unexposed and exposed zone, respectively.

The SERS activity of the obtained patterns is then evaluated. As shown in Figure 2.8a, the SERS peak at 150 cm^{-1} corresponds to titania [3-5]. This peak in the nanoprism-decorated zones is 20% more intense compared to the UV exposed, nanosphere-decorated zones suggesting that nanoprisms are better SERS enhancers. This makes it possible to obtain a spatially-resolved SERS imaging of the surface, from which the pattern of prisms clearly emerges (Figure 2.8b).

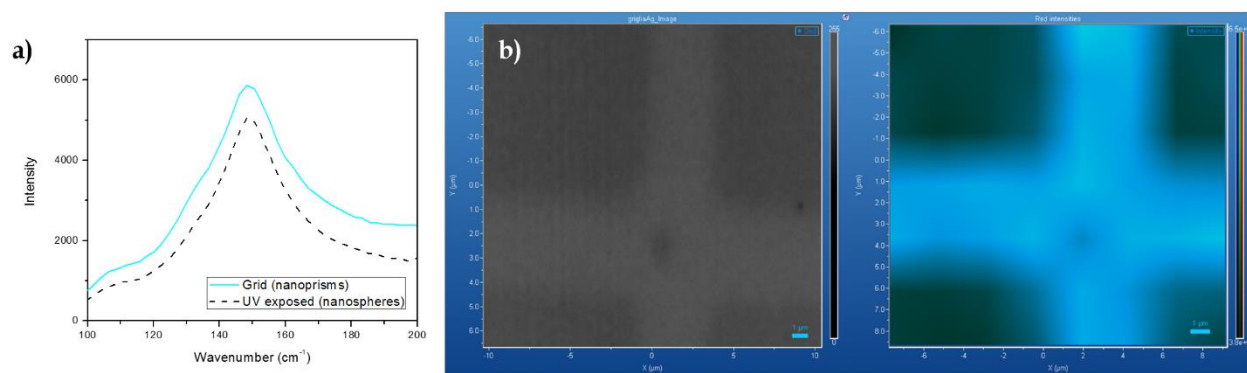


Figure 2.8 a) Intensity of the SERS signal for titanium dioxide in presence of silver nanoprisms and nanospheres. b) Optical and spatially-resolved SERS image of a patterned sample.

Since the silver nanoprisms are quite near to each other the density of “hot-spots” *i.e.* of local electric field concentration (due to plasmon resonance) is probably very high, thus leading to the observed enhancement of the SERS signal [15]. The nanospheres not only lack sharp tips, they are also more distant to each other, thus reducing the density of hot-spots.

Preliminary investigations of the shaping mechanism

In order to understand the mechanism for the observed shaping of silver nanoprisms, irradiation experiments are conducted also in the remote photocatalysis mode: silver

nanoprisms assembled on APTES-functionalized silicon wafer are irradiated through a titania-coated glass slide for increasing times. However, no appreciable change in the shape and surface density of particles could be detected even after 4 h of irradiation (Figure 2.9). That points out that silver nanoprisms must be in contact with the irradiated titanium dioxide for the shaping process to occur. Another proof for such hypothesis is obtained by performing irradiation of the samples under ethanol. Ethanol is considered to be an efficient hole scavenger [16]. When irradiation is performed under ethanol, the shaping process is considerably slowed down: after 1 h of UV light exposure, bigger prisms retain their shape as observed for irradiation experiments performed in air for 15 min. These results confirm the photocatalytic nature of the process and indicate that a direct transfer of holes to nanoprisms could be the primary event leading to their shaping into nanospheres.

2.3 Conclusion

Triangular silver nanoprisms can be shaped into spherical nanoparticles using direct photocatalysis. Silver nanoprisms self-assembled on titanium dioxide films are changed into nanospheres upon irradiation with 365 nm-UV light. According to preliminary mechanistic study, this phenomenon is based on the etching of metallic silver through direct transfer of photogenerated holes from the titania to the nanoprisms. Patterned structures can be obtained using simple contact photomasks and their suitability as scaffolds for spatially-resolved SERS is demonstrated.

2.4 Specific procedures

Materials: All reagents are purchased from Aldrich (reagent grade or analytical purity) and used as received. Silicon (100) wafers, single-polished, n type, phosphorus doped, 3 – 6 (Ω cm), with a native oxide layer ca. 1.5 nm thick, were purchased from Ultrasil Corporation. A Jelosil HG500 halogen lamp (230 V, 500 W, effective power density from 40 cm: 47.5 (mW cm^{-2}) between 280 and 400 nm) and titania-coated glass and silicon wafer slides are used for the photocatalysis experiments. For all the details refer to Appendix C.

Characterization methods: Optical microscopy images are acquired using a Nicolet™ iN™10 Infrared Microscope. Scanning electron microscopy (SEM) is performed, on samples fixed on conducting carbon tape, using a Jeol JSM 7600f Schottky Field Emission Scanning Electron Microscope. High resolution transmission electron microscopy (TEM) is performed using a JEM 2010 equipped with a LAB6 electron gun (beam energy 200 keV) and a Gatan CCD camera allowing high resolution imaging. UV-vis spectra are acquired using a Jasco V-630 spectrophotometer. Surface-Enhanced Raman Scattering (SERS) is conducted with a Horiba Jobin Yvon LabRam HR800 equipped with a peltier-cooled CCD Synapse detector, using a 473 nm-laser (power: 5 mW), spectral range 50–1200 cm^{-1} , a 300 nm-hole, a 600 grooves mm^{-1} grating, a 50x objective (aperture 0.75), a 2 μm -step spatial resolution, 2 s acquisition time (four accumulations per step).

SYNTHESIS OF TRIANGULAR SILVER NANOPRISMS

The synthesis of silver nanoprisms is accomplished according to a reported procedure [13]. Briefly, 100 μL of 0.1 M silver nitrate, 1.5 mL of 0.1 M trisodium citrate and 280 μL of 30% hydrogen peroxide are mixed and diluted to 100 mL with water in a three-necked 500 mL round-bottomed flask open to air. The solution is vigorously stirred for 10 min, then the stirring rate is reduced and 1 mL of 0.1 M sodium borohydride is rapidly added (to ensure reproducibility, this solution must be prepared immediately before use, with ice water). After an induction time of 1–2 min the colorless solution turns yellow then rapidly darkens until a stable blue color develops after ~5 min. The flask is covered with aluminum foil and left under gentle stirring for additional 10 min. The suspension is stored first at room temperature in the dark for at least 6 h to decompose excess sodium borohydride and then

at +4°C. Silver nanoprisms can be concentrated by centrifugation at 10000 rpm for 30 min and resuspension in water or ethanol.

SELF-ASSEMBLY OF SILVER NANOPRISMS ON APTES-FUNCTIONALIZED SUBSTRATES

Before functionalization with APTES, silicon and titania substrates are cleaned until they reached superhydrophilicity (WCA 0°). Cleaning of silicon substrates is accomplished by immersion in a 3:1 v/v mixture of 98 % sulphuric acid and 30 % hydrogen peroxide (“piranha solution”) at 100 °C for 1 h, rinsed extensively with water and dried with a nitrogen stream. (*Caution: piranha solution reacts violently with organic matter!*). Titania films are cleaned by sonication in water and irradiation using a Spectroline crosslinker equipped with four 254 nm-UV lamps.

Each substrate is immersed in 9 mL of anhydrous toluene in an oil bath at 55 °C for 1 h under nitrogen. After adding a solution obtained by dissolving 23 µL of APTES in 1 mL of anhydrous toluene (10 mM final concentration) the substrates are left at 70 °C for 2 h. The substrates are sonicated in toluene and in ethanol for 5 min each, rinsed with water, then with ethanol and eventually dried under a nitrogen stream. The water rinse step helps to get rid of hydrogen-bonded APTES molecules.

A concentrated (~0.1 mg mL⁻¹) aqueous suspension of silver nanoprisms is cast on freshly functionalized substrates (~500 µL cm⁻²) which are left for 1 h in the dark to allow self-assembly of the particles. The substrates are then rinsed thoroughly with pure water and dried under a gentle stream of nitrogen.

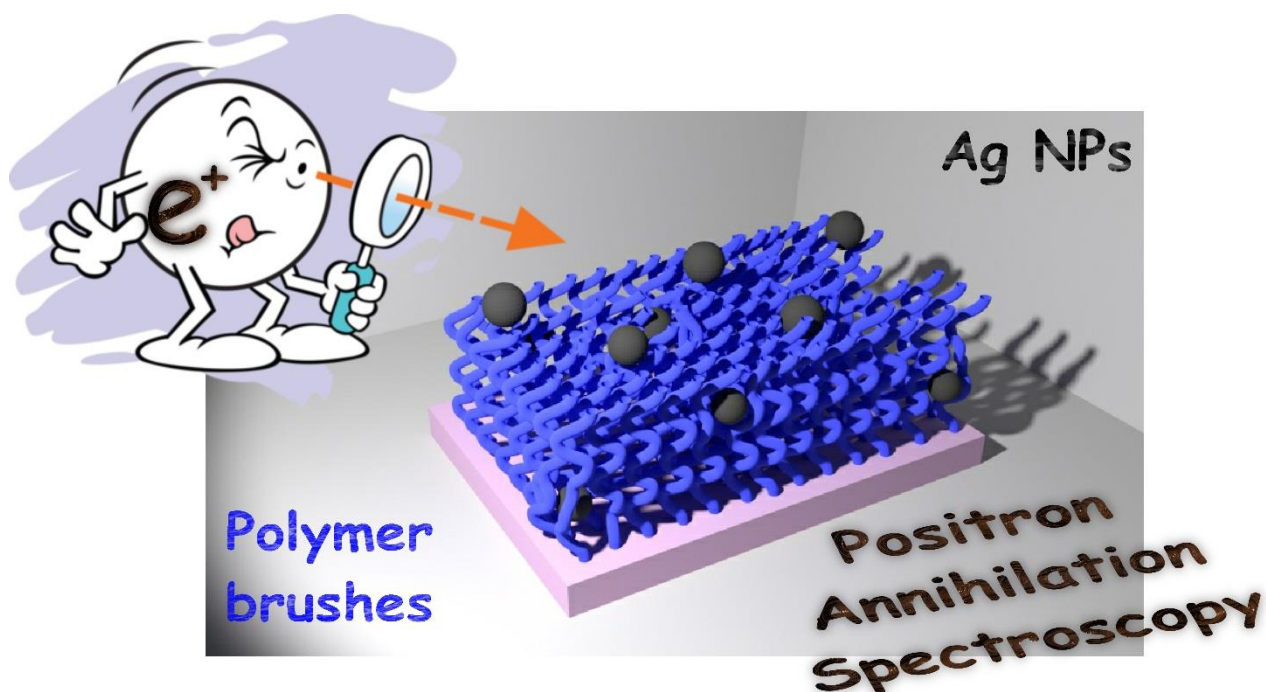
2.5 References

- [1] B. Sharma, R. R. Frontiera, A.-I. Henry, E. Ringe, and R. P. Van Duyne, *Materials Today*, **2012**, *15*, 16–25.
- [2] H. Wei, H. Xu, *Nanoscale*, **2013**, *5*, 10794–10805
- [3] L. Yang, X. Jiang, W. Ruan, B. Zhao, W. Xu, and J. R. Lombardi, *J. Phys. Chem. C*, **2008**, *112*, 20095–20098.

- [4] A. Musumeci, D. Gosztola, T. Schiller, N. M. Dimitrijevic, V. Mujica, D. Martin, and T. Rajh, *J. Am. Chem. Soc.* **2009**, *131*, 6040–6041.
- [5] I. Alessandri, *J. Am. Chem. Soc.*, **2013**, *135*, 5541–5544.
- [6] X. Zou, R. Silva, X. Huang, J. F. Al-Sharab and T. Asefa, *Chem. Commun.*, **2013**, *49*, 382–384.
- [7] Y. Zhou, J. Chen, L. Zhang, and L. Yang, *Eur. J. Inorg. Chem.*, **2012**, 3176–3182.
- [8] S. Schlücker, *Angew. Chem. Int. Ed.*, **2014**, *53*, 4756–4795.
- [9] L. J. Sherry, R. Jin, C. A. Mirkin, G. C. Schatz, R. P. Van Duyne, *Nano Lett.*, **2006**, *6*, 2060–2065.
- [10] S.-H. Ciou, Y.-W. Cao, H.-C. Huang, D.-Y. Su, C.-L. Huang, *J. Phys. Chem. C*, **2009**, *113*, 9520–9525.
- [11] J. C. Hulteen, D. A. Treichel, M. T. Smith, M. L. Duval, T. R. Jensen, R. P. Van Duyne, *J. Phys. Chem. B*, **1999**, *103*, 3854–3863.
- [12] Z. Starowicz, M. Lipinski, R. P. Socha, K. Berent, G. Kulesza, P. Ozga, *J. Sol-Gel Sci. Technol.*, **2015**, *73*, 563–571.
- [13] G. Panzarasa, *J. Chem. Educ.*, **2015**, *92*, 1918–1923.
- [14] D. Aherne, D. Ledwith, M. Gara, and J. M. Kelly, *Adv. Funct. Mater.*, **2008**, *18*, 2005–2016.
- [15] M. D. Doherty, A. Murphy, R. J. Pollard, and P. Dawson, *Phys. Rev. X*, **2013**, *3*, 011001.
- [16] T. Tan, D. Beydoun, R. Amal, *J. Photochem. Photobiol. A Chem.*, **2003**, *159*, 273–280.

II

Polymer Brushes: Innovative Characterization Techniques and Advanced Applications



Chapter 3

Grafted-From Polymer Brushes Make Silicon Wafer Electrochemically Responsive

ABSTRACT Silicon wafer is the material of choice for microfabrication. However, the development of innovative on-chip electrochemical sensors is hampered by its poor electrochemical properties. Here we demonstrate how grafted-from micropatterned polymer brushes dramatically enhance the electrochemical response of silicon electrodes. Our results are relevant not only for a deeper understanding of the structure and behavior of polymer brushes, but also for the combination of the versatility of surface-initiated polymerization and of an innovative patterning technique (remote photocatalytic lithography) which paves the way for the fabrication of integrated devices.

3.1 Introduction

The development of reliable, fast and inexpensive signal-responsive material systems as sensing platforms to monitor target molecules is a flourishing field of investigation [1-3]. The miniaturization and incorporation of such systems onto microchip assemblies is highly desirable for the realization of compact, portable, implantable devices. Silicon wafer would be the substrate of choice for such applications, but even its nm-thick native oxide impairs its electrochemical response (Figure 3.1) [4]. To overcome this problem, a typical strategy involves the grafting of redox-active molecules on the surface of hydride-terminated silicon, but this approach requires specific techniques such as the handling of dangerous hydrofluoric acid for the removal of native oxide [5,6].

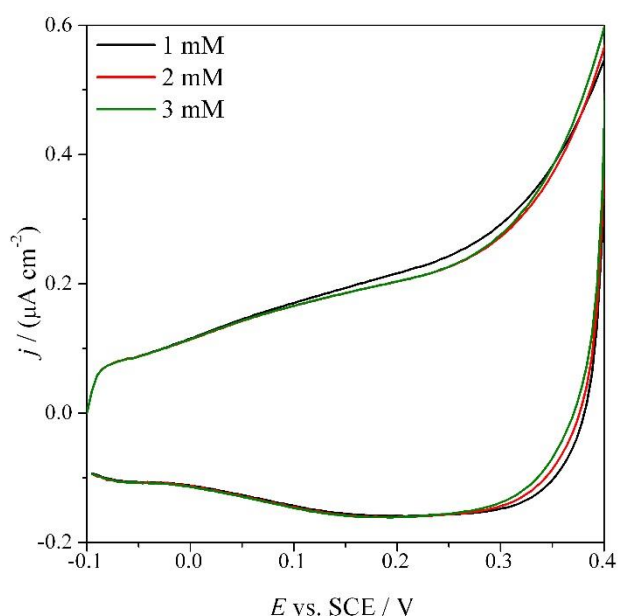


Figure 3.1 Cyclic voltammetry plots for native oxide-coated silicon wafer in presence of increasing amounts of a redox probe (ferrocyanide). The complete absence of the redox peaks expected from the probe demonstrates the electrochemical inertness of silicon.

Here we report for the first time a potentially powerful approach for the fabrication of integrated lab-on-a-chip and microfluidic devices: we found that the electrochemical response of silicon wafer is dramatically improved when polymer brushes are grafted directly from its surface. Moreover, this behaviour is enhanced if the brushes are micropatterned.

Polymer brushes, as discussed in Appendix A, are dense arrays of chains tethered on a surface by one end [7]. Thanks to their peculiar physico-chemical properties, they provide extraordinary opportunities for surface functionalization, generating thin films for integration into various devices [8]. Being able to control immobilization and preconcentration of analytes through specific interactions, thanks to the high concentration of functional groups exposed at the brush interface [9], polymer brushes can be used to significantly enhance the response of different kind of sensors [10,11].

Understanding the electrochemical properties of polymer thin films is of great importance for a wide range of technologies, from the development of biosensors to the miniaturization of batteries (battery-on-chip) [12] for autonomous microelectronic devices and microsensors. Electrochemistry has already proven to be a useful tool to elucidate the internal structure of polymer brushes [13,14]. The diffusion of probe molecules in and out of the macromolecular environments plays a key role in the response of polymer-based sensor materials or in the design of drug delivery systems. On a molecular level, the effect of the grafting density on the transport through thermoresponsive poly(N-isopropylacrylamide) (PNIPAM) brushes grafted on gold substrates was investigated using cyclic voltammetry (CV) and electrochemical impedance spectroscopy (EIS) [15]. EIS has been used to

determine the effectiveness of fluorinated poly(2-hydroxyethyl methacrylate) (PHEMA) films as barriers against the transport of redox species [16,17]. Ion exchange inside polyelectrolyte brushes, in which the polymer chains have fixed electrostatic charges, is the subject of extensive study [18-21]. However, a detailed understanding of their electrochemical behaviour has not been obtained yet. In addition, all of these studies have been performed for brushes grafted from highly conductive gold or indium tin oxide (ITO)-coated surfaces: not a single report is available in the literature for polymer brush-modified silicon electrodes. Here, we would like to fill this gap by studying the electrochemical behaviour of homo- and co- polymer brushes made from 2-hydroxyethyl methacrylate (HEMA) and 2-aminoethyl methacrylate hydrochloride (AMA). Poly(HEMA) is an hydrophilic polymer with current uses in contact lenses, biocompatibilization and drug delivery [22]. On the other hand, poly(AMA) is a cationic polymer which has already found promising application in the biomedical field for the development of antimicrobial surfaces [23] and for the bioconjugation of antigens and proteins, thanks to its primary amine groups allowing post-functionalization reactions [24].

Here, by means of cyclic voltammetry (CV) and electrochemical impedance spectroscopy (EIS), meaningful correlations are found between the charge transfer resistance, the length and the chemical composition of the brushes, which in turn reveal precious information about the structure and dynamics of the brushes themselves.

The most electrochemically-active brushes are selected to perform micropatterning studies. Patterning is a fundamental tool for the engineering of surfaces and micropatterned polymer brushes can display new useful features compared to bulk

analogues [25,26]. As expected, the electrochemical response of the patterned brushes is dramatically different compared to that of non-patterned ones.

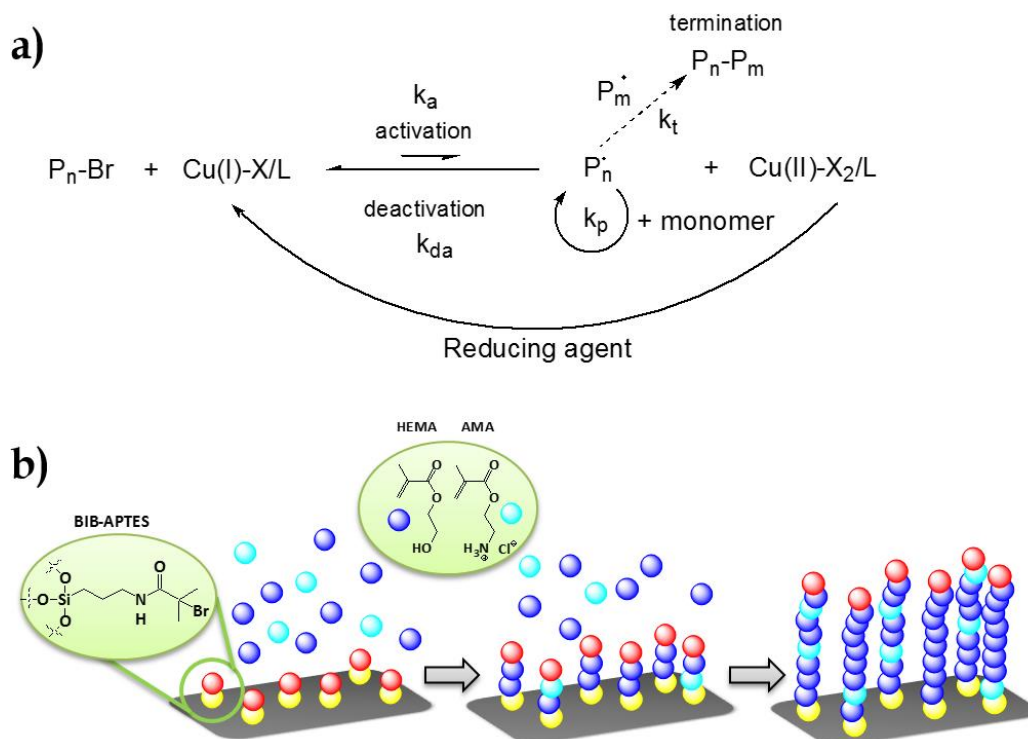
The crucial development reported in the present study demonstrates how, by choosing the thickness, composition and microstructurization of polymer brushes, we are able to tune the electrochemical behaviour of silicon wafer, an otherwise poor electrode material, with tremendous importance for the realization of integrated sensing devices.

3.2 Results and Discussion

Grafting-from of polymer brushes by SI-ATRP

The grafting-from technique allows the direct growth of polymer chains by starting polymerization from an initiator-functionalized surface. If a controlled radical polymerization such as Atom Transfer Radical Polymerization (ATRP) is used, brushes with increasing thickness can be obtained simply by varying the time of polymerization. The mechanism of ATRP is based on the reversible formation of radicals by the halogen atom abstraction from an alkyl halide (typically a secondary or tertiary bromide) by a copper(I)-ligand complex. This latter breaks the C-Br bond of the initiator and the resulting carbon carbon-centered radical attacks a monomer molecule starting chain growth. At the same time, copper(I) oxidizes to copper(II). Since this process is reversible Cu(II) acts as a deactivator, reducing the overall concentration of active radicals and thus the occurrence of termination events [29]. In the Activators Regenerated by Electron Transfer (ARGET) ATRP, Cu(II) is continuously reduced to active Cu(I) by a reducing agent (Scheme 3.1) and thus only

ppm amounts of copper salt are required [27], which is beneficial when working with metal-complexing monomers such as AMA.



Scheme 3.1 a) Schematic mechanism of ARGET ATRP. b) Grafting-from of functional, random copolymer brushes from an ATRP initiator-functionalized surface.

Polymer brushes are grown at 30°C in a 4:1 v/v methanol–water mixture using a CuBr_2 /tris(2-pyridylmethyl)amine (TPMA) catalyst in the presence of an excess of ascorbic acid as reducing agent. The following molar ratios are employed: CuBr_2 /TPMA/ascorbic acid/monomer = 0.036 : 0.3 : 0.5 : 150. The solvent mixture is chosen to ensure the complete solubilisation of monomers. Water is also known to significantly speed-up the polymerization process (“water-accelerated ATRP”) [30–31]. More importantly, under these conditions we are able to polymerize commercial AMA without the need to remove the added phenothiazine, which is considered a

powerful inhibitor for conventional free-radical polymerization (Figure 3.2b, details are available in the Specific procedures paragraph).

The kinetics of polymerization (Figure 3.2a, Table 3.1) show a pseudo-linear increase of the brush thickness as a function of the polymerization time suggesting that a good control is attained. The evolution of brush thickness slows down as a result of the increased fraction of AMA in the polymerization feed: this behaviour could be attributed to the so-called “halogen exchange effect” [32]. If chloride ions are added in a concentration significantly higher than bromide, as for AMA homopolymerization in the present case (Cl/Br molar ratio > 4000), the kinetics will be slowed down due to a reduced rate of radical formation, $\text{C}-\text{Cl}$ being more stable compared to the $\text{C}-\text{Br}$ bond. Another indication of halogen exchange comes from the cyclic voltammograms (as discussed below) where a significant shift of the peak attributed to bromine is observed for brushes made with increasing concentrations of AMA, thus suggesting its substitution with chlorine atoms.

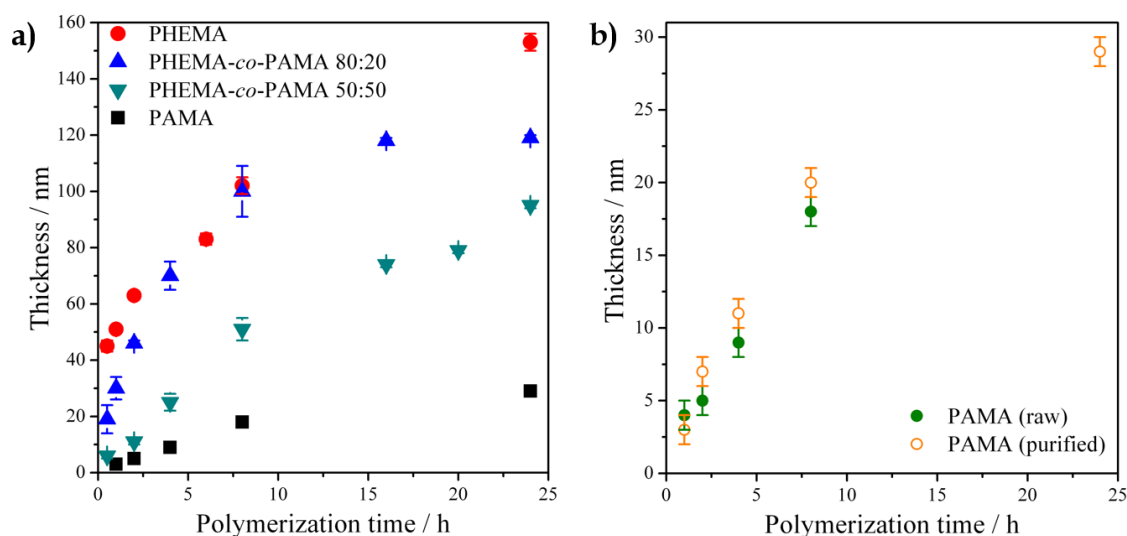


Figure 3.2 a) Kinetics of polymerization for brushes obtained with different monomer feed ratios. b) Comparison between the kinetics of polymerization for raw AMA and purified AMA. For the 24 h polymerization time the two data points are superimposed.

Table 3.1 Thickness of the brushes obtained as a function of polymerization time and composition of the feed.

<i>Series</i>	<i>Time of polymerization (h)</i>	<i>Thickness (nm)</i>
PHEMA	0.5	45 ± 2
	1	51 ± 1
	2	63 ± 1
	6	83 ± 2
	8	102 ± 3
	24	153 ± 3
PHEMA-co-PAMA 80:20	0.5	19 ± 5
	1	30 ± 4
	2	46 ± 1
	4	70 ± 5
	8	100 ± 9
	16	118 ± 1
	24	119 ± 1
PHEMA-co-PAMA 50:50	0.5	6 ± 1
	2	11 ± 1
	4	25 ± 3
	8	51 ± 4
	16	74 ± 1
	20	79 ± 1
	24	95 ± 1
PAMA	1	3 ± 1
	2	5 ± 1
	4	9 ± 1
	8	18 ± 1
	24	29 ± 1

Electrochemical investigation of polymer brushes: Cyclic voltammetry

Cyclic voltammograms registered at bare silicon wafer in presence of ferrocyanide show that no redox reaction takes place because the voltammograms superimpose and no peaks are detectable. However, all the tested brushes samples shows the same behavior. In the voltammograms of the brushes (Figure 3.3) only a peak between 0 V and +0.1 V is detected, which is not present in those for bare silicon wafer.

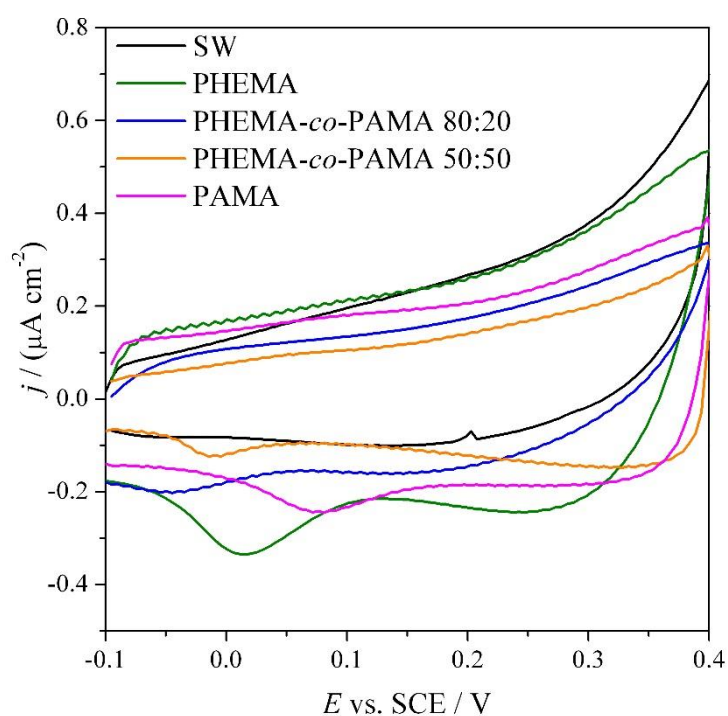
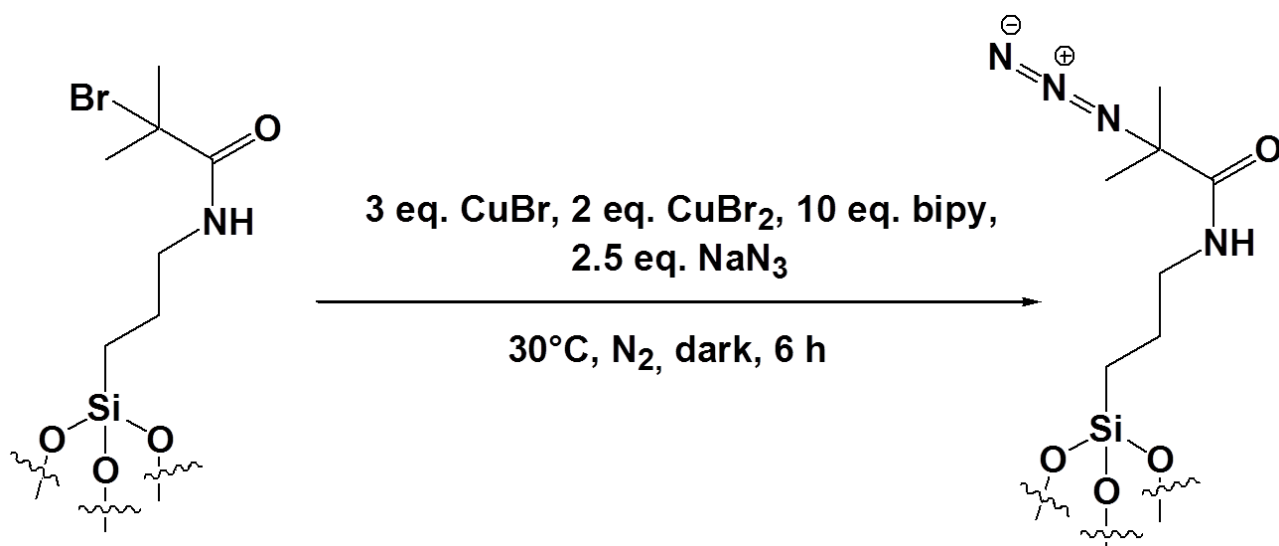


Figure 3.3 Comparison between the cyclic voltammetry plots of silicon wafer and of representative polymer brushes.

The nature of this peak, tentatively assigned to the Br (or Cl) chain ends of the polymer brushes, is demonstrated by selective substitution with azide (Scheme 3.2).



Scheme 3.2. Bromine substitution with azide for BIB-APTES molecules self-assembled on a silicon surface.

To confirm the attribution of the +0.1 V peak to bromine, its selective substitution with azide is carried out on initiator-functionalized substrates according to a procedure originally reported by de Graaf *et al.* [40]. Briefly, 0.026 g (0.18 mmol) CuBr, 0.027 g (0.12 mmol) CuBr₂ and 0.094 g (0.60 mmol) bipyridyl are dissolved under nitrogen in a degassed mixture of 1.8 mL acetonitrile and 2 mL water. Then, 0.01 g (0.15 mmol) sodium azide are dissolved in 2 mL of degassed water and were added to the previous solution. Initiator-functionalized silicon substrates are then covered with the resulting mixture under nitrogen and the reaction was allowed to proceed at 30°C in the dark for 6 h. After this time, the substrates are washed with ethanol and water, rinsed with ethanol and eventually dried with a stream of nitrogen. The treated substrates are then subjected toARGET ATRP with HEMA as a monomer for 4 h: no formation of polymer brushes can be observed, thus demonstrating the successful substitution of bromine with azide. The disappearance of the peak at +0.1 V after

bromine substitution with azide in the cyclic voltammogram definitely confirms its attribution (Figure 3.4).

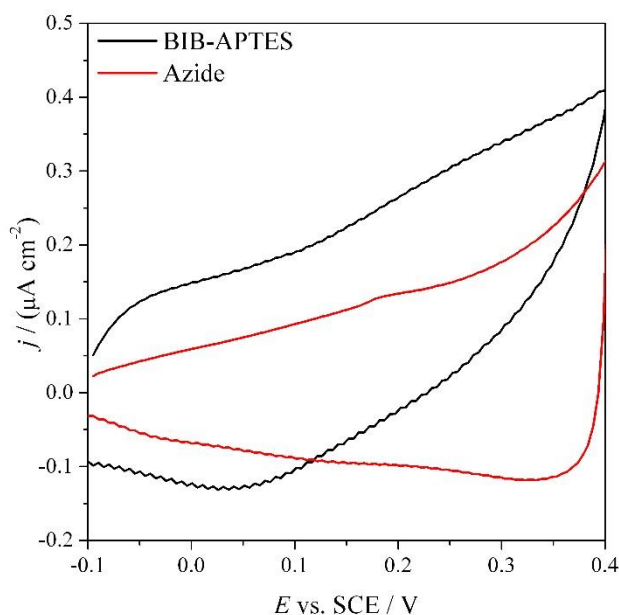


Figure 3.4 Comparison between the cyclic voltammograms for initiator-functionalized silicon (BIB-APTES) and the same after bromine substitution with azide (Azide).

Micropatterning of polymer brushes by remote photocatalytic lithography

We previously demonstrated in Chapter 1 the suitability of remote photocatalytic lithography [33,34] as a versatile means for the patterning of polymer brushes [27]. Here, this approach has been preferred compared to classic photolithography both to avoid possible contamination from residual photoresist and to make the procedure easier and faster. Two different kinds of photomask (the “donut”, to obtain a macropatterning and the TEM “grid”, to obtain a micropatterning, details are available in the Specific procedures paragraph) are employed to evaluate the impact of macro- and micro-structuration on the electrochemical performance of brush-decorated electrodes (Figure 3.5).

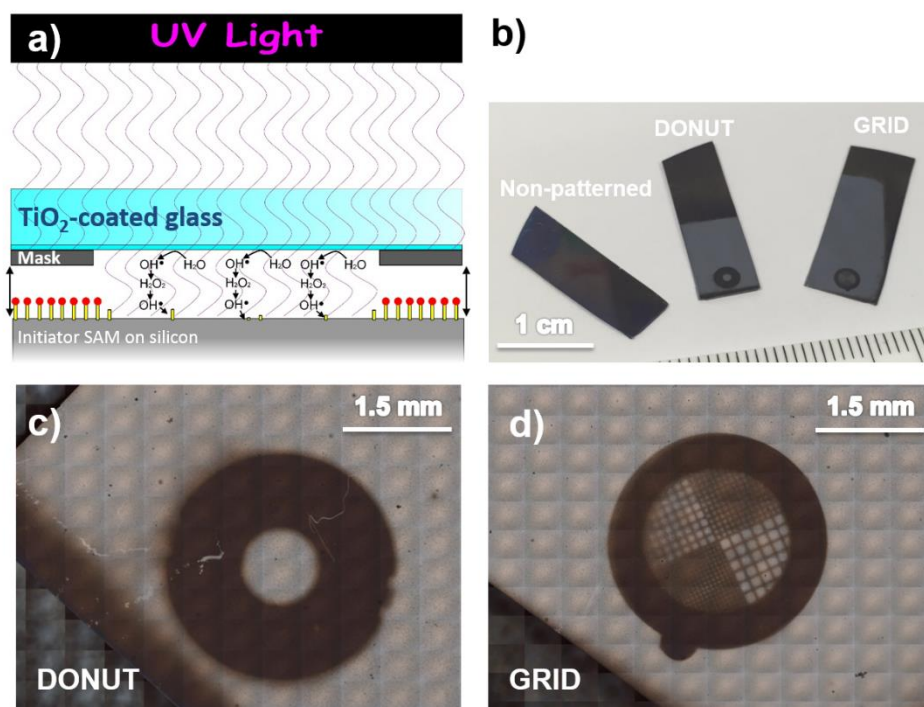


Figure 3.5 a) Scheme of remote photocatalytic lithography. b) Photographs of three representative samples, non-patterned and patterned. c) Optical microscopy images of donut-patterned (DONUT) and grid-patterned (GRID) brushes.

Electrochemical investigation of polymer brushes: Electrochemical impedance spectroscopy

Non-patterned polymer brushes

The complex plane plots obtained in the electrolyte solution at +0.25 V (SCE), in the absence of the redox probe, for bare (SW), initiator-functionalized (BIB-APTES) silicon and for two representative polymer brushes are shown in Figure 3.6a. All the spectra display the same trend with a semicircle at high frequencies followed by a straight vertical line at low frequencies, already mentioned in papers dealing with silicon-based electrodes [35].

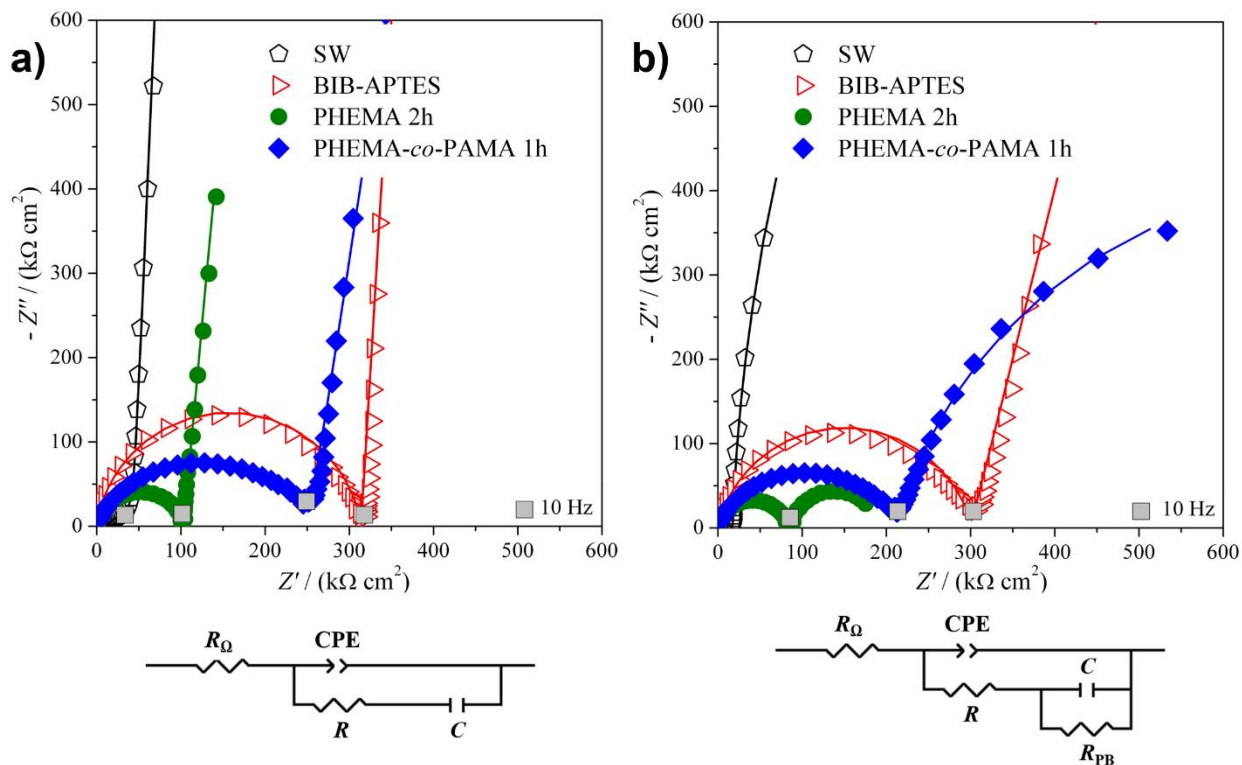


Figure 3.6 Complex plane plots measured for bare (SW) and initiator-functionalized (BIB-APTES) silicon wafer and for two representative brushes, along with the equivalent electrical circuits used for the interpretation of EIS plots, obtained a) in the absence and b) in the presence of redox probe.

Data fitting is achieved using an equivalent circuit already described in the Literature for similar samples (Figure 3.6, scheme) [21,36,37]. The circuit is made of the electrolyte resistance R_{Ω} in series with a constant phase element (CPE) (accounting for the film and silicon native oxide capacitance) and a resistance R (comprising the resistance of silicon substrate and the polymeric film) in parallel (together represented by the semicircle). In series with the last element, a capacitance (C) can be found, representing the double layer and substrate capacitance (described by the vertical straight line). The constant phase element CPE served to model the non-homogeneity of the electrode surface (giving a depressed semicircle). It is defined as (eq. 1):

$$CPE = [(C_{CPE}i\omega)^\alpha]^{-1} \quad (1)$$

where the α parameter indicates the deviation from a purely capacitive behaviour ($\alpha = 1$) to a non-capacitive one ($\alpha = 0.5$) and is thus an indicator of surface homogeneity. Table 3.2 shows the parameters influenced by the presence of the polymeric films (R , C_{CPE} and α) obtained from the spectra fitting since, as expected, R_Ω and C maintain similar values for all the samples (the solution and the substrate are always the same).

Table 3.2 Electrochemical parameters obtained by fitting the EIS data (without redox probe) for the different samples.

Sample	R ($k\Omega \text{ cm}^{-2}$)	C_{CPE} ($\mu\text{F cm}^{-2}$)	α
SW	19	0.04	0.63
BIB-APTES	315	0.0006	0.90
PHEMA	103	0.007	0.85
PHEMA-co-PAMA 80:20	255	0.01	0.71

The reported R values are in accordance with the trend of the semicircle diameters showed. Bare silicon wafer (SW) and initiator-functionalized silicon wafer (BIB-APTES) showed the lowest and highest values of resistance R , respectively, suggesting that the initiator layer behaves as strong electrical insulator. The resistance R for the brushes presents intermediate values thanks to the hydrophilic and polarizable groups, which increased their conductivity. Moreover, PHEMA brushes are more conductive with respect to PHEMA-co-PAMA 80:20 ones.

Bare silicon and initiator-functionalized silicon showed the highest and lowest values of C_{CPE} , respectively. When the electrode surface is covered with an insulator layer (*e.g.* the BIB-APTES layer), the overall capacitance decreases because the capacitance of the insulating layer sums to that of the native oxide. PHEMA brushes, as well as

the (PHEMA-*co*-PAMA) brushes, had lower insulating properties thanks to hydrophilic -OH groups and electrically charged primary amine groups.

As previously mentioned, the α values can give information about surface homogeneity. The low α values found for bare silicon and the copolymer brushes indicate a lower surface homogeneity, due to the presence of native oxide or of a non-homogeneous polymer. On the other hand, the initiator layer and PHEMA brushes are characterized by homogeneous surfaces, giving α values very close to 1.

The EIS data trends for bare and initiator-functionalized silicon wafer were unaffected by the addition of the redox probe potassium ferrocyanide, confirming the electrochemical inertness of those samples. Contrarily, the polymer brushes impedance at low frequencies showed important changes (Figure 3.6b): the vertical straight line became another semicircle, requiring the introduction of R_{PB} , the resistance to probe electron transfer, in parallel to C . This indicates that the reaction of the redox probe took place efficiently at brush-modified electrodes [18-21,37,38]. The phenomenon could be due to interactions between the negatively charged probe with polar -OH (PHEMA) and positively charged -NH₃ groups (PHEMA-*co*-PAMA).

A study of swelling

Swelling is an important feature to consider when dealing with polymer-modified electrodes. The conformation of polymer brushes in a solvent is mainly governed by solvation forces and excluded volume effects. If the brush is made of a polyelectrolyte, such as PAMA and PHEMA-PAMA copolymers, electrostatic interactions add up. Water can be considered as a good solvent for all our investigated brushes and their chains would adopt a stretched conformation in pure water due to excluded volume effects of the solvated chain side groups and to the electrostatic repulsion between

neighbouring charge-like chains. However, in presence of free electrolytes, the charges of the pendant groups in the polymer chains would be screened according to the relative counterions concentration, minimizing electrostatic repulsion and leading to a more entropically-favorable collapsed conformation.

From an electrochemical point of view, the swelling-collapse behaviour will affect charge-transfer processes, the interface resistance and the capacitance of the brushes. EIS allows following this process as a function of time and thus to obtain information about the mobility and internal structure of polymer chains [37].

To monitor the swelling process (a representative complex plane plot is shown in Figure 3.7a), EIS spectra are first recorded immediately after immersion in the supporting electrolyte and then after 2 and 4 hours of immersion.

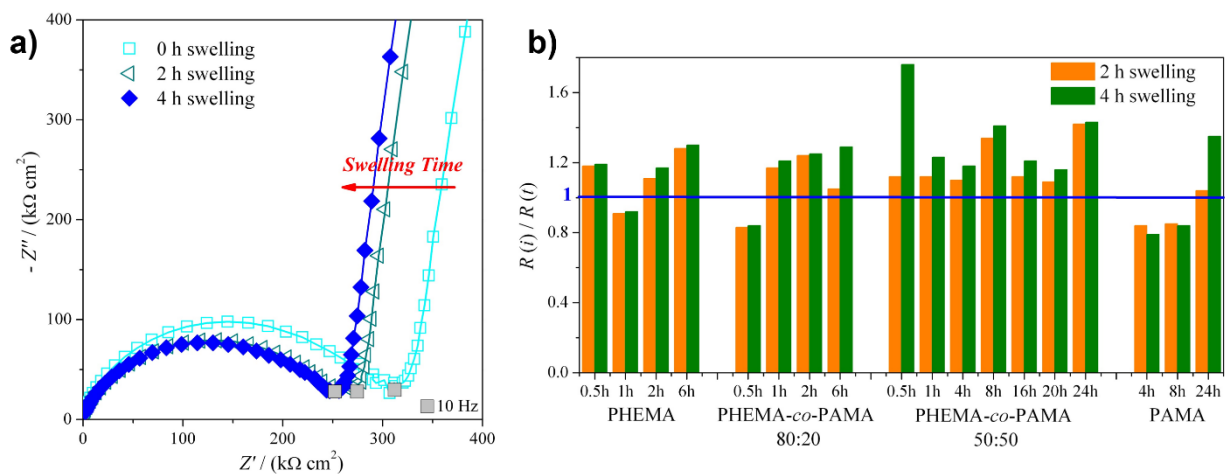


Figure 3.7 a) Complex plane plots showing the swelling of 1 h-polymerized PHEMA-co-PAMA 80:20 brushes. b) Comparison of the swelling behaviour for all the investigated brushes.

The only detectable change is the decrease in diameter of the semicircle, corresponding to a decrease of R , indicating an increase in polymer permeability with swelling. Figure 3.7b

summarize the swelling behavior for all the analysed brushes, reported as the ratio between the initial $R(i)$ and the time-dependent $R(t)$. The straight line at $R(i)/R(t) = 1$ corresponds to the value registered immediately after immersion. Data suggest that swelling reaches completion after the first 2 h. For times longer than 4 h, the impedance spectra are superimposable. That time is considered as the optimum time to reach complete swelling and allow equilibration of the brushes with the electrolyte.

Effect of thickness

The effect of thickness on the electrochemical properties of the brushes could be easily evaluated by considering the changes in R and R_{PB} values [19]. To this aim, EIS analyses are carried out in the absence and in the presence of the redox probe, respectively. As expected, different brush compositions induce different permeability and response behaviour to the redox probe.

Figure 3.8a shows the complex plane spectra for the complete series of PHEMA-*co*-PAMA 80:20 brushes as an example: only the diameter of the semicircle increased with increasing thickness, without relevant changes for the other parameters. A higher thickness can be related to higher values of R , since the electrostatic charge carriers (ions, according to a generally accepted theory [39]) face a longer way to reach the electrode surface.

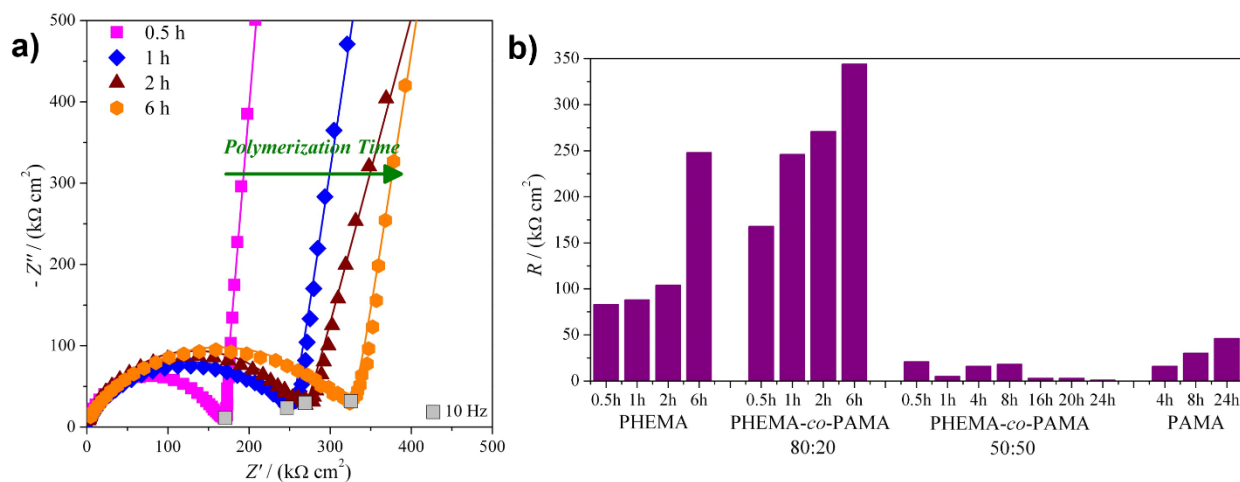


Figure 3.8 Behaviour of R as a function of thickness: a) complex plane plot for a representative 1 h-polymerized PHEMA-co-PAMA 80:20, b) comparison among the series. These data were obtained without the redox probe.

In Figure 3.8b the R values are reported for all the series to allow a comparison. PAMA and PHEMA-co-PAMA 50:50 brushes display the lowest values: apparently, a high density of charged groups helping the movement of ions inside the brushes was a more determinant factor than thickness. The R values of the PHEMA-co-PAMA 50:50 brushes seem to be independent to thickness, probably due to a random distribution of the two monomers. The behaviour of PHEMA brushes is intermediate, while the highest values are found for the PHEMA-co-PAMA 80:20 ones. In general, R increases proportionally to the thickness, probably because longer chains impair diffusion.

EIS spectra are then collected in the presence of the redox probe. According to previous swelling studies, the brushes are allowed to completely swell for 4 h, then ferrocyanide (3 mM) are added to the supporting electrolyte and the analysis is carried out after additional 2 h to allow the probe diffusion in the brushes and any other possible interaction to take place. While for PHEMA the interaction with the

redox probe is supposed to occur simply by diffusion, PAMA and PHEMA-PAMA copolymer brushes can be considered as polyelectrolytes due to the presence of positively charged primary amine groups, which can facilitate their interaction with the anionic redox probe and consequently the electron transfer. According to Huck *et al.* [39], one molecule of ferrocyanide would be supposed to coordinate with four amine groups, at least for PAMA brushes. For the 80:20 and 50:50 copolymer brushes, different degrees of coordination would be possible due to the more or less intra- and inter-chain proximity of AMA units (we assume that the copolymers are random). As previously discussed, in the complex plane plot at low frequencies the vertical straight line becomes a semicircle for all the polymers, indicating that the brushes interact with the probe: a lower resistance R_{PB} means an easier reaction of the probe at the electrode. All the series can interact with the probe, but different R_{PB} values are obtained depending on the brush composition and thickness. Figure 3.9a shows the EIS complex plane plots obtained PHEMA-co-PAMA 80:20 series as an example, where the lowest resistances were obtained for intermediate thicknesses, probably as a result of a compromise between the quantity of charged groups that can interact with the probe and the thickness. Figure 3.9b reports all the obtained R_{PB} values. The lowest resistance values were displayed by the thickest PHEMA brushes.

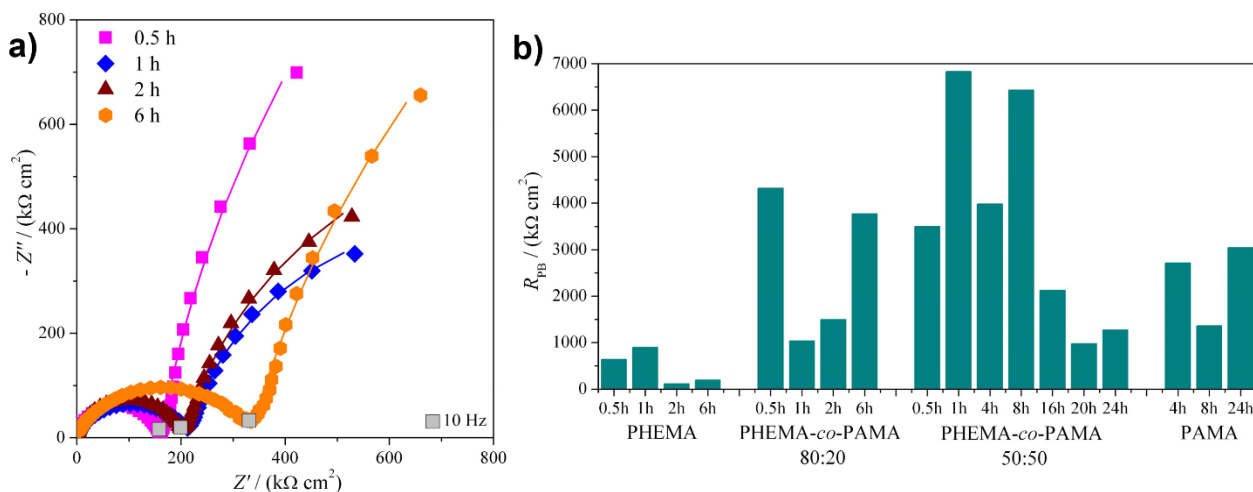


Figure 3.9 Behavior of the R_{PB} as a function of thickness: a) complex plane plot for a representative brushes PHEMA-*co*-PAMA, b) comparison among the series. These data are obtained in presence of the redox probe (3 mM).

Probably, probe diffusion is facilitated by the homogeneous distribution of polar but neutral-OH groups while the thicker polymer layer allowed storing a higher concentration of probe, which in turn is forced to react at the electrode giving a low resistance value. PAMA brushes expose at the surface only charged amine groups, which promote strong interactions with the anionic probe but at the same time increase the overall resistance due to local collapse after the coordination of ferrocyanide with amine groups, thus blocking diffusion of other probe molecules. For the PHEMA-*co*-PAMA 80:20 series higher resistances are obtained in comparison to PHEMA, but the best situation is reached for intermediate polymerization times, probably thanks to a sufficient density of charged groups, while the electron transfer is not complicated by excessive chain length. Similar or even lower values are obtained in comparison with PAMA, even more considering the lower thicknesses, indicating how the presence of only amine groups was not so favorable to obtain low resistance values. Especially in case of high thicknesses, brushes with a low density of amine groups are more desirable. The PHEMA-*co*-PAMA 50:50 series display the

highest R_{PB} values: it is likely that those brushes suffer from the so-called hydrophobic or ion-pairing collapse, which has been described for similar polyelectrolytes, e.g. poly[2-(methacryloyloxy)ethyl]trimethylammonium chloride (PMETAC). Such transition between the extended and collapsed conformational states could be due to a strong interaction between the cationic groups of the brushes with scarcely hydrated, large and highly polarizable ions such as ClO_4^- or, in this case, $[\text{Fe}(\text{CN})_6]^{4-}$. The hydrophobic collapse typically results in a large water loss for the brush, thus increasing the overall electrical resistance [21]. However, for higher thicknesses the resistance values decrease, probably due to the increase number and availability of interaction sites with the probe.

The influence of patterning on the electrochemical properties of polymer brushes

The previously described electrochemical analyses allowed us to select two types of brushes to study the effect of patterning: 1 h-polymerized PHEMA-co-PAMA 80:20 brushes and 2 h-polymerized PHEMA brushes are chosen due to their desirable properties, especially low resistance to probe reaction. For each brush type, three samples were prepared: a non-patterned one, a macropatterned one with a donut shape (“DONUT”) and a micropatterned one with a TEM grid (“GRID”).

The electrochemical response of electrodes modified with patterned polymer brushes is dramatically different compared to that of non-patterned ones. Significant changes are observed in their EIS plots for both the low and high frequency zones suggesting different (and more efficient) interaction mechanisms with the redox probe.

According to Figure 3.10a, for PHEMA series there was a clear increase in the first semicircle diameter as a function of patterning, reflecting changes in the film resistance (R) of the surface. The trend observed for R is: PHEMA(non-patterned) <

DONUT < GRID, which is plausible considering the reduced amount of active polymer for the patterned samples (of the order of $8 \mu\text{g cm}^{-1}$ for non-patterned brushes and $0.5 \mu\text{g cm}^{-1}$ for patterned brushes) and the correspondingly decreased permeability.

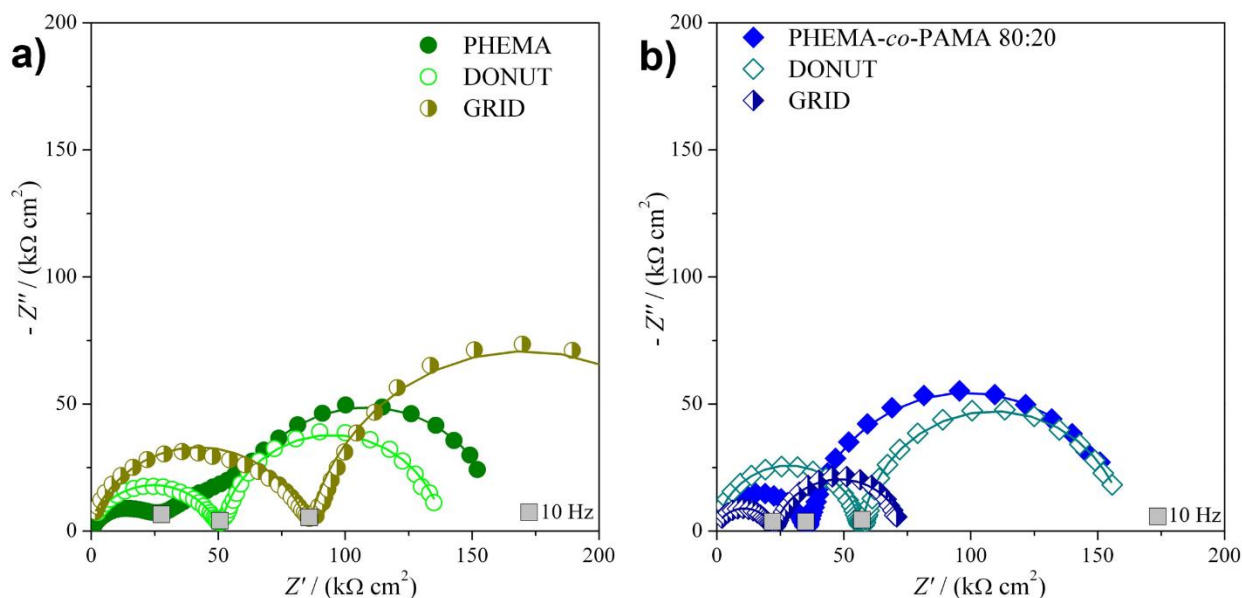


Figure 3.10 Complex plane plots showing the effect of patterning in the presence of redox probe (3 mM) for a) PHEMA brushes and b) PHEMA-*co*-PAMA 80:20 brushes.

On the other hand, the values obtained for the resistance toward the probe reaction R_{PB} , reported in Table 3.3 for both the oxidation (+0.1 V) and reduction (+0.25 V) potentials of the redox probe, were very similar for the non-patterned and DONUT samples, but were slightly increasing for the GRID sample. Since the resistance values remained of the same order of magnitude, this difference was probably due to an overall increase in disorder as a result of micropatterning.

Table 3.3 R_{PB} values obtained in case of the non-patterned and patterned samples for homopolymer and copolymer brushes.

Sample	PHEMA		PHEMA-co-PAMA 80:20	
	+ 0.1 V	+ 0.25 V	+0.1 V	+0.25 V
Non-patterned	1413	91	3190	160
DONUT	1289	88	1048	104
GRID	1759	172	623	52

The situation observed for the PHEMA-co-PAMA 80:20 brushes is far more different (Figure 3.10b). The trend of the first semicircle diameters is GRID < PHEMA-co-PAMA(non-patterned) < DONUT, which is different for that observed for PHEMA samples. The DONUT sample has the highest R value, probably because its reduced overall density of charged groups (which improved ion permeability) compared to the non-patterned sample. Interestingly, the lowest R value is obtained for the GRID sample, since in this case a higher concentration of charged groups is directly exposed to the electrolyte, enhancing the lateral diffusion. The R_{PB} reported in Table 3.2 assign the lowest value to the GRID sample, followed by the DONUT. It is noteworthy that these values are consistently lower compared to those obtained for the corresponding non-patterned PHEMA-co-PAMA sample, confirming the relevance of patterning to increase the redox probe uptake ability of the brushes. Moreover, GRID shows also a lower resistance than non-patterned PHEMA, which has the lowest resistance among all the non-patterned samples. All these findings suggest that micropatterning increase the availability of cationic amine groups thanks to the higher surface area of the brushes.

Moreover, all these results clearly demonstrate the power of patterning and especially micropatterning to control the values of probe reaction resistance.

3.3 Conclusion

The need for on-chip electrochemical sensors calls for innovative microfabrication strategies. Here we demonstrated for the first time that silicon wafer modified with grafted-from polymer brushes holds all the premises for the development of integrated electrochemical microsensors. We employed PHEMA, PAMA and their copolymers as a proof-of-concept. However, it is possible to tune the characteristics of the brushes *e.g.* to make them negatively charged, less or more hydrophilic, to confer antifouling properties (especially for biological applications) simply by choosing the appropriate monomer. More importantly, this means that the system can be designed for specific target molecules. Hydrophilic polymer brushes allow a typical redox probe, ferrocyanide, to react at an otherwise electrochemically inert surface, suggesting that the grafted chains behaved as “tentacles” to capture the redox probe and holding it in the proximity of the electrode surface. Moreover, such behaviour is found to be dramatically enhanced for micropatterned polymer brushes. This is another unprecedented result, which paves the way for miniaturization and on-chip applications, especially considering the remote photolithography approach employed for the micropatterning: mild, dry and highly compatible with conventional microfabrication processes.

3.4 Specific procedures

Materials: All the chemicals are reagent grade, purchased from Aldrich and used as received unless otherwise stated. Hydroxyethyl methacrylate (HEMA) is filtered through an inhibitor-remover column and stored at +4 °C until use. 2-Aminoethyl methacrylate hydrochloride (AMA, 90%, contains ~500 ppm phenothiazine as stabilizer) is used as received or purified by washing with inhibitor-free THF (for details see below). The ATRP initiator (3-(2-bromoisobutyramido)propyl)triethoxysilane (BIB-APTES) is synthesized and used to functionalize silicon substrates as described in Appendix C. Water obtained from a Millipore MilliQ purification system (resistivity $\geq 18.2 \text{ M}\Omega \text{ cm}^{-1}$) is thoroughly used. Silicon (100) wafers, single-polished, n type, phosphorus doped, 3 – 6 ($\Omega \text{ cm}$), with a native oxide layer ca. 1.5 nm thick, are purchased from Ultrasil Corporation.

Preparation of inhibitor-free AMA: Commercial AMA contains ~500 ppm of phenothiazine (PTZ) as inhibitor. To remove it from AMA, the raw product is mixed with THF (inhibitor-free, CHROMASOLV® Plus, for HPLC) in a 1:20 m/v ratio (e.g. 1 g raw AMA per 20 mL THF) and left in the dark under stirring for 2 h. The purified, white AMA is collected by filtration on porous glass, washed with THF and eventually dried under vacuum at room temperature. To check the purity of the resulting product, UV-vis spectroscopy (Figure 3.11) is performed on solutions made by dissolving 0.0075 g of sample in 5 mL of a 4:1 v/v methanol-water mixture. UV-vis spectra are collected using a Jasco V-630 double-beam spectrophotometer. The removal of phenothiazine is evident both from the aspect of the purified product (raw AMA is greenish white, Figure 3.11a) and from the UV-vis spectra: the signals at 250 nm and 314 nm characteristic for phenothiazine [41], clearly visible for raw AMA, are absent in the spectrum of purified AMA (Figure 3.11b). To check the influence of PTZ on the polymerization kinetics of AMA, a batch of samples is synthesized using the purified AMA and compared to that obtained using commercial AMA. As shown in Figure 3.2b, the two kinetic plots overlap indicating no effect of PTZ on the ATRP polymerization of AMA in the conditions selected.

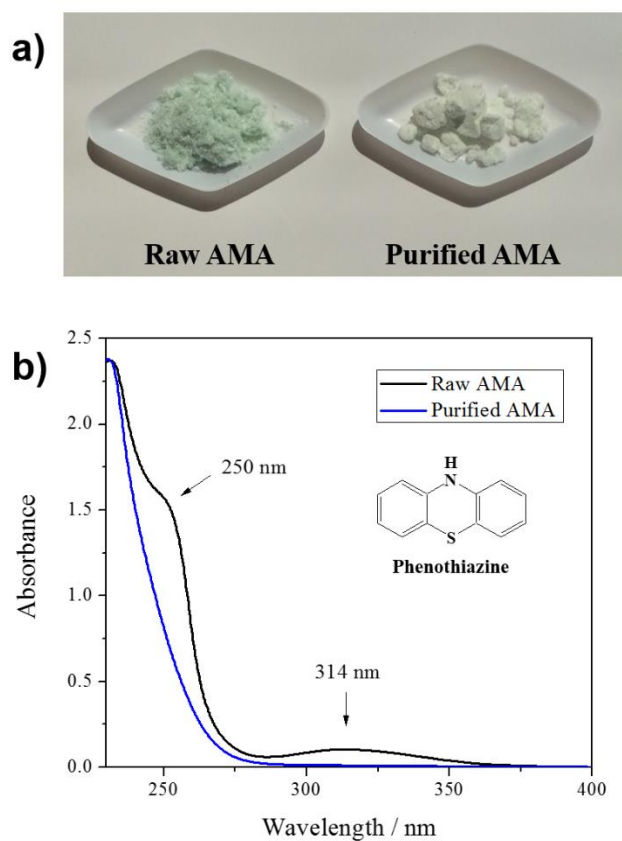


Figure 3.11 Comparison of raw and purified AMA by a) color and b) UV-vis spectroscopy.

Characterization methods: Thickness of polymer brushes is measured using a Filmetrics F20 reflectometer. Each data is the result of three measurements on different spots of a same sample. Scanning electron microscopy (SEM) is performed, on samples fixed on conducting carbon tape, using a Jeol JSM 7600f Schottky Field Emission Scanning Electron Microscope. A potentiostat/galvanostat Autolab PGSTAT204 (Metrohm, The Netherlands) equipped with a FRA module is employed to perform electrochemical measurements using a standard three electrode-cell with a saturated calomel, a Pt wire and a modified silicon wafer as reference, counter and working electrodes, respectively. Aqueous 0.1 M KCl is thoroughly used as the supporting electrolyte. Cyclic voltammetry (CV) was performed by scanning the potential between -0.1 V and $+0.4$ V (SCE) (scan rate 0.1 V s^{-1}). Electrochemical impedance spectroscopy (EIS) is carried out at -0.1 V, $+0.1$ V and $+0.25$ V (SCE) in the presence or in the absence of 3 mM $K_4Fe(CN)_6$ as redox probe. Impedance data are fitted by using ZView 2.0 software.

Grafting-from of homo- and copolymer brushes by SI-ATRP: Surface-Initiated ATRP is performed on both non-patterned and patterned substrates. To ensure reproducibility, each series is polymerized in a same batch.

PHEMA brushes are obtained using the following recipe. First, 0.0214 g (0.074 mmol) tris(2-pyridylmethyl)amine (TPMA), 0.002 g (0.009 mmol) CuBr₂ and 0.023 g (0.13 mmol) ascorbic acid are combined in a Schlenck flask under nitrogen, dissolved under stirring in 15.4 mL of a 4:1 v/v methanol-water mixture previously degassed by bubbling nitrogen. Then, 4.6 mL (0.038 mol) of degassed HEMA are added. Each substrate, contained in a Schlenck flask, is immersed in 5 mL of the resulting mixture under nitrogen and polymerization is allowed to proceed at 30 °C for the desired time. After polymerization the substrates are washed with ethanol, gently sonicated in the same solvent and dried under a nitrogen stream.

PAMA brushes are obtained using the same protocol described for PHEMA brushes, using 6.3 g (0.038 mol) of AMA and 20 mL of the 4:1 v/v methanol-water solution. After polymerization the substrates are washed with water, gently sonicated in the same solvent and dried under a nitrogen stream.

PHEMA-*co*-PAMA copolymer brushes are obtained using the same basic procedure for PHEMA brushes. For the 80:20 HEMA-AMA monomer ratio, 3.6 mL (0.03 mol) of HEMA, 1.36 g (0.0082 mol) AMA and 17 mL of the methanol-water mixture are combined. For the 50:50 HEMA-AMA monomer ratio, 2.3 mL (0.019 mol) HEMA and 3.41 g (0.0206 mol) AMA are combined with 18 mL of methanol-water. Polymerization proceeds at 30°C for a chosen amount of time, the workup is the same as previously described.

Micropatterning by remote photocatalytic lithography: Patterning by remote photocatalytic lithography is achieved following the procedure discussed in Chapter 1, using glass slides coated with a titanium dioxide film (for details see Appendix C). Before use, the titania-coated glass slides are cleaned by a rapid sonication in water followed by UV irradiation for 1 h. Remote photocatalytic lithography is performed by irradiating with 365 nm near-UV light from a Jelosil HG500 halogen lamp (230 V, 500 W, effective power density from 40 cm: 57.5 (mW cm⁻²) between 280 and 400 nm) the initiator-functionalized silicon substrates through the titania-coated glass, with the photocatalytic oxide facing the

substrate, separated from the surface by a 100 μm -thick Teflon spacer. Micropatterning is achieved using TEM grids (Gilder Grids, nickel, d 3.05 mm, square mesh) or hollow, circular grid supports (d_{ext} 3 mm, d_{hole} 1 mm, referred to as “donuts”) as contact photomasks. To obtain the best pattern resolution, the initiator-functionalized substrates are subjected to remote photocatalytic lithography for 5 h.

3.5 References

- [1] U. Guth, W. Vonau and J. Zosel, *Meas. Sci. Technol.*, **2009**, *20*, 042002.
- [2] G. Soliveri, V. Pifferi, G. Panzarasa, S. Ardizzone, G. Cappelletti, D. Meroni, K. Sparnacci and L. Falciola, *Analyst*, **2015**, *140*, 1486–1494.
- [3] V. Pifferi, G. Soliveri, G. Panzarasa, S. Ardizzone, G. Cappelletti, D. Meroni and L. Falciola, *RSC Adv.*, **2015**, *5*, 71210–71214.
- [4] S. Xun, X. Song, L. Wang, M. E. Grass, Z. Liu, V. S. Battaglia and G. Liu, *J. Electrochem. Soc.*, **2011**, *158*, A1260.
- [5] S. Ciampi, P. K. Eggers, G. Le Saux, M. James, J. B. Harper and J. J. Gooding, *Langmuir*, **2009**, *25*, 2530–2539.
- [6] R. D. Rohde, H. D. Agnew, W. S. Yeo, R. C. Bailey and J. R. Heath, *J. Am. Chem. Soc.*, **2006**, *128*, 9518–9525.
- [7] R. Barbey, L. Lavanant, D. Paripovic, N. Schüwer, C. Sugnaux, S. Tugulu and H.-A. Klok, *Chem. Rev.*, **2009**, *109*, 5437–527.
- [8] S. Minko, *Polym. Rev.*, **2006**, *46*, 397–420.
- [9] J.-K. Chen, Z.-Y. Chen, H.-C. Lin, P.-D. Hong and F.-C. Chang, *ACS Appl. Mater. Interfaces*, **2009**, *1*, 1525–32.
- [10] N. Ayres, *Polym. Chem.*, **2010**, *1*, 769.
- [11] M. Welch, A. Rastogi and C. Ober, *Soft Matter*, **2011**, *7*, 297.
- [12] Y. Wang, M. Hung, C.-H. Lin, H. Lin and J. Lee, *Chem. Commun.*, **2011**, *47*, 1249–1251.
- [13] S. Cosnier and A. Karyakin (Eds), *Electropolymerization*, Wiley 2010.
- [14] W. Knoll and R. C. Advincula (Eds), *Funct. Polym. Film.*, Wiley 2011, voll. 1-2.

- [15] T. A. García, C. A. Gervasi, M. J. Rodríguez Presa, J. I. Otamendi, S. E. Moya and O. Azzaroni, *J. Phys. Chem. C*, **2012**, *116*, 13944–13953.
- [16] M. R. Bantz, E. L. Brantley, R. D. Weinstein, J. Moriarty and G. K. Jennings, *J. Phys. Chem. B*, **2004**, *108*, 9787–9794.
- [17] E. L. Brantley, T. C. Holmes and G. K. Jennings, *J. Phys. Chem. B*, **2004**, *108*, 16077–16084.
- [18] E.-Y. Choi, O. Azzaroni, N. Cheng, F. Zhou, T. Kelby and W. T. S. Huck, *Langmuir*, **2007**, *23*, 10389–94.
- [19] C. Combellas, F. Kanoufi, S. Sanjuan, C. Slim and Y. Tran, *Langmuir*, **2009**, *25*, 5360–70.
- [20] T. Alonso-García, M. J. Rodríguez-Presa, C. Gervasi, S. Moya and O. Azzaroni, *Anal. Chem.*, **2013**, *85*, 6561–6565.
- [21] T. Alonso-García, C. A. Gervasi, M. J. Rodríguez-Presa, E. Gutierrez-Pineda, S. E. Moya and O. Azzaroni, *J. Phys. Chem. C*, **2013**, *117*, 26680–26688.
- [22] M. Krishnamoorthy, S. Hakobyan, M. Ramstedt and J. E. Gautrot, *Chem. Rev.*, **2014**, *114*, 10976–11026.
- [23] A. E. Madkour, J. M. Dabkowski, K. Nüsslein and G. N. Tew, *Langmuir*, **2009**, *25*, 1060–1067.
- [24] Y. Zhang, N. Islam, R. G. Carbonell and O. J. Rojas, *ACS Appl. Mater. Interfaces*, **2013**, *5*, 8030–8037.
- [25] M. E. Welch and C. K. Ober, *J. Polym. Sci. Part B Polym. Phys.*, **2013**, *51*, 1457–1472.
- [26] T. Chen, I. Amin and R. Jordan, *Chem. Soc. Rev.*, **2012**, *41*, 3280–96.
- [27] G. Panzarasa, G. Soliveri, K. Sparnacci and S. Ardizzone, *Chem. Commun.*, **2015**, *51*, 7313–7316.
- [28] G. Maino, D. Meroni, V. Pifferi, L. Falciola, G. Soliveri, G. Cappelletti and S. Ardizzone, *J. Nanopart. Res.*, **2013**, *15*, 2087.
- [29] K. Matyjaszewski, *Macromolecules*, **2012**, *45*, 4015–4039.
- [30] W. Huang, J. B. Kim, M. L. Bruening and G. L. Baker, *Macromolecules*, **2002**, *35*, 1175–1179.
- [31] M. Fantin, A. a. Isse, A. Gennaro and K. Matyjaszewski, *Macromolecules*, **2015**, DOI: 10.1021/acs.macromol.5b01454.
- [32] C. H. Peng, J. Kong, F. Seeliger and K. Matyjaszewski, *Macromolecules*, **2011**, *44*, 7546–7557.
- [33] O. Carp, *Prog. Solid State Chem.*, **2004**, *32*, 33–177.

- [34] W. Kubo and T. Tatsuma, *J. Am. Chem. Soc.*, **2006**, *128*, 16034–16035.
- [35] G. Soliveri, V. Pifferi, R. Annunziata, L. Rimoldi, V. Aina, G. Cerrato, L. Falciola, G. Cappelletti and D. Meroni, *J. Phys. Chem. C*, **2015**, *119*, 15390–15400.
- [36] R. N. Vyas and B. Wang, *Int. J. Mol. Sci.*, **2010**, *11*, 1956–1972.
- [37] F. Zhou, H. Hu, B. Yu, V. L. Osborne, W. T. S. Huck and W. Liu, *Anal. Chem.*, **2007**, *79*, 176–182.
- [38] M. R. Presa and L. Gassa, *Anal. Chem.*, **2009**, *81*, 7936–7943.
- [39] E. Spruijt, E. Choi and W. Huck, *Langmuir*, **2008**, *24*, 11253–11260.
- [40] de Graaf, A. J.; Mastrobattista, E.; van Nostrum, C. F.; Rijkers, D. T. S.; Hennink, W. E.; Vermonden, T. *Chem. Commun.*, **2011**, *47*, 6972–6974.
- [41] Van Allan, J. A.; Reynolds, G. A.; Adel, R. E. *J. Org. Chem.* **1962**, *27*, 1659–1664.

Chapter 4

Positron Annihilation Spectroscopy: A New Frontier for Understanding Nanoparticle-Loaded Polymer Brushes

ABSTRACT Nanoparticle-loaded polymer brushes are powerful tools for the development of innovative devices. However, their characterization is challenging and arrays of different techniques are typically required to gain sufficient insight. Here we demonstrate for the first time the suitability of Positron Annihilation Spectroscopy (PAS) to investigate, with unprecedented detail and without making the least damage to samples, the physico-chemical changes experienced by pH-responsive polymer brushes after protonation and after loading of silver nanoparticles. One of the most important findings is the depth profiling of silver nanoparticles inside the brushes. These results open up a completely new way to understand the structure and behavior of such complex systems.

4.1 Introduction

Polymer brushes are at the cutting edge of modern polymer science, thanks not only to their unique properties but also for the problems posed by their characterization. Polymer brushes are defined as assemblies of polymer chains anchored by one end to a surface, with a coverage sufficiently high that the chains are forced to stretch away from the surface to avoid crowding. The analysis of these structures is challenging: because of their reduced dimensionality, assumptions based on analogous solution or bulk systems do not necessarily hold. For this reason, there is a strong desire to understand their fundamental properties at interfaces and in developing new applications [1,2]. The basic physics of polymer brushes was established already three decades ago and notable progresses have been made since.

However, one of the less understood and still challenging problem in polymer science and technology is the behavior of hybrid systems made of polymer brushes and nanoparticles. Both theoretical [3-8] and experimental [9-11] studies are stimulated not only by the variety of useful applications for the resulting nanocomposites [12] but also because to understand their behavior is of paramount importance in many different domains ranging from biology to organic electronics. In biology and related disciplines, being able to predict the behavior of polymer layers with nanoscale objects like proteins means the possibility to design efficient antimicrobial, antifouling, blood- and tissue-compatible surfaces [13-17]. Applications in drug delivery [18] and microfluidics [19] are promising as well. In organic electronics, photovoltaic devices exploiting the interaction of quantum dots with donor-acceptor brushes has already been demonstrated [20], but still the conditions governing nanoparticle distribution are unknown. The development of novel optical sensors [21,22]

and actuators [23] will also benefit from plasmonic noble metal nanoparticles embedded in stimuli-responsive (*e.g.* pH- and thermo-responsive) brushes.

Whereas theoretical studies are gaining momentum, thanks especially to progress in computer simulations, the lack of techniques allowing physical observation of such complex systems is a great hamper to significant progress in the development of brush-nanoparticle composites. To take a glimpse to the real system is the ultimate way to know the actual properties of a composite. It is already difficult to properly characterize nanometer-sized polymer layers such as polymer brushes and the problems posed by nanoparticle-loaded polymer brushes are especially tough. Despite several groups investigating the formation of nanoparticles inside or on top of polymer brushes only few experimental studies are available on nanoparticle infiltration into polymer brushes. To determine the distribution of nanoparticles inside the brushes is of paramount importance, however direct visualization of polymer brush-embedded nanoparticles is possible only by transmission electron microscopy on cut samples. The special skills required, the occurrence of artifacts due to incorrect sample preparation along with its intrinsically destructive nature make this approach not practical. For this reason, the vast majority of the studies relied on the use of indirect techniques such as ellipsometry [24], X-ray reflectivity [25] and UV-vis spectroscopy [26,27].

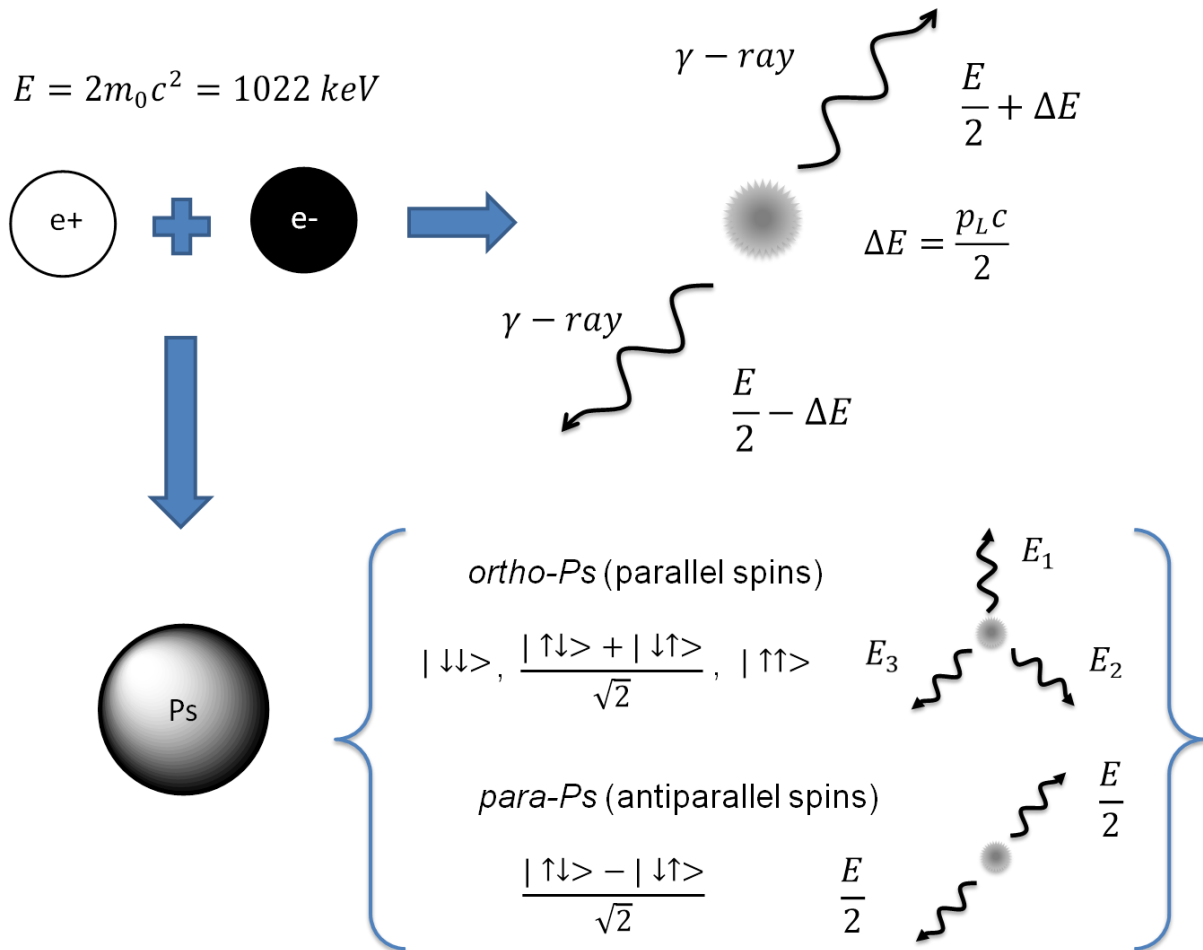
The introduction of a one-step, non-invasive technique that allows probing the distribution of nanoparticles in polymer brushes would act as a true game-changer for this field of applied research. We report here for the first time the use of Positron Annihilation Spectroscopy (PAS) as a powerful means to investigate nanoparticle loading into stimuli-responsive polymer brushes.

The key motivation of the present study is to demonstrate that Positron Annihilation Spectroscopy is the only actual technique allowing the study of nanoparticle distribution in polymer brushes with a single analysis and without damaging the sample. A system made of silver nanoparticles (AgNPs) embedded in grafted-from poly(dimethylaminoethyl methacrylate) (PDMAEMA) brushes obtained by surface-initiated atom transfer radical polymerization (SI-ATRP) was chosen as a representative case study for plasmonic nanoparticle-loaded stimuli-responsive polymer brushes, a system with promising applications especially for the development of sensors [41,42].

Positron Annihilation Spectroscopy

In the PAS technique positrons, positively charged antiparticles of electrons, are implanted with a controlled kinetic energy into the studied material and annihilate either as free positrons with the electrons in two 511 keV gamma-rays or in the form of a positron-electron bonded state called positronium. Positronium (Ps) is the lightest element, about 10^{-3} times lighter than hydrogen, and exists in the ground state in two sublevels: singlet (para-Ps, p-Ps) and triplet (ortho-Ps, o-Ps), according to the spins of the electron and positron (antiparallel or parallel, respectively) (Scheme 4.1). In vacuum, their lifetimes are very different, 0.125 and 142 ns for p-Ps and o-Ps, respectively. Also annihilation features in vacuum are different: p-Ps annihilates with emission of two γ -rays (511 keV each), while o-Ps annihilates by emitting three γ -rays, producing a continuous energy distribution for each photon between 0 and 511 keV, where the energy sum of the three photons of the o-Ps annihilation is 1022 keV. When o-Ps is formed inside a cavity of a material (such as a free volume hole in a polymer, a cage in a zeolite, a pore in a porous medium), the three- γ annihilation probability is reduced by the pick-off effect, that is, the positron of the o-Ps may

annihilate with an electron of the cavity surface in a relative singlet state with emission of two γ -rays instead of three.



Scheme 4.1 Scheme of possible electron-positron interactions. The positron can annihilate as a free positron with an electron of a material in two antiparallel gamma-rays of 511 keV (upper right sector). The gamma-ray energy is shifted by a quantity ΔE due to the Doppler effect; this quantity is proportional to the momentum of the electron-positron couple p_L along the gamma-rays direction. In cavities or free volumes positronium (Ps) can be formed (lower sector), following the spin selection rule, as ortho-Ps and para-Ps. The first annihilates in vacuum in three gamma-rays while the second in two gamma-rays. The Doppler shifts are not indicated because are rather small compared to the free annihilation process.

Under the collective name of PAS is grouped an array of techniques that have been developed to probe atomic/molecular defects and interfacial properties in materials, with applications ranging from metallurgy [28] to soft matter [29-31]. As has been demonstrated, Ps forms into the free volumes of many polymers and PAS can detect buried, isolated pores of 0.2–50 nm size, which are not accessible to conventional probes. Therefore, by monitoring the annihilation of positronium, the study of free volumes in polymers [32] and of transport mechanisms in membranes [28-33] is enabled in a completely non-invasive way. In the field of polymer research, the most frequently PAS techniques are [34]: i) Positron Annihilation Lifetime Spectroscopy (PALS) which measures the positron lifetime implanted in a sample material and ii) Doppler broadening of annihilation radiation which measures the broadening of the 511 keV peak coming from the positron-electron annihilations. When the size of the open spaces is at the nanometer scale (>1 nm) and ortho-Ps annihilation in three gamma-rays can be observed [35-36], another PAS technique known as the “3 γ -method” is also useful.

In recent years, PAS with a variable-energy positron beam has emerged as a powerful technique for the characterization of thin films [39,40], allowing depth-profiles from tens of nanometers up to several micrometers. To carry out PAS measurements on thin films it is necessary to tune the positron implantation energy in order to conduct a depth-profile study. The LNESS facility in Como is equipped with an electrostatic slow energy positron beam (by this point onwards referred to as the VEPAS beam), whose energies range from 0.1 keV to 20 keV, coupled with two hyperpure Ge detectors. In the VEPAS beam (see the Specific procedures paragraph for details) positrons are emitted from a 10 mCi radioactive ^{22}Na source and they are subsequently moderated by means of a W thin monocrystalline film (1 μm thick, [100] oriented). Since the ^{22}Na positron energy distribution is very spread

with a maximum at about 0.54 MeV, in order to tune the energy of the beam a W micrometric foil which re-emits positrons at ~ 2.5 eV with an efficiency of 10^{-3} - 10^{-4} is employed. The moderated positrons are then accelerated and implanted into the samples at a tunable kinetic energy. Once implanted positrons penetrate to a depth which depends on their initial kinetic energy and then thermalize, *i.e.* slow down, on a timescale of picoseconds. Afterwards the positrons diffuse and, as described above, can annihilate as free positrons or as positronium.

4.2 Results and Discussion

4.2.1 Nanoparticle-loaded, stimuli-responsive polymer brushes

The use of a controlled radical polymerization technique like SI-ATRP allows to obtain brushes with different thicknesses simply by varying the polymerization time. According to previous studies [43], the grafting density σ of the chains is expected to be at least 0.4 chains nm^{-2} . The distance between two adjacent grafted end-groups can be estimated as $g = \frac{1}{\sqrt{\sigma}} \approx 1.6$ nm. This value can be compared to the characteristic size of the chains in order to evaluate their conformation. As the polymer layer is in a dry state, it is reasonable to assume that the grafted chains will adopt a collapsed state with a characteristic dimension $G \approx aN^{0.33}$, where a is a characteristic dimension of the repeating unit (0.25 nm for methacrylates) and N is the average number of repeating units (*i.e.* the molecular mass) of the polymer chains. N can be estimated from XRR data. The brush conformation prevails at high grafting density or $g \ll G$, a condition our estimates suggest to be fulfilled for the investigated samples ($G > 8$ nm) which can then be considered as polymer brushes.

The brushes investigated in this work are made of poly(dimethylaminoethyl methacrylate) (PDMAEMA). As already discussed in Chapter 1, PDMAEMA is a weak polyelectrolyte with $pK_a \sim 7$, which makes its tertiary amine group to be easily protonated and deprotonated by immersion in acid or basic solutions respectively [44]. Protonation induces the formation of positive electrostatic charges and this effect, combined with excluded volume interactions and the osmotic pressure due to counterions, cause the chains to repel each other and swell after water absorption. The positive charges on protonated PDMAEMA brushes facilitate the incorporation of pre-made, negatively charged silver nanoparticles with a simple immersion step (Figure 4.1) [45,46].

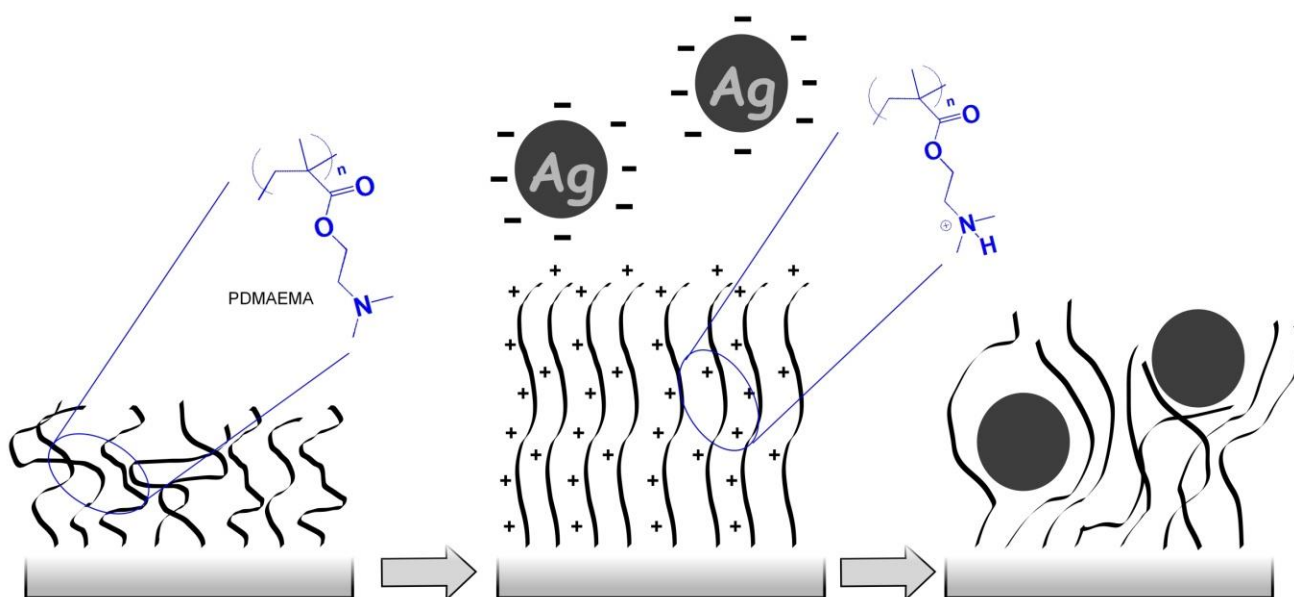


Figure 4.1 Schematic representation of the PDMAEMA brushes before and after protonation and the uptake of silver nanoparticles.

The incorporation of silver nanoparticles (Figure 4.4b) into the brushes induces evident morphological changes in the latter. The surface of as-prepared PDMAEMA brushes

appeared to be homogenous and smooth (Figure 4.2) but became rough after being dipped in the suspension of AgNPs.

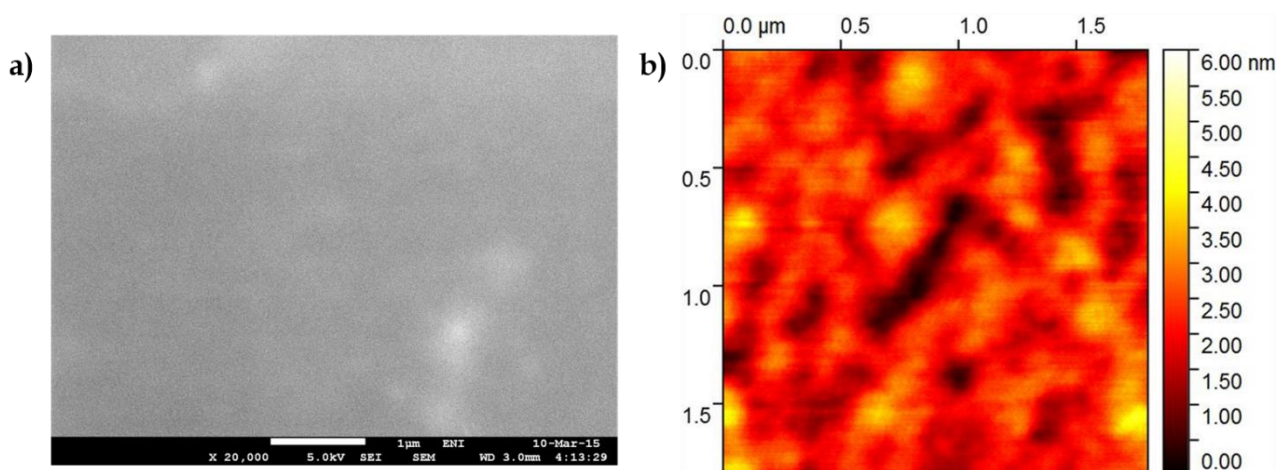


Figure 4.1 a) SEM and b) AFM images of PDMAEMA brushes before the incorporation of silver nanoparticles (roughness, rms: 0.79 nm).

From scanning electron microscopy images, silver nanoparticles are identifiable as spherical shapes protruding from the surface of the brushes (Figure 4.3). Backscattered electrons (Figure 4.3) were used to check for the presence of free nanoparticles on top of the brushes but the particles were buried in the polymer film, which appears reasonable considering that the mean thickness of the brushes was at least double respect to the mean diameter of AgNPs (~10 nm).

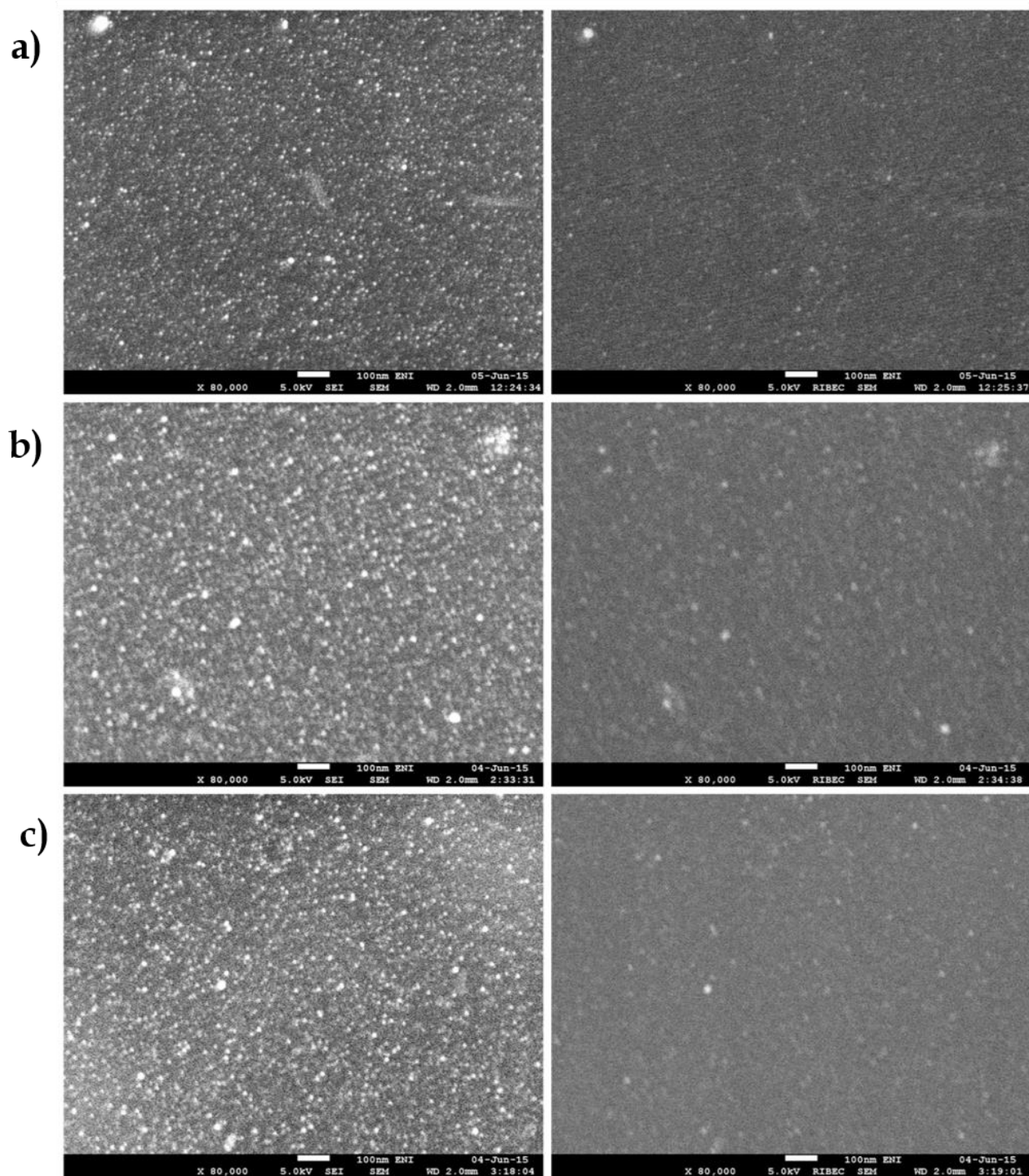


Figure 4.3. SEM images (left: topographic images; right: backscattered electrons) of silver nanoparticle-loaded polymer brushes. Samples: a) **Ag1**, b) **Ag2**, c) **Ag3**.

Due to the relevant optical applications described for noble metal particle-polymer brushes nanocomposites, the UV-visible absorption spectra for the AgNPs-PDMAEMA brushes are acquired for samples grown on transparent glass substrates, revealing a strong absorption

band attributable to the surface plasmon resonance (SPR) of the embedded silver nanoparticles (Figure 4.4). The original aqueous suspension of silver nanoparticles displays a sharp peak centered at 400 nm which is characteristic of monodisperse silver nanospheres with a mean diameter < 30 nm and is the fingerprint of a dipole surface plasmon resonance (SPR). SPR is known to be highly sensitive to variations of the particle aggregation state and of the refractive index of particle-surrounding medium. Three brush samples (**PB21 AgNPs**, **PB40 AgNPs** and **PB74 AgNPs**) with different thicknesses (21, 40 and 74 nm, respectively) are grown on glass substrates and loaded with silver nanoparticles. The UV-visible absorption spectra of the resulting particle-brush nanocomposites (Figure 4.4b) reveals a broader, tailed and red-shifted band compared to that displayed by “free” nanoparticles (Figure 4.4a). This could be a consequence of both steric and optical effect: not only brush-embedded silver nanoparticles are closer to each other due also to the collapse of polymer chains upon drying, they experience also a significant variation in the refractive index of the surrounding medium passing from water ($n_{water} = 1.33$) to PDMAEMA ($n_{PDMAEMA} = 1.52$).

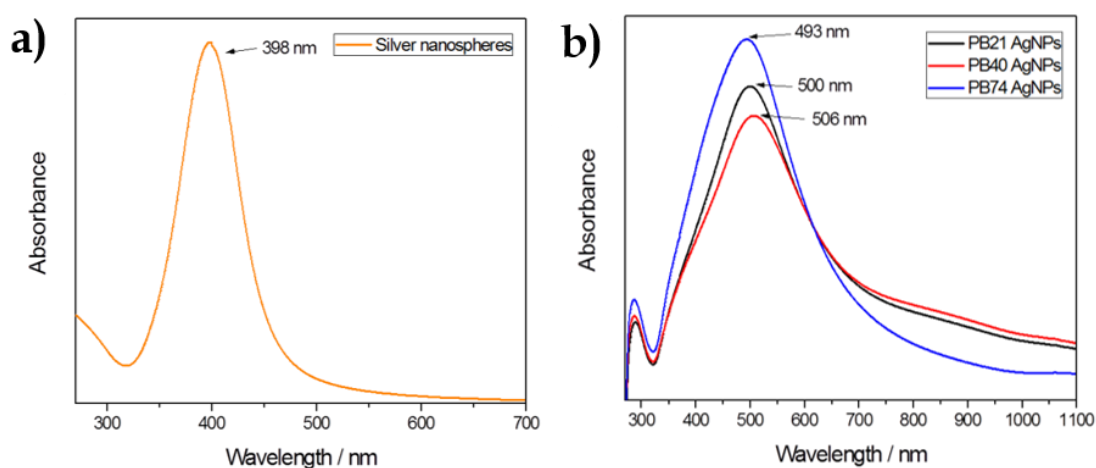


Figure 4.4 UV-vis absorption spectra of a) silver nanoparticles (aqueous suspension) and b) nanoparticle-loaded polymer brushes. The spectra have been normalized.

X-ray photoelectron spectroscopy (XPS) is used to investigate each synthetic step (Figure 4.5 and Figure 4.6) and to demonstrate the effective incorporation of silver nanoparticles. Despite in the AgNP-loaded brushes the N 1s signal was confused by the strong Ag 3d peak, precious information about the chemical environment of the nanoparticle surface can be obtained. It is noteworthy to highlight that the Ag 3d peak at 367.5 eV is typical of Ag⁰, because the Ag peaks for pristine AgNPs (Figure 4.5a) showed a dramatic shift indicative of a strong coordination, of the type (O=C-O)⁻ Ag⁺, between adsorbed citrate anions and surface silver atoms. After incorporation into the brushes the negatively charged citrate molecules are neutralized together with the positively charged protonated PDMAEMA brushes, thus leaving the surface of nanoparticles “free” (Figure 4.5b).

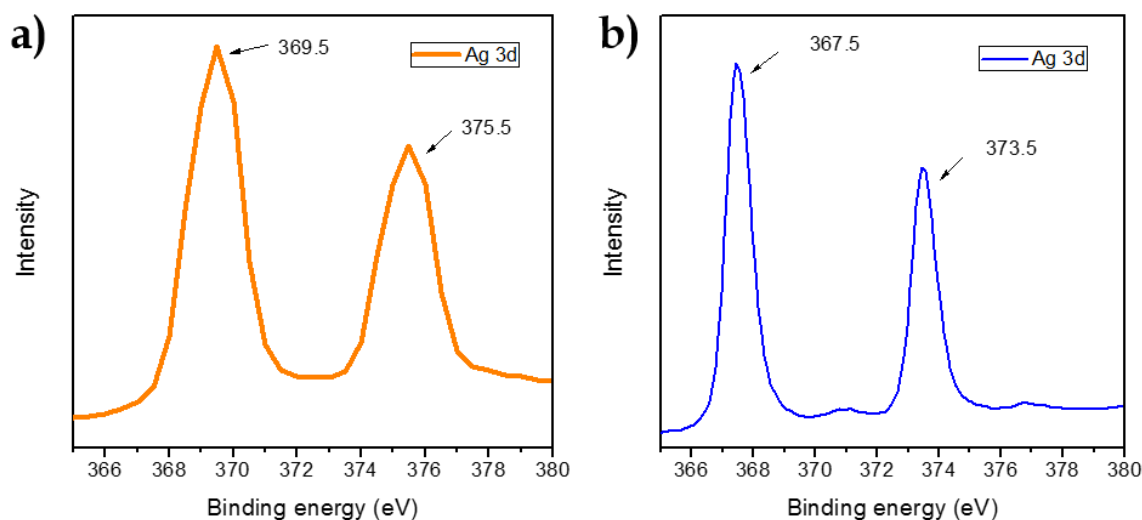


Figure 4.5 XPS spectra of a) pristine silver nanoparticles and of b) silver nanoparticles loaded in PDMAEMA brushes.

To perform XPS studies a sample, referred to as **PB50**, is cut into three samples of which two are protonated and only one is eventually loaded with AgNPs. The C 1s and O 1s high resolution spectra for all the three kind of samples shows easily recognizable features for C-C (284 eV), C=O (289 eV C 1s and 531.5 eV O 1s), C-N (533 eV). The N 1s spectrum shows

clearly the tertiary amine group at 399 eV and a shoulder at 402 eV indicating that a minor fraction of the amine groups is in the protonated state. After soaking in dilute nitric acid, along with the 399 eV peak, this shoulder at 402 eV becomes more pronounced confirming that the protonation step is successful. In addition, a peak at 406 eV appears which is assigned to the nitrate anion. This peak is underestimated, suggesting that some nitrate anions are stripped off by the high vacuum.

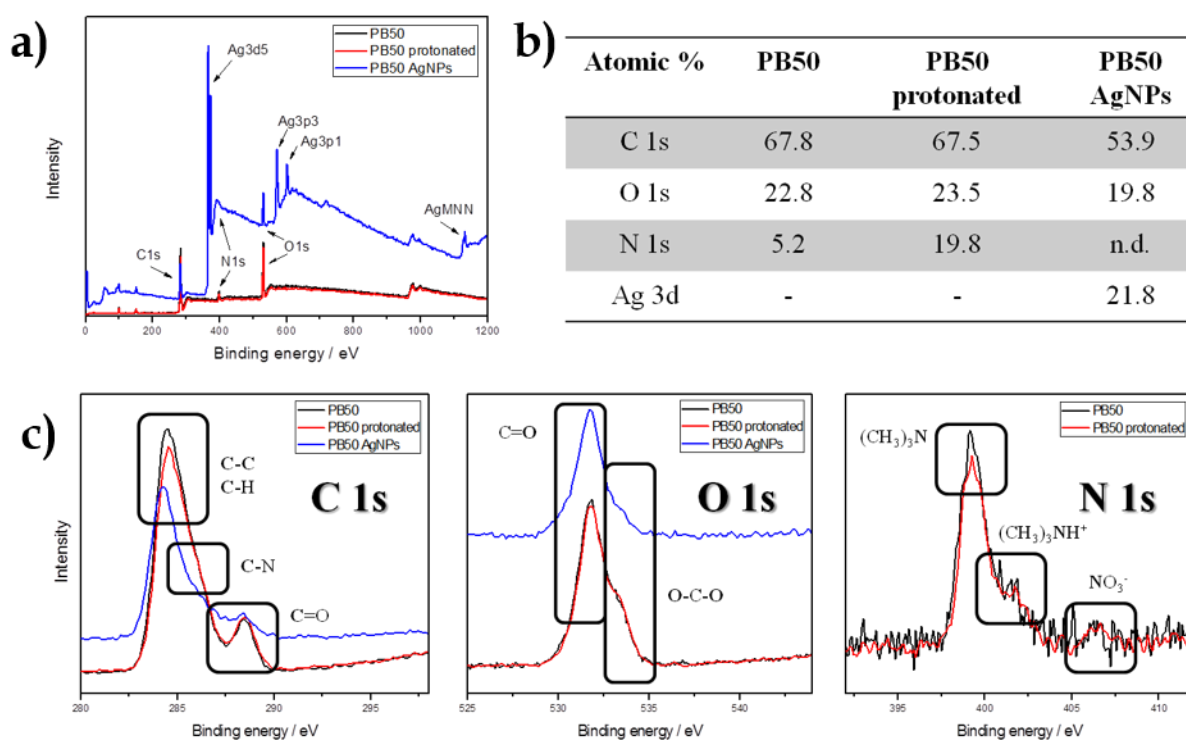


Figure 4.6 XPS spectra for 50 nm-thick PDMAEMA brushes before and after protonation, after loading of silver nanoparticles. a) survey, b) calculated atomic % and c) high-resolution spectra (for C 1s, O 1s and N 1s).

Polymer brushes before and after the uptake of AgNPs are investigated also with X-ray reflectivity (Figure 4.6), which allows to determine their thickness and density. However, XRR is unable to confirm the presence of silver nanoparticles inside the brushes. Due to the homogenous distribution of silver nanoparticles in the polymer matrix the fitted density

values were clearly underestimated (Table 4.1 and Table 4.2). This was due to the less definite character of the layers, as could be seen from the quenching of the Kiessig fringes at low angles.

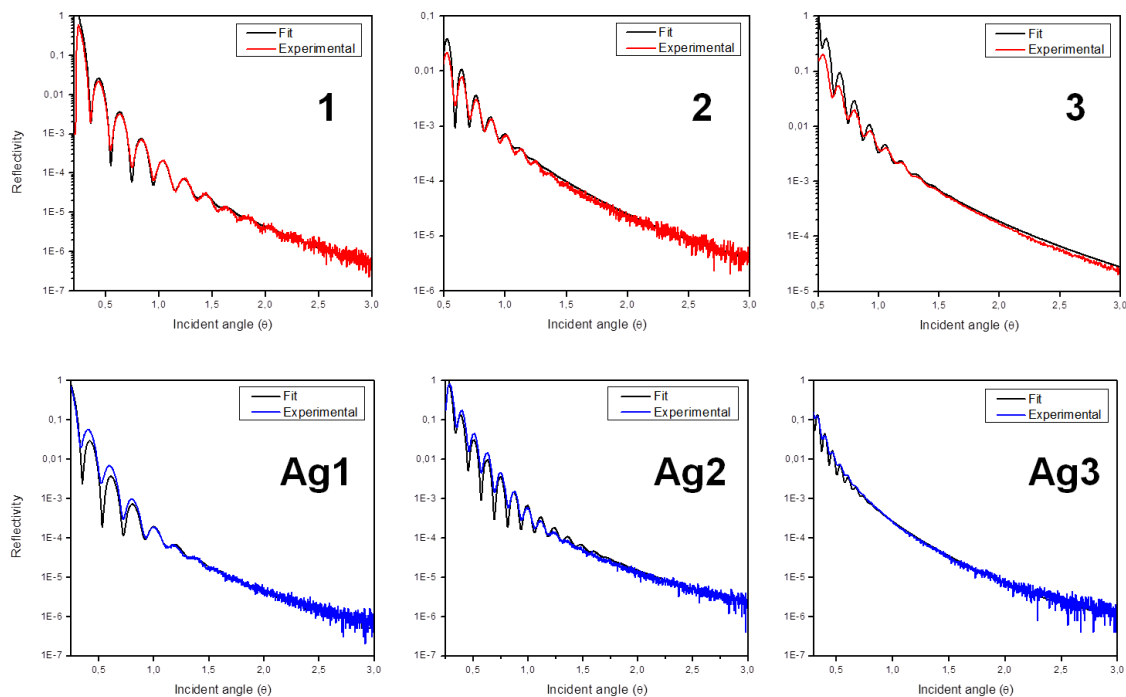


Figure 4.6 XRR spectra of PDMAEMA brushes before (red lines) and after (blue lines) incorporation of silver nanoparticles along with the fitted curves (black lines). The spectra are normalized.

Table 4.1 XRR values obtained for pristine PDMAEMA brushes.

Sample	Polymerization time <i>h</i>	Thickness <i>nm</i>	Density <i>g/cm³</i>	Surface coverage <i>μg/cm²</i>	Estimated <i>M_n</i> <i>g/mol</i>
1	0.25	21	1.5	3	47423
2	0.5	36	1.8	6	97556
3	2	63	1.8	11	170724

Table 4.2 XRR values obtained for silver nanoparticle-loaded PDMAEMA brushes.

Sample	Thickness (before AgNPs) <i>nm</i>	Density (before AgNPs) <i>g cm⁻³</i>	Initiator layer-brush interface roughness (before AgNPs) <i>nm</i>	Brush-air interface roughness (before AgNPs) <i>nm</i>
Ag1	22 (21)	1.49 (1.5)	0.3 (0.32)	1.4 (3)
Ag2	36 (36)	0.9 (1.8)	0.25 (0.25)	0.26 (1.8)
Ag3	60 (63)	1.34 (1.8)	0.4 (0.4)	2.6 (1.1)

4.2.2. What can Positron Annihilation Spectroscopy tell about nanoparticle-loaded polymer brushes?

Five different samples of PDMAEMA brushes grafted from silicon substrates (*n*-type, 3-6 Ω cm⁻¹) are investigated with positron annihilation spectroscopy (PAS). Table 4.3 summarizes the principal characteristics of these samples. Protonation of the brushes and uptake of silver nanoparticles are investigated. The first sample listed in Table 4.3 (PDMAEMA), representative of the as-prepared brushes, is composed of a thin layer of polymer grafted from the silicon substrate. The second sample (H⁺) was protonated by immersion in dilute nitric acid. The other three samples *i.e.* Ag1, Ag2, and Ag3 have increasing thicknesses. They were protonated and then immersed in an aqueous suspension of silver nanoparticles to allow the uptake of the latter.

Table 4.3 Polymer brushes samples studied by means of PAS.

Sample	Protonation	AgNPs	Thickness <i>nm</i>
PDMAEMA	No	No	18 ± 1
H+	Yes	No	20 ± 1
Ag1	Yes	Yes	27 ± 1
Ag2	Yes	Yes	40 ± 1
Ag3	Yes	Yes	66 ± 1

PAS measurements are conducted by means of the VEPAS beam. Thirty-eight values for the positron implantation energy are chosen between 0.1 keV and 18 keV and, for each energy value, two hyperpure Ge detectors coupled with a MCA system recorded the annihilation spectrum. The positron annihilation peak is centered at 511 keV. Its broadening is a consequence of the Doppler effect due to the electron-positron center of mass momentum respect to the laboratory frame of reference. The *S*-parameter is then defined as the ratio between the area in the central part of the annihilation peak, within the energy range of 511 ± 0.85 keV ($|p_L| \leq 0.456$ atomic units). The *W*-parameter (“wing” or core annihilation parameter) is taken in high-momentum region far from the center part of the peak, within the range from 511 ± 1.8 keV to 511 ± 4 keV. The total area of the peak is taken in the range 511 ± 4.25 keV.

For each implantation energy the *S*-parameter and the three-gamma fraction $F_{3\gamma}$ are measured and shown in Figure 4.7. The corresponding values obtained for the *W*-parameter are shown in Figure 4.8 and Figure 4.9.

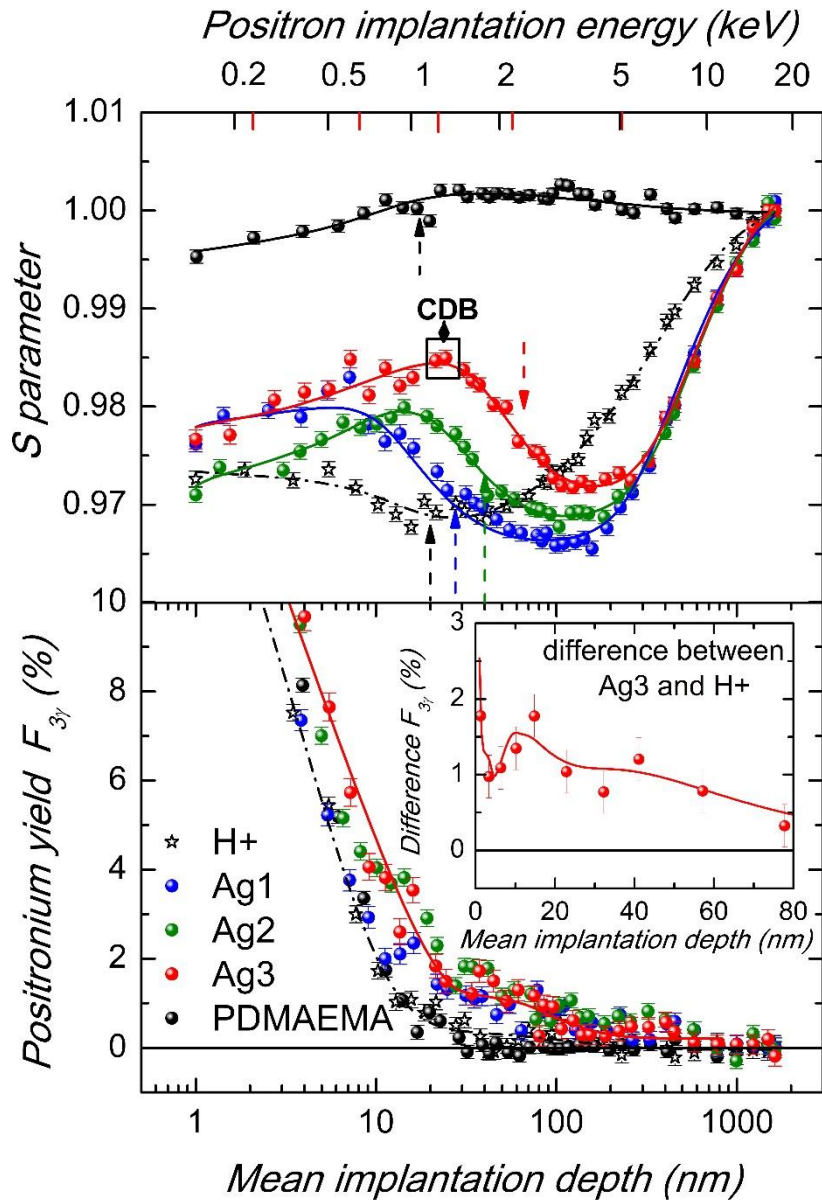


Figure 4.7 Upper panel: normalized S -parameter as a function of the positron mean implantation depth for various samples of PDMAEMA brushes on silicon substrates: as-made (PDMAEMA), after protonation (H+) and after loading of silver nanoparticles (Ag1, Ag2, Ag3). The lines through the experimental data represent the results of a best-fit procedure obtained with VEPFIT. The black and red color ticks correspond to the average of the samples without and with silver respectively. Lower panel: positronium fraction profile in the studied samples. The insertion shows the difference between the $F_{3\gamma}$ for Ag3 and H+ samples (the data points are the average of two adjacent data points).

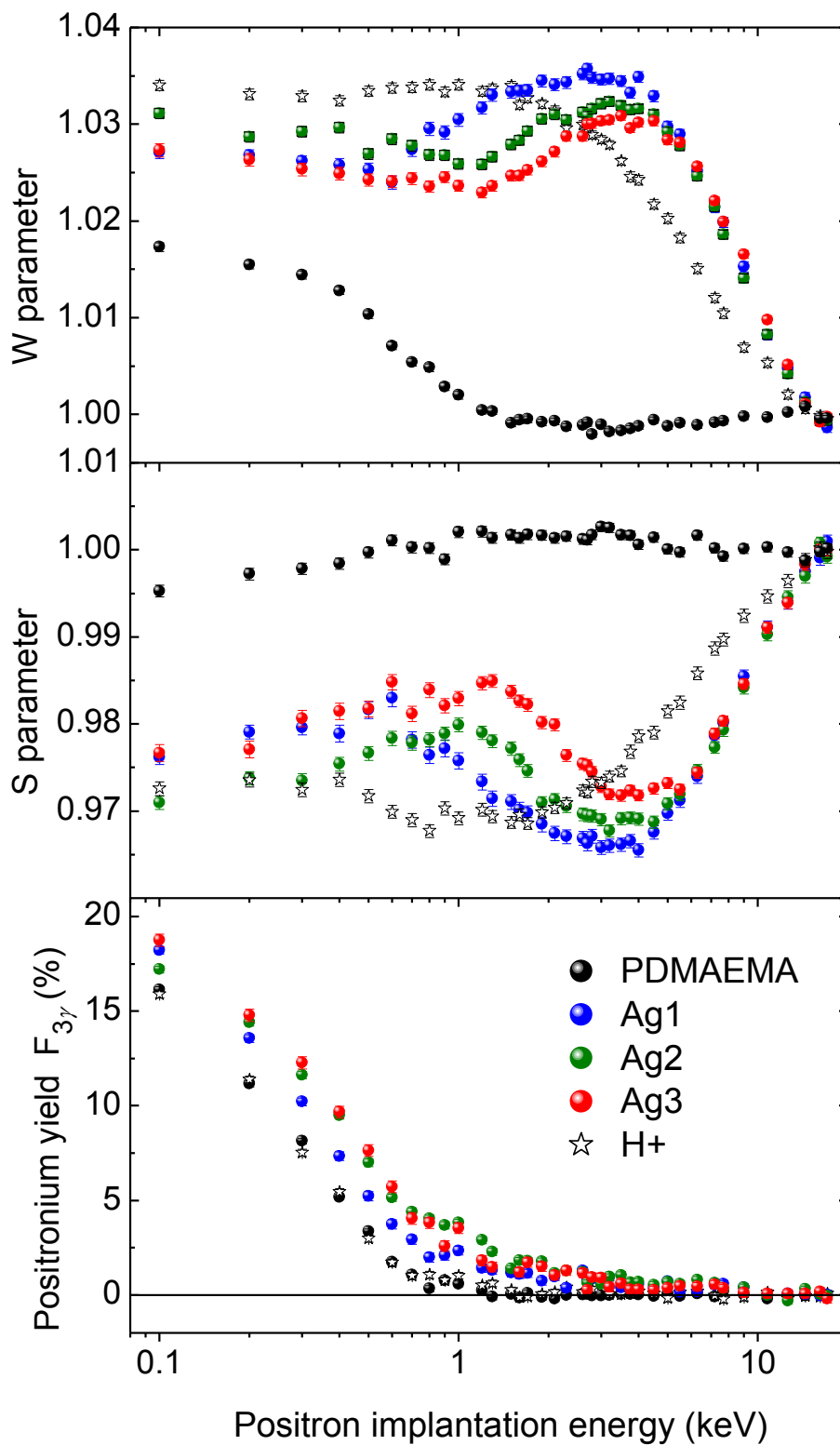


Figure 4.8 S , W and $F_{3\gamma}$ parameters as a function of the positron implantation energy for pristine, protonated and silver nanoparticles-loaded PDMAEMA brushes grown on silicon substrate.

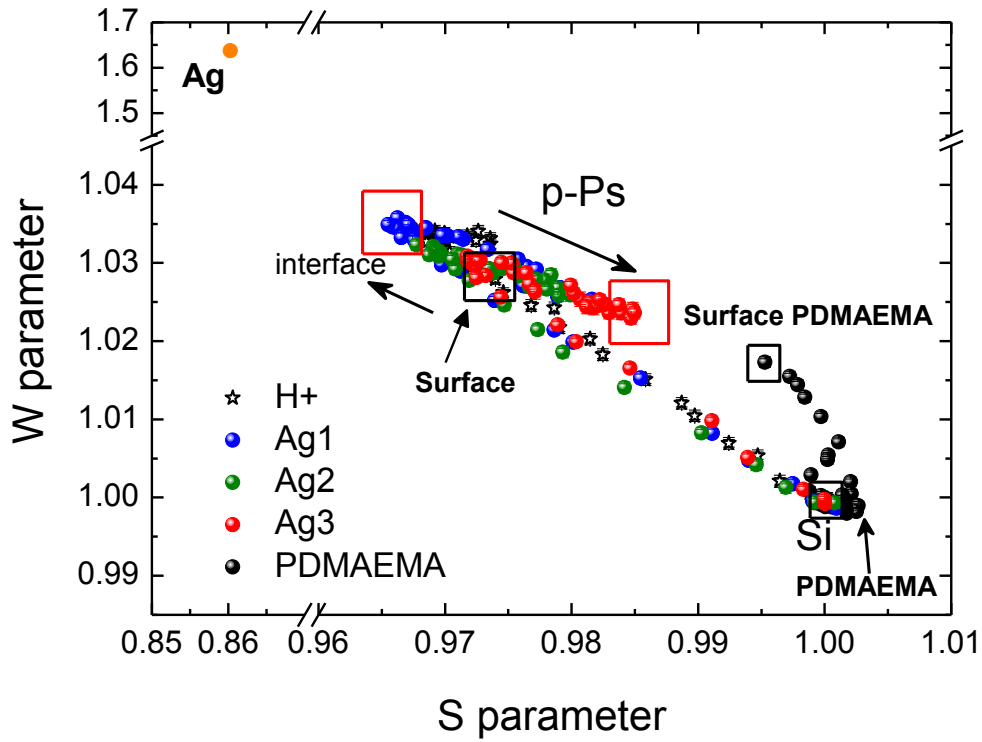


Figure 4.9 W parameter vs. S parameter plot (data of Figure 4.8).

The S -parameter corresponds to the annihilation of the positrons with the valence electrons of the material, p -Ps annihilation or the o -Ps atoms undergoing a pick-off annihilation. The three-gamma fraction $F_{3\gamma}$ is calculated according to the “ 3γ method”. When the studied material contains big cavities (>1 nm), the annihilation of o -Ps in three gamma-rays is observed and in this case $F_{3\gamma}$ is proportional to the Ps yield. The energy distribution of each of the three gamma rays is continuous between 0 and 511 keV. By defining $R(E)$, E being the positron implantation energy, as:

$$R(E) = \frac{V}{P} \quad (1)$$

where P are the integrated counts in the peak area, within the energy region 511 ± 4.25 keV, and V is the valley area above the Compton edge, from 350 keV up to 500 keV, the three-gamma fraction $F_{3\gamma}$ is given by:

$$F_{3\gamma} = \left[1 + \frac{P_1 R_1 - R(E)}{P_0 R(E) - R_0} \right]^{-1} \quad (2)$$

where the subscripts 0 and 1 refer to the cases with 0 % and 100 % Ps production, respectively.

Figure 4.7 shows the S -parameter normalized to the value of this parameter in silicon ($S = S_m/S_{Si}$, where $S_{Si} \approx 0.543$ and S_m is the measured value) and the three gamma fraction $F_{3\gamma}$ as well (lower panel), for the samples listed in Table 4.3. The data points are the average of the data obtained by the two Ge detectors. The S and $F_{3\gamma}$ parameters are represented as a function of the mean positron implantation depth (lower abscissa) and of the positron implantation energy (upper abscissa, black and red correspond to the samples without and with Ag nanoparticles respectively). The mean implantation depths are evaluated by adopting the Makhov profiles as the stopping profiles of the implanted positrons (see the Specific procedures paragraph for details). The dashed arrows indicate the positron implantation depths corresponding to the different brush thicknesses. It is possible to consider them as thresholds beyond which the positrons annihilate within the interface and the silicon substrate. The continuous lines through the data points in the upper panel represent the best fits obtained with the VEPFIT program [47]. This software is a best-fit procedure based on the solution of the diffusion equation in each layer of a heterostructure, taking into account the energy dependent positron implantation profiles. The model free parameters, for each layer, are the following: the S -parameter value, the positron diffusion length, the electric field (when present) and the layer density.

By comparing the data shown for the **PDMAEMA** and **H+** samples in Figure 4.7 it is possible to observe that protonation causes a dramatic change of the S -parameter value for the brush layer. For the **PDMAEMA** (non-protonated) sample the implanted positrons form

positronium atoms that remain confined into the free volumes (sub-nanometric cavities ~ 0.3 nm) [48-50], annihilating by pick-off and giving the maximum S -parameter value of the distributions ($S > 1$). The profile of the S -parameter after protonation (sample **H+**) drops with respect to the non-protonated sample (**PDMAEMA**), a fact that demonstrates the inhibition of Ps formation. This effect is a consequence that positron traps for the **H+** sample are of a different nature with respect to the not protonated samples. By the acid-base reaction of nitric acid with the PDMAEMA tertiary amine groups, *i.e.* the protonation step, electric dipoles are formed along each polymer chain with the positive charges located on the protons and the negative ones on the polarized nitrogen atoms of PDMAEMA chains, which in turn attract the positrons.

The $F_{3\gamma}$ parameter profiles (lower panel in Figure 4.7) show a practically identical behavior of the samples before and after protonation (**PDMAEMA** and **H+**, respectively). It is known that all materials form Ps at the surface (between 16 and 18% at the minimum positron implantation energy in the studied materials, see Figure 4.8) and low $F_{3\gamma}$ values, almost zero, inside the brushes are symptomatic of only two-gamma annihilation events (free, para-Ps and ortho-Ps by pick-off annihilation without three-gamma photons).

The effect of the uptake of Ag nanoparticles in brushes with different thicknesses (27, 40 and 66 nm) is also shown in Figure 4.7. The distribution for each sample (**Ag1**, **Ag2** and **Ag3**) shows a bump with a maximum centered near to the half-value of the thickness. These results clearly indicate the successful loading of AgNPs into the brushes. The changes in the S -parameter can be attributed to modifications in the chemistry of the annihilation sites or to the occurrence of cavities able to form positronium (para-Ps and pick-off-annihilated ortho-Ps). Since the tails of the two-gamma peak at a high Doppler shift come from annihilation with inner atomic shells, their study allows to understand the nature of

microstructural changes generated by the loading of AgNPs. The high momentum region is more sensitive than the S -parameter to the average chemical composition in the annihilation region, *i.e.* it is possible to obtain a fingerprint of the chemical environment where the positrons annihilate. However, the low counting rate in the high momentum region requires background suppression by adopting the coincidence Doppler broadening technique (CDB), *i.e.* to take both annihilation gammas in coincidence. CDB spectra with about 2×10^7 total counts are measured with a peak/background ratio of 10^5 to 10^6 . The momentum resolution (FWHM) was $3.6 \times 10^{-3} m_0 c$. The experimental procedure used in this study is similar to those described in ref. [51].

CDB measurements are performed in sample **Ag3** at the maximum of the S -parameter bump (black square in Figure 4.10, positron implantation energy 1.4 keV corresponding to a mean depth of 28 nm). Another CDB measure was performed for the **H+** sample at 1 keV (near to the minimum value of the S -parameter). The lower panel of Figure 4.10 shows the momentum distributions ρ of the electron-positron pairs during annihilation (related mainly to the electron velocity distribution) that contains information about the atomic orbitals from the atoms of the annihilation environment. For comparison, a CDB measurement of a high purity silver bulk sample (99.999% Ag) is included. The upper panel of Figure 4.10 shows the relative difference of the momentum distributions $(\rho - \rho_{H+})/\rho_{H+}$ of the thin brush film **Ag3** and the Ag bulk sample respect to the protonated brushes **H+**. This representation enhances the distribution at high momentum where the chemical fingerprint of the annihilation sites is present. The bulk Ag distribution shows a remarkable difference with respect to the **H+** brushes (line through zero). The distribution of the relative difference of Ag bulk (upper panel) is divided by ten in order to make possible a comparison with the **Ag3** distribution on the same scale. The Ag distribution presents

peaks at ± 1.8 atomic units of momentum ($\sim \pm 13 \times 10^{-3} m_0 c$) that correspond to the 4d-orbitals of Ag [52,53]. The distribution of the relative difference of sample **Ag3** (red points in Figure 4.10) shows a central narrow peak and two lateral bumps. The maximum of the lateral peaks is in good agreement with the position of the 4d-orbitals of Ag but is about 40 times less intense.

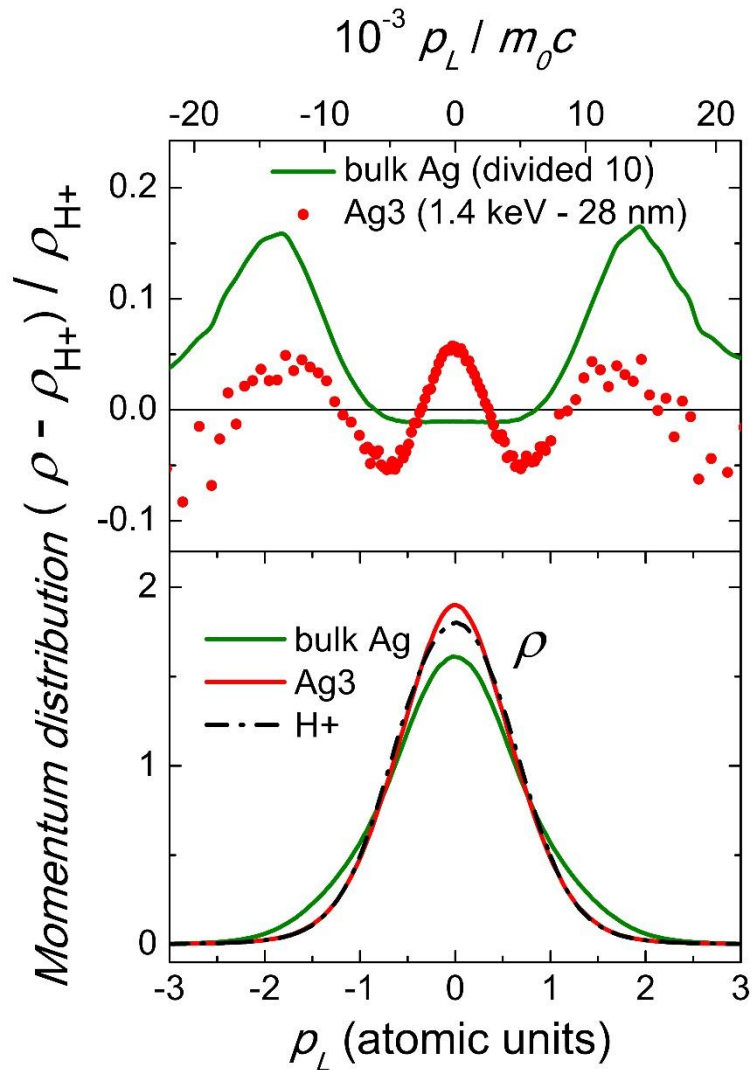


Figure 4.10 Lower panel: CDB spectra of **Ag3** (1.4 keV) and **H+** (1 keV). For comparison, a CDB measurement of a high purity silver bulk sample (99.999% Ag) is included. Upper panel: relative difference of the momentum distributions, $(\rho - \rho_{H+})/\rho_{H+}$, of the **Ag3** brush and of the Ag bulk sample respect to the protonated brush **H+**.

The results indicate that the S -parameter would have been decreased if positrons had annihilated in Ag. However, an enhancement is observed: the reason is the central narrow peak that appears for **Ag3**, which, according to our interpretation, is due to the o-Ps pick-off annihilation, p-Ps annihilation and to positron annihilation in defects associated to the nanoparticle surface. These facts indicate that positrons do not actually annihilate inside the AgNPs of only 10 nm in diameter (this dimension is one order of magnitude lower than the typical positron diffusion length in Ag). Positrons are trapped at the nanoparticle surface defects and mainly form positronium into the cavities formed by the polymer chains wrapped around the nanoparticles. This explanation is coherent with $F_{3\gamma}$ results show in Figure 4.7 (lower panel): the insert shows the difference between the distribution of the AgNPs-loaded brushes (**Ag3** sample) and of the protonated brushes **H+**. The samples infiltrated with nanoparticles show an increase of three gamma annihilation (1-1.5% in **Ag3**, see inset of Figure 4.7) which can be only explained with the presence of open spaces with a mean diameter $>\sim 1$ nm [33,34]. Thus, the presence of nanoparticles in the brushes are associated with the formation of cavities with a size distribution that, at least in part, overcomes nanometer dimensions.

The S -parameter data of the upper panel of Figure 4.7 were fitted with VEPFIT in order to estimate the layer densities (Table 4.4). To fit **PDMAEMA** and **H+** experimental data a three-layer model is chosen based on a brush layer, an interface and the silicon substrate. The other experimental data are fitted using a four-layer model made of a brush layer, an interlayer and the silicon substrate divided in two sections: a first layer in which acts an electrical field, and a second free from any electrical field. The use of an electric field in the four-layer model is justified because the plateaus of the S -parameter beyond the brushes layer (from 1 keV to 3 keV roughly), for all the samples except **PDMAEMA**, are ascribable

to the presence of electric fields inside the silicon substrates: such fields drive the positrons, implanted in the silicon, towards the interface. The value of the electric field is 2.5 ± 1.3 kV cm⁻¹ in the samples infiltrated with silver nanoparticles (**Ag1**, **Ag2** and **Ag3**) while that for the protonated sample (**H+**) is lower, about 0.25 ± 0.1 kV/cm. The depletion region in the silicon substrate is 400 ± 100 nm for all of these samples. The electric fields are likely due to the pinning of the Fermi level at the silicon-silicon oxide interface which is composed of a native, ~1.5 nm-thick, silicon dioxide blended with the grafted alkoxy silane-type initiator layer of the same thickness and which acts as a trapping layer for positrons.

Table 4.4 VEPFIT results for the brush samples studied with PAS.

Sample	Density $g\ cm^{-3}$	Ag filling %	Fit variance χ^2
PDMAEMA	1.5 ± 0.2	0	1.73
H+	1.5 ± 0.2	0	1.12
Ag1	2.1 ± 0.2	6 ± 3	1.52
Ag2	2.8 ± 0.2	13 ± 3	0.81
Ag3	2.5 ± 0.2	10 ± 3	1.47

The calculated densities are 1.5 ± 0.2 g cm⁻³ for the **PDMAEMA** and **H+** samples while the densities for **Ag1**, **Ag2** and **Ag3** are 2.1 ± 0.2 , 2.8 ± 0.2 , 2.5 ± 0.2 g cm⁻³, respectively. By using a linear relation:

$$d = d_{Ag} x + d_{PDMAEMA}(1 - x) \quad (4)$$

where d_{Ag} is the Ag density (10.49 g cm⁻³) and $d_{PDMAEMA}$ is the brushes density (1.5 g cm⁻³, according to XRR measurements), it has been possible to evaluate the percentage in mass x of the Ag nanoparticles ("Ag filling", Table 4.4) for **Ag1**, **Ag2** and **Ag3**. The values are 6 ± 3 , 13 ± 3 and 10 ± 3 %, respectively.

4.3 Conclusion

We demonstrated here for the first time a completely new way to understand the structure of nanoparticle-loaded polymer brushes. Applied to pH-responsive PDMAEMA brushes, Positron Annihilation Spectroscopy was able to discriminate between their non-protonated and the protonated forms, to give substantial information about the conformational changes experienced by the brushes after loading with silver nanoparticles and allowed to calculate the distribution and mass concentration of the latter inside the brushes. Noteworthy, all those information were obtained by carrying one single analysis, without making the least damage to the samples. With such premises, we are sure that PAS will soon impose as a key technique to unlock many of the mysteries of polymer brushes.

4.4 Specific procedures

Materials: All the chemicals, unless otherwise stated, were reagent grade, purchased from Aldrich and used as received. Water obtained from a Millipore MilliQ purification system (resistivity $\geq 18.2 \text{ M}\Omega \text{ cm}^{-1}$) was thoroughly used. DMAEMA monomer was filtered through an inhibitor-remover column and stored at -18°C until use. Silicon (100) wafers, single-polished, n type, phosphorus doped, 3 – 6 ($\Omega \text{ cm}$), with a native oxide layer ca. 1.5 nm thick, were purchased from Ultrasil Corporation. The wafers were cut into substrates of convenient size and cleaned by immersion for 1 h at 100°C in a piranha solution made of a 3:1_{v/v} mixture of concentrated sulphuric acid and hydrogen peroxide, respectively (*Caution: hot, concentrated piranha solution is corrosive and dangerous!*). Each substrate was then rinsed extensively with MilliQ water and dried under a nitrogen stream. Glass microscope slides were used as transparent substrates and were treated as described for the silicon substrates. For the functionalization with BIB-APTES (its synthesis is discussed in Appendix C), piranha-cleaned silicon substrates were immersed in a 10 mM BIB-APTES solution in anhydrous toluene for 4 h at 55°C , left overnight at 30°C , washed and gently sonicated

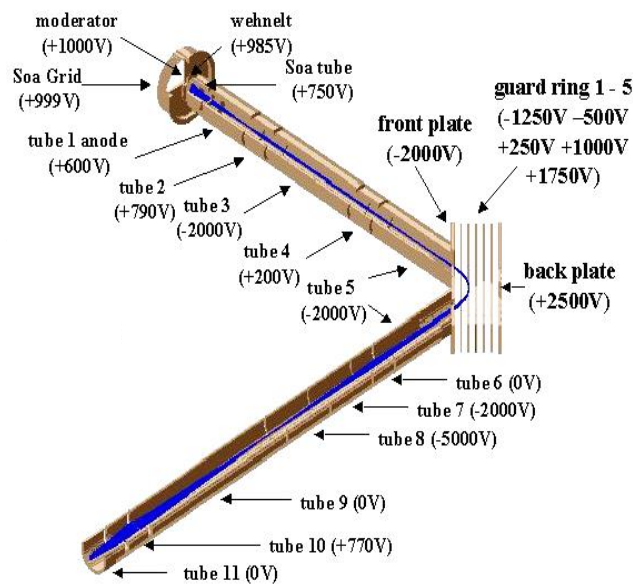
with toluene, acetone and ethanol and dried with a nitrogen stream. The functionalized substrates were stored at room temperature in the dark until use.

Grafting-from of PDMAEMA brushes by SI-ATRP: Poly(dimethylaminoethyl methacrylate) (PDMAEMA) brushes are grown by means of surface-initiated atom transfer radical polymerization (SI-ATRP) as previously described in Chapter 1. Briefly, each initiator-functionalized substrate is placed in a nitrogen-purged Schlenk flask and covered with 5 mL of a polymerization mixture prepared as follow. In a nitrogen-purged Schlenk flask 0.312 g (2.0 mmol) of bipyridyl and 0.144 g (1.0 mmol) of copper(I) bromide are dissolved in 6 mL of a 4:1 v/v methanol-water mixture previously degassed by bubbling nitrogen. 14 mL (83 mmol) of degassed DMAEMA are added and the mixture is stirred under nitrogen to obtain a homogeneous solution. For polymerizations with added deactivator the polymerization mixture contains also 11 mg (0.05 mmol) of copper(II) bromide. Polymerization proceeds at 30 °C for different times to obtain different brush thicknesses. After polymerization the samples are rinsed extensively with ethanol, gently sonicated in the same solvent and dried under a nitrogen stream.

Loading of silver nanoparticles into PDMAEMA brushes: PDMAEMA brushes are immersed into aqueous 0.1 M HNO₃ for 1 h to allow their complete protonation. The brushes are then washed with water, dried with a stream of nitrogen and dipped in an aqueous suspension of negatively charged silver nanoparticles, synthesized according to the procedure reported in Appendix C, for 10 min under gentle stirring. Eventually the nanoparticle-loaded brushes are washed with water, sonicated in the same solvent for 5 min to detach loosely-bound particles and dried under a nitrogen stream.

The VEPAS beam: In order to perform thin film depth profile studies, i.e. to obtain a small penetration depth, the use of a positron beam is mandatory. A positron beam is made of monoenergetic (“slow”) positrons that can be set to defined energies by simple linear accelerators. The VEPAS beam allows the tuning of the positron implantation energy from 0.1 to 20 keV. These energies allow to study thin films in the range of depth from the surface up to some microns, depending on the massive density of the studied material. The positrons are emitted by a ²²Na radioactive source and filtered by a moderator, i.e. a monocrystalline, [100]-oriented, W foil. With regard to Scheme 4.2, the beam consists of two

perpendicular tracks where electrostatic tubular lenses have been placed into a vacuum chamber (10^{-6} - 10^{-8} mbar).



Scheme 4.2 Design of the electrostatic optics of the VEPAS slow positron beam. The potentials correspond to the optics for positrons that arrive to the sample (focus point) with a kinetic energy of 1 keV. The positron trajectories represented in blue are simulated using SIMION 3D v7.0.

The positrons are initially gathered through a series of electrodes, placed according to a modified design of a Soa gun, which potentials are optimized in order to bring to the first anode the highest number of positrons. The first track has to accelerate the beam and make it parallel. Since the sample should not come in direct contact with the positrons emitted by the source, next to the fifth electrostatic lens there is a deflection unity (bender), similar to an analyser with parallel flat faces, which bends the beam by 90° . Then, after the bender, there are three lenses. The first lens refocuses the beam, the second accelerates the beam, and the third, consisting of three electrodes, focuses the beam on the sample. The gamma radiation, that possesses the information of the annihilation process, is collected by two high-purity germanium detectors (HPGe) each one located at 4 cm to the sample.

The final kinetic energy of positrons corresponds to the potential difference between the sample and the moderator. Between the moderator and the sample there has to be a potential difference of at least 1 kV so as to have an high enough transport efficiency. To obtain implantation energies between 1 keV and 20 keV, the tension of the whole apparatus must be increased until the eighth tube and, for the energy range between 0.1 keV and 1 keV, a potential applied to the sample between 0 and 0.9 kV is required.

Details on the calculation of the positron implantation profile: The mean implantation depth of the positrons as a function of the positron implantation energy is calculated using a numeric algorithm based on the Makhov implantation profile. This calculation is essential to represent and compare data of samples with the same nature but containing layers with different densities. The probability of a positron, having an implantation energy E , to penetrate to a depth z into a sample with density d is given by the so-called Makhov profile:

$$P(z, E) = \frac{mz^{m-1}}{z_0^m} e^{-\left(\frac{z}{z_0}\right)^m} \quad (\text{S2})$$

with

$$z_0 = \frac{AE^r}{d \Gamma\left(1 + \frac{1}{m}\right)} \quad (\text{S3})$$

where m , r and A are empirical parameters and Γ is the gamma function. The most accepted values of these parameters are $m = 2$, $r = 1.6$ and $A = 40 \mu\text{g cm}^{-2} \text{keV}^{-r}$ (when z is expressed in nm).

For the monodimensional probability distribution function in eq. S2, the mean implantation depth is given by:

$$\bar{z} = \int_0^\infty zP(z, E) dz = \frac{AE^r}{d} \quad (\text{S4})$$

The PDMAEMA samples which PAS results are showed in Figure 4.7 are modeled as composed of two layers: i) the brushes layer characterized by the thickness indirectly measured with XRR and the density estimated with VEPFIT and ii) the silicon, a semi-infinite layer of 2.33 g cm^{-3} density.

The Makhov profiles for the bilayered samples have been approximated with:

$$P(z, E) = \left\{ \begin{array}{ll} \frac{mz^{m-1}}{z_{0,1}^m} e^{-\left(\frac{z}{z_{0,1}}\right)^m}, & z \leq z_1 \\ \frac{m(z-z_1+\delta z)^{m-1}}{z_{0,2}^m} e^{-\left(\frac{z-z_1+\delta z}{z_{0,2}}\right)^m}, & z > z_1 \end{array} \right\} \quad (S5)$$

where z_1 is the thickness of the first layer, $z_{0,1}$ and $z_{0,2}$ are calculated according to eq. S3 for each layer and δz is a depth for which the following relation is valid:

$$P = \int_0^{z_1} P_1(z, E) dz = \int_0^{\delta z} P_2(z, E) dz \quad (S6)$$

In Figure 4.11 the mean implantation depth trends are represented as a function of the positron implantation energy for the PDMAEMA sample obtained by using the method described above.

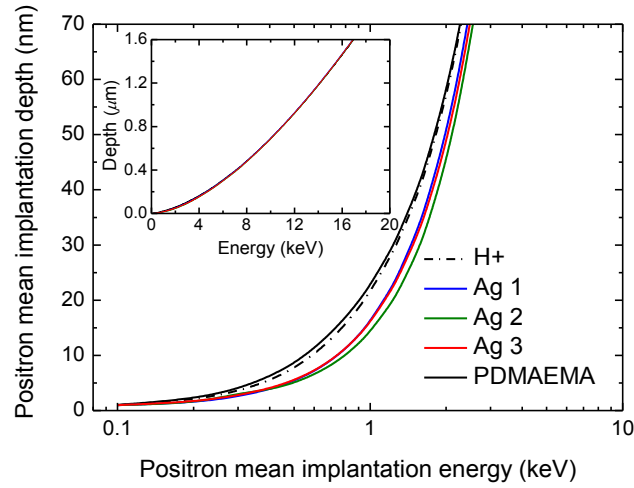


Figure 4.11 Calculated positron mean implantation depth as a function of the kinetic implantation energy.

4.4 References

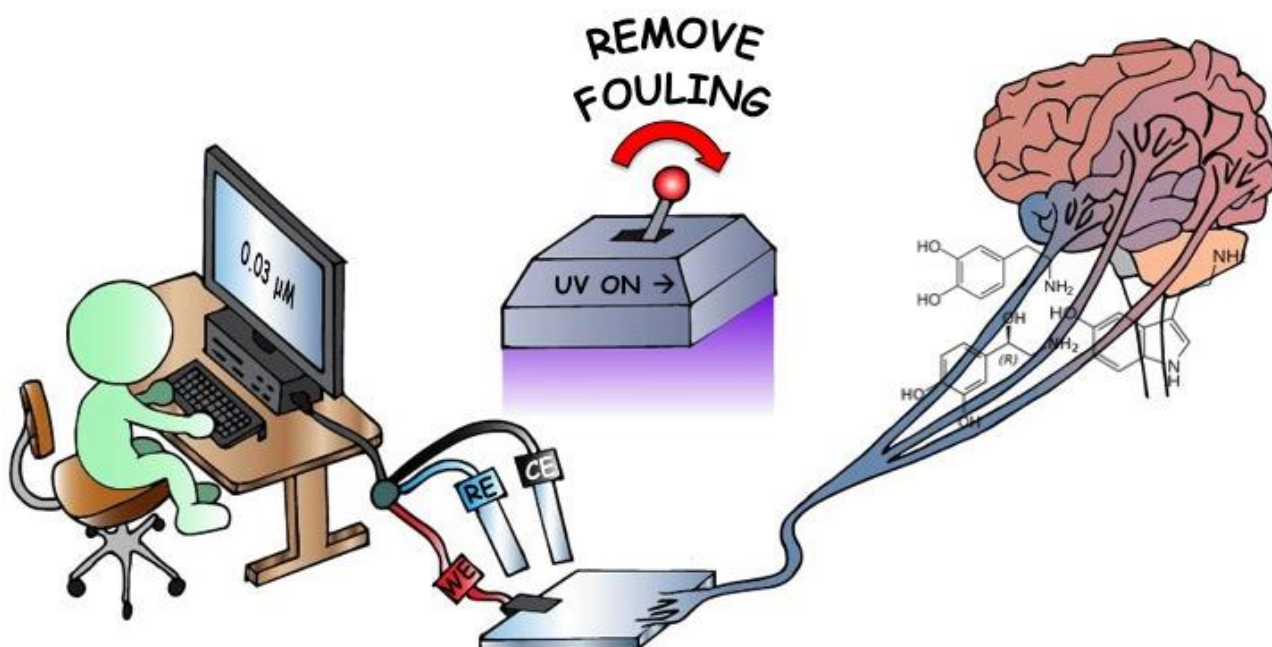
- [1] G. Panzarasa, G. Soliveri, K. Sparnacci, S. Ardizzone, *Chem. Commun.*, **2015**, 51, 7313–7316.
- [2] R. Barbey, L. Lavanant, D. Paripovic, *Chem. Rev.*, **2009**, 109, 5437–5527.
- [3] Y. Chen, J. Z. Y. Chen, *J. Polym. Sci. Part B Polym. Phys.*, **2012**, 50, 21–26.
- [4] T. Curk, F. J. Martinez-Veracochea, D. Frenkel, J. Dobnikar, *Nano Lett.*, **2014**, 14, 2617–2622.
- [5] J. U. Kim, M. W. Matsen, *Macromolecules*, **2008**, 41, 246–252.
- [6] A. Milchev, D. I. Dimitrov, K. Binder, *Polymer*, **2008**, 49, 3611–3618.
- [7] M. G. Opferman,; R. D. Coalson, D. Jasnow, A. Zilman, *Langmuir*, **2013**, 29, 8584–8591.
- [8] J. U. Kim, B. O’Shaughnessy, *Macromolecules*, **2006**, 39, 413–425.
- [9] Z. Liu, K. Pappacena, J. Cerise, J. Kim, C. J. Durning, B. O’Shaughnessy, R. Levicky, *Nano Lett.*, **2002**, 2, 219–224.
- [10] R. Oren, Z. Liang, J. S. Barnard, S. C. Warren, U. Wiesner, W. T. S. Huck, *J. Am. Chem. Soc.*, **2009**, 131, 1670–1671.
- [11] G. Dunderdale, J. Howse, J. Fairclough, *Langmuir*, **2011**, 27, 11801–11805.
- [12] I. Luzinov, S. Minko, V. V. Tsukruk, *Soft Matter*, **2008**, 4, 714–725.
- [13] M. Krishnamoorthy, S. Hakobyan, *Chem. Rev.*, **2014**, 114, 10976–1026.
- [14] N. Hadesfandiari, K. Yu, Y. Mei, J. N. Kizhakkedathu, *J. Mater. Chem. B*, **2014**, 2, 4968–4978.
- [15] G. Gunkel, M. Weinhart, T. Becherer, R. Haag, W. T. S. Huck, *Biomacromolecules*, **2011**, 12, 4169–4172.
- [16] Q. Yu, P. Shivapooja, L. M. Johnson, G. Tizazu, G. J. Leggett, G. P. López, *Nanoscale*, **2013**, 5, 3632–3637.
- [17] N. Ayres, *Polymer Chemistry*, **2010**, 1, 769–777.
- [18] L. Moroni, M. Klein, E. M. Benetti, *Acta Biomater.*, **2014**, 10, 2367–2378.
- [19] L. Ionov, N. Houbenov, A. Sidorenko, M. Stamm, S. Minko, *Adv. Funct. Mater.*, **2006**, 16, 1153–1160.

- [20] H. J. Snaith, G. L. Whiting, B. Sun, N. C. Greenham, W. T. S. Huck, R. H. Friend, *Nano Lett.*, **2005**, 5, 1653-1657.
- [21] Y. Lu, G. L. Liu, L. P. Lee, *Nano Lett.*, **2005**, 5, 5-9.
- [22] I. Tokareva, S. Minko, J. H. Fendler, E. Hutter, *J. Am. Chem. Soc.*, **2004**, 126, 15950-15951.
- [23] Y. Roiter, I. Minko, D. Nykypanchuk, I. Tokarev, S. Minko, *Nanoscale*, **2012**, 4, 284-292.
- [24] R. R. Bhat, M. R. Tomlinson, J. Genzer, *Macromol. Rapid Commun.*, **2004**, 25, 270-274.
- [25] S. Christau, Z. Yenice, J. Genzer, *Langmuir*, **2014**, 30, 13033-13041.
- [26] S. Gupta, P. Uhlmann, M. Agrawal, S. Chapuis, U. Oertel, M. Stamm, *Macromolecules*, **2008**, 41, 2874-2879.
- [27] S. Gupta, M. Agrawal, P. Uhlmann, F. Simon, U. Oertel, M. Stamm, *Macromolecules*, **2008**, 41, 8152-8158.
- [28] T. Fujioka, N. Oshima, R. Suzuki, W. E. Price, L. D. Nghiem, *J. Memb. Sci.*, **2015**, 486, 106-118.
- [29] S. H. Kim, S. Y. Kwak, T. Suzuki, *Environ. Sci. Technol.*, **2005**, 39, 1764-1770.
- [30] A. Cano-Odena, P. Vandezande, K. Hendrix, R. Zaman, K. Mostafa, W. Egger, P. Sperr, J. De Baerdemaeker, I. F. J. Vankelecom, *J. Phys. Chem. B*, **2009**, 113, 10170-10176.
- [31] C. Nagel, K. Günther-Schade, D. Fritsch, T. Strunskus, F. Faupel, *Macromolecules*, **2002**, 35, 2071-2077.
- [32] K. S. Liao, H. Chen, S. Awad, J. P. Yuan, W. S. Hung, K. R. Lee, J. Y. Lai, C. C. Hu, Y. C. Jean, *Macromolecules*, **2011**, 44, 6818-6826.
- [33] W. S. Hung, M. De Guzman, S. H. Huang, K. R. Lee, Y. C. Jean, J. Y. Lai, *Macromolecules*, **2010**, 43, 6127-6134.
- [34] P. G. Coleman, in *Principles and Applications of positron and positronium chemistry*, Y. C. Jean, P. E. Mallon and D. M. Schrader (Eds.); World Scientific, Singapore, 2003; pp. 37-72.
- [35] G. W. Rubloff, *J Vac Sci Technol A*, **1990**, 8, 3, 1857-1863.
- [36] X. Yu, J. Smith, N. Zhou, L. Zeng, P. Guo, Y. Xia, A. Alvarez, S. Aghion, J. Lin, J. Yu, R. P. H. Chang, M. J. Bedzyk, R. Ferragut, T. J. Marks, A. Facchetti, *PNAS*, **2015**, 112, 3217-3222.
- [37] D. W. Gidley, H. G. Peng, R. S. Vallery, *Annu. Rev. Mater. Res.*, **2006**, 36, 49-79.
- [38] G. Consolati, R. Ferragut, A. Galarneau, F. Di Renzo, F. Quasso, *Chem. Soc. Rev.*, **2013**, 42, 3821-3832.

- [39] C. L. Soles, J. F. Douglas, W. L. Wu, H. Peng, D. W. Gidley, *Macromolecules*, **2004**, *37*, 2890–2900.
- [40] C. Ohrt, K. Rätzke, N. Oshima, Y. Kobayashi, B. E. O'Rourke, R. Suzuki, A. Uedono, F. Faupel, *Macromolecules*, **2015**, *48*, 1493–1498.
- [41] S. Christau, S. Thurandt, Z. Yenice, R. von Klitzing, *Polymers (Basel)*, **2014**, *6*, 1877–1896.
- [42] J. K. Chen, P. C. Pai, J. Y. Chang, S. K. Fan, *ACS Appl. Mater. Interfaces* **2012**, *4*, 1935–1947.
- [43] D. M. Jones, A. Brown, W. T. S. Huck, *Langmuir*, **2002**, *18*, 1265–1269.
- [44] O. A. G. J. Van Der Houwen, W. J. M. Underberg, W. E. Hennink, *Macromolecules*, **1998**, *31*, 8063–8068.
- [45] G. Soliveri, G.; V. Pifferi, G. Panzarasa, S. Ardizzone, G. Cappelletti, D. Meroni, K. Sparnacci, L. Falciola, *Analyst*, **2015**, *140*, 1486–1494.
- [46] G. Panzarasa, *J. Chem. Educ.*, **2014**, *91*, 696–700.
- [47] A. Van Veen, H. Schut, J. de Vries, R. A. Hakvoort, M. R. Upma, *AIP Conf. Proc.* P. J. Shultz, G. R. Massoumiand, P. J. Simpson (Eds.); AIP: New York 1990, *218*, pp 171-196.
- [48] Süvegh, K.; Domján, A.; Vankó, G.; Iván, B.; Vértes A. *Macromolecules*, **1998**, *31*, 7770-7775.
- [49] M. Mohsen, N. A. Maziad, E. Gomaa, E. Hassan Aly, R. Mohammed, *Open Journal of Organic Polymer Materials*, **2015**, *5*, 43-52.
- [50] J. Yang, B. Zhu, W. Zha, M. L. J. Lee, H. Chen, Y. C. Jean, *AIChE Annual Meeting, Conference Proceedings*, **2008**, 16-21.
- [51] R. Ferragut, *Physica B*, **2012**, *407*, 2676-2683.
- [52] R. S. Brusa, W. Deng, G. P. Karwasz, A. Zecca, *Nuclear Instruments and Methods in Physics Research B*, **2002**, *194*, 519–531.
- [53] P. Folegati, I. Makkonen, R. Ferragut, M. J. Puska, *Physical Review B*, **2007**, *75*, 054201.

III

Self-Cleaning Properties in Engineered Sensors for the Electroanalytical Detection of Catecholamine Neurotransmitters



Chapter 5

Developing an Efficient, Self-Cleaning Device for the Electroanalysis of Catecholamine Neurotransmitters

ABSTRACT

Fouling and passivation are the major drawbacks for a wide applicability of electroanalytical sensors based on nanomaterials, especially in biomedical and environmental fields. Highly engineered devices, designed *ad hoc* for specific applications, are key factors in the direction of overcoming these problems and gaining access to efficient sensors. Here we describe how, by tailoring of a SiO₂-AgNPs-TiO₂ multifunctional system made of silver nanoparticles sandwiched between layers of silica (bottom) and titania (top), we are able to achieve a complex goal of great biomedical relevance: the detection of catecholamine neurotransmitters.

5.1 Introduction

The development of innovative sensing devices is one of the faster-developing fields of applied research especially because of increasing environmental concerns and biomedical demands [1-7]. Moreover, the fast development of nanotechnology has paved the way for the design of tailored systems exhibiting superior properties [8-12].

Composite, oxide/metal systems based on silver nanoparticles (AgNPs) have gained increasing attention [8,9,13] especially for trace-detection electroanalysis, thanks to the unique properties of the latter [8,9]. Silver has many desirable properties: it shows the highest electrical conductivity among metals, has good stability at different potentials and pH, and it allows electrocatalysis. For these reasons, silver is a widely used electrode material and the advent of nanotechnology has further improved its possibilities.

Compared to traditional bulk noble-metal electrodes, nanostructured surface morphologies can lead to a dramatic enhance of the sensing system response. The high surface-to-volume ratio and nanoscale dimensions increase of orders of magnitude the availability of interaction sites for the analyte, improving the sensitivity and lowering detection limits, which are both fundamental features of trace analysis. Moreover, the small dimensions may allow a local control of the sensing process in terms of analyte diffusion mechanism and site-analyte recognition.

However, passivation and fouling problems are exacerbated for nanosized complex devices making their stability and reusability a real issue [1,8]. Passivation and fouling are mainly due to irreversible adsorption (chemisorption) on the electrode surface of electrochemical by-products, interfering compounds already present in the analyzed sample or even the

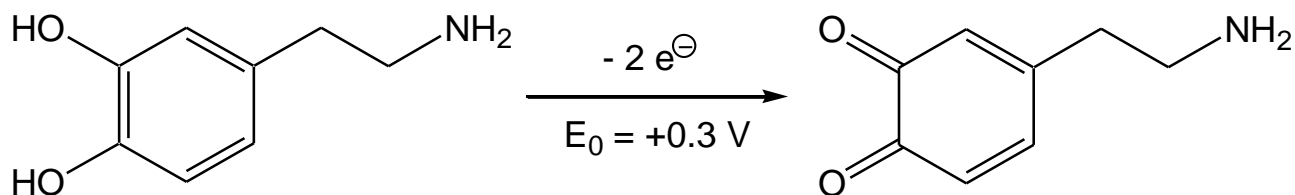
analyte(s) under study. Conventional cleaning procedures for bulk metal electrodes, which comprise mechanical or electrochemical etching, are inapplicable for metal nanoparticle-modified electrodes: such harsh treatments would lead to irreversible modification and eventually lead to nanoparticle detachment from the electrode surface. This limitation is critical especially for the development of commercial sensors, which should be portable, robust and reusable apart from displaying high sensitivity, low detection limits and high selectivity.

In this context, self-cleaning electrodes represent a significant step beyond the current state-of-the-art electrochemical sensors. Materials with self-cleaning properties enabled by UV and visible light have played a pivotal role in both fundamental and applicative research in the last 30 years [14,15]. Self-cleaning coatings [16], windows and concretes, also self-sterilizing medical devices and paints for surgical rooms are, nowadays, highly appealing products for the market [14]. Titanium dioxide TiO_2 is the most characteristic and studied photoactive material for the development of such products. Interest about this oxide arose thanks to its high photo-oxidation and photo-reduction powers, along with its appealing band-gap (3.2 eV for anatase and 3.0 eV for rutile) which allow the study of these properties with conventional UV sources and even solar light. Besides its semiconductor properties, titanium dioxide is non-toxic, highly biocompatible, has a high refractive index and, above all, is easily available and cheap.

Only a few examples of non-classical self-cleaning electrodes are available in the Literature. In a recent work, Kamat *et al.* [17] reported a “detect-and-destroy” approach for Surface-Enhanced Raman Spectroscopy (SERS)-based sensors, in which SERS analysis enabled by AgNPs was followed by photocatalytic degradation of the adsorbed analyte by TiO_2 . Other

reports described systems based on anodized titania nanotubes decorated with noble metals (Pt and Pd), where the titania photocatalytic effect is exploited to restore the activity of the device after hydrogen detection [18], methanol electro-oxidation or glucose determination [19,20]. However, neither an electrode design devoted to assure its re-usability, nor a thorough study of the effect of fouling/cleaning cycles on the stability of electroanalytical parameters were investigated.

We want to fill this gap, in such a promising context, by proposing an innovative electroanalytical device with unprecedented versatility and self-cleaning properties. Moreover, the electroanalytical detection of dopamine is chosen as a proof-of-concept method to demonstrate the ability of our device to efficiently tackle complex analytical problems. Dopamine is a molecule of great interest both from a biomedical and analytical point of view: being a catecholamine neurotransmitter, its levels are diagnostic for many behavioral disturbs and neurological pathologies such as the Parkinson's disease. Its quantitative determination has been, however, a complex task to achieve especially for direct *in vivo* analyses. This subject will be discussed in detail in Chapter 6.



Scheme 5.1. The electrochemical oxidation of dopamine, the reaction at the basis of its electroanalytical detection [21,22].

It is sufficient to say here that innumerable electrode conformations and electrochemical techniques have been described in the Literature to perform electroanalysis of dopamine, although in all cases the measurements were affected by fouling and passivation of the electrode surface [23-25]. Dopamine's high affinity to metal and metal oxide surfaces, while is desirable to increase sensitivity, on the other hand leads to its irreversible chemisorption and consequent deactivation of active sites on the electrode [21]. In practice, this picture is even worsened, because the electrochemical oxidation of dopamine leads to polymeric products with the same (if not higher) surface affinity already described for dopamine.

5.2 Results and Discussion

5.2.1 Introducing Our Electrochemical Device

The electrochemical device developed by us is, basically, a composite coating in which silver nanoparticles (AgNPs) are assembled between a bottom silica and a top titania layer, deposited on a conductive substrate (Figure). However, despite its apparent simplicity, it displays all the desirable properties for an ideal sensor. Not only it enables the efficient electroanalytical detection of difficult analytes such as catecholamine neurotransmitters, it is also:

- Transparent
- Mechanically robust
- Self-cleaning
- Reusable
- Reliable

- Cheap

It is difficult to find all these properties combined in a single, highly engineered device as we will demonstrate point-by-point in the following paragraphs.

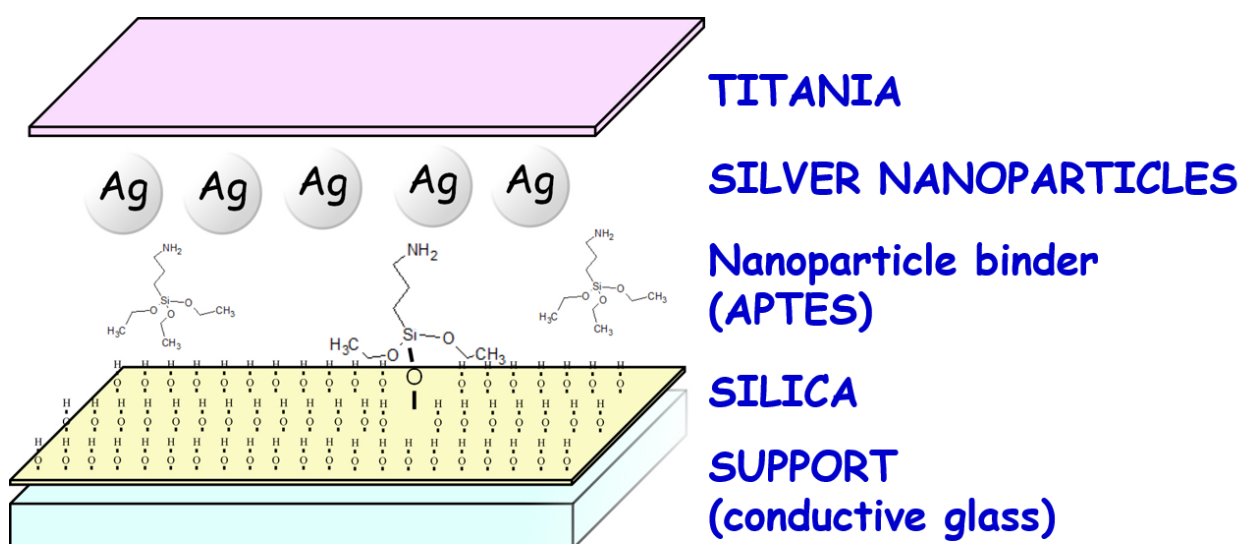


Figure 5.1 Schematic structure of our electrochemical device (not in scale).

The present self-cleaning sensor is designed for the detection of catecholamine neurotransmitters. It affords a total sensitivity recovery after fouling and cleaning by a simple UV irradiation step. Moreover, aging, over-usage and environmental conditions have not appreciable effects to the overall electrode performance.

Each component (Support, Silica layer, Nanoparticle binder, Silver nanoparticles and Titania overlayer) is optimized in order to assure the best performance of the resulting device, as discussed in the following sections.

About the SUPPORT

Electrically conductive and transparent fluorine-doped tin oxide (FTO)-coated glass slide is used as the support for the assembly of active coating. It is chosen because, in addition to the previously mentioned properties and to its good chemical stability, it can withstand the calcination processes required for the deposition of the silica and titania layers.

About the SILICA layer

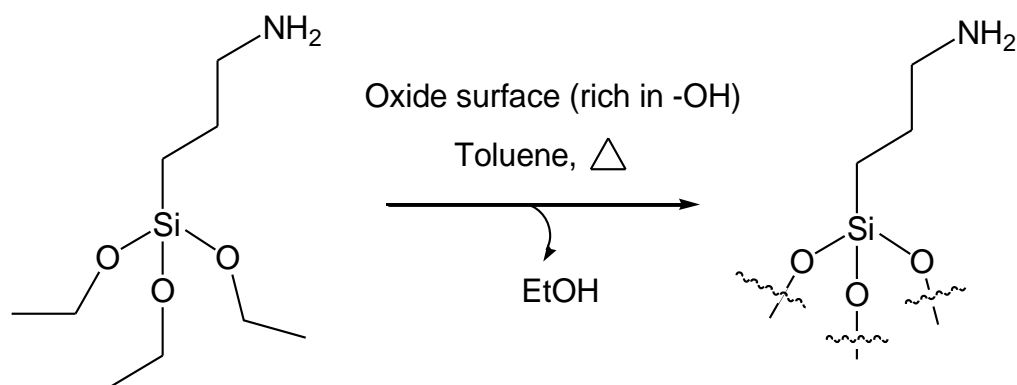
The silica layer is obtained by dip-coating the FTO-glass slide in a non-aqueous sol, synthesized according to a literature procedure (Wang *et al.* [26]) followed by calcination. This high temperature treatment was previously optimized by studying the roles played by time, temperature and atmosphere. That was necessary to achieve complete decomposition of the organic components of the sol while maintaining the final film transparency and to increase its mechanical stability and adhesion to the support. A calcination step of one hour at 400 °C under N₂ flow was eventually adopted.

The role of the silica layer is crucial. It governs the morphology by reducing the roughness of the FTO surface and modifies its reactivity towards the deposition of the nanoparticle binder. It eventually helps to promote the subsequent self-assembly of AgNPs, which are the active core of the device, generating a particular distribution of the particles on the surface.

About the NANOPARTICLE BINDER

The surface of the calcined silica layer is then functionalized with a functional siloxane which acts as a nanoparticle binder, promoting the stable attachment of AgNPs. (3-Aminopropyl)triethoxysilane (APTES) was chosen for this purpose (Scheme 5.2). The three ethoxy groups of APTES can react with the -OH groups exposed by the silicon oxide surface, generating a primary amine-terminated self-assembled monolayer (SAM) [27].

It is known that SAMs of APTES have a great affinity toward metal nanoparticles, promoting their attachment to a surface. In the present case, it is sufficient to dip the APTES-functionalized substrate into an aqueous suspension of previously synthesized silver nanoparticles to obtain a nanoparticle-decorated surface.



Scheme 5.2 Chemical structure of APTES and its mechanism for grafting on a generic oxide surface.

Since the surface concentration and disposition of AgNPs strongly depend on the surface density of amine groups, this latter was determined according to the method of Moon *et al.* [46] (Scheme 5.3). The surface density of amine groups was almost double for bare FTO (10 NH₂ nm⁻²) compared to silica coated-FTO (5 NH₂ nm⁻²) substrates functionalized with APTES under the same conditions. Such difference is expected to reflect in a different

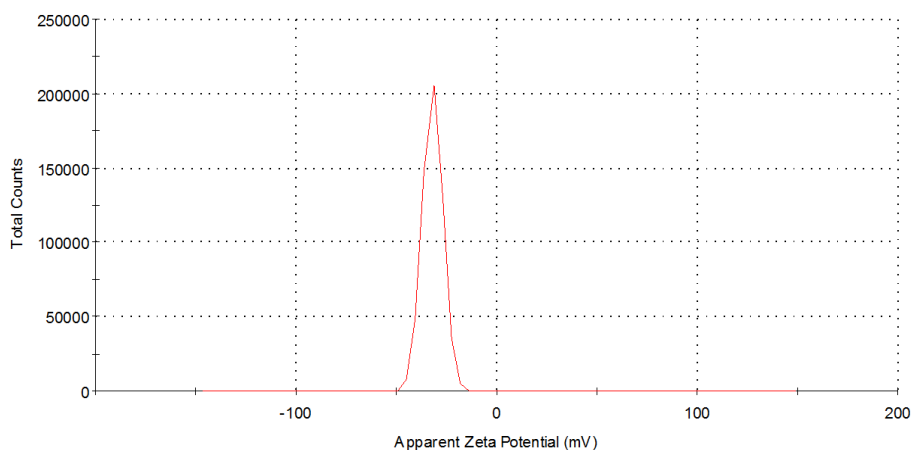


Figure 5.2 Zeta-potential spectrum of as-obtained silver nanoparticles.

HRTEM (Figure 5.3a) shows spherical nanoparticles with good uniformity (11 ± 2 nm diameter). The particles are crystalline, as judged by the lattice spacing of ~ 230 pm which corresponds to the (111) planes of a silver fcc cell. The aqueous suspension displays a sharp absorption band centered at about 400 nm originating from the surface plasmon resonance, which is typically associated with AgNPs of dimensions lower than 30 nm (Figure 5.3b, inset) [29].

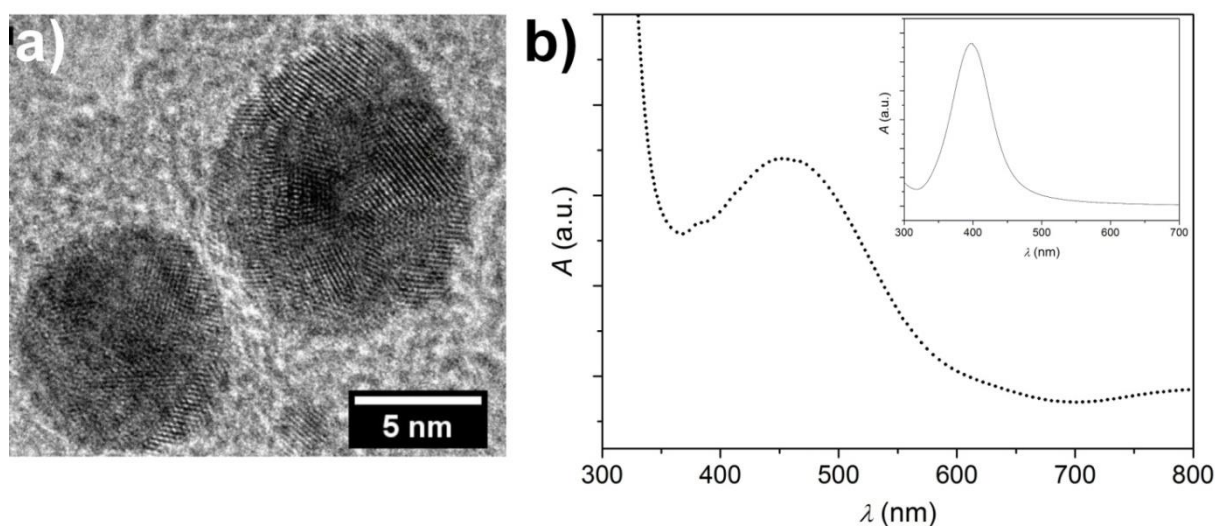


Figure 5.3 a) HRTEM picture of AgNPs, showing high crystallinity and lattice spacing of about 230 pm. b) UV-Vis spectrum of AgNPs grafted on the silica surface (inset: UV-Vis spectrum of the AgNPs aqueous suspension).

The APTES-functionalized, silica coated-FTO develops an orange color after being dipped for 15 minutes in this silver nanoparticle suspension. This color is correlated with the UV-vis absorption spectrum shown in Figure 5.3b, which confirms the successful decoration of the surface with nanoparticles. The plasmon band is red-shifted due to the change in the dielectric constant of the environment experienced by the nanoparticles, as reported by Evanoff *et al.* [30].

About the TITANIA overlayer

The silica coated-, APTES functionalized- and AgNPs decorated-FTO substrate is eventually coated by a titanium dioxide TiO₂ layer. This external layer is crucial to confer further properties to the resulting device. To obtain it, the substrate is dip-coated using a non-aqueous titania sol followed by a high-temperature treatment [31]. Again, a careful selection of the temperature and especially of the atmosphere of calcination is of paramount importance in order to obtain the desired results. A fast calcination for 1 hour at 400 °C under N₂ flow allowed to achieve complete mineralization of organic compounds and to increase the crystallinity of titanium oxide without altering the film transparency.

The resulting device, analyzed by X-ray diffraction (XRD), clearly shows (Figure 5.4) a predominance of the anatase polymorph of titania, with only traces of brookite. This is important because anatase is known to be the most photoactive form of titanium dioxide. The size of anatase crystallites was evaluated to be 17 nm. The peaks of cassiterite SnO₂ from the underlying FTO substrate are also appreciable.

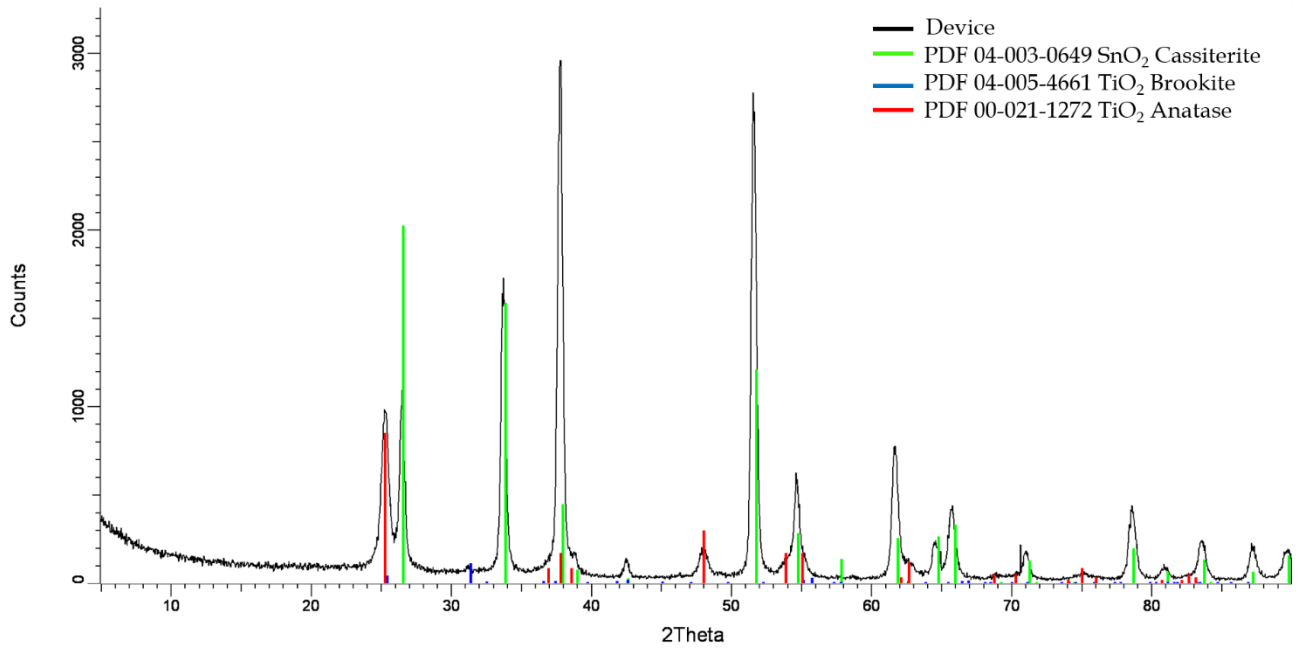


Figure 5.4 X-Ray Diffraction spectrum obtained for the Device.

The SEM cross-section image of the Device, as shown in Figure 5.5, reveals two distinct and homogeneous layers, 550 nm and 150 nm thick respectively, corresponding to the SiO₂ and TiO₂ layers. Such thickness data are confirmed by UV-vis reflectivity, which gave reproducible values for different areas of the film, thus confirming the homogeneity of the layered structure.

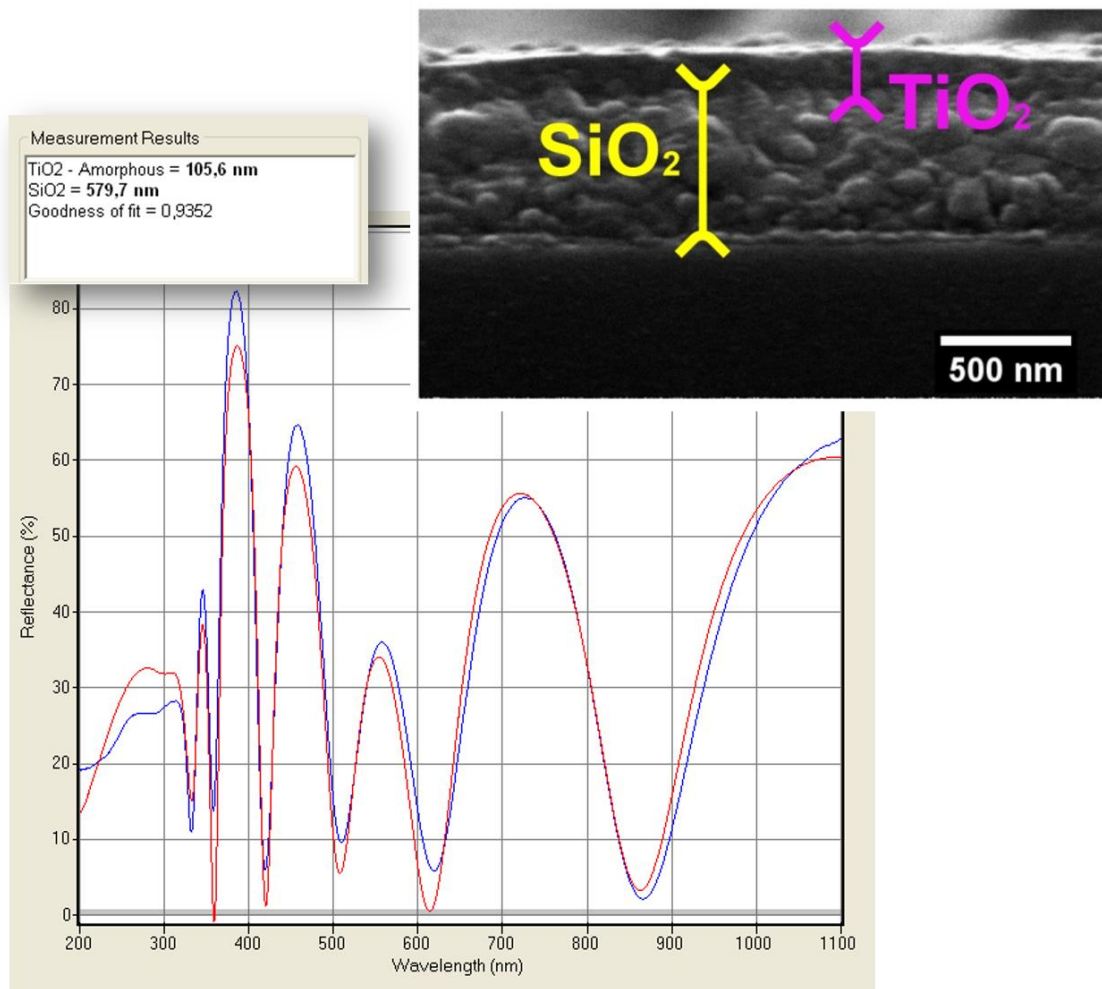


Figure 5.5 Cross-section SEM image of a cut Device showing the silica and titania layers. The experimental and theoretical reflectivity spectra are also reported along with the calculated layer thicknesses.

The titania overlayer imaged by scanning electron microscopy (SEM) reveals an homogeneous surface (Figure 5.6a), however, a picture taken at higher resolution highlights its porous structure (Figure 5.6b).

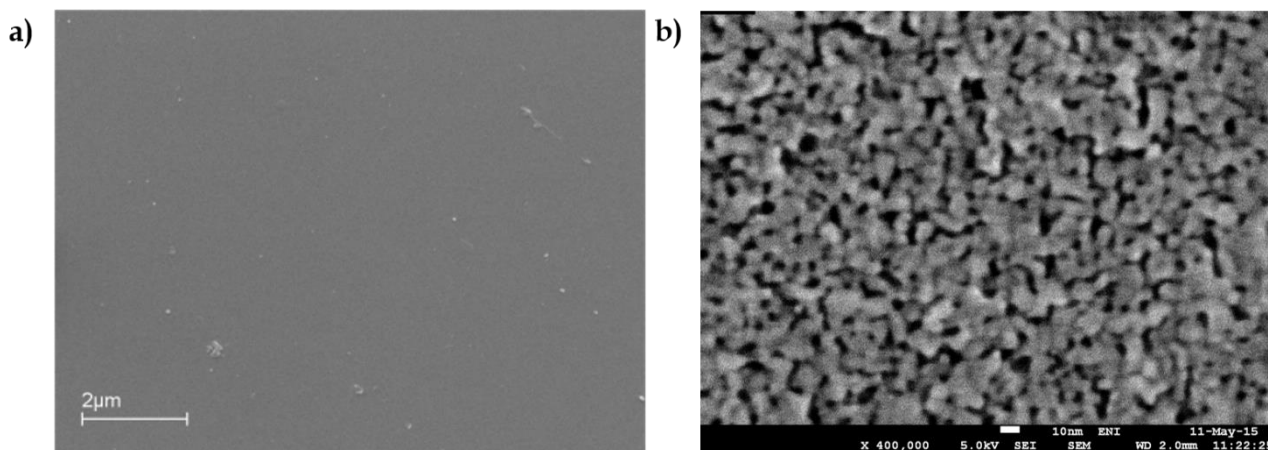


Figure 5.6 a) Low-resolution and b) high-resolution scanning electron microscopy images of the titanium dioxide overlayer.

5.2.2 The Central Role of Silver Nanoparticles (AgNPs)

Silver nanoparticles are the active core of our device. Briefly, the particles arrange homogeneously and are well separated, allowing to gain the maximum faradic currents with the minimum quantity of active metal through the onset of the convergent diffusion regime, an effect accompanied by the lowering of the capacitive currents, as described by Compton *et al.* This situation represents an undoubtedly advantage from the electroanalytical point of view.

The role of silver in electrocatalysis both as a massive electrode and as a nanoparticle has been amply discussed in the Literature [32-34]. For sensing applications, Ag can favorably change the potential of redox reactions allowing *e.g.* better management of interfering compounds [8,9,35]. That silver as nanoscale particles is actually present in our device is confirmed by the results obtained from cyclic voltammetry in the absence of an electroactive probe. The electrochemical behavior of multilayered ($\text{SiO}_2\text{-TiO}_2$) electrodes without AgNPs

was very similar to that of bare FTO and in general of oxide materials, *i.e.* complete absence of peaks in purely capacitive voltammograms (Figure 5.7a, curve 1). On the other hand, when AgNPs are present (Figure 5.7a, curve 2 and 3), peaks at around +0.25 V (SCE) and +0.1 V (SCE) appeared which are attributable to oxidation and reduction of silver, as confirmed by Literature data [36,37].

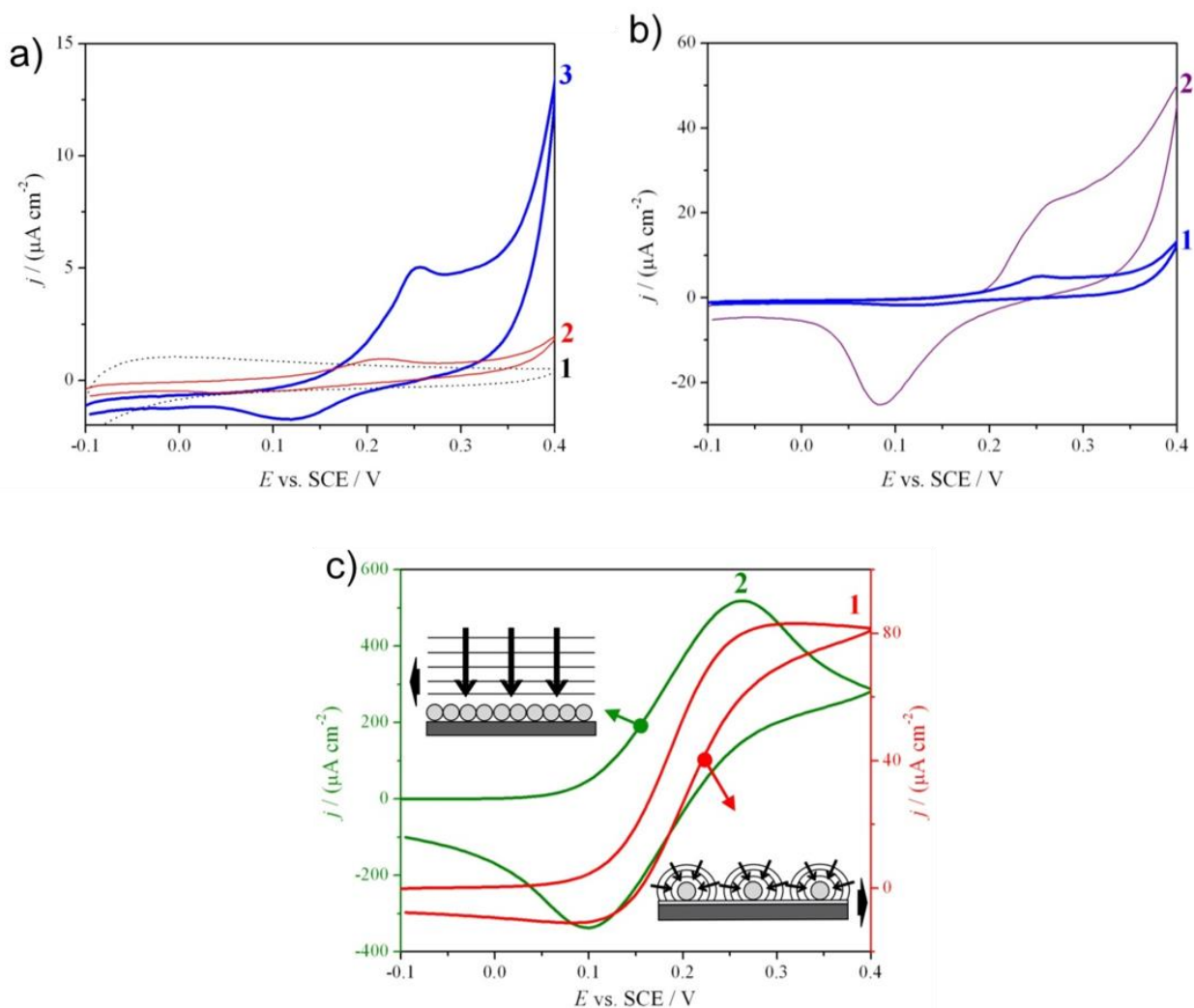


Figure 5.7 Cyclic voltammograms in the a,b) absence or c) presence of $K_4[Fe(CN)_6]$ probe molecule. Study of a) the effect of titania layer (curve 1: FTO+SiO₂+TiO₂; curve 2: FTO+SiO₂+Ag; curve 3: FTO+SiO₂+Ag+TiO₂), b) the effect of silica layer (curve 1: FTO+SiO₂+Ag+TiO₂, curve 2: FTO+Ag+TiO₂), c) the distribution of Ag NPs (curve 1: FTO+SiO₂+Ag; curve 2: FTO+Ag).

Nanoscale silver is obviously more reactive than bulk silver and can be oxidized even by atmospheric oxygen resulting in passivation effects. To avoid this phenomenon, active metal surfaces are often coated with protective oxide layers [38]. In our case, it is the titania layer that provides a protective action toward oxidation of AgNPs, as will be discussed in detail in the following paragraph. This effect is demonstrated by comparing the final electrode (Figure 5.7a, curve 3) with a device prepared in the same way but without the external TiO₂ layer (Figure 5.7a, curve 2). In the case of titania-coated, silver nanoparticle-decorated device, higher Ag peak currents are observed, reflecting the presence of more active and non-oxidized silver nanoparticles.

A key point to take into consideration when using silver nanoparticle-modified electrodes for the development of sensors is the density, distribution and organization of nanoparticles on the electrode surface [8]. In electroanalysis, the analyte(s) react on the electrode surface, resulting in an increase of the measured current. This signal is the sum of the capacitive background current (*i.e.* due to the double layer) and of the faradic (*i.e.* originated by a chemical reaction) current, the latter being totally related to the analyte concentration. However, for nanoparticle-modified electrodes, the voltammogram shape can be related to the size and surface density of the nanoparticles [39,40]. A steady-state sigmoidal step can be registered for a convergent independent diffusion at low nanoparticle coverage (Figure 5.7c, curve 1), while a peak is obtained in the case of a planar diffusion regime at high nanoparticle coverage (Figure 5.7c, curve 2). To maximize the sensitivity and to lower the detection limits, it is best to achieve low capacitive currents and high faradic currents. An optimal disposition for this purpose is an ordered array of isolated nanoparticles, where the convergent mass transport must be predominant [40-42]. In such case, the current response

is greater with respect to that of a bulk electrode. In fact, while the current at a macroelectrode follows the Randles–Sevcik equation (equation 1) [43]:

$$I_{peak} = 2.69 \times 10^5 n^3/2 D^{1/2} C_{bulk} v^{1/2} A \quad (1)$$

where I_{peak} is the current (ampere), n is the number of electrons involved in the reaction, D is the diffusion coefficient ($\text{cm}^2 \text{s}^{-1}$), C_{bulk} is the bulk concentration of the active species (mol cm^{-3}), v is the potential scan rate (V s^{-1}) and A is the surface area (cm^2). In the case of a nanoparticle array of the same macro-dimensions as the previously discussed bulk electrode in which the nanoparticles were at a distance of $10r$ (where r is the radius of the nanoparticle), the limiting current at each nanoparticle and the total array current are given by equations (2) and (3) [8,9,41,44]:

$$I_{lim} = 8.71 n F D C_{bulk} r \quad (2)$$

$$I_{tot} = I_{lim} [A / (10 r)^2] = (8.71 n F D C_{bulk} A) / (100 r) \quad (3)$$

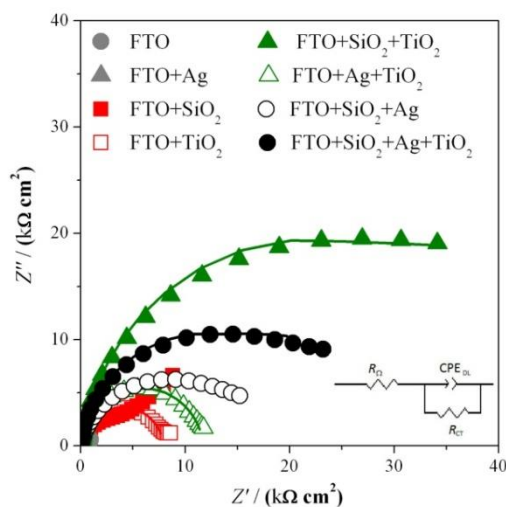
From equation (3), it is evident that the current depends on the particle radius (the smaller, the better) and is independent of the potential scan rate, since a convergent mechanism is attained. Using typical values for the parameters and a value of $r = 10 \text{ nm}$, a current increase of seven hundred times can be obtained with respect to the bulk electrode [8]. It is worthwhile to note that the above considerations are valid assuming that the nanoparticles are sufficiently far apart to be diffusionally independent. Electrodes with too close-packed arrays of nanoparticle are characterized by the loss of convergent diffusion due to the overlapping of the diffusion layers. The nearest nanoparticle-neighbor minimum distance of $10r$ required for diffusional independency, although still debated [40,45], is assumed to be a good indicative value [8]. Moreover, the nanoparticle array is characterized by a larger surface area-to-volume ratio of the electrocatalytic material. This lowers the costs of the

electrodes and, by increasing the active sites, enhances the signal-to-noise ratio, especially abating the capacitive background currents which are dependent on the real active surface area [8]. Devices based on ordered arrays are conventionally obtained using dedicated lithographic procedures and only a few papers rely on simple and effective techniques [41], since simpler methodologies usually produce random or uncontrollable distributions. However, our method allows the development of optimally-distributed arrays of AgNPs by a simple and low cost procedure. The key factor here is represented by the interaction between the APTES SAM and silver nanoparticles. As described before, we collected evidence that the surface density of amine groups was almost double for bare FTO ($10 \text{ NH}_2 \text{ nm}^{-2}$) compared to silica-coated FTO ($5 \text{ NH}_2 \text{ nm}^{-2}$). In this latter case, a lower quantity of silver nanoparticles is expected to be deposited on the silica layer. Figure shows the corresponding voltammograms for two AgNP-decorated electrodes which differs only by the presence or absence of the underlying silica layer. For the FTO-SiO₂-AgNPs electrode (Figure 5.7b, curve 1), a lower peak current is registered in comparison with an electrode in which AgNPs are directly deposited on APTES-functionalized FTO (Figure 5.7b, curve 2) thus demonstrating that a lower quantity of the metal is present. It is important to highlight that the current registered in the presence of a 500 nm-thick, electrically-insulating silica layer is, anyway, really high and of the same order of magnitude as those measured for the electrode without silica. This highlights the contribution of isolated nanoparticles (enabling convergent diffusion) and is of paramount importance for the detection of analyte(s) at trace levels, as already explained.

The distribution of silver nanoparticles on silica is studied by performing cyclic voltammetry in the presence of an electroactive probe (potassium ferrocyanide, K₄[Fe(CN)₆]) (Figure 5.7c), because only in the presence of a redox reaction the diffusion

mechanism and, as a consequence, the distribution of nanoparticles can be studied. Figure 5.7c (curve 1) shows a step-shaped voltammogram typical of a convergent diffusion mechanism on isolated ordered nanoparticles in the case of AgNPs deposited on silica-coated FTO. On the other hand, a peak-shaped voltammogram (Figure 5.7c, curve 2), reflecting a semi-infinite diffusion on non-isolated particles, was observed in the case of silver nanoparticles deposited directly on FTO.

To gain a deeper understanding of the electrical properties of our Device, electrochemical impedance spectroscopy (EIS) measurements are also performed, on electrodes at different steps of preparation and with different device layer compositions, in the presence of the redox probe $K_4[Fe(CN)_6]$ (Figure 5.8). Impedance measures the current response of the device to an external potential variation and allows modelling the systems by an electrical circuit. In the complex plane plots (Figure 5.8), the semicircle shape common to all the examined combinations can be represented by the same equivalent circuit (Figure 5.8, inset), composed of the solution resistance R_{Ω} in series with a parallel formed by the charge transfer resistance R_{CT} and double layer capacitance CPE_{DL} .



Samples	$R_{CT} / (k\Omega \text{ cm}^2)$
FTO	0.29
FTO+Ag	0.02
FTO+SiO ₂	4.48
FTO+TiO ₂	7.87
FTO+SiO ₂ +TiO ₂	44.12
FTO+Ag+TiO ₂	11.62
FTO+SiO ₂ +Ag	15.74
FTO+SiO ₂ +Ag+TiO ₂	23.78

Figure 5.8 Complex plane plot spectra for all the electrode architectures, registered at + 0.1 V (SCE) in the presence of the model probe molecule $K_4[Fe(CN)_6]$; inset: equivalent circuit used to fit data. Table: charge transfer resistance (R_{CT}) values calculated from data fitting.

From the diameter of the semicircle the values for charge transfer resistance, which are critical to describe the electron transfer between the model probe and the electrode, are obtained (Figure 5.8, table). As expected, these values increase by increasing the number of layers, while a drastic decrease in resistance is observed when AgNPs are present in otherwise identical conditions. This clearly demonstrates another crucial role of Ag nanoparticles, other than enabling electrocatalysis that is to enhance the electrical conductivity of our layered electrode, facilitating the passage of electrons from the probe dissolved in the surrounding electrolyte through the oxide layers to the conductive substrate.

However, this is not the end of the story: we already have data suggesting that silver nanoparticles play more subtle roles as a result of their surface functionalization and interaction with the embedding titania. Our research is actively in progress in this direction.

5.2.3 The Top Roles of Titania Overlayer

As discussed in the previous paragraph, one of the first role of titania is to protect AgNPs from unavoidable oxidation/deactivation processes originating from direct contact with the external environment. In the absence of a protective TiO_2 overlayer, degradation of AgNPs is observed from an electrochemical point of view even after few days of exposure to environmental conditions.

Here, other useful features of the final device, such as self-cleaning properties and enhanced selectivity towards the analyte(s), enabled by the presence of a titania overlayer are demonstrated. An accurate engineering of this final layer is necessary to obtain the desired properties without altering transparency, mechanical properties and the state of AgNPs in the resulting device. Actually, the growth of crystallites and the degradation of the organic components promoted by calcination is crucial to achieve photoactivity [14]. In our procedure a careful modulation of the titania sol composition, associated with a rapid calcination step at 400 °C under an inert atmosphere not only assured high photoactivity under UV-A irradiation, but also preserved the film transparency.

Photoactivity is checked using an already reported procedure for the simulation of fingerprint/oily stains self-cleaning of surfaces [47,48]. It is based on monitoring the decrease in water contact angle θ_w , which follows the degradation of chemisorbed hydrophobic siloxanes (Silres® 1701, Basf). The chemisorption of Silres 1701 on the electrode surface (Figure, scheme) shifted its θ_w from $\sim 30-0^\circ$ (highly hydrophilic) to $\sim 110^\circ$ (highly hydrophobic). The evolution of water contact angle is then followed under UV irradiation as shown in Figure 5.9, in which the results obtained for the bare silica layer and for the photoactive titania layer are compared.

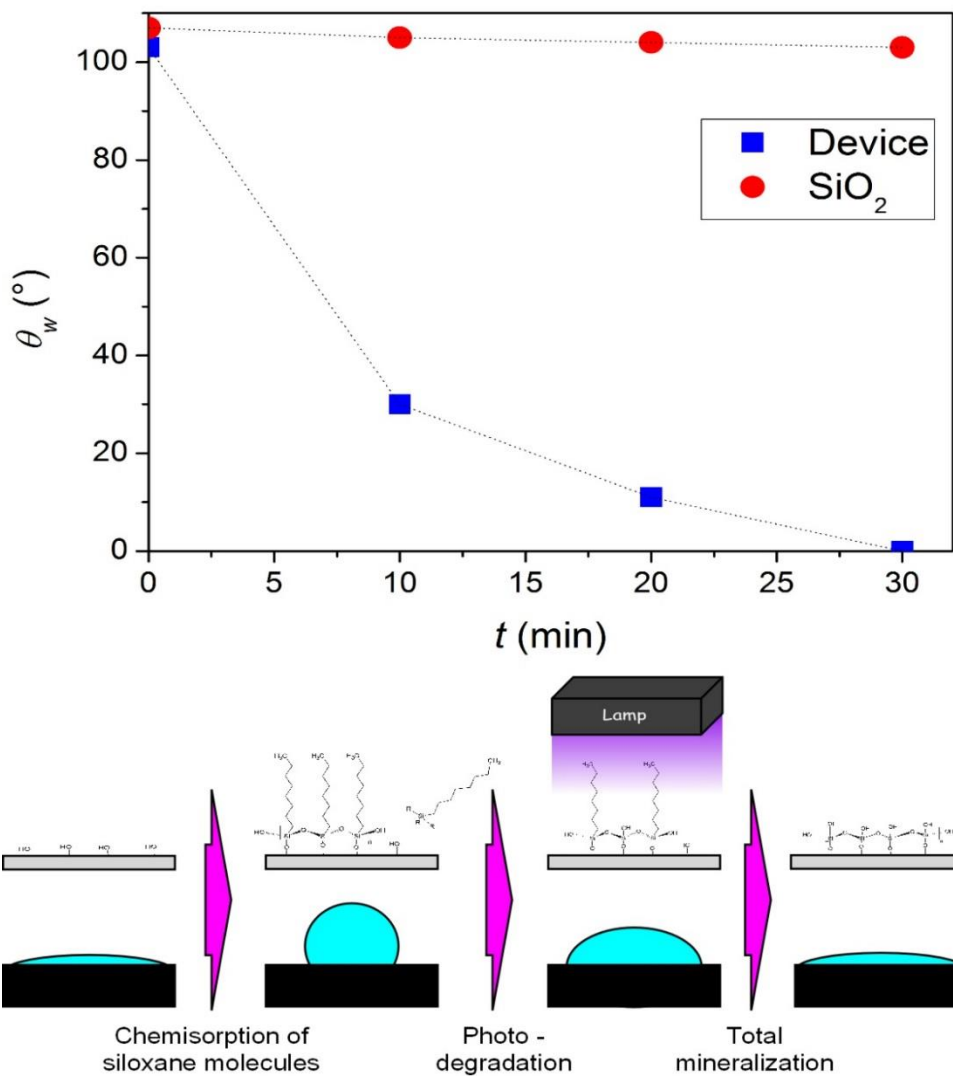


Figure 5.9 Kinetics of θ_w decrease of the Device covered by a chemisorbed siloxane layer under UV irradiation; schematic of the process used for siloxane chemisorption and photocatalytic degradation.

As thoroughly discussed in Appendix B, when titania is irradiated with UV light electron-hole pairs are generated and split into free holes and electrons. When they reach the surface, they react with adsorbed oxygen and water molecules generating reactive oxygen species (ROS, *e.g.* peroxide and superoxide radical) which in turn react with adsorbed organic molecules, oxidizing them to carbon dioxide and water and bringing back θ_w to hydrophilic value [14]. Compared to soiled silica, there is a dramatic and rapid decrease of θ_w for soiled titania under UV light which directly reflects the degradation kinetics of chemisorbed

organic molecules. This proves that the organic chain mineralization was carried out by the radicals produced by the irradiated titania and not by photolytic C–C bond scission processes. Eventually, this simple test proves the suitability of our device as a self-cleaning electrode.

However, titania plays other crucial roles. First, thanks to its porosity (see Figure) it allows the analyte(s) to reach the silver nanoparticle surface where the electrocatalytic reaction can take place. Second, because at physiologically relevant pH (*e.g.* pH = 7.4) its surface is negatively charged while the primary amine group of dopamine is protonated ($pK_{a1} = 8.87$), it increases the selectivity through electrostatic attraction of the analyte of interest and, at the same time, through electrostatic repulsion of negatively charged interferents (such as ascorbic and uric acid, see Chapter 6).

5.2.4 Demonstrating the Device Efficiency for the Electrochemical Detection of Dopamine

Dopamine, a molecule of great biomedical interest [21,22], is chosen as a model analyte to test the electroanalytical performances of our optimized multilayer electrode. After an extensive Literature search and experimental investigation, differential pulse voltammetry (DPV) is chosen as the most suitable technique for the electrochemical detection of dopamine. Figure 5.10a shows the calibration plot obtained for the complete device (FTO-SiO₂-AgNPs-TiO₂, empty circles) in the 5–35 ppm dopamine concentration range, and, as an inset, the corresponding differential pulse voltammograms. In presence of the silica layer, a convergent diffusion state on silver nanoparticles is reached leading to lower limits of

detection. Detection of dopamine with good sensitivity can be achieved also on a device without silica layer (FTO-AgNPs-TiO₂, Figure 5.10a, full circles). However, in this latter case, a strong saturation effect is observed and the calibration plot deviates from linearity. The electrocatalytic effect of silver nanoparticles is shown in Figure 5.10b, where a decrease in the dopamine peak potential from +0.26 V (SCE, curve 1) to +0.15 V (SCE, curve 2) is observed when AgNPs are present.

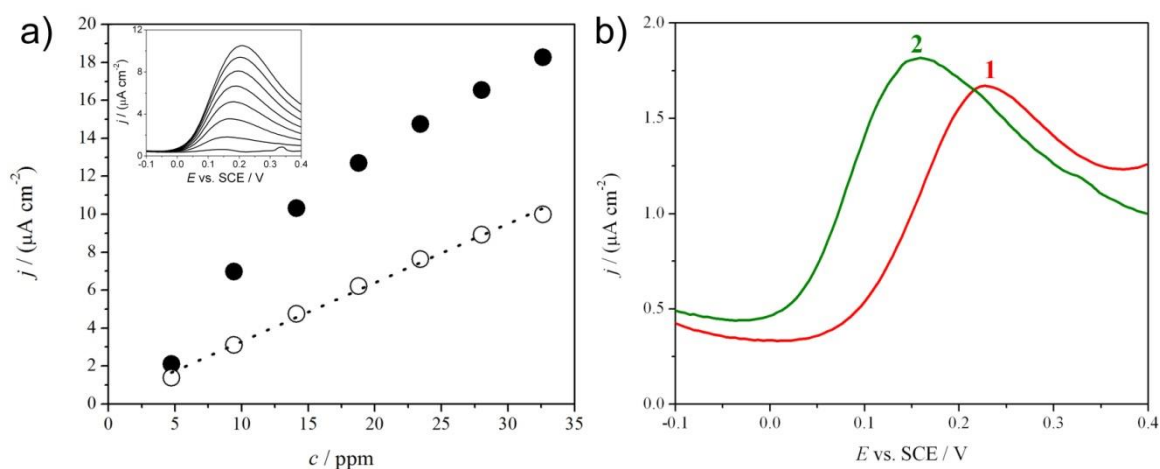


Figure 5.10 (a) DPV calibration plots obtained for dopamine detection on two different electrode architectures (FTO+Ag+TiO₂ (●), FTO+SiO₂+Ag+TiO₂(○)). The inset shows the differential pulse voltammograms referred to (○) data. (b) Differential pulse voltammograms showing electrocatalytic peak displacement caused by AgNPs (curve 1: FTO+SiO₂+TiO₂; curve 2: FTO+SiO₂+Ag+TiO₂).

As previously discussed, chemisorption and subsequent fouling of the electrode surface is a general concern in electroanalysis, especially when dealing with trace level-detection of organic analytes [1,21]. Fouling adversely affects the analytical sensitivity, leading to the necessity of harsh surface cleaning treatments or even to the complete replacement of the electrode. In the present case, fouling is significant as judged by the decrease in analytical sensitivity of the electrode. This latter is evaluated by the observed decrease in the

calibration plot slope in Figure 5.11a (triangles), compared to the fresh one (circles) for consecutive analyses.

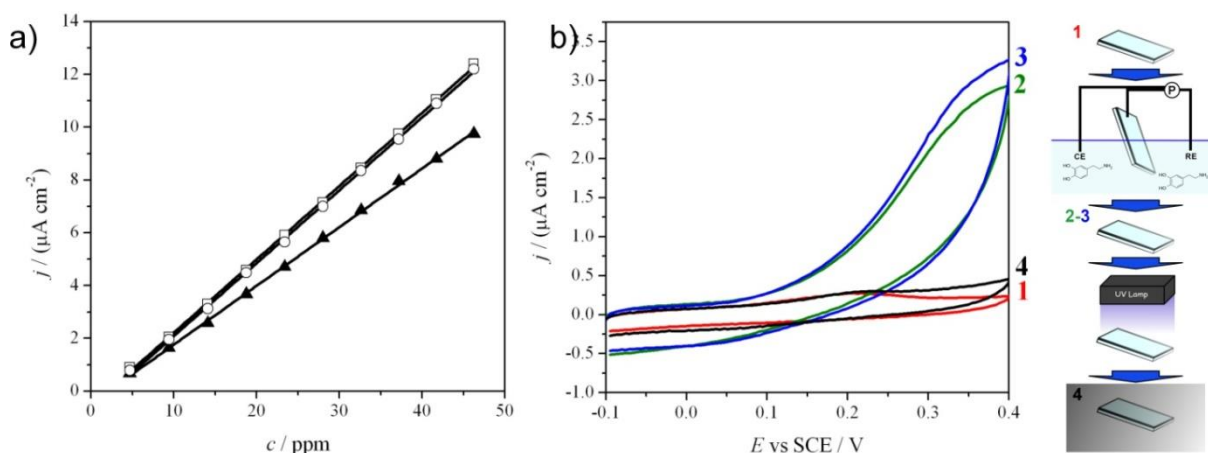
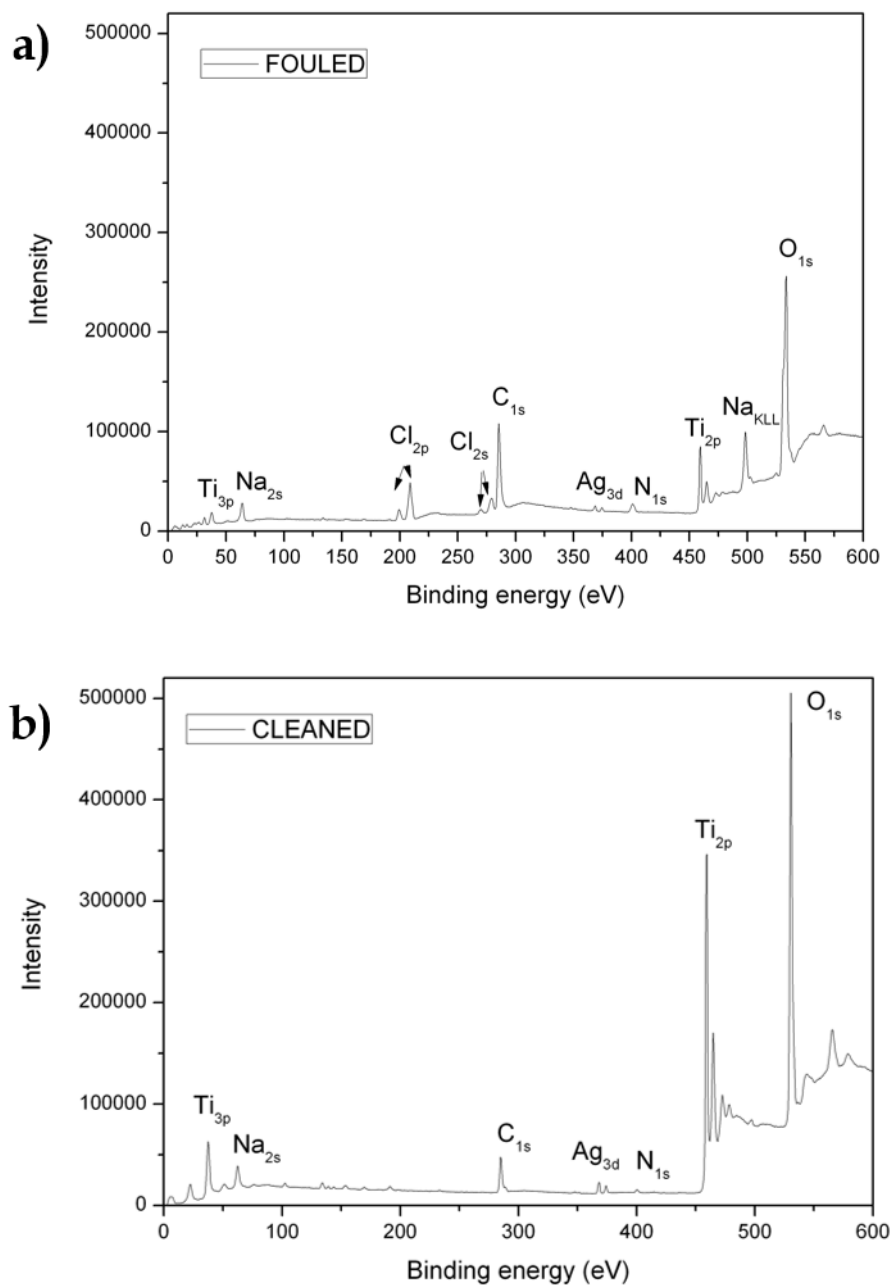


Figure 5.11 a) Dopamine calibration plots obtained at different analytical steps [squares (\square): first calibration plot; triangles (\blacktriangle): calibration plot after fouling; circles (\circ): calibration plot after UV cleaning]. b) Cyclic voltammograms registered at 0.1 V s^{-1} at different analytical steps during the fouling/cleaning procedure and the relevant schematic.

X-ray photoelectron spectroscopy (XPS) confirms surface fouling through the appearance of carbon and nitrogen signals (Figure 5.12). The fouled electrode is then irradiated with UV-A light for one hour. By this simple treatment, the electrode completely recovers its sensitivity as shown in Figure 5.11a (squares), where the calibration plot obtained for the electrode after UV irradiation is perfectly overlapping with that of pristine electrode (circles). XPS confirmed surface restoration by showing an almost complete disappearance of the carbon and nitrogen signals along with a significant increase of the titanium and oxygen ones. Based on our previous discussion, such results strongly suggest that the titania layer, thanks to its high photoactivity, is able to “clean” the electrode surface by removing the byproducts and the residues originated by the electrochemical detection of dopamine.



Sample	Treatment	O 1s (at.% ± 10%)	Ti 2p (at.% ± 10%)	N 1s (at.% ± 10%)	C 1s (at.% ± 10%)
Fouled	/	38.57	4.93	2.56	32.54
UV- cleaned	1 h 365 nm-UV irradiation	51.51	20.44	0.54	11.57

Figure 5.12 XPS spectra of the Device a) before (fouled) and b) after the UV-cleaning step. The table reports the calculated atomic percentages for the most relevant elements detected.

To achieve a better understanding of this phenomenon, we recorded the cyclic voltammograms of the same electrode in a fresh electrolyte solution (*i.e.* in the absence of dopamine) in different moments of the fouling-cleaning process (Figure 5.11b). Line 1 corresponds to the clean electrode before dopamine sensing and clearly shows the AgNPs peaks at around +0.2 V, as expected. Line 2 represents the voltammogram registered for the electrode after one dopamine calibration experiment (ten additions of 10^{-2} M dopamine) and washing with water. Line 3 is obtained for the washed electrode after two dopamine calibration steps. Voltammograms 2 and 3 are significantly different compared to voltammogram 1 as they clearly demonstrate a progressive fouling of the electrode surface. Both voltammograms 2 and 3 show peak shoulders at around +0.35 V and a narrowing of the accessible potential window, probably due to the presence of adsorbed dopamine or other fouling byproducts derived from its electrochemical reaction. Line 4 shows the voltammogram of the electrode after one hour of UV-A irradiation and 24 h of storage in the dark. In this latter case, the electrode completely recovers the initial shape (line 1), demonstrating the high efficiency of the cleaning process. The removal of adsorbed species is achieved and the possibility to reuse the electrode reuse is proved.

Eventually, the robustness of our device against aging and wear is considered. Our electrode has been able to maintain its original sensitivity even after hundreds of fouling-cleaning steps, during months, without adopting any specific care in storage. Each analysis caused the partial or total fouling of the electrode and each time complete sensitivity was recovered after UV irradiation. In Chapter 6 we will show that the self-cleaning ability of our electrode is not limited to dopamine and to its byproducts, but efficiently takes rid of fouling caused by interferents (*e.g.* ascorbic and uric acid) and other organic molecules typically present in

complex biological matrixes (*e.g.* proteins). Such impressive results are the best demonstration of the high reliability of our device.

5.3. Conclusions

Widespread application of electroanalytical methods for biomedical, industrial and environmental analyses is highly desirable thanks to the many advantages of such techniques. However, fouling and excessive fragility have since clipped the wings for the development of robust yet highly engineered electrodes. In this Chapter we described how to develop a self-cleaning electrode which is able to efficiently tackle this problems by a tailored combination of electrocatalytic silver nanoparticles and photoactive titanium dioxide. Each component of the resulting device has its own function that eventually combine in a synergistic way. The resulting device allows efficient detection of dopamine in physiologically relevant concentrations, in addition is transparent, mechanically robust and cheap. We solved the problem of fouling by equipping the device with a photoactive titania top layer and we demonstrated its total recovery of sensitivity simply after irradiation with UV-A light. No appreciable change in sensitivity was observed even after hundreds of fouling and cleaning cycles. Our device is versatile, reusable and commercially appealing, characteristics that will be further discussed in the following Chapters.

5.4 Specific procedures

Materials: all the chemicals used are of reagent grade purity and used as received. Distilled water purified with a Millipore Milli-Q apparatus (resistivity $\geq 18.2 \text{ M}\Omega \text{ cm}^{-1}$) is used to prepare solutions and sols. A UV iron halogenide lamp Jelosil HG500 with an effective power density, measured using a Thorlabs S314C radiometer, of 23 mW cm^{-2} emitting between 280 and 400 nm is used for the photocatalytic tests and for the irradiation steps included in the device synthesis.

Making the Device: fluorine-doped tin oxide-coated glass slides (FTO, Sigma-Aldrich®, $\sim 7 \text{ }\Omega \text{ sq}$, $2 \times 3 \text{ cm}$) used as supports are previously sonicated in a cleaning solution ($\text{H}_2\text{O} : \text{acetone} : \text{propanol} = 1 : 1 : 1$) and irradiated for 1 hour under UV light. The silica sol is prepared by the procedure reported by Wang *et al.* Briefly, 10 g of TEOS are added into a solution containing 25 g of ethanol and 4.5 g of hydrochloric acid solution (0.1 M). The mixture is stirred at lab temperature for 2 hours and then refluxed at $60 \text{ }^\circ\text{C}$ for 60 min. Eventually, 25 g of an ethanol solution of the CTAB cationic surfactant (2 g in 25 mL) are dissolved in the as-obtained solution by slowly stirring at lab temperature for 1 hour. The cleaned FTO slide is dipped in such a sol and quickly calcined at $500 \text{ }^\circ\text{C}$ for 1 hour under N_2 flow to develop the silica layer. For its functionalization with (3-aminopropyl)triethoxysilane (APTES), the silica layer is first irradiated under UV for 1 hour and then is dipped into anhydrous toluene under N_2 at $70 \text{ }^\circ\text{C}$. After 1 hour, a solution of APTES in anhydrous toluene is added (final APTES concentration: 10 mM). After 3 hours at $70 \text{ }^\circ\text{C}$ the sample is cleaned by sonication for a few minutes in toluene, ethanol and water in order to eliminate the un-grafted siloxane and eventually dried under a nitrogen stream. The sample is then immersed in a pre-made aqueous suspension of AgNPs (see Appendix C for details) for 15 minutes and then dried with a N_2 flux. The external titania layer is obtained by dipping the substrate in a titania sol (see Appendix C for details) and calcining it under N_2 flow for 1 hour at $400 \text{ }^\circ\text{C}$.

Techniques used for the Device characterization: room-temperature X-ray diffraction (XRD) patterns are collected between 5° and 90° with a powder diffractometer Philips X'Pert $\theta/2\theta$ in grazing angle geometry, $\omega = 1.0^\circ$, using X Cu $\text{K}\alpha$ radiation ($\lambda = 1.5416 \text{ \AA}$ and power

1.6 kW). The results are obtained on the basis of the Hanawalt method on the data set of PDF-2 (Powder Diffraction File, ICDD). Scanning electron microscopy (SEM) images are obtained using a Zeiss LEO 1430 working at 30 keV. HRTEM images are acquired using a JEM 2010 equipped with a LAB6 electron gun (beam energy 200 keV) and a Gatan CCD camera allowing high resolution imaging. Film transparency and plasmonic resonance are evaluated by UV-Visible spectroscopy (Beckman DU640). Z-potential is measured using a Malvern Zetasizer Nano-ZS equipped with a universal dip cell (Malvern) and standard polystyrene cuvettes. Water contact angles were measured by a Krüss Easydrop. Film thicknesses are evaluated using a Filmetrics® F20 reflectometer (Filmetrics). CV and EIS experiments are carried out with an Autolab PGStat30 (Ecochemie, The Netherlands) potentiostat/galvanostat equipped with an FRA module and controlled by GPES and FRA softwares. Impedance data are processed with Z-View 3.1 software. Cyclic voltammetric characterization is performed in a 0.1 M NaClO₄ aqueous solution at room temperature, in a three-electrode conventional cell, with a saturated calomel and a platinum wire as the reference and counter electrodes, respectively. No N₂ degassing of the solution is necessary, since dissolved O₂ did not affect measurements. The potential is varied between -0.1 V and +0.4 V (SCE) at 0.1 (V s⁻¹) scan rate. This potential window is chosen considering the Pourbaix diagrams for TiO₂ and for metallic Ag. Electrochemical impedance spectra are registered at -0.1, +0.1 and +0.25 V (SCE), with a range of frequencies between 65 000 and 0.1 Hz and an amplitude of 10 mV under the same experimental conditions of cyclic voltammetry. The electrode behavior is studied both in the presence and in the absence of a redox reaction, using K₄[Fe(CN)₆] as a model probe molecule.

Determination of surface density of the amine groups: First, 10 mg of 4-nitrobenzaldehyde are dissolved in 17 mL of ethanol containing 14 µL of glacial acetic acid. Each sample is immersed in this solution for 3 h at 50 °C, then rinsed, sonicated in ethanol and dried under a stream of nitrogen. Each sample is immersed for 1 h in 3 mL of 0.35 M aqueous acetic acid at 30 °C. The absorbance at 267 nm of the resulting solution is measured using a UV-vis spectrophotometer. Using the extinction coefficient for 4-nitrobenzaldehyde ($1.45 \cdot 10^4 \text{ M}^{-1} \text{ cm}^{-1}$) its concentration, which is equal to the concentration of amine groups, is calculated. The surface density of amine groups is then derived accordingly.

Photoactivity test: the photocatalytic activity of the device is tested by following the kinetics of degradation for a hydrophobizing organic molecule deposited directly on the titania layer. The adopted hydrophobizing molecule (SILRES BS 1701) is produced and commercialized by Wacker Chemie AG. It is a mixture of isomeric octyltriethoxysilanes with iso-octyltriethoxysilane as the main component. These molecules are chemisorbed on the tested surface by a chemical vapor deposition protocol [49]: first the device is placed in a glass container together with a Teflon® cup filled with siloxane. The container is then placed in an oven at 100 °C for 3 hours to vaporize siloxane. Eventually, the substrate is sonicated in toluene and dried. The degradation of the organic moieties is monitored by measuring the water contact angle as a function of the time of UV irradiation.

Electrochemical detection of dopamine using our Device: dopamine hydrochloride is of analytical purity and is purchased from Sigma-Aldrich. Its electroanalytical detection is performed using Differential Pulse Voltammetry, scanning the potential between -0.1 V and +0.4 V (SCE), with the following parameters: modulation time 0.05 s, interval time 0.5 s, step potential 0.005 V, modulation amplitude 0.05 V, in a three-electrode cell. Three voltammograms for each studied dopamine concentration are recorded. The calibration curve is repeated three times, obtaining comparable results. Saturated calomel, Pt wire and our Device were used as the reference, counter and working electrodes, respectively. Phosphate buffer (pH 7.4, 0.1 M) is used as the supporting electrolyte.

5.5 References

- [1] C. M. A. Brett, *Pure Appl. Chem.*, **2001**, 73, 1969–1977.
- [2] L. Rassaei, M. Amiri, C. M. Cirtiu, M. Sillanpaa and F. Marken, *Trends Anal. Chem.*, **2011**, 30, 1704–1715.
- [3] M. Pumera, S. Sánchez, I. Ichinose and J. Tang, *Sens. Actuators B*, **2007**, 123, 1195–1205.
- [4] G. Hanrahan, D. G. Patil and J. Wang, *J. Environ. Monit.*, **2004**, 6, 657–664.
- [5] S.-J. Bao, C. M. Li, J.-F. Zang, X.-Q. Cui, Y. Qiao and J. Guo, *Adv. Funct. Mater.*, **2008**, 18, 591–599.

- [6] X. Ma, W. Hu, C. Guo, L. Yu, L. Gao, J. Xie and C. M. Li, *Adv. Funct. Mater.*, **2014**, *24*, 5897–5903.
- [7] M. Zhang, C. Liao, Y. Yao, Z. Liu, F. Gong and F. Yan, *Adv. Funct. Mater.*, **2014**, *24*, 978–985.
- [8] C. M. Welch and R. G. Compton, *Anal. Bioanal. Chem.*, **2006**, *384*, 601–619.
- [9] F. W. Campbell and R. G. Compton, *Anal. Bioanal. Chem.*, **2010**, *396*, 241–259.
- [10] I. Streeter, R. Baron and R. G. Compton, *J. Phys. Chem. C*, **2007**, *111*, 17008–17014.
- [11] Q. Wang and Y. Yun, *Microchim. Acta*, **2012**, *180*, 261–268.
- [12] X. L. Luo, A. Morrin, A. J. Killard and M. R. Smyth, *Electroanalysis*, **2006**, *18*, 319–326.
- [13] D. Meroni, S. Ardizzone, U. S. Schubert and S. Hoepfener, *Adv. Funct. Mater.*, **2012**, *22*, 4376–4382.
- [14] A. Fujishima, X. Zhang and D. A. Tryk, *Surf. Sci. Rep.*, **2008**, *63*, 515–582.
- [15] X. Chen and S. S. Mao, *Chem. Rev.*, **2007**, *107*, 2891–2959.
- [16] G. Soliveri, R. Annunziata, S. Ardizzone, G. Cappelletti and D. Meroni, *J. Phys. Chem. C*, **2012**, *116*, 26405–26413.
- [17] R. Alam, I. V. Lightcap, C. J. Karwacki and P. V. Kamat, *ACS Nano*, **2014**, *8*, 7272–7278.
- [18] G. K. Mor, M. A. Carvalho, O. K. Varghese, M. V. Pishko and C. A. Grimes, *J. Mater. Res.*, **2011**, *19*, 628–634.
- [19] Y.-Y. Song, Z. Gao, K. Lee and P. Schmuki, *Electrochem. Commun.*, **2011**, *13*, 1217–1220.
- [20] Y.-Y. Song, Z.-D. Gao and P. Schmuki, *Electrochem. Commun.*, **2011**, *13*, 290–293.
- [21] K. Jackowska and P. Kryszewski, *Anal. Bioanal. Chem.*, **2013**, *405*, 3753–3771.
- [22] M. Perry, Q. Li and R. T. Kennedy, *Anal. Chim. Acta*, **2009**, *653*, 1–22.
- [23] N. G. Shang, P. Papakonstantinou, M. McMullan, M. Chu, A. Stamboulis, A. Potenza, S. S. Dhesi and H. Marchetto, *Adv. Funct. Mater.*, **2008**, *18*, 3506–3514.
- [24] X. Wang, X. Liu, L. Lai, S. Li, J. Weng, Z. Zhou, Q. Cui, X. Chen, M. Cao and Q. Zhang, *Adv. Funct. Mater.*, **2008**, *18*, 1809–1823.
- [25] M. Wei, L.-G. Sun, Z.-Y. Xie, J.-F. Zhii, A. Fujishima, Y. Einaga, D.-G. Fu, X.-M. Wang and Z.-Z. Gu, *Adv. Funct. Mater.*, **2008**, *18*, 1414–1421.
- [26] X. Wang, R. Xiong and G. Wei, *Surf. Coat. Technol.*, **2010**, *204*, 2187–2192.
- [27] R. G. Acres, A. V. Ellis, J. Alvino, C. E. Lenahan, D. A. Khodakov, G. F. Metha and G. G. Andersson, *J. Phys. Chem. C*, **2012**, *116*, 6289–6297.

- [28] G. Panzarasa, *J. Chem. Educ.*, **2014**, *91*, 696–700.
- [29] D. D. Evanoff and G. Chumanov, *Chemphyschem*, **2005**, *6*, 1221–1231.
- [30] D. D. Evanoff, R. L. White and G. Chumanov, *J. Phys. Chem. B*, **2004**, *108*, 1522–1524.
- [31] G. Maino, D. Meroni, V. Pifferi, L. Falciola, G. Soliveri, G. Cappelletti and S. Ardizzone, *J. Nanopart. Res.*, **2013**, *15*, 2087.
- [32] V. Pifferi, G. Facchinetti, A. Villa, L. Prati and L. Falciola, *Catal. Today*, **2015**, *249*, 265–269.
- [33] L. Falciola, A. Gennaro, A. A. Isse, P. R. Mussini and M. Rossi, *J. Electroanal. Chem.*, **2006**, *593*, 47–56.
- [34] C. Bellomunno, D. Bonanomi, L. Falciola, M. Longhi, P. R. Mussini, L. M. Doubova and G. Di Silvestro, *Electrochim. Acta*, **2005**, *50*, 2331–2341.
- [35] V. Pifferi, V. Marona, M. Longhi and L. Falciola, *Electrochim. Acta*, **2013**, *109*, 447–453.
- [36] M. Giovanni and M. Pumera, *Electroanalysis*, **2012**, *24*, 615–617.
- [37] I. Boskovic, S. V. Mentus and M. Pjescic, *Electrochim. Acta*, **2006**, *51*, 2793–2799.
- [38] S. D. Standridge, G. C. Schatz and J. T. Hupp, *Langmuir*, **2009**, *25*, 2596–2600.
- [39] Y.-G. Zhou, F. W. Campbell, S. R. Belding and R. G. Compton, *Chem. Phys. Lett.*, **2010**, *497*, 200–204.
- [40] G. Herzog and V. Beni, *Anal. Chim. Acta*, **2013**, *769*, 10–21.
- [41] A. O. Simm, S. Ward-Jones, C. E. Banks and R. G. Compton, *Anal. Sci.*, **2005**, *21*, 667–671.
- [42] S. Daniele, M. Baldo and C. Bragato, *Curr. Anal. Chem.*, **2008**, *4*, 215–228.
- [43] A. J. Bard and L. R. Faulkner, *Electrochemical Methods: Fundamentals and Applications*, 2001.
- [44] I. Streeter and R. G. Compton, *J. Phys. Chem. C*, **2007**, *111*, 18049–18054.
- [45] T. J. Davies and R. G. Compton, *J. Electroanal. Chem.*, **2005**, *585*, 63–82.
- [46] J. H. Moon, J. W. Shin, S. Y. Kim and J. W. Park, *Langmuir*, **1996**, *12*, 4621–4624.
- [47] A. Antonello, G. Soliveri, D. Meroni, G. Cappelletti and S. Ardizzone, *Catal. Today*, **2014**, *230*, 35–40.
- [48] Y. Paz, *Beilstein J. Nanotechnol.*, **2011**, *2*, 845–861.
- [49] G. Soliveri, D. Meroni, G. Cappelletti, R. Annunziata, V. Aina, G. Cerrato and S. Ardizzone, *J. Mater. Sci.*, **2014**, *49*, 2734–2744.

Chapter 6

Self-Cleaning Electrochemical Sensors, Part I: Towards Clinical Applications

ABSTRACT

Neurotransmitters in biological samples are a critical issue in analytical chemistry: low sensitivity, low selectivity and heavy fouling make their electrochemical determination a difficult and time consuming task. However, we show here how our reusable and self-cleaning device, a composite electrode with a layered structure combining the electrocatalytic properties of silver nanoparticles and the photoactivity of titania, can efficiently overcome this issue. The detection of dopamine, norepinephrine and serotonin is achieved with low detection limits ($0.03 \mu\text{M}$) even in the presence of conventional interferents (ascorbic and uric acid). Fouling issues associated with biological matrixes, such as cerebrospinal liquor and blood serum, are solved thanks to photocatalytic self-cleaning of the electrode surface. Moreover, the contemporary detection of two analytes in simulated human urine is demonstrated as a first step towards clinical applications.

6.1 Introduction

The ability to achieve quantitative detection of neurotransmitters under physiological conditions is of critical importance in clinical diagnosis [1-3]. This is especially true for catecholamine neurotransmitters because of their key roles in behavior expression, during excessive oxidative stress events, for the early diagnosis of neurodegenerative diseases (such as Parkinson disease) [4,5] and some kinds of tumors (*e.g.* pheochromocytoma) [6]. The most studied neurotransmitter is dopamine, along with norepinephrine and serotonin. In conventional clinical settings, the most used analytical method is based on HPLC coupled with a conductivity detector. This protocol, although allowing the contemporaneous detection of numerous analytes, requires a complicated pretreatment (acid hydrolysis at high temperature followed by solid phase extraction) of the sample, long time of analysis and high costs. For these reasons, many reports are available in the Literature proposing robust alternatives, especially for pre-screening applications [7]. The ultimate goal, however, is the development of an analytical method with comparable sensitivity, reduced sample pretreatment and the amount time required (and consequently a reduced cost per analysis).

In this context, as discussed in the previous Chapter, electroanalytical techniques seem to be the most promising since they display all the desired characteristics in terms of efficiency and low cost. Moreover, catecholamine neurotransmitters are well suited for electroanalytical detection because their reaction potentials lie within those for carbon- and metal-based electrodes in physiological buffer.

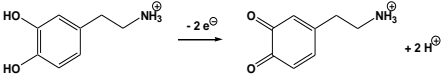
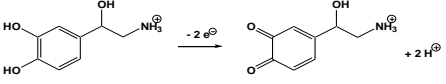
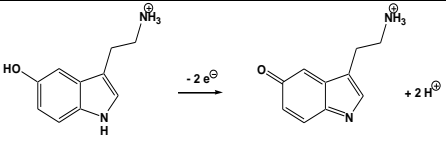
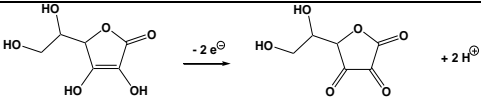
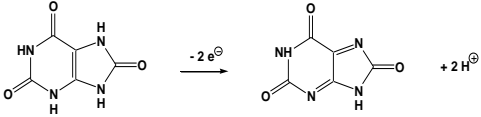
However, performing efficient electroanalysis of such molecules has always been a challenge because of both selectivity and fouling issues [8,9]. First, all such analytes show

similar oxidation reactions with similar peak potentials at physiological pH. This makes the discrimination between different catecholamines on the ground of their oxidation ability a tougher task compared to the conventional HPLC method. Second, many of these compounds undergo secondary reactions after the initial electron transfers and can generate insulating polymeric products that give rise to fouling and rapid inactivation of the electrode. Third, the problem of the interferents is severe: not only ascorbic acid and uric acid are always present together with catecholamines in biological fluids at a concentration 100- to 1000-fold higher than that of neurotransmitters (nanomolar range), also their oxidation peaks occur at the same potential of those for the analytes (Table 6.1), resulting in poor selectivity and reproducibility.

Gaining the ability to selectively determine dopamine and other catecholamines in the presence of such interferents has always been a major goal for electroanalytical research and the development of chemical sensors for clinical, biomedical purposes and for *in vivo* monitoring studies [1,7]. Also, the requirements are stringent: the methods need to be selective, so that the measured responses are unequivocally due to a specific molecule, and they need to be sensitive, so that they can detect these substances in the physiological range. These results can be achieved by a difficult balance between the required affinity of the electrode surface toward the analyte(s) and irreversible adsorption of the target molecule/by-products/interferents.

As a matter of fact, chemisorption, whereas being in principle the most favorable kind of interaction in order to maximize signal response, is usually undesirable due to fouling effects such as signal drifting, lowering of sensitivity and lack of reproducibility.

Table 6.1 Redox reactions for the studied catecholamines and for common interferents [1].

Molecule	Redox reaction	Oxidation potential <i>vs</i> Ag/AgCl
<i>Catecholamine neurotransmitters</i>		
Dopamine		+ 0.2 V
Norepinephrine		+ 0.2 V
Serotonin		+ 0.35 V
<i>Interferents</i>		
Ascorbic acid		+ 0.2 V
Uric acid		+ 0.3 V

During the last years different approaches were attempted in order to solve this problem, however, despite the numerous attempts, no groundbreaking result have been obtained. The electrochemical detection of catecholamines by direct oxidation is almost impossible to achieve on conventional electrodes (*i.e.* graphite, glassy carbon, gold, platinum etc.) due to their high overpotential and heavy electrode fouling [13]. Innovative approaches include the use of highly engineered electrodes modified with nanomaterials (especially nanoparticles of noble metals such as Ag, Au, Pt), self-assembled monolayers, polymer brushes, etc. [14]. Higher selectivity could be achieved in this way thanks to the increased affinity of the surface for the analyte(s) and the detection limits reached the values required for the biological fluids. However, the fouling issues worsened, especially for analyses performed in biological matrixes, affecting the reproducibility of the measure and even the

near-term stability of such complex devices which could not withstand conventional harsh treatments for surface regeneration. Electrode surface regeneration techniques such as mechanical cleaning with grit paper or aggressive chemical etching, or electrochemical cleaning (for platinum or gold electrodes for examples), despite being of common practice for bulk-metal electrodes [15] are not always practical nor desirable for more sophisticated sensors. An accurate pretreatment could be of help in the case of protein-rich samples such as body fluids, but when the problem arises also from the analyte(s) themselves, the scenario toughens.

This is why the efficient regeneration of the electrode surface represents today the main challenge toward the widespread application of electroanalysis to “difficult” analytes [13,14]. A first approach to solve this problem focuses on the development of cheap, single-use electrodes: a good example is represented by electrochemically-treated pencil leads [16]. For these systems, the fouling is obviously overcome but sensitivity and reproducibility can be questionable, apart from the increased generation of waste.

In the Literature, only few examples of self-cleaning sensors are reported and are applied to solve specific fouling issues, thus lacking general applicability. Despite the huge variety of sensors and biosensors, the case represented by the detection of catecholamines in biological fluid is especially puzzling for three main reasons. First, less than a half of the sensors reach the detection limits required for the medical applications. Second, such sensors are principally studied for the detection of dopamine, while norepinephrine and serotonin are less considered due to their more complex electrochemical behavior. Third, to ensure long-term stability and high reproducibility of the final device, despite being a fundamental challenge for this field, is generally not considered. In the case of catecholamine neurotransmitters, as a consequence of the electrochemical formation of reactive quinones

and phenoxy radicals, the formation of passivating polymeric films on the electrode is observed. Additional sources of fouling and passivation are the coexistence of many interfering compounds in biological matrixes, which could be oxidized at the same potentials used for the detection of analytes.

Our approach, as already discussed in Chapter 5, is based on the development of “smart” electrode surfaces which can regenerate themselves without the need of complex treatments. In this context, we have reported the first example of an electrochemical sensor which, thanks to its photo-active surface, could be simply cleaned simply by irradiation with UV-A light and reused indefinitely [17]. The excellent results obtained prompted us to focus more on the critical issue of catecholamines detection: dopamine, norepinephrine and serotonin. To the best of our knowledge, this is the first time that an electrochemical device has been *ad hoc* designed solving all the problems related to the detection of these three fundamental analytes.

6.2 Results and Discussion

6.2.1 Structure and Features of the Electrochemical Sensor

The structure of our device is engineered to condense the more desirable features toward efficient electroanalysis of catecholamines (Figure 6.1a). However, in this paragraph we will only summarize its most important features, since its structure is discussed in detail in Chapter 5.

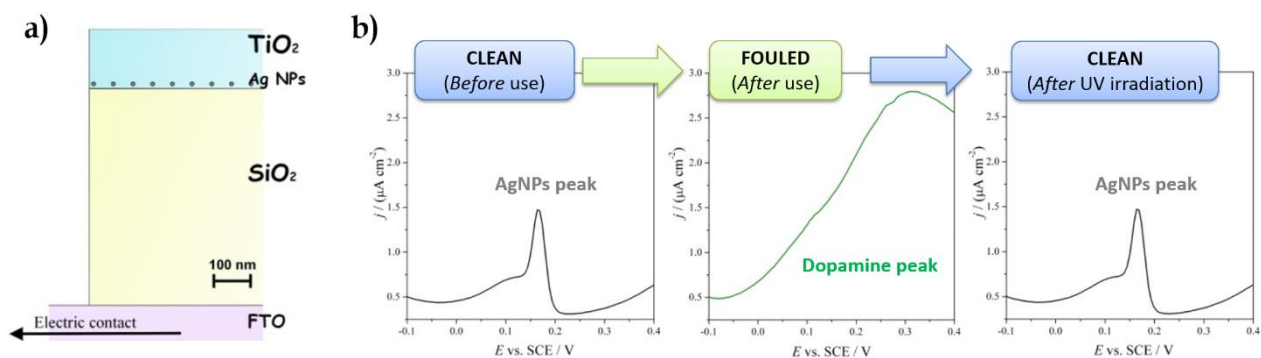


Figure 6.1 a) Schematic structure of our electrochemical device. b) Differential pulse voltammetry plots demonstrating the self-cleaning ability of the device.

On the Electrochemical Properties of Our Device Towards the Detection of Catecholamines

As previously discussed in Chapter 5, the presence of electrocatalytically active silver nanoparticles [22-25] arranged with a sparse distribution [26,27] has a pivotal importance in determining the overall efficiency of our electrochemical sensor or Device. This central role of AgNPs will be further highlighted by comparing their performance with those of an electrode built without embedding AgNPs (named as Control).

Differential Pulse Voltammetry (DPV) is, among the other tested electroanalytical techniques (*i.e.* linear and cyclic voltammetry, square wave voltammetry and chronoamperometry) the most performant in terms of detection limits and sensitivity. These favorable properties are further optimized through a careful selection of parameters and interval times. Probably the failure of the other techniques could be attributed to the fixed potential used for amperometry and to the fast scan rates typical of the cited voltammetric techniques, which make them more affected by electrode fouling than DPV.

Analyses were performed in 0.1 M phosphate buffer solution (pH = 7.4), which is routinely used to simulate the biological environment.

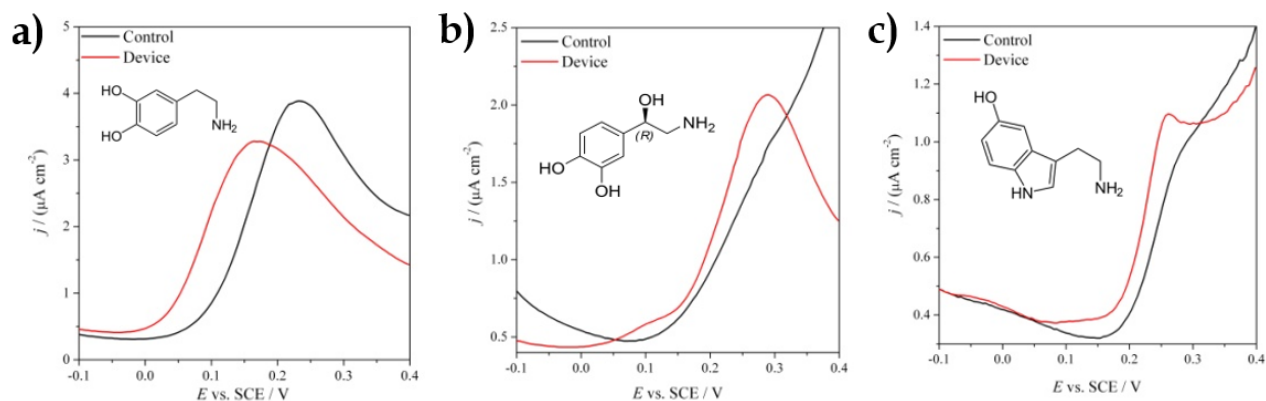


Figure 6.2 Differential pulse voltammograms obtained in the presence of the three neurotransmitters (concentration: 0.1 mM) for the control and the device: a) dopamine, b) norepinephrine, c) serotonin.

Figure 6.2 shows the differential pulse voltammetry plots obtained for three catecholamine neurotransmitters, in which the performance of the electrode with AgNPs is compared with that without AgNPs (Device and Control, respectively). In the case of dopamine (Figure 6.2a), the peak displacement towards less positive potential (from +0.23 V to +0.16 V) indicates the electrocatalytic role of silver. On the other hand, only a shoulder (which increases with neurotransmitter concentration) at +0.30 V and +0.27 V is displayed for norepinephrine and serotonin, respectively (Figure 6.2b,c), analyzed with the Control electrode. However, these shoulders become well-defined peaks when our AgNPs embedding Device is used, making the detection of such molecules undoubtedly easier. The appearance of such defined peak is probably due to the establishment of a convergent diffusion regime on a random assembly of silver nanoelectrodes, which is capable of increasing the peak currents [28-30].

Figure 6.3 shows the impedance complex plane spectra registered for the electrode with (Device) and without (Control) silver nanoparticles in the presence of these three catecholamines at three different potentials: +0.25 V, +0.1 V and -0.1 V.

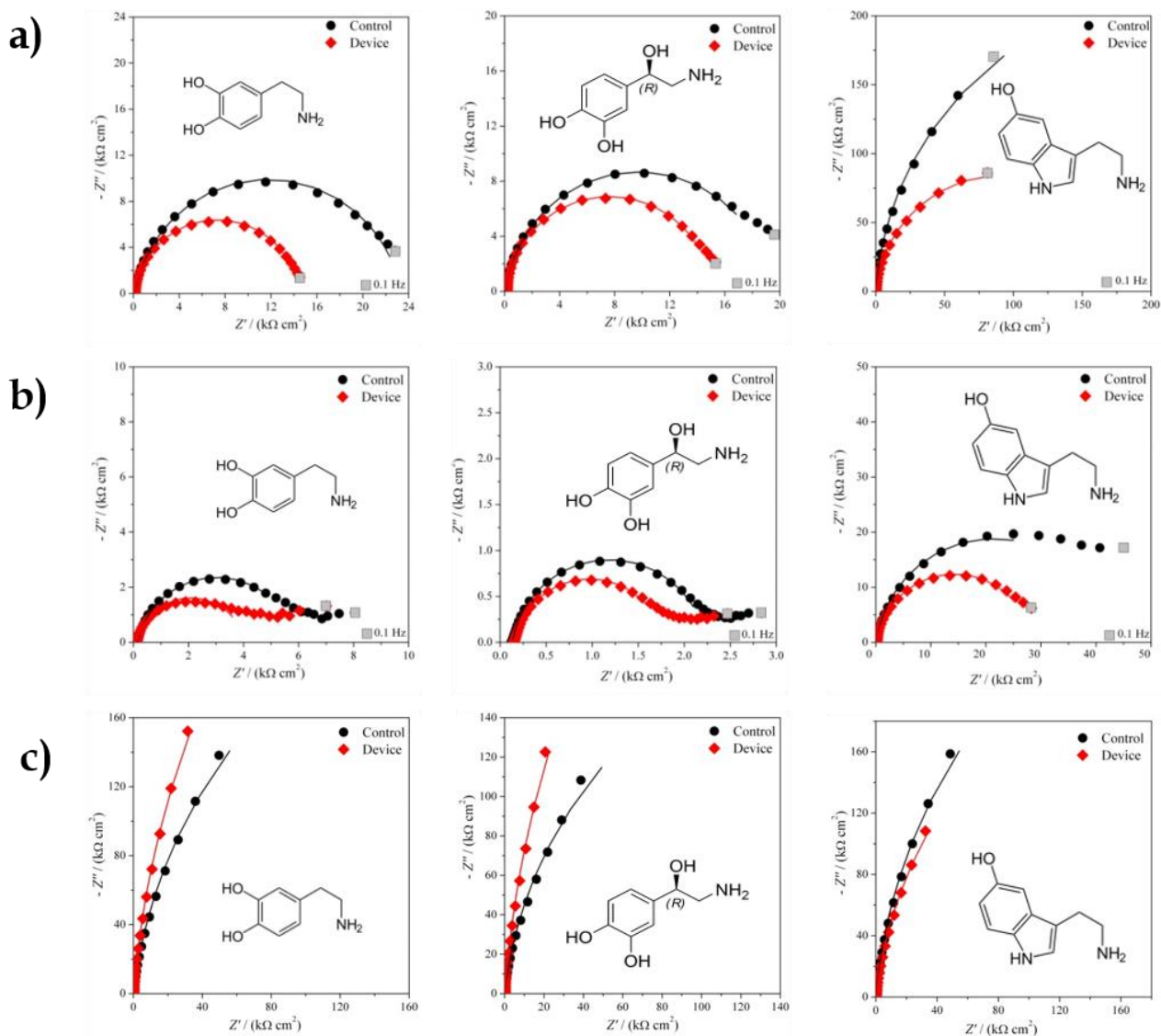
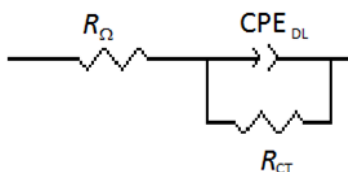


Figure 6.3 Complex plane plots (frequency range: from 65000 to 0.1 Hz) measured for the Control and the Device in the presence of dopamine, norepinephrine or serotonin. Potentials: a) +0.1 V, b) +0.25 V and c) -0.1 V.

The impedance spectra display the typical trend expected for faradic reactions, with a semicircle covering the entire frequency range. The equivalent circuit (Scheme 6.1) used to fit impedance data is made by the resistance of solution R_{Ω} in series with the charge transfer resistance R_{CT} and double layer capacitance, in parallel.



Scheme 6.1 The equivalent electrical circuit used to fit the electrochemical impedance spectroscopy data.

This last parameter was modeled as a constant phase element $CPE_{dl} = [(Ci\omega)^{\alpha}]^{-1}$, representing the charge separation of the double layers, which behaves as a pure capacitor in the case of $\alpha = 1$ or as a non-ideal capacitor, due to the porosity and non-homogeneity of the surface, for $0.5 < \alpha < 1$. The samples here considered present values of α around 0.9 (Table 6.2), indicating quite homogeneous surfaces. Table 6.3 shows the charge transfer resistance values obtained from the fitting. The capacitance values and solution resistance values are very similar for all the analyzed samples.

Table 6.2 Solution resistance and capacitance values obtained from impedance data fitting for the Control and the Device at -0.1 V, +0.1 V and +0.25 V (SCE) in presence of neurotransmitters (Dopa = dopamine, Nore = norepinephrine, Sero = serotonin).

Sample	E (V)	R_{Ω} ($\Omega \text{ cm}^2$)			C_{DL} ($\mu\text{F cm}^{-2} \text{ s}^{\alpha-1}$)			A		
		Dopa	Nore	Sero	Dopa	Nore	Sero	Dopa	Nore	Sero
Control	-0.1	165	134	147	9.52	11.42	8.72	0.93	0.93	0.95
	+0.1	145	136	149	9.82	10.08	7.07	0.90	0.94	0.96
	+0.25	145	133	147	11.14	12.76	8.44	0.87	0.90	0.92
Device	-0.1	136	163	145	9.71	12.29	12.89	0.95	0.96	0.93
	+0.1	127	163	147	9.72	10.65	9.22	0.93	0.95	0.95
	+0.25	119	158	144	12.79	14.49	10.21	0.87	0.90	0.92

Table 6.3 Values of charge transfer resistance obtained from impedance data fitting.

R_{ct} ($k\Omega\text{ cm}^2$)	<i>Dopamine</i>		<i>Norepinephrine</i>		<i>Serotonin</i>	
	+0.1 V	+0.25 V	+0.1 V	+0.25 V	+0.1 V	+0.25 V
Control	23	6	19	2	461	42
Device	14	4	15	1	184	28

Dopamine and norepinephrine present lower absolute impedance and charge transfer resistance values with respect to serotonin, indicating an easier reaction. This could probably be due to their intrinsic molecular structure: in particular, dopamine and norepinephrine could have a higher affinity for the electrode's titania surface thanks to their catechol groups. It is worthwhile to note that, as previously discussed, the presence of silver nanoparticles in our Device is crucial to obtain easier electrode reactions, which are characterized by lower R_{CT} and impedance values.

On the Electroanalytical Parameters of Our Device Towards the Quantitation of Catecholamines

Our optimized Device is then tested for the electroanalytical detection of the three previously cited neurotransmitters (dopamine, norepinephrine and serotonin) by Differential Pulse Voltammetry. Table 6.4 reports the analytical parameters, obtained for consecutive additions of the analytes in the 0 – 5 μM range.

Table 6.4 Analytical parameters obtained for the Control and the Device during the detection of neurotransmitters.

	Control			Device		
	<i>Dopa</i>	<i>Nore</i>	<i>Sero</i>	<i>Dopa</i>	<i>Nore</i>	<i>Sero</i>
S ($\mu\text{A cm}^{-2} \mu\text{M}^{-1}$)	0.0286 \pm 0.0007	0.048 \pm 0.001	0.008 \pm 0.002	0.0256 \pm 0.0008	0.159 \pm 0.003	0.213 \pm 0.005
LoD (μM)	0.37	0.37	0.33	0.03	0.04	0.04
LoQ (μM)	1.12	1.13	1.00	0.10	0.13	0.11
R²	0.995	0.995	0.996	0.993	0.993	0.995
R²_{adj}	0.994	0.994	0.995	0.993	0.992	0.995
RSD %	3	5	0.8	3	2	2
ARF %	104-100-98	104-100-98	104-100-98	101-99-99	101-99-99	101-99-99

The sensitivity *S* of the method is obtained from the slope of the calibration plots and LoD (eq. 1) and LoQ (eq. 2) are calculated according to the IUPAC protocol [31,32]:

$$LoD = 3.29 \frac{\sigma_{Blank}}{S} \quad (1)$$

$$LoQ = 10 \frac{\sigma_{Blank}}{S} \quad (2)$$

Where σ_{Blank} is the blank standard deviation. Since no blank signal is detected, this parameter is identified as the standard deviation obtained from the calibration plot.

Uniformly distributed residues and very good correlation coefficients witness the good linearity of the calibration plots. It is clear that silver nanoparticles promote a significant increase in sensitivity along with a significant decrease of LoD and LoQ (of one order of magnitude).

The repeatability, thus the best achievable internal precision, of this method is evaluated by measuring in a short interval of time the peak current of 10 repeated scans of the same sample solution at different concentrations. The very good relative standard deviation of

these measurements (RSD %) obtained for three different concentrations and for three different electrodes is reported in Table 6.4.

The intermediate (run-to-run or extra-day) repeatability is demonstrated by evaluating the precision in different days for one month. Trueness is evaluated by spiking and recovery. We follow the analyte addition methodology, where the pseudo-unknown sample at three different values of concentration (the 2nd, the 5th and the 8th of the calibration plot), is spiked in the solution after consecutive additions of a standard. The % apparent recovery factors (ARF %) are calculated as the percentage relative error between the measured and the true values. The results are excellent, very close to 100 % in all cases.

Do Common Interferents Affect Our Device's Performance? (No, They Don't)

Ascorbic and uric acids are reported to be the major interferents during neurotransmitters detection, because they usually react at the same potential of the analytes. Moreover, they are present in biological fluids in concentrations 100-1000 times higher than those of neurotransmitters, causing a critical matrix effect which is often very difficult to properly manage [7,14]. Furthermore, especially in the case of ascorbic acid, its oxidation products can increase fouling problems by irreversible adsorption.

However, using our approach, we are able to perform the electroanalytical detection of the three neurotransmitters even in the presence of high quantities of ascorbic and uric acids (0.1 mM for both). Calibration plots with good linearity are obtained for both the Device and the Control (Figure 6.4 and Table 6.5). That means very low to absent interferents' effect. One possible explanation for this behavior could be found by considering that in our working conditions (pH 7.4) the external titania layer is negatively charged [34] and can

thus act as a repelling barrier for negatively charged interferents (ascorbic acid $pK_{a1} = 4.10$; uric acid $pK_{a1} = 5.4$ [35]). On the other hand, for such pH value catecholamine analytes are positively charged (due to protonation of primary amine groups) (dopamine $pK_{a1} = 8.87$; norepinephrine $pK_{a1} = 8.58$; serotonin $pK_{a1} = 10.73$) and are therefore electrostatically attracted by the negatively-charged titania.

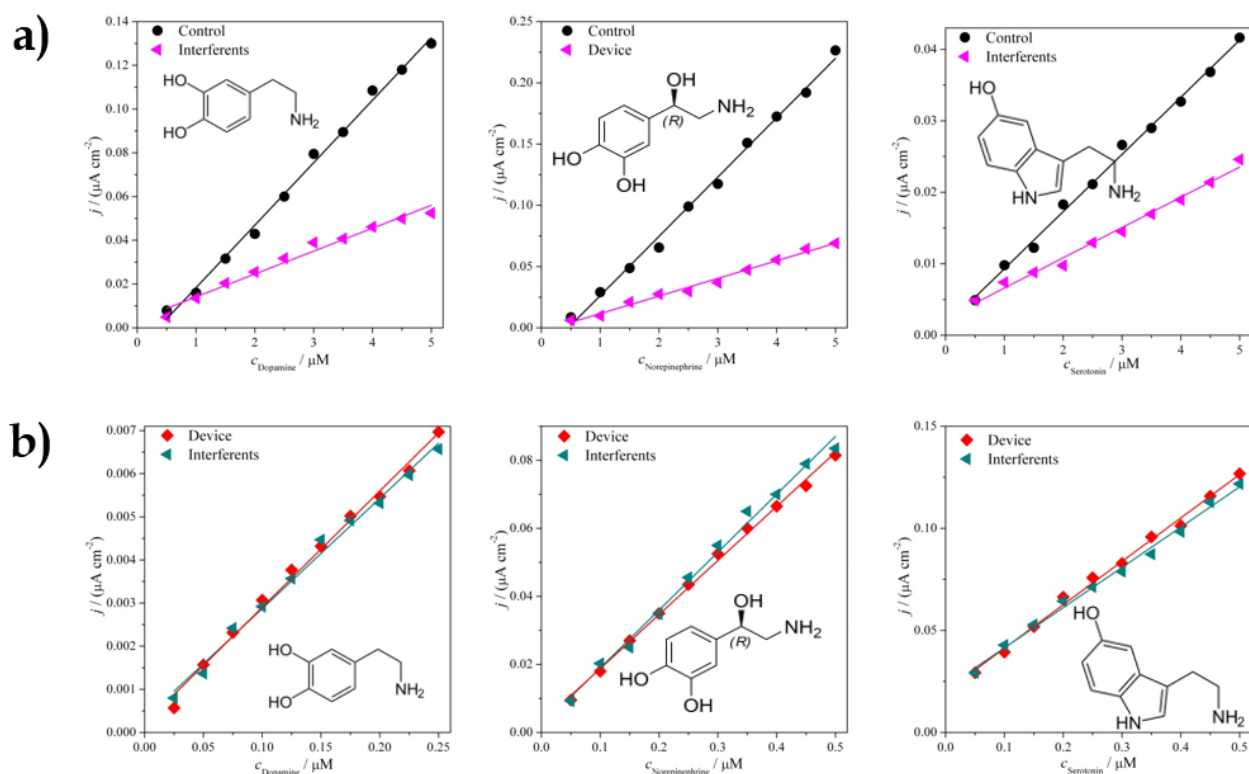


Figure 6.4 Calibration plots obtained for a) the Control and b) the Device showing the performances of both sensors for the detection of the three neurotransmitters in absence and in presence of interferents (ascorbic and uric acid).

Table 6.5 Sensitivities calculated from the slope of the calibration plots showing the performances of Control and Device for the detection of the three neurotransmitters in absence and in presence of interferents (AA = ascorbic acid, UA = uric acid).

<i>S</i> ($\mu\text{A cm}^{-2}\mu\text{M}^{-1}$)	<i>Dopamine</i>		<i>Norepinephrine</i>		<i>Serotonin</i>	
	Alone	AA+UA	Alone	AA+UA	Alone	AA+UA
Control	0.0286	0.010	0.048	0.014	0.008	0.004
Device	0.0256	0.026	0.159	0.170	0.213	0.197

For the AgNPs-containing Device, not only the sensitivities are better (Table 6.5) and the analytical working range lower (Figure 6.4), compared to the Control, also interferents do not affect the measurements at all and the sensitivities are completely maintained (Figure 6.4), thus demonstrating once more the key role of convergent diffusion on AgNPs.

Towards Real-World Applications: Electroanalysis of Catecholamines in Liquor and Serum Mimics

In order to test the efficiency of the sensor in real matrixes the detection in two biological fluids was investigated: artificially reproduced cerebrospinal fluid (liquor) [36-38] and serum [39-41], both presenting high concentrations of interfering inorganic and organic substances.

Artificial liquor and serum were prepared according to established protocols [36-41] (see paragraph 6.4, "Specific procedures", for details). For obvious reasons, the use of a supporting electrolyte was not necessary to perform electrochemical measurements on these kind of matrixes.

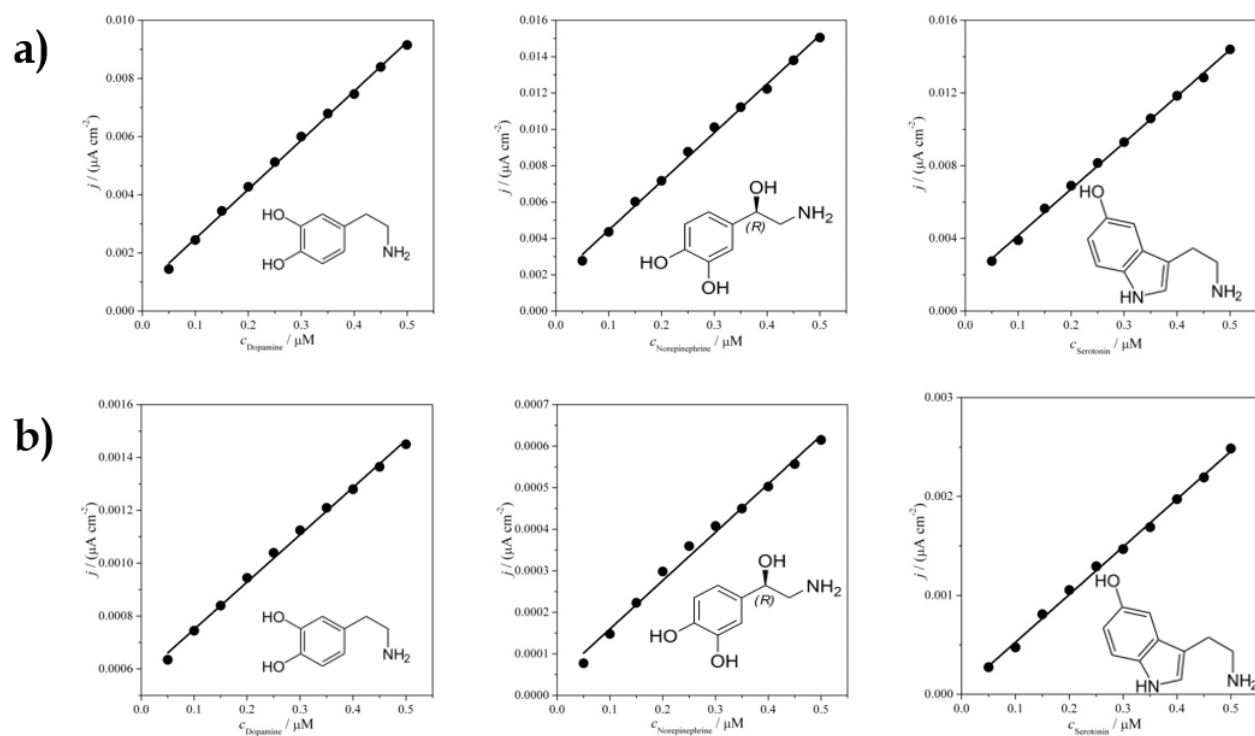


Figure 6.5 Calibration plots obtained for the detection of the three investigated neurotransmitters in biological fluids mimics: a) liquor, b) serum.

Figure 6.5 show the calibration plots obtained for the three neurotransmitters detected in liquor and serum. Detection (Table 6.6) is characterized by good linearity ranges and good sensitivities (albeit lower, particularly for serum, with respect to the analysis performed in phosphate buffer). However, the limits of detection remain low, well below the requirements of the clinical application ($0.1 \mu\text{M}$).

Table 6.6 Analytical parameters obtained for the detection of neurotransmitters in liquor and serum mimics.

	Liquor		
	<i>Dopamine</i>	<i>Norepinephrine</i>	<i>Serotonin</i>
S ($\mu\text{A cm}^{-2}\mu\text{M}^{-1}$)	0.0169	0.0268	0.0255
LoD (μM)	0.02	0.03	0.02
	Serum		
	<i>Dopamine</i>	<i>Norepinephrine</i>	<i>Serotonin</i>
S ($\mu\text{A cm}^{-2}\mu\text{M}^{-1}$)	0.00179	0.00116	0.00483
LoD (μM)	0.09	0.05	0.03

Towards Real-World Applications: The Urine Case

Among all the possible matrixes where catecholamines can be found, human urine represents one of the most challenging [7,14]. In such matrix, only dopamine and norepinephrine can be found and their determination is usually complicated due to the difficulty of conventional electrodes to discriminate between the two neurotransmitters and due to strong fouling issues. Our Device, however, can easily solve this challenge. In this first attempt towards the contemporaneous determination of dopamine and norepinephrine, the two molecules are studied at concentrations in accordance with the levels normally detected in the urine biological matrix.

The analysis is performed by the standard addition technique exploiting dopamine and norepinephrine different peak potentials, which allow their discrimination.

Dopamine, in the presence of not-interfering norepinephrine, was revealed at +0.15 V, (Figure 6.6a). At a higher potential value of +0.3 V both molecules were detected (Figure 6.6b) and the quantity of norepinephrine was calculated from the difference of the two values. As reported in Table 6.7, apparent recovery factors (ARF %) for the two molecules are really good, showing the trueness of the method for their contemporaneous determination.

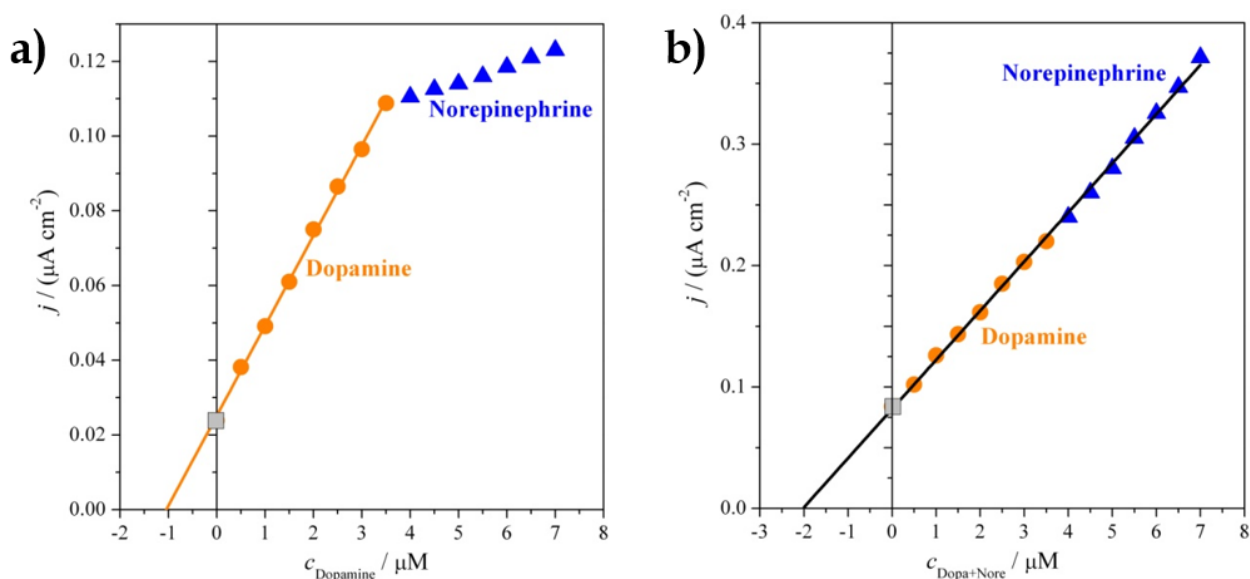


Figure 6.6 Standard additions of dopamine and norepinephrine in a matrix spiked with 1.00 μM of both neurotransmitters. Determination of dopamine at a) 0.15 V and of the mix of dopamine and norepinephrine at b) 0.3 V.

Table 6.7 Apparent Recovery Factors (ARF %) calculated for the contemporaneous detection of dopamine and norepinephrine.

	Added (μM)	Found (μM)	ARF %
Dopamine	1.00	1.04	104
Norepinephrine	1.00	0.98	98

6.3 Conclusions

Neurotransmitters detection in body fluids is described as a tough challenge in clinical analysis. Electrochemical sensors have been proposed to make their analysis cheaper and faster, but obstacles in terms of selectivity, interferences and fouling issues have always clipped their wings. Here, a new electroanalytical method is described for the determination of dopamine, norepinephrine and serotonin based on a multilayered sensor, designed *ad hoc* for this application. Sparsely arranged silver nanoparticles, allowing the instauration of a convergent diffusion regime, are literally at the core of our electrode where they play a key role in the recognition process. Such particles were covered by a photoactive titania layer, which allowed the fast regeneration of electrode surface simply by UV irradiation. Thanks to this special configuration, the detection limits were found to be much lower ($0.03 \mu\text{M}$) compared to those typically required in clinical settings for routine analysis, also in the presence of high concentrations of interferent compounds (ascorbic and uric acid). In biological matrixes, such as liquor and serum, the situation is worsened by the presence of many charged compounds and proteins, which cause interference by reaction at the electrode and passivation of the active surface. However, TiO_2 demonstrated its key role also to address this challenges, by electrostatically repelling negatively charged interferents and facilitating the detection of analytes with high selectivity. Moreover, its self-cleaning ability is crucial to overcome the fouling phenomenon due to byproducts, collateral reactions of interferents and passivation of the sensor. Simply by irradiation with UV light, the electrode surface is completely regenerated and can be reused for many further analysis. The outstanding properties of our system, for the first time found in a single Device, and its

efficiency towards the detection of neurotransmitters disclose the disruptive effects that this kind of electrodes would generate for the future of medical diagnosis.

6.4 Specific procedures

Materials: Dopamine, norepinephrine and serotonin hydrochlorides are purchased from Sigma-Aldrich. Ascorbic and uric acids (Sigma-Aldrich) are used as interferents. Sodium chloride, sodium bicarbonate, sodium sulphate, potassium chloride, potassium phosphate dibasic trihydrate, magnesium chloride hexahydrate, calcium chloride, hydrochloric acid, tris(hydroxymethyl)aminomethane, glucose, disodium phosphate and monosodium phosphate are used to prepare the artificial liquor and serum (Table 6.8).

Table 6.8 Composition of liquor and serum mimics.

Compounds	Liquor	Serum
NaCl	128 mM	137 mM
KCl	3 mM	3 mM
MgCl ₂	1 mM	1.5 mM
CaCl ₂	1.3 mM	2.6 mM
Na ₂ HPO ₄	21 mM	-
NaH ₂ PO ₄	1.3 mM	-
K ₂ HPO ₄	-	0.7 mM
NaHCO ₃	-	4.2 mM
Na ₂ SO ₄	-	0.5 mM
TRIS	-	50 mM
Glucose	0.61 g L ⁻¹	-
HCl	-	1 M
Bovine Serum Albumin	-	50 g L ⁻¹

Bovine serum albumin (Sigma-Aldrich) is employed as a mimic of serum proteins. All chemicals are of reagent grade purity and used as received. Distilled water purified with a

Millipore Milli-Q apparatus (resistivity $\geq 18.2 \text{ M}\Omega \text{ cm}^{-1}$) is used to prepare solutions and sols. The preparation of our electrochemical Device is described in detail in Chapter 5.

Methods: The detection of neurotransmitters is performed in a three electrodes cell, using a saturated calomel, a Pt wire and the device as reference, counter and working electrodes, respectively. Phosphate buffer (pH 7.4, 0.1 M) is used as supporting electrolyte for the optimization of the analytical method.

Cyclic voltammetry (CV), electrochemical impedance spectroscopy (EIS), pulsed and linear voltammetry and chrono- methods are carried out with an Autolab PGStat30 (Ecochemie, The Netherlands) potentiostat/galvanostat equipped with FRA module and controlled by GPES and FRA softwares. Impedance data are processed with Z-View 3.1 software. No N_2 degassing of the solution is necessary, since dissolved O_2 does not affect the measurements. All the linear and pulsed voltammetries and the chronoamperometry are performed with the parameters reported in the Results and Discussion paragraph.

Electrochemical impedance spectra are registered at -0.1 , $+0.1$ and $+0.25 \text{ V (SCE)}$, with a range of frequencies between 65000 and 0.1 Hz and an amplitude of 10 mV.

Self-cleaning experiments: Fouling of the electrode is verified by registering voltammograms in the electrolyte solution, detecting the presence of the neurotransmitter peak and the decrease/disappearance of silver peak. The regeneration of the electrode surface is performed by irradiation for 1 h under UV light. An UV iron halogenide lamp Jelosil HG500 with an effective power density, measured using a Thorlabs S314C radiometer, of $23 \text{ (mW cm}^{-2}\text{)}$ emitting between 280 and 400 nm is used for the electrode self-cleaning procedure. After irradiation, success of the cleaning procedure is confirmed by registering a new voltammogram in the electrolyte solution and verifying the absence of neurotransmitter peak along with the restoration of the AgNPs' peak.

6.5 References

- [1] D. L. Robinson, A. Hermans, A. T. Seipel and R. M. Wightman, *Chem. Rev.*, **2008**, *108*, 2554–2584.
- [2] B. J. Venton and R. M. Wightman, *Anal. Chem.*, **2003**, *75*, 414–421.
- [3] J. Meiser, D. Weindl and K. Hiller, *Cell Commun. Signal.*, **2013**, *11*, 34.
- [4] J. Segura-Aguilar, I. Paris, P. Muñoz, E. Ferrari, L. Zecca and F. a. Zucca, *J. Neurochem.*, **2014**, *129*, 898–915.
- [5] A. Curulli, *Sensors*, **2009**, *9*, 2437–2445.
- [6] G. E. Karel Pacak, Jacques W. M. Lenders, *Pheochromocytoma. Diagnosis, Localization, and Treatment*, 2007.
- [7] M. Perry, Q. Li and R. T. Kennedy, *Anal. Chim. Acta*, **2009**, *653*, 1–22.
- [8] R. F. Lane and a T. Hubbard, *Anal. Chem.*, **1976**, *48*, 1287–1292.
- [9] M. C. Henstridge, E. J. F. Dickinson, M. Aslanoglu, C. Batchelor-McAuley and R. G. Compton, *Sensors Actuators B Chem.*, **2010**, *145*, 417–427.
- [10] M. Rice, B. Moghaddam, C. R. Creveling and K. L. Kirk, *Anal. Chem.*, **1987**, *59*, 1534–1538.
- [11] B. V Sarada, T. N. Rao, D. A. Tryk and A. Fujishima, *Anal. Chem.*, **2000**, *72*, 1632–1638.
- [12] P. S. Ganesh and B. E. K. Swamy, *J. Electroanal. Chem.*, **2015**, *752*, 17–24.
- [13] B. J. Sanghavi, O. S. Wolfbeis, T. Hirsch and N. S. Swami, *Microchim. Acta*, **2015**, *182*, 1–41.
- [14] K. Jackowska and P. Krysinski, *Anal. Bioanal. Chem.*, **2013**, *405*, 3753–71.
- [15] J. Olsson, F. Winqvist and I. Lundström, *Sensors Actuators, B Chem.*, **2006**, *118*, 461–465.
- [16] A. Özcan and Y. Şahin, *Electroanalysis*, **2009**, *21*, 2363–2370.
- [17] G. Soliveri, V. Pifferi, G. Panzarasa, S. Ardizzone, G. Cappelletti, D. Meroni, K. Sparnacci and L. Falciola, *Analyst*, **2015**, *140*, 1486–1494.
- [18] X. Wang, R. Xiong and G. Wei, *Surf. Coatings Technol.*, **2010**, *204*, 2187–2192.

- [19] G. Maino, D. Meroni, V. Pifferi, L. Falciola, G. Soliveri, G. Cappelletti and S. Ardizzone, *J. Nanoparticle Res.*, **2013**, *15*, 2087.
- [20] A. Antonello, G. Soliveri, D. Meroni, G. Cappelletti and S. Ardizzone, *Catal. Today*, **2014**, *230*, 35–40.
- [21] G. Panzarasa, *J. Chem. Educ.*, **2014**, *91*, 696–700.
- [22] V. Pifferi, G. Facchinetti, A. Villa, L. Prati and L. Falciola, *Catal. Today*, **2015**, *249*, 265–269.
- [23] L. Falciola, A. Gennaro, A. A. Isse, P. R. Mussini and M. Rossi, *J. Electroanal. Chem.*, **2006**, *593*, 47–56.
- [24] C. Bellomunno, D. Bonanomi, L. Falciola, M. Longhi, P. R. Mussini, L. M. Doubova and G. Di Silvestro, *Electrochim. Acta*, **2005**, *50*, 2331–2341.
- [25] V. Pifferi, V. Marona, M. Longhi and L. Falciola, *Electrochim. Acta*, **2013**, *109*, 447–453.
- [26] C. M. Welch and R. G. Compton, *Anal. Bioanal. Chem.*, **2006**, *384*, 601–19.
- [27] F. W. Campbell and R. G. Compton, *Anal. Bioanal. Chem.*, **2010**, *396*, 241–59.
- [28] G. Herzog and V. Beni, *Anal. Chim. Acta*, **2013**, *769*, 10–21.
- [29] A. O. Simm, S. Ward-Jones, C. E. Banks and R. G. Compton, *Anal. Sci.*, **2005**, *21*, 667–671.
- [30] S. Daniele, M. Baldo and C. Bragato, *Curr. Anal. Chem.*, **2008**, *4*, 215–228.
- [31] L. A. Currie, *Pure Appl. Chem.*, **1995**, *67*, 1699–1723.
- [32] M. Thompson, S. L. R. Ellison and R. Wood, *Pure Appl. Chem.*, **2002**, *74*, 835–855.
- [33] T. Yin, W. Wei and J. Zeng, *Anal. Bioanal. Chem.*, **2006**, *386*, 2087–94.
- [34] G. Hanly, D. Fornasiero, J. Ralston and R. Sedev, *J. Phys. Chem. C*, **2011**, *115*, 14914–14921.
- [35] D. S. Koktysh, X. Liang, B.-G. Yun, I. Pastoriza-Santos, R. L. Matts, M. Giersig, C. Serra-Rodríguez, L. M. Liz-Marzán and N. A. Kotov, *Adv. Funct. Mater.*, **2002**, *12*, 255.
- [36] E. C. McNay and R. S. Sherwin, *J. Neurosci. Methods*, **2004**, *132*, 35–43.
- [37] R. Shiobara, T. Ohira, K. Doi, M. Nishimura and T. Kawase, *J. Neurol. Neurophysiol.*, **2013**, *04(05)*, 173.

- [38] Z. Wang, J. Wu, S. Wu and A. Bao, *Anal. Chim. Acta*, **2013**, 774, 1-10.
- [39] L. Fang, Y. Lv, X. Sheng and S. Yao, *J. Chromatogr. Sci.*, **2012**, 50, 450-456.
- [40] M. Meintjes, S. J. Chantilis, D. C. Ward, J. D. Douglas, A. J. Rodriguez, A. R. Guerami, D. M. Bookout, B. D. Barnett and J. D. Madden, *Hum. Reprod.*, **2009**, 24, 782-789.
- [41] C. Rauch, E. Feifel, E.-M. Amann, H. P. Spötl, H. Schennach, W. Pfaller and G. Gstraunthaler, *ALTEX*, **2011**, 28, 305-16.

Chapter 7

Self-Cleaning Electrochemical Sensors, *Part II: A Proof-of-Concept for On-Field Applications*

ABSTRACT

We demonstrate now the potential for on-site applications of our self-cleaning electrode, which structure and performances have been presented in Chapter 5 and Chapter 6. Dopamine is used both as an analyte and as a fouling agent. The cleaning rates achieved with three UV lamps with different power and emission features (a powerful lamp for photocatalysis, a TLC lamp and a commercial LED torch) are compared. Moreover, our results indicate that total recovery of the electroanalytical performances can be achieved by perform UV irradiation directly in the solution of interest, thus opening the path for on-site, on-line applications.

7.1 Introduction

The demand of more selective and accurate analytical sensors is growing from different fields, ranging from environmental control and food quality to medical diagnostics. As a result, nanotechnology has rapidly gained popularity in the sensoristics field, an interest that is spreading in almost all classes of sensing platforms (optical, electrical, spectroscopic, electrochemical, etc.) because of the tremendous performance boost enabled by the use of nanostructures [1-3]. Nanostructured devices allow a more precise control of the sensing process, increase sensitivity and lower detection limits. These requirements reach the climax for trace electroanalysis [4,5], where, thanks to the ease of the methodological procedures, standardization of protocols, availability of the needed instrumentations and competitive cost per analysis, remarkable market areas are shaping. However, nowadays the development of electroanalytical devices is impaired by fouling and passivation issues that affect sensing surfaces causing irreproducible measurements and premature device failure [1,4,6,7]. These phenomena, which have been introduced already in Chapter 5 and 6, are originating from the surface adsorption of analytes, interferences present in the analyzed matrix and of their electrochemical by-products. This causes a decrease in sensitivity, which eventually leads to complete loss of the analytical signal and to the irreversible deactivation of the sensing apparatus, with the consequent need to clean or replace it. Conventional electrode cleaning procedures, based on harsh mechanical and/or electrochemical procedures, are too invasive for highly engineered nanostructured sensors and can cause irreversible physico-chemical device modifications. Moreover, not only they require the removal of sensor from the cell, but are also tedious and time consuming.

In this context, developing a tailored device with a simple reactivation ability or, better, a strategy by which it could be possible to confer such properties to a generic sensing surface, represents a big challenge for the scientific and metrological community. Notwithstanding its high relevance, however, only few attempts are described in the Literature dealing with such a big issue [8-10], starting from the pioneering work of McCreery in which passivating films of oxide layers, formed on glassy carbon and platinum electrodes, were removed by laser pulses [7,11]. However, to the authors' best knowledge, no Literature data are available regarding the general applicability and robustness required for an eventual applicative, market impact. Those could permit the development of an integrated system *e.g.* for on-field monitoring. In Chapter 5 and Chapter 6, we reported the use of a titanium dioxide thin and mechanically robust layer as an efficient strategy to confer self-cleaning properties to a sensor surface. We demonstrated that the photocatalytic properties of anatase titanium dioxide on the electrode surface can give rise to the self-cleaning of the interface simply by UV irradiation without affecting the morphological structure and the chemical nature of the multilayered sensor [12,13]. As a proof of concept, we tested such a device for the quantitative determination of catecholamine neurotransmitters, highly relevant bio-medical analytes also well known to cause heavy electrode fouling issues [14-17]. An expert in this field, Prof. C.M.A. Brett, congratulated us in a note recently appeared on *Chemistry World* for our innovative results [18], but underlined the need to adopt shorter reactivation times and, preferably, low-power UV sources. On the ground of Prof. Brett's suggestion and of the extremely promising results observed in fouling environments, we started a more specific investigation. First, we optimized the self-cleaning conditions of our Device in terms of time of treatment, power and wavelength of the UV light. Second, we studied the possibility of on-site reactivation *i.e.* directly in solution. Moreover, the above-mentioned

Device is developed with the final aim to be used by scientists with different backgrounds, not only in academic research labs, but also in clinical and industrial laboratories. That requires the implementation of a methodology, which uses safer and more commonly available UV lamps. In our previous work, we obtained the self-cleaning effect by irradiating the device with a UV lamp, *ad hoc* developed for photocatalytic studies. However, such a lamp is not commonly available in analytical labs and presents significant UV exposure hazard. For this reason, we now consider less powerful UV sources, namely: a conventional lamp for the visualization of TLC plates and a UV LED-torch, commercially available online at an average price of 30 \$, with the final aim to make such technology portable, simple and user-friendly.

7.2 Results and Discussion

Our self-cleaning Device can be conveniently used as the working electrode (WE) in an electrochemical cell, along with a calomel reference electrode (RE) and a platinum wire as the counter electrode (CE) (Figure 7.1). Its excellent performances for the detection of dopamine and other catecholamine neurotransmitters, even in the presence of strong interferences, has been demonstrated in Chapter 6. Here, we will quickly review the self-cleaning properties of our Device in order to better introduce the topic of the present Chapter *i.e.* to investigate potential on-site applications for our Device.

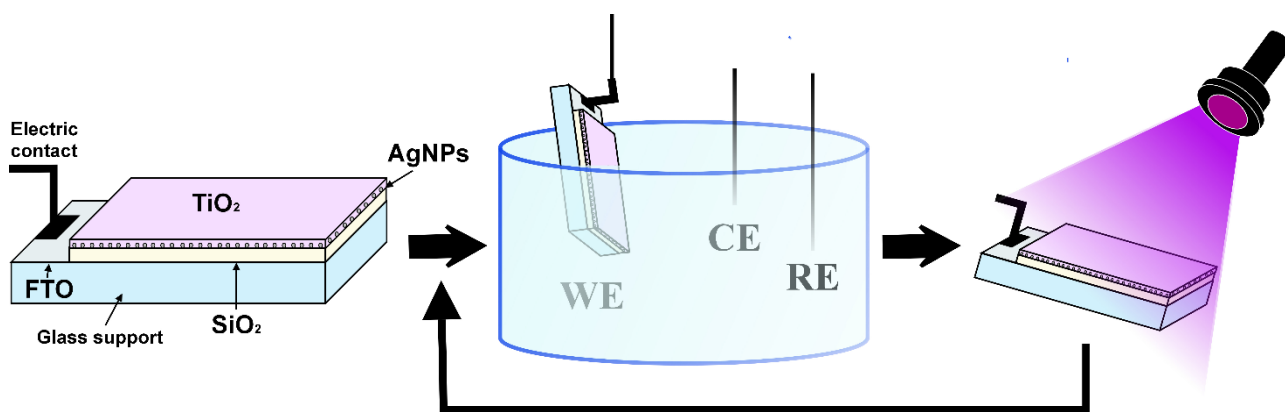


Figure 7.1 Schematic representation of our Device, its use in an electrochemical cell and its cleaning under UV light.

We already described how the fouling problem associated with irreversible adsorption of analytes, interferents and of their electrochemical by-products on the electrode surface is solved for our Device by irradiating its surface with near-UV light after having performed the analysis. During the irradiation process, the active anatase surface photo-catalytically promotes the formation of electron-hole pairs that in turn react with atmospheric O₂ and H₂O molecules [25-27]. The subsequent formation of reactive oxygen species (ROS) leads to efficient degradation of fouling molecules, making the Device reusable hundreds of times. As shown by the UV-vis transmittance spectrum of our Device (Figure 7.2), we expect the titania surface to be active also in the near-UV region (> 300 nm).

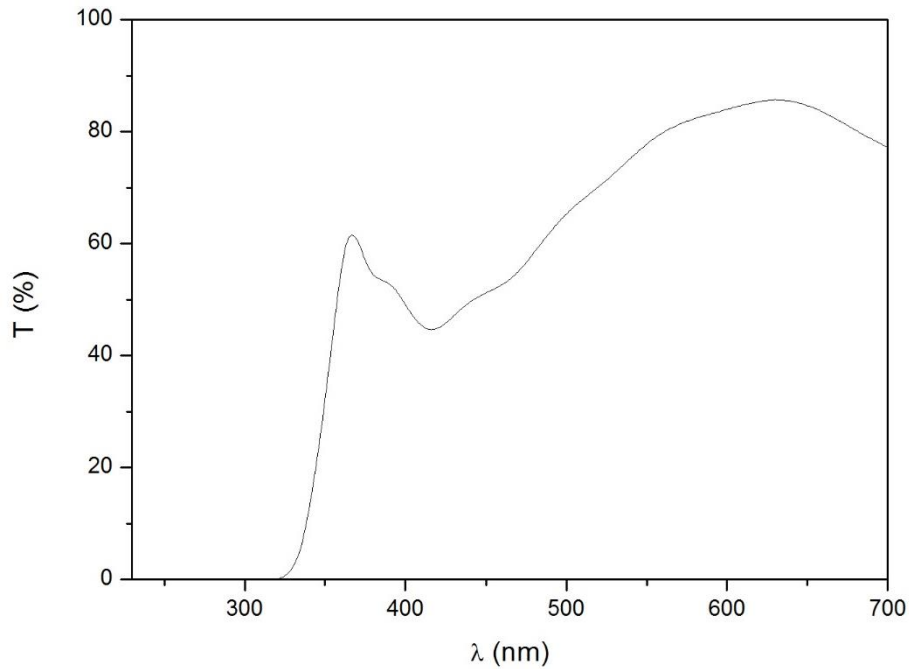


Figure 7.2 UV-Vis transmittance spectrum of our Device.

Shining light on the self-cleaning process

In Figure 7.3, the emission spectra and the effective power density are reported for the three adopted lamps. “UV-LAMP” is a powerful (45 mW cm^{-2}) iron-halogenide lamp originally developed for photocatalysis studies: it shows one major emission peak in the UV region at 360 nm and two further peaks in the visible region (400 and 440 nm). “TLC LAMP” is a conventional mercury lamp used for the development of spots in thin layer chromatography (TLC), which emits mostly at 310 and 360 nm with a 1.7 mW cm^{-2}). “TORCH” is a commercially available LED torch with a quite sharp emission at 380 nm (14 mW cm^{-2}), without any specific safety requirements.

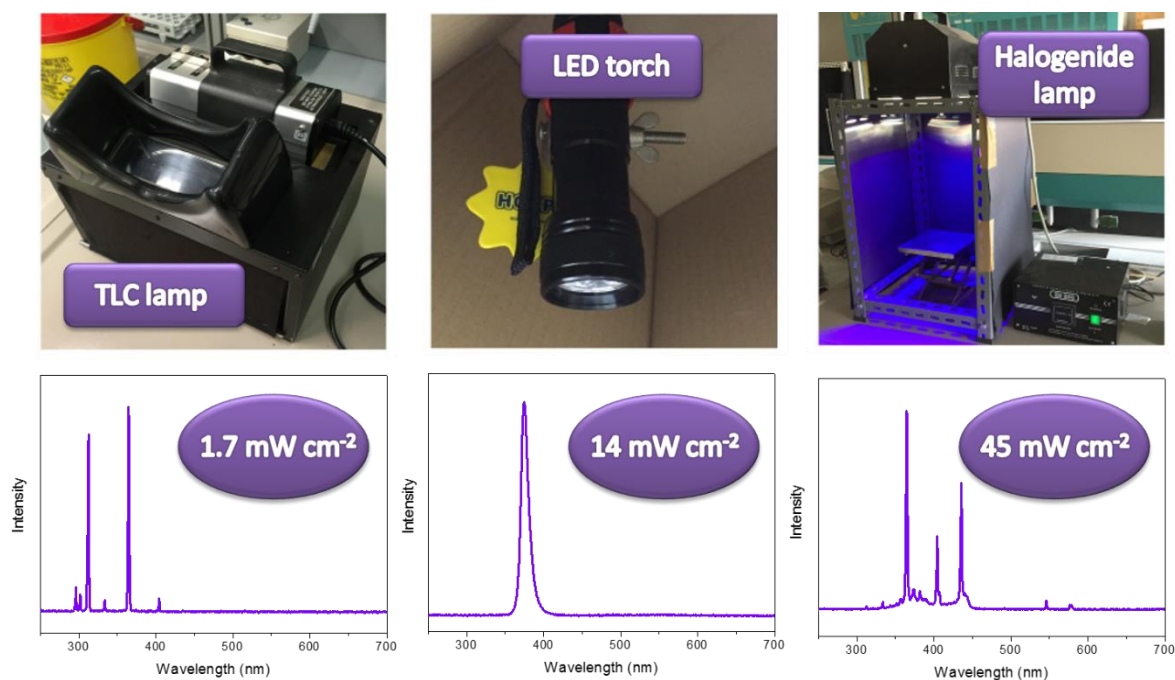


Figure 7.3 Photographs, emission spectra and effective power density of the lamps employed for self-cleaning experiments.

The self-cleaning efficiency of the sensor with respect to irradiation conditions (time and lamp power) is investigated by an *ad hoc* fouling/cleaning procedure based on three steps: (1) background acquisition, (2) fouling (mechanism proposed in Figure 7.4, according to the Literature [28,29]) and (3) cleaning. Dopamine (1 mM, in 0.1 M phosphate buffer solution at pH = 7.4) is used as fouling agent and probe. Differential Pulse Voltammetry (DPV, range -0.1 V/+0.4 V (SCE), modulation time 0.05 s, interval time 0.5 s, step potential 0.005 V, modulation amplitude 0.05 V) is chosen as the electroanalytical technique.

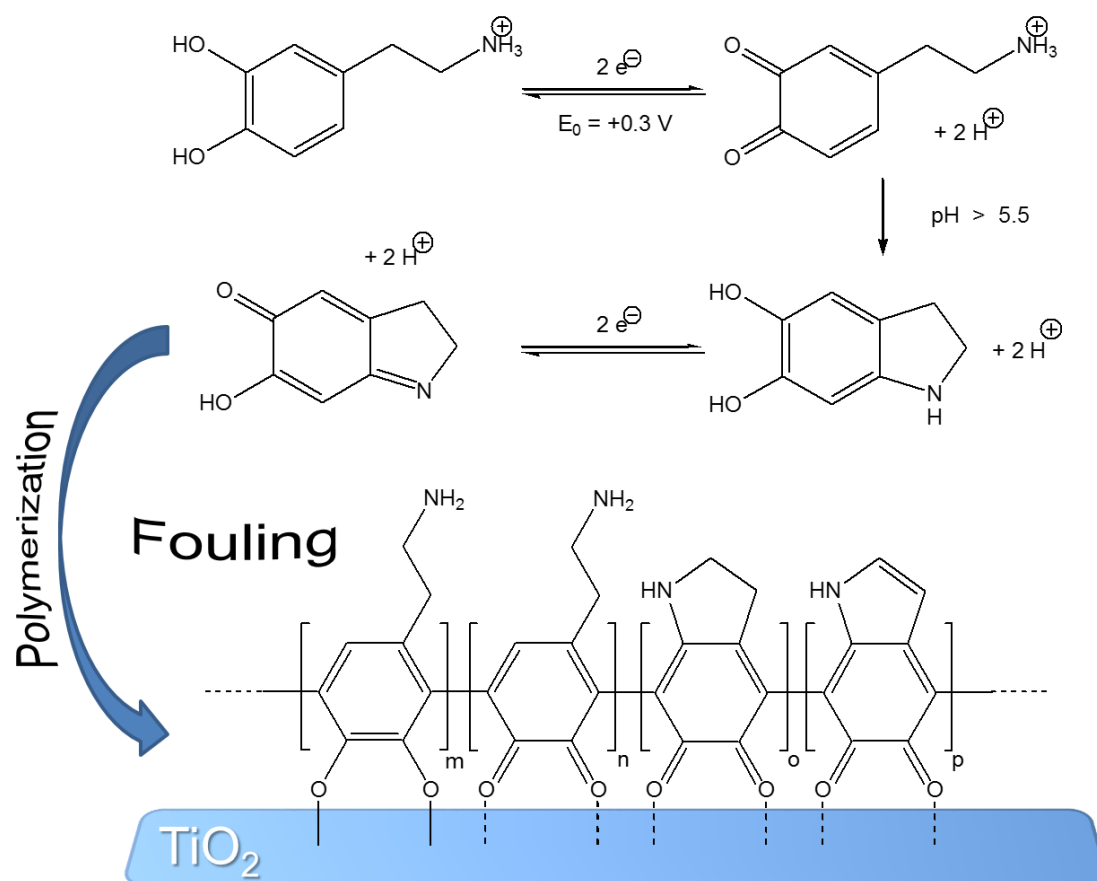


Figure 7.4 Schematic representation of commonly accepted mechanism for dopamine electroanalytical reaction leading to fouling.

For the background acquisition (Figure 7.5, curve 1), the electrode is dipped in the phosphate buffer solution (in the absence of dopamine). Only the oxidation peak of silver nanoparticles at $+0.165 \text{ V}$ (SCE) can be detected, indicating that the surface is clean and electroactive. This peak is strongly affected by dopamine fouling. The fouling effect manifests in all its deactivating efficiency starting from very low dopamine concentrations (below 0.03 mM , which is the LOD of our device). However, in order to promote fast deactivation and to test the potentialities of our self-cleaning device, a concentrated 1 mM solution of dopamine suits perfectly. After the addition of dopamine, voltammetric cycling

caused the electrode fouling by the adsorption of dopamine itself and of its by-products onto titania (Figure 7.4).

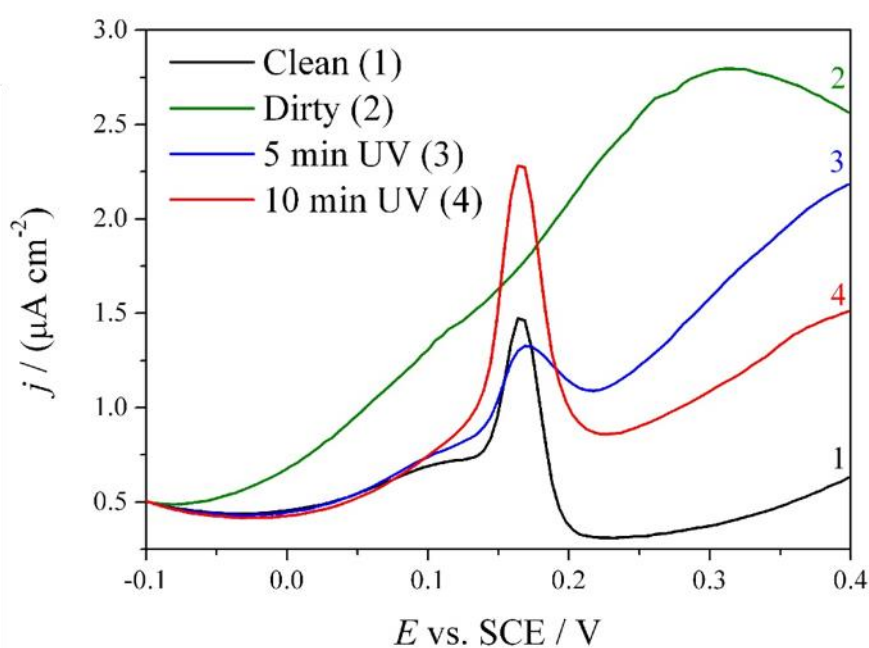


Figure 7.5 Differential pulse voltammograms acquired during the fouling/cleaning procedure. In the absence of dopamine, the AgNPs peak is clearly visible at +0.165 V (curve 1). After fouling only the dopamine signal is visible (curve 2), but the AgNPs peak is restored after UV-irradiation (curves 3-4).

The voltammogram acquired in fresh phosphate buffer (in the absence of dopamine, Figure 7.5 curve 2), after dopamine detection and subsequent chemisorption, clearly shows the disappearance of the AgNPs oxidation peak and the persistence of the dopamine shoulder at +0.3 V after washing [12]. The electrode is removed from the solution, irradiated for a chosen time and tested again in pure phosphate buffer solution (Figure 7.5, curves 3-4). As a function of irradiation time, the dopamine shoulder decreased while the silver nanoparticles peak increased, as a clear evidence of a successful cleaning process. The time of irradiation is varied from zero to 30 minutes for all the three lamps tested. A “blank” is

also acquired, where the electrode is not exposed to UV light. In order to describe the fouling and cleaning process of the electrode surface, a % Reactivation parameter is introduced and defined as:

$$\% \text{ Reactivation} = \frac{\Phi - I(t)}{\Phi - B} \times 100$$

where Φ is the value of the current measured at +0.3 V (dopamine peak) after the fouling step, $I(t)$ is the current measured at +0.3 V after irradiation for a time t and B is the current measured at +0.3 V for the background scan. According to our definition, reactivation values of 0% and 100% correspond to the completely fouled and to the perfectly clean electrode, respectively. Figure 7.6 shows the % Reactivation parameter with respect to the irradiation time obtained for the three different tested lamps and for an electrode stored in the dark for the same time (identified as “blank”). The reactivation value measured for the blank is 0% for all the tested times, demonstrating the crucial effect of UV light for electrode regeneration. Complete reactivation (100%) is obtained after at least 20 minutes of irradiation, with different rates, depending on the lamp features.

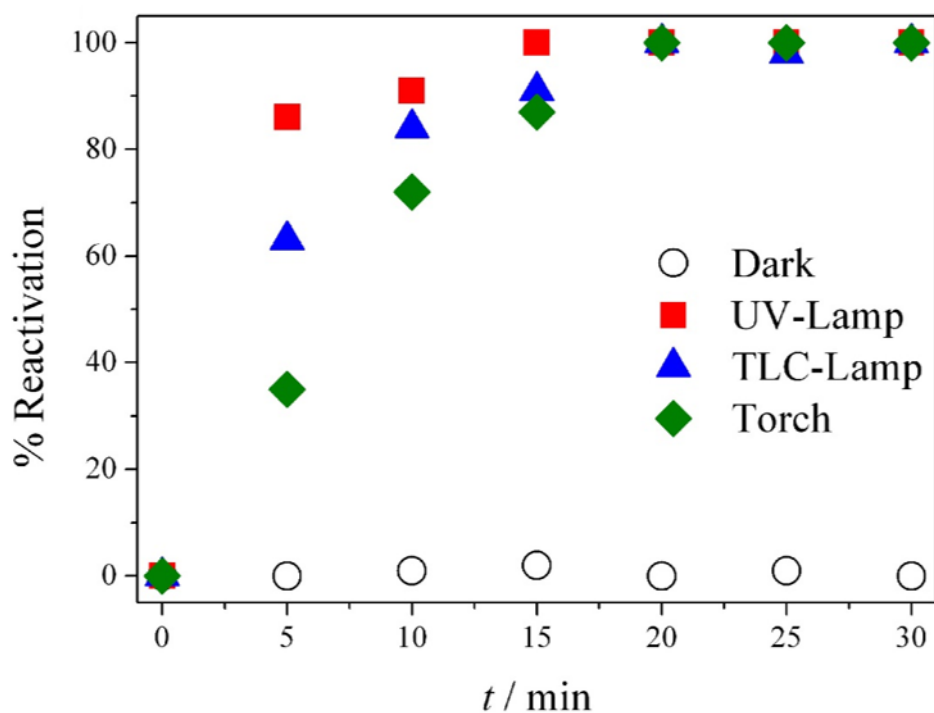


Figure 7.6 % Reactivation values obtained for irradiation with the three lamps and in the dark.

As expected, the most efficient is the UV-LAMP, which, thanks to a combination of high power and low wavelength emission (Figure 7.3) leads to faster degradation of the fouling products. With such a lamp, after only 5 minutes of irradiation, the electrode recovered more than 90% of its initial condition and recovered totally after 10 minutes. Irradiation wavelengths also seem to be a crucial variable to consider for evaluating the lamp performance. TLC-LAMP displays an emission component of 310 nm (higher energetic radiation, Figure 7.3). Notwithstanding its low irradiation power, the presence of a low-wavelength emission in the spectrum of TLC-LAMP could lead to enhanced absorption of radiation by the titania layer and consequently to an abundance of photo-catalytic events, leading to a high cleaning efficiency. However, we consider the results obtained with the UV LED TORCH as the most intriguing and valuable. TORCH emits a low energy radiation,

near to the visible edge (Figure 7.3), which makes it safer compared with the other two lamps. Nevertheless, it shows a similar cleaning kinetics compared to UV-LAMP and TLC-LAMP, allowing complete regeneration of the electrode after 20 minutes. In addition, its intrinsic portability makes it perfect for on-field, on-line applications. For this purpose, the development of a procedure that allows direct, on site, cleaning of the device without the need to remove it from the working environment is highly desirable.

Towards on-field applications

To demonstrate the feasibility of *in situ* cleaning, the Device is fouled (according to the previously reported procedure) and then immersed in the electrolyte solution. TORCH is chosen as the UV source and irradiation is performed from outside the pyrex glass reactor (Figure 7.7).

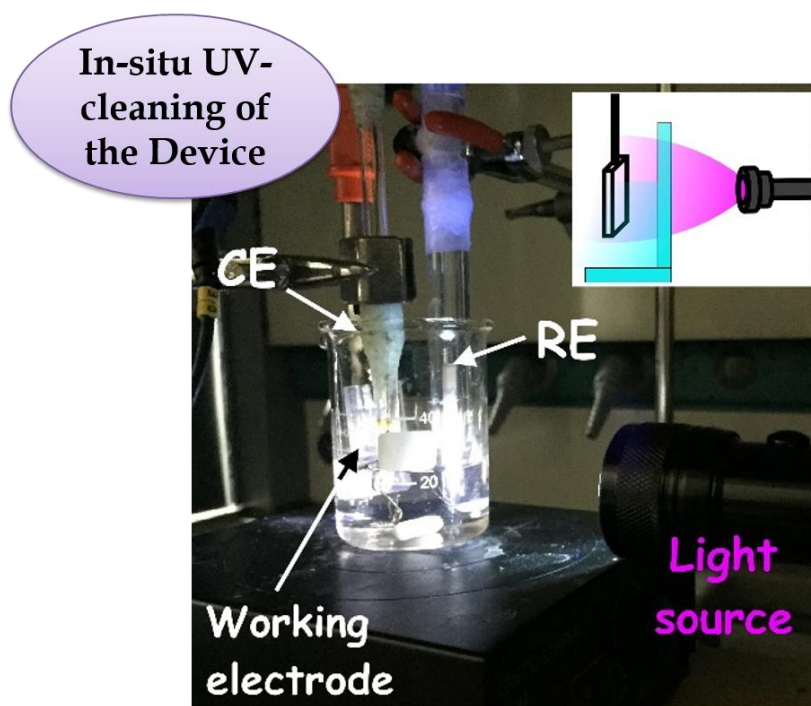


Figure 7.7 Experimental setup used to perform the on-site self-cleaning experiments.

Figure 7.8 shows the decrease of fouling at the electrode for different irradiation times. The extent of fouling is expressed as % Fouling, calculated as the ratio between the current of the tested Device and of the completely fouled electrode, measured at +0.3 V (SCE). Despite the use of the less performing lamp, the intrinsic filter effect of water and of the glass container (borosilicate glass), any fouling effect completely disappear after 30 minutes.

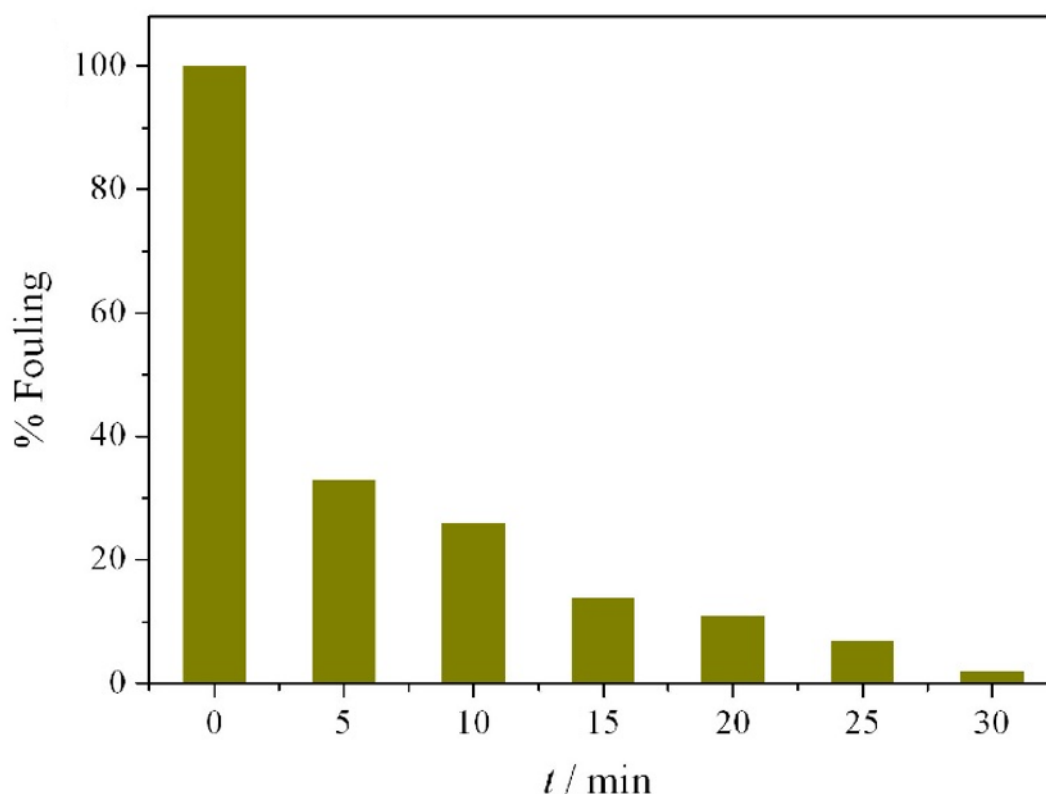


Figure 7.8 Study of fouling remediation directly in the electrolyte solution.

To demonstrate further the robustness of our Device and cleaning method towards on-site analytical applications, an on-purpose fouled electrode (soiled after dipping and CV cycling in 1 mM dopamine solution) is immersed in a freshly prepared electrolyte solution, spiked with dopamine to a final concentration of 1 mM. Sample analysis is performed as previously described, registering the apparent recoveries at fixed time (every 5 minutes) during the cleaning procedure. As expected, apparent recoveries higher than 100% are obtained (Figure

7.9) indicating heavy fouling and thus overestimation of the analyte. However, after 30 minutes of on-site irradiation the device is completely cleaned and reactivated, with apparent recovery (IUPAC [30]) values around 100%. Further cleaning does not affect the recovery values, demonstrating that only fouling compounds are degraded and no soluble by-products can be electrochemically detected, while dopamine in solution is not affected by the cleaning procedure. It is worthwhile to highlight that this is not an obvious result: the confinement of photocatalytic degradation processes to the electrode surface allows to degrade the adsorbates without altering the (very low) concentration of the analyte in solution.

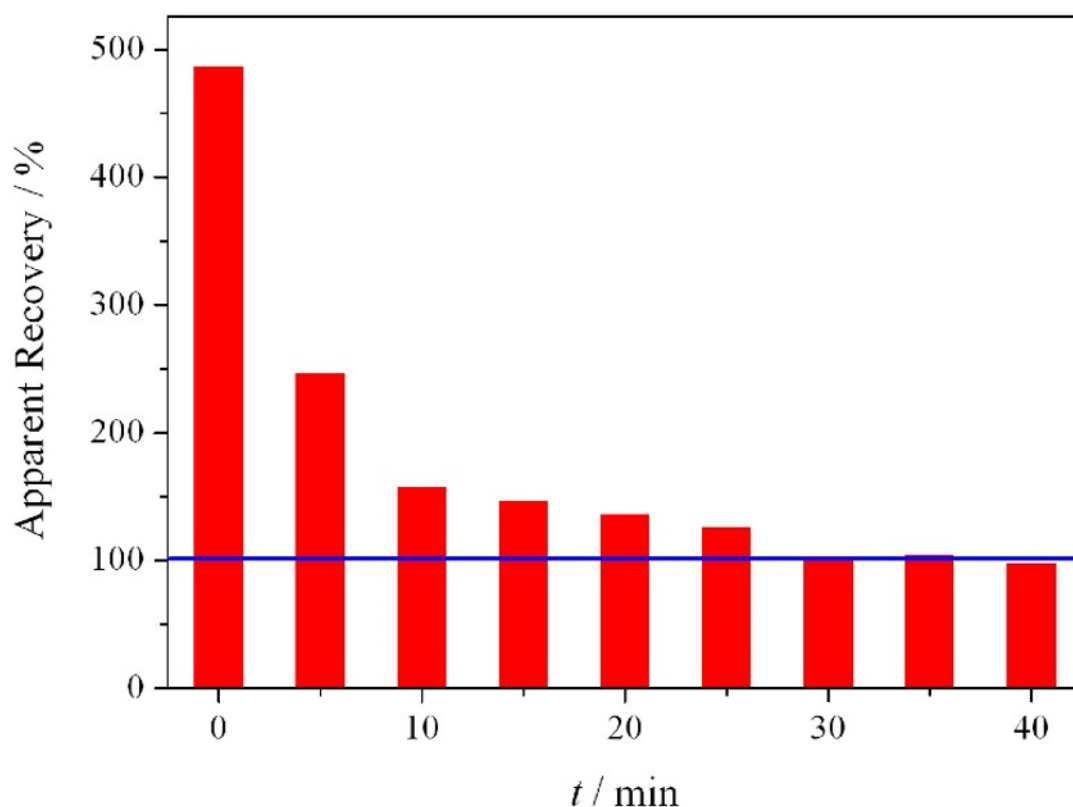


Figure 7.9 Apparent Recovery obtained for 1 μM of dopamine after performing the cleaning procedure in situ with the TORCH.

7.3 Conclusion

We successfully demonstrated that using our Device we can achieve self-cleaning even in solution in the presence of the analyte of interest. This is a fundamental result toward the development of an integrated device able to perform *in situ* measurements with remote control.

It is important to underline that in order to test our hypothesis we selected extremely hard fouling conditions: dopamine was chosen not only as a highly representative analyte, but also because it is known to be a strongly passivating molecule which irreversibly chemisorbs and polymerizes at oxide surfaces. To demonstrate the potentialities of our self-cleaning Device, we employed dopamine concentrations much higher than those found in body fluids (40 nM). Apart from the previously proved robustness, trueness and precision of the Device, here we demonstrated the possibility to use short-time cleaning steps with low energy and low power UV-LED sources. Moreover, the cleaning procedure can be performed directly on site, in the solution of interest. For all the above reasons, the authors forecast on-line/on-field applications: a small UV emitting LED incorporated in the final device, for example, could switch on and off for few minutes between two subsequent analyses. This would allow a continuous regeneration of the electrode surface, eliminating the need of any other maintenance work and eventually the use of this sensor in remote integrated monitoring systems and for flow analysis, where fast detection is crucial.

7.4 Specific procedures

Electrochemical measurements: Electrochemical measurements are performed in a standard three-electrode cell, equipped with a saturated calomel as reference electrode, a platinum wire as counter electrode and our Device as the working electrode. Differential pulse voltammograms are recorded in 0.1 M phosphate buffer (PBS, pH=7.4), using an Autolab PGStat30 (Ecochemie, The Netherlands) potentiostat/galvanostat controlled by GPES software. Parameters: potential range from -0.1 V to +0.4 V, modulation time 0.05 s, interval time 0.5 s, step potential 0.005 V, modulation amplitude 0.05 V.

Detailed fouling/cleaning procedure:

- 1) The background signal of the device dipped in the supporting electrolyte is recorded as described in the Results and Discussion paragraph.
- 2) Dopamine is added to a final concentration of 1 mM and a voltammogram is recorded to observe its oxidation at the electrode.
- 3) The electrode is immersed in a fresh solution of supporting electrolyte and a voltammogram is recorded to attest the effective fouling degree of the electrode.
- 4) The electrode is dried and placed under UV light or stored in the dark for a chosen interval of time.
- 5) A new voltammogram in supporting electrolyte is acquired to demonstrate the success of the cleaning procedure.

Characteristics of the UV lamps employed:

- UV-LAMP: UV iron halogenide lamp Jelosil HG500: effective power density 45 (mW cm⁻²) at 40 cm (sample location), emitting mostly between 350 and 450 nm.
- TLC-LAMP: Spectroline Model ENF-240C/FE: effective power density 1.7 (mW cm⁻²), emitting between 280 and 400 nm.
- UV LED TORCH: HQRP® effective power density 14 (mW cm⁻²), maximum emission at 380 nm.

The emission spectra and the effective power densities are respectively measured by a SM442 Spectrometer (Spectral Products) and a PM100A Optical Power Meter (Thorlabs).

7.5 References

- [1] C. M. A. Brett, *Pure Appl. Chem.*, **2001**, 73, 1969–1977.
- [2] L. Rassaei, M. Amiri, C. M. Cirtiu, M. Sillanpaa and F. Marken, *Trends Anal. Chem.*, **2011**, 30, 1704–1715.
- [3] X. Ma, W. Hu, C. Guo, L. Yu, L. Gao, J. Xie and C. M. Li, *Adv. Funct. Mater.*, **2014**, 24, 5897–5903.
- [4] C. M. Welch and R. G. Compton, *Anal. Bioanal. Chem.*, **2006**, 384, 601–19.
- [5] F. W. Campbell and R. G. Compton, *Anal. Bioanal. Chem.*, **2010**, 396, 241–59.
- [6] G. Hanrahan, D. G. Patil and J. Wang, *J. Environ. Monit.*, **2004**, 6, 657–64.
- [7] M. Poon and R. L. McCreery, *Anal. Chem.*, **1987**, 59, 1615–1620.
- [8] G. K. Mor, M. A. Carvalho, O. K. Varghese, M. V. Pishko and C. A. Grimes, *J. Mater. Res.*, **2011**, 19, 628–634.
- [9] Y.-Y. Song, Z. Gao, K. Lee and P. Schmuki, *Electrochem. commun.*, **2011**, 13, 1217–1220.
- [10] Y.-Y. Song, Z.-D. Gao and P. Schmuki, *Electrochem. commun.*, **2011**, 13, 290–293.
- [11] M. Poon and R. L. McCreery, *Anal. Chem.*, **1986**, 58, 2745–2750.
- [12] G. Soliveri, V. Pifferi, G. Panzarasa, S. Ardizzone, G. Cappelletti, D. Meroni, K. Sparnacci and L. Falciola, *Analyst*, **2015**, 140, 1486–1494.
- [13] A. Antonello, G. Soliveri, D. Meroni, G. Cappelletti and S. Ardizzone, *Catal. Today*, **2014**, 230, 35–40.
- [14] K. Jackowska and P. Krysinski, *Anal. Bioanal. Chem.*, **2013**, 405, 3753–71.
- [15] M. Perry, Q. Li and R. T. Kennedy, *Anal. Chim. Acta*, **2009**, 653, 1–22.
- [16] R. A. Zangmeister, T. A. Morris and M. J. Tarlov, *Langmuir*, **2013**, 29, 8619–28.
- [17] M. C. Henstridge, E. J. F. Dickinson, M. Aslanoglu, C. Batchelor-McAuley and R. G. Compton, *Sensors Actuators, B Chem.*, **2010**, 145, 417–427.
- [18] Simon Neil, Chemistry World, Royal Society of Chemistry; <http://www.rsc.org/chemistryworld/2015/01/self-cleaning-electrochemical-sensor-ultraviolet-light>

- [19] V. Pifferi, G. Facchinetti, A. Villa, L. Prati and L. Falciola, *Catal. Today*, **2015**, 249, 265–269.
- [20] V. Pifferi, V. Marona, M. Longhi and L. Falciola, *Electrochim. Acta*, **2013**, 109, 447–453.
- [21] L. Falciola, A. Gennaro, A. A. Isse, P. R. Mussini and M. Rossi, *J. Electroanal. Chem.*, **2006**, 593, 47–56.
- [22] X. Wang, R. Xiong and G. Wei, *Surf. Coatings Technol.*, **2010**, 204, 2187–2192.
- [23] G. Maino, D. Meroni, V. Pifferi, L. Falciola, G. Soliveri, G. Cappelletti and S. Ardizzone, *J. Nanoparticle Res.*, **2013**, 15, 2087.
- [24] G. Panzarasa, *J. Chem. Educ.*, **2014**, 91, 696–700.
- [25] A. Fujishima, X. Zhang and D. Tryk, *Surf. Sci. Rep.*, **2008**, 63, 515–582.
- [26] G. Panzarasa, G. Soliveri, K. Sparnacci and S. Ardizzone, *Chem. Commun.*, **2015**, 51, 7313–7316.
- [27] K. Nakata and A. Fujishima, *J. Photochem. Photobiol. C Photochem. Rev.*, **2012**, 13, 169–189.
- [28] J. Liebscher, R. Mrówczyński, H. A. Scheidt, C. Filip, N. D. Haidade, R. Turcu, A. Bende and S. Beck, *Langmuir*, **2013**, 29, 10539–10548.
- [29] W. Harreither, R. Trouillon, P. Poulin, W. Neri, A.G. Ewing, G. Safina, *Anal. Chem.*, **2013**, 85, 7447–7453.
- [30] L. A. Currie, *Anal. Chim. Acta*, **1999**, 391, 105–126.

Conclusion and Perspectives

Nihil difficile volenti

When I started my PhD, the research topic was “polymer brushes”. As I rapidly learned from a thorough study of the related state-of-the-art literature, polymer brushes are arrays of polymer chains grafted from a substrate by one end with a surface coverage sufficiently high to make them highly stretched by inter-chain repulsion. They have been – and still are – subject of intense research thanks to their peculiar properties, which make them exceptional tools for the engineering of surfaces.

It took me about a year to acquire the necessary synthetic skills to deal with such structures, then a fundamental question arose: “What kind of relevant contribution can I make in this highly exploited field? What’s left?” I am sure this question commonly arise in the mind of students and young researchers who are approaching a new field, especially when faced by an overwhelming amount of already published work.

I was stuck. However, it was then that I met Colleagues from other disciplines and my research eventually started to gain momentum.

The possibility to directly collaborate with highly motivated and skilled professionals in the fields of Physical Chemistry, Electrochemistry and Particle Physics allowed me to broaden my research spectrum, which eventually refocused on the study and development of innovative sensors.

It is worth to summarize here the most important findings of this research.

As described in **Chapter 1**, direct and remote photocatalytic lithography were applied for the first time to obtain patterned polymer brushes: in this way, micro- and even nanostructures could be obtained with very good resolution using a simple and versatile approach. Direct photocatalysis proved also to be useful to modify the shape of self-assembled silver nanoprisms, allowing the development of scaffolds for SERS analysis (**Chapter 2**).

Micropatterned brushes obtained by remote photocatalytic lithography were also used to perform some of the electrochemical studies described in **Chapter 3**. As another unprecedented result, polymer brushes were found to dramatically improve the electrochemical properties of native-oxide coated silicon wafer, which is otherwise electrochemically inert.

In **Chapter 4**, the application of Positron Annihilation Spectroscopy is described for the first time to determine the structure of nanoparticle-loaded, pH-responsive polymer brushes. These findings open up a completely new way to look at such complex systems.

Chapters 5, 6 and 7 are all devoted to describe the development and performance study of an innovative self-cleaning sensor for the electroanalysis of catecholamine neurotransmitters. Our Device, based on a combination of silver nanoparticles and titania in a multilayered structure, not only makes possible to electrochemically determine dopamine, norepinephrine and serotonin in biologically relevant conditions, it can be reused indefinitely as its performances can be completely restored simply by near-UV irradiation.

Fortunately, these excellent results came along with great personal achievements. I learned a lot, especially how to make bridges across disciplines and – more importantly, from a

practical point of view – how to deal with people who are experts of different fields. Finding a common language is of paramount importance in order to perform truly interdisciplinary work and I was able to develop efficient communicative skills that already helped me generating a network of fruitful scientific relationships.

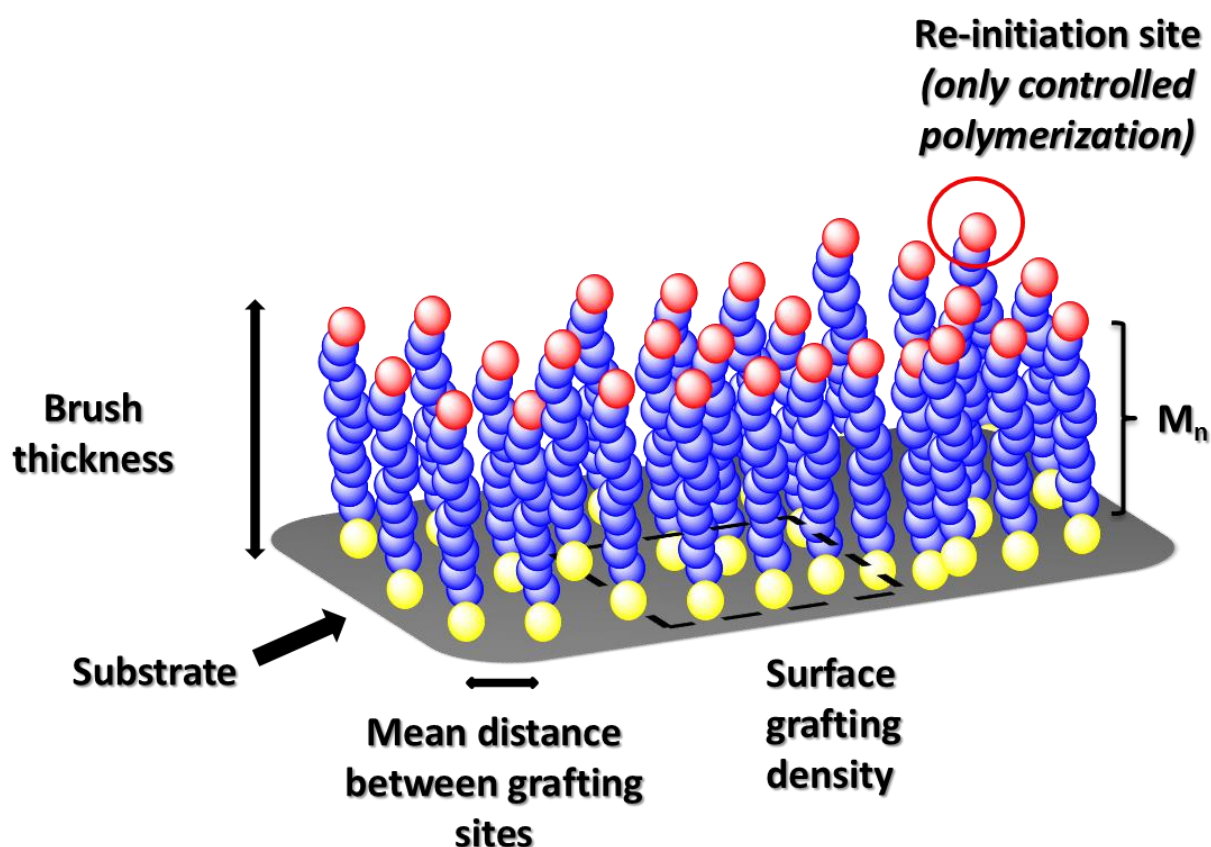
During these three years, I was able to accomplish excellent results from a professional point of view: I had the opportunity to share my results with the broadest scientific community by publishing and presenting them during international Congresses as well as during invited lectures at different Universities.

Nevertheless, what I value the most is the human side: during these three, though, years I not only met new Colleagues, I made new Friends. I gained so much in terms of personal evolution as an individual and of course as a member of society. These People not only allowed me to do meaningful work, they gave me Hope when I needed it the most.

Now the question is: “What’s next?”

Appendix A

Polymer Brushes



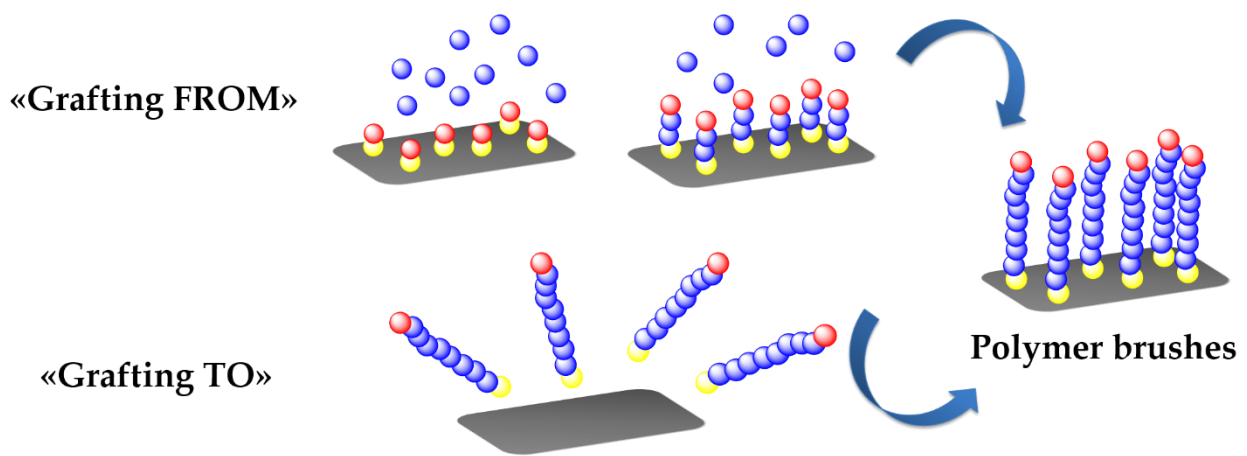
Scheme A.1 Schematic representation of polymer brushes along with some of their associated parameters. The yellow spheres represent the grafting sites, the blue spheres the monomer units and the red spheres the reinitiation sites (for brushes obtained using controlled radical polymerization techniques).

In the field of organic and polymer thin films, one may be familiar with the more common industrial techniques like spin-coating, dip-coating, doctor blade coating and roll-to-roll coating processes. At the few nm thickness regimes, the application of both self-assembly and directed-assembly methods becomes fascinating. In fact, one of the most important

aspect of the nanotechnology revolution has been to demonstrate how order could be obtained “spontaneously” by a proper use of fundamental forces. Some of the more “nanostructured” assemblies include: Langmuir-Blodgett films, self-assembled mono- and multilayers (SAMs), sequential alternate polyelectrolyte deposition (layer-by-layer, LbL) and thermal and molecular beam epitaxy methods of evaporated organic molecules. To these examples, from about 20 years it is possible to mention the method of thin films by *polymer brushes* (Scheme A.1).

The study of polymer brushes has long been almost theoretical, because of interest in investigating macromolecule phenomena in confined environments: end-tethering of polymer chains reduces the degrees of freedom for different macromolecule conformations such that it is possible to define a “stretch” conformation for a neutral polymer. With the advances in polymer synthetic methodologies, especially the introduction of controlled radical polymerization techniques (such as NMP, RAFT and ATRP) and their adaptation to surface chemistry, it has become possible for synthetic chemists to reclaim this field, which is now flourishing and is indeed very interdisciplinary [1].

From a practical point of view, polymer brushes are perfect example of stimuli-responsive coatings. Their applications ranging from sensors and actuators, responding to changes in pH, light or heat, to bioactive coatings with antimicrobial and antifouling properties. The interest in polymer brushes as smart coatings arises from the combination of the intrinsic flexibility of polymers with the peculiar properties displayed by polymer chains when end-grafted to a surface. Polymer brushes can be conveniently obtained using either by “grafting-from” *i.e.* by starting the chain growth directly from a substrate functionalized with a suitable initiator, or by “grafting to” *i.e.* by attaching pre-formed chains on a surface (Scheme A.2).



Scheme A.2 Towards polymer brushes: grafting-from *vs* grafting-to.

End-functionalized polymer chemically grafted to a surface can be characterized according to the distance between different grafting points and the thickness of the polymer layer: some quantities and relations can be derived to describe these systems [2,3].

For example, the **reduced tethered (grafting) density** Σ

$$\Sigma = \pi \sigma R_g^2 = \frac{\pi R_g^2}{D^2}$$

is a measure for the degree of overlapping of the grafted chains. Σ is proportional to the **grafting density** σ (chains/nm²)

$$\sigma = \frac{h \rho N_A}{M_n}$$

and the square of the radius of gyration R_g . Here the grafting density σ can be calculated from the ellipsometrically obtained layer thickness h , the polymer brushes density ρ , Avogadro's constant and the number average molecular weight M_n of the polymer chains. Additionally the amount Γ of polymer per unit surface area (also known as **surface coverage**

or adsorbed amount, g/m²) can be calculated from the polymer brush density and the layer thickness:

$$\Gamma = h\rho$$

whereas often the brush density is unknown and the polymer bulk density is taken for the calculations of σ and Γ to obtain approximate results.

With the reduced tethered density Σ , grafted polymers at a surface can be classified into *brush*, *mushroom* or *pancake* regime. Physically speaking, Σ is the number of chains within the area that a free non-overlapping chain would occupy at the same environmental conditions. The Σ parameter for the transition between mushroom and brush regime depends on the excluded volume, which varies for different systems. Nevertheless it was found for several brush systems that the brush regime is often present for $\Sigma > 5$ whereas for $1 < \Sigma < 5$ a transition regime occurs followed by mushroom conformations for $\Sigma < 1$.

At low grafting densities, when the polymer chains are in the mushroom regime, the thickness of the polymer layer is independent of the grafting density. However, in a brush regime, at high polymer chain densities, the thickness increases with increasing the molecular weight of the polymer. Jones and co-workers [4] reported that the initiator density on a surface was associated with the final polymer grafting density. Using ω -mercaptoundecyl bromoisobutyrate to initiate the radical polymerization of methyl methacrylate from a gold-covered surface, a linear relationship between the initiator density and polymer grafting density was found.

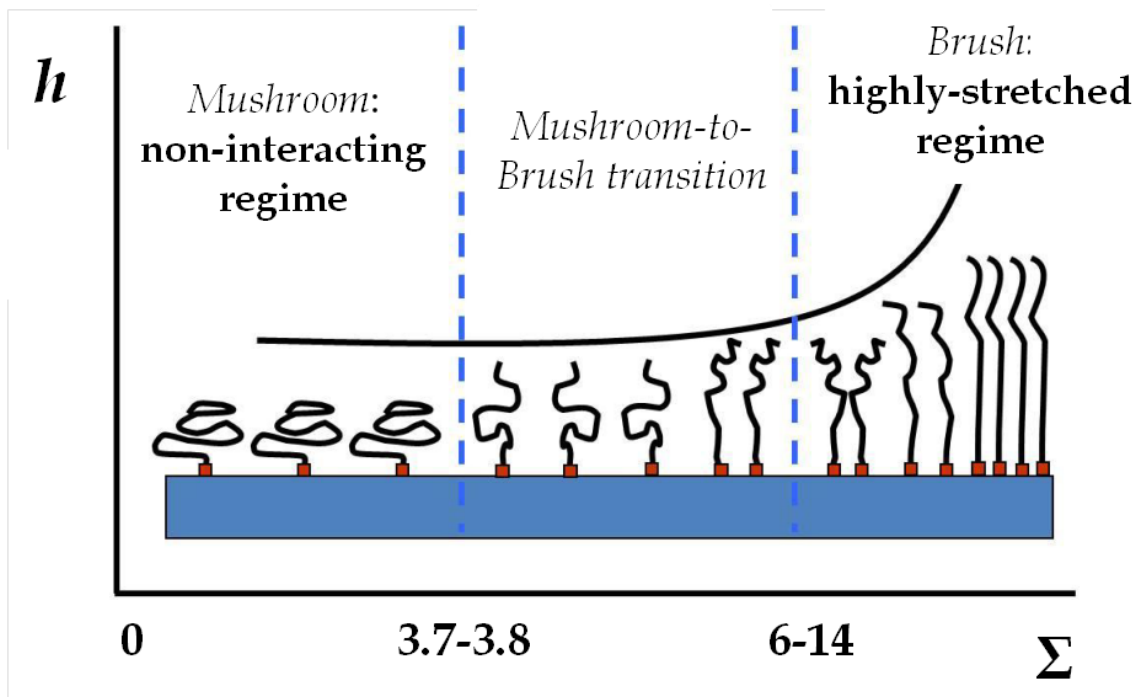


Figure A.1 Depiction of mushroom, crossover, and brush regimes of grafted polymer thin films in relation to brush thickness (h) and reduced tethered density (Σ). The figure is not drawn to scale. Brush thickness can be related to the characteristic size of the chains, R : $R = N\sigma^x$ where N is the average number of monomers per chain (i.e. the degree of polymerization), σ is the chain density and x is a constant. By comparing the calculated D with the calculated R it is possible to evaluate the conformation of the chains: pancake and mushroom conformations are specific to polymer chains tethered at low grafting density (or $D > R$) while the brush conformation prevails at high grafting density (or $D \ll R$). If a dry layer contains only polymer chains, because the volume V occupied by a single chain is given by $V = Na^3 = hD^2$ (where h is the dry thickness), then the dry thickness h and the grafting density σ can be linked by the relation $h = Na^3\sigma$.

The distance between grafted polymer chains is typically much less than the size of the polymer coil, or Flory radius. The ratio of grafted chains that occupy the same surface area as a free overlapping chain is known as the reduced tethered density, represented by Σ . This value is an indication of how stretched the polymer chains are.

This highly extended polymer chain configuration is known as the “brush regime,” where the brush thickness is proportional to $N\sigma^{1/3}$. Due to excluded volume effects, the polymer

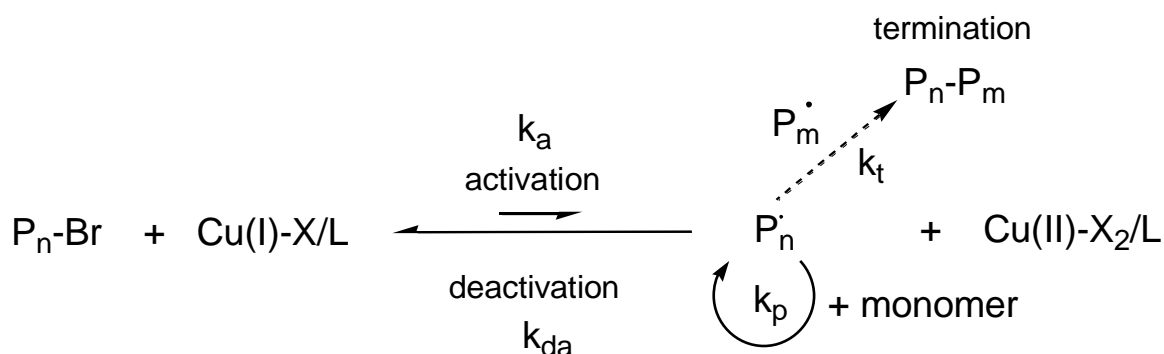
chain will forcibly grow in a more extended conformation as the polymerization proceeds. While this extended conformation has entropic energy loss, the stretched chains can interact more collectively. In this geometry, selective control of the polymer brush nano-environment, brought about by conformational changes using stimuli such as temperature or polymer solvation, can dramatically alter film properties such as thickness and morphology. These properties are vital, and can be used to generate and control polymer brush interfaces.

Surface-initiated ATRP

As stated before, surface-initiated controlled radical polymerization is the most exploited approach for the realization of grafted-from polymer brushes. It allows to obtain highly dense polymer brushes with control over thickness, composition and chains polydispersity. Atom Transfer Radical Polymerization (ATRP) is especially suitable for this purpose thanks to its high versatility and relative user-friendliness [5].

ATRP is a controlled radical polymerization process where all the chains are expected to grow at the same rate. The mechanism of conventional ATRP (Scheme A.3) is based on the reversible formation of radicals by the halogen atom abstraction from an alkyl halide (typically a secondary or tertiary bromide) by a copper(I)-ligand complex. This latter breaks the C-Br bond of the initiator and the resulting carbon carbon-centered radical attacks a monomer molecule starting chain growth. At the same time, copper(I) oxidizes to copper(II). Since this process is reversible, Cu(II) acts as a deactivator reducing the overall concentration of active radicals and thus the occurrence of irreversible termination events. In other words, the controlled aspect of ATRP is due to a fast initiation and rapid reversible

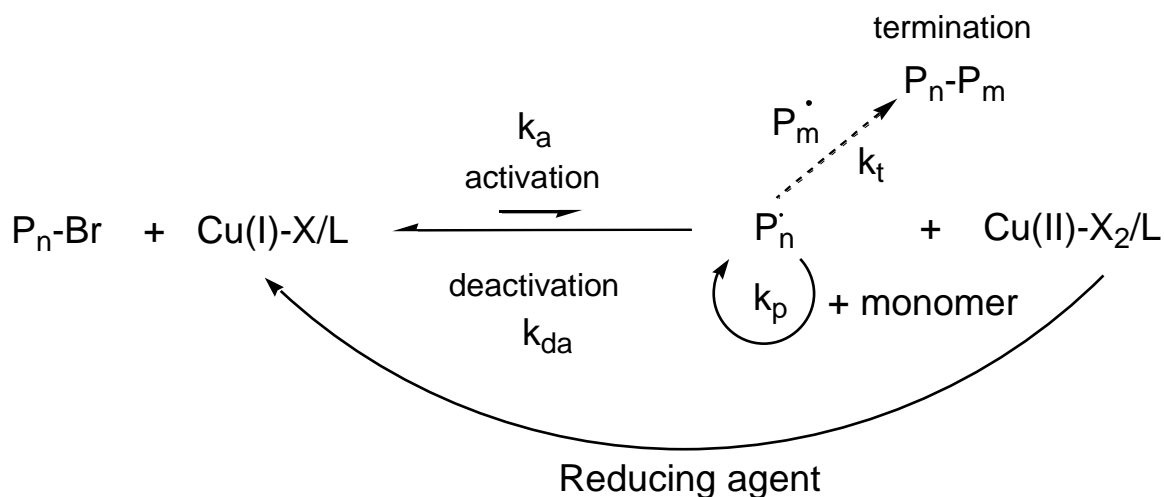
deactivation of radicals $P\cdot$ into dormant species $P-X$ (where $X = \text{halogen}$) thus minimizing the contribution of irreversible termination.



Scheme A.3 Mechanism of conventional ATRP.

When ATRP is confined to surfaces, the key parameter for controlling the growth of the chains at the substrate is the addition of (i) a deactivator (e.g. Cu^{2+}) or (ii) a sacrificial initiator in solution. The first approach is more practical compared to performing ATRP in presence of sacrificial initiator: in this case no polymer (although some polymer can form as a result of stray chain transfer reactions or thermal initiation) forms in solution and a simple solvent rinse can clean the polymer brushes on the surface without the need of e.g. Soxhlet extraction [6,7].

A recent advance in ATRP is Activators Regenerated by Electron Transfer (ARGET) ATRP: this approach which uses an excess amount of reducing agent to regenerate Cu(I) from Cu(II) to maintain an appropriate $\text{Cu(I)}/\text{Cu(II)}$ balance (Scheme A.4). An added advantage over traditional ATRP, apart from the possibility to lower to ppm the amount of catalyst needed, is the increased tolerance towards oxygen: in some cases, deoxygenation of the polymerization mixture is not needed at all. This is because the excess reducing agent can act as a scavenger of oxygen, consuming it completely before starting polymerization [8].



Scheme A.4 Mechanism of ARGET ATRP.

References

- [1] R. Barbey, L. Lavanant, D. Paripovic, N. Schüwer, C. Sugnaux, S. Tugulu and Harm-Anton Klok, *Chem. Rev.* **2009**, *109*, 5437–5527.
- [2] W. J. Brittain and S. Minko, *J. Polym. Sci. A Polym. Chem.*, **2007**, *45*, 3505–3512.
- [3] S. G. Boyes, A. M. Granville, M. Baum, B. Akgun, B. K. Mirous and W. J. Brittain, *Surf. Sci.*, **2004**, *570*, 1–12.
- [4] D. M. Jones, A. A. Brown and W. T. S. Huck, *Langmuir*, **2002**, *18*, 1265–1269.
- [5] K. Matyjaszewski and J. Xia, *Chem. Rev.* **2001**, *101*, 2921–2990.
- [6] J. D. Jeyaprakash, S. Samuel, R. Dhamodharan and J. Rühle, *Macromol. Rapid. Commun.*, **2002**, *23*, 277–281.
- [7] D. Zhou, X. Gao, W.-J. Wang and S. Zhu, *Macromolecules*, **2012**, *45*, 1198–1207.
- [8] K. Matyjaszewski, *Macromolecules*, **2012**, *45*, 4015–4039.

Appendix B

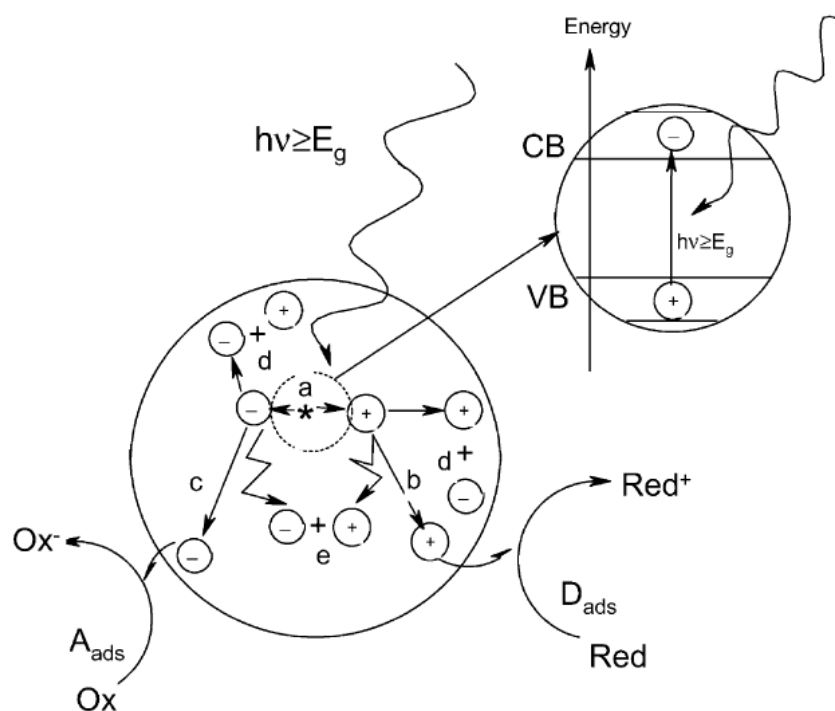
Titanium Dioxide and Photocatalysis

Photocatalysis has recently become a common word and various products using photocatalytic functions are already commercially available. Among many promising candidates as photocatalytic materials, titanium dioxide (titania, TiO_2) is almost the only material suitable for industrial use at present and also probably in the future. This is because TiO_2 has the most efficient photoactivity, the highest stability and the lowest cost. More significantly, it has been used as a white pigment from ancient times, thus its safety to humans and the environment is guaranteed by history [1].

There are two types of photochemical reaction proceeding on a TiO_2 surface when irradiated with ultraviolet light ($\lambda < 400 \text{ nm}$). One includes the photo-induced redox reactions of adsorbed substances, and the other is the photo-induced hydrophilic conversion of TiO_2 itself [2]. The former type has been known since the early part of the 20th century, but the latter was found only at the end of the century. The combination of these two functions has opened up various novel applications of TiO_2 , ranging from photoenergy conversion, self-cleaning surfaces (and sensors) and innovative lithographic techniques to environmental remediation and energy-saving buildings.

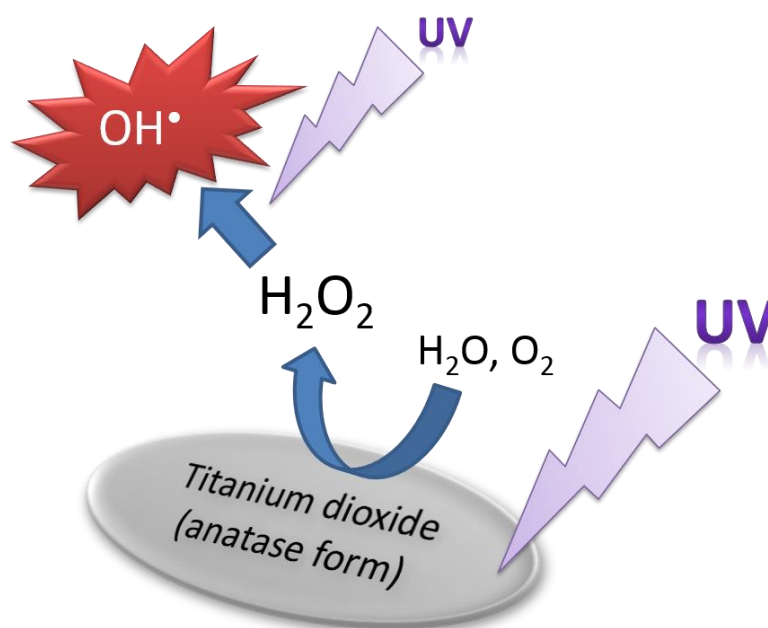
Photo-induced redox reactions of adsorbed molecules

There are three main types of TiO₂ structures: rutile, anatase and brookite. These have different activities for photocatalytic reactions and anatase is the most used for this kind of applications. Titanium dioxide is a semiconductor, and all its photo-induced processes originate from its band-gap. When incident photons have a higher energy compared to that of the band-gap, they can be absorbed and an electron is then promoted to the conduction band (CB), leaving a hole in the valence band (VB). This excited electron can either be used directly to generate electricity in photovoltaic solar cells or drive a chemical reaction, which is called *photocatalysis*. All photo-induced phenomena involve surface-bound redox reactions (Scheme B.1).



Scheme B.1 A depiction of the main processes occurring on a semiconductor particle: a) electron-hole generation, b) oxidation of a donor (D), c) reduction of an acceptor (A), d,e) electron-hole recombination at surface and in bulk, respectively [3].

For example, adsorbed oxygen can be reduced to the superoxide anion radical by photogenerated electrons while adsorbed water can be oxidized to the hydroxyl radical by photogenerated holes. Both are extremely reactive species, which can in turn react with adsorbed organic molecules. These latter are first turned into oxidized species and are eventually mineralized to *e.g.* carbon dioxide and water (Scheme B.2).



Scheme B.2 Schematic mechanism for the generation of reactive oxygen species (e.g. hydroxyl radical) on the surface of UV-irradiated titanium dioxide.

Photo-induced hydrophilicity

A TiO₂ thin film exhibits an initial contact angle (CA) of several tens of degrees depending on the surface conditions *e.g.* surface roughness. When this surface is exposed to UV light, water starts to exhibit a decreasing CA, that is, it tends to spread out flat instead of beading up). Eventually, the CA reaches almost 0°. At this stage, the surface becomes completely non-water-repellant and is termed "highly hydrophilic". The surface retains a CA of a few

degrees for a day or two under the ambient condition without being exposed to UV light. Then, the CA slowly increases, and the surface becomes the initial less hydrophilic state again. At this point, the high hydrophilicity can be recovered simply by exposing the surface again to UV light. In short, this type of TiO₂-coated material is the only known practical highly hydrophilic one that shows stable and semi-permanent properties. It seems that surface-trapping of holes should be the major cause. Despite years of careful examination of the controversial aspects of this photo-induced hydrophilic effect, a definitive answer on its effective nature is not available yet. However, the researchers have reached the conclusion that photo-induced hydrophilicity is accompanied by a clear increase of surface -OH groups and that, whereas there is an aspect of this effect that does not involve simply the cleaning of the surface due to photo-oxidation phenomena, the surface species involved are basically the same ones involved with conventional photocatalysis. Nevertheless, the absence of a complete explanation does not impair its use for the most practical applications of titanium dioxide such as self-cleaning exterior tiles and anti-fogging mirrors.

References

- [1] A. Fujishima, X. Zhang and D. A. Tryk, *Surf. Sci. Reports*, **2008**, 63, 515–582.
- [2] O. Carp, C. L. Huisman and A. Reller, *Prog. Solid State Chem.*, **2004**, 32, 33–177.
- [3] A. Mills and S. Le Hunte, *J. Photochem. Photobiol. A: Chem.*, **1997**, 108, 1.

Appendix C

General Procedures

PHOTOCATALYTIC LITHOGRAPHY

All the photocatalytic lithography experiments are performed using a Jelosil HG500 halogen lamp (Figure C.1, left). Its technical characteristics are: 230 V, 500 W, effective power density from 40 cm: 57.5 (mW cm^{-2}) between 280 and 400 nm. Its emission spectrum is shown in Figure C.1 (right).

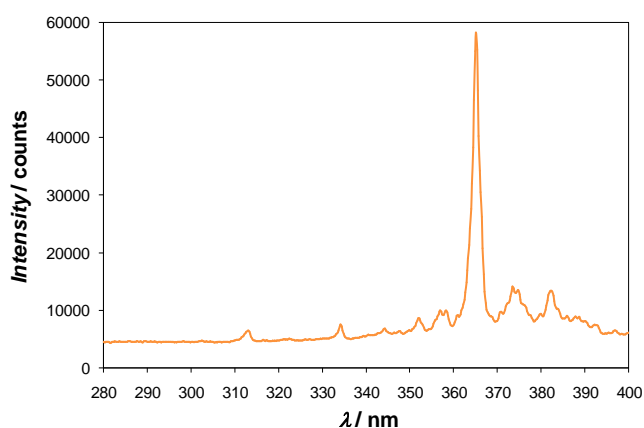


Figure C.1 A picture of the lamp used to perform photocatalytic lithography (left) and its emission spectrum (right).

TEM grids (Gilder Grids, nickel, d 3.05 mm, square mesh) are used as photomasks to perform photocatalytic lithography experiments (Figure C.2).

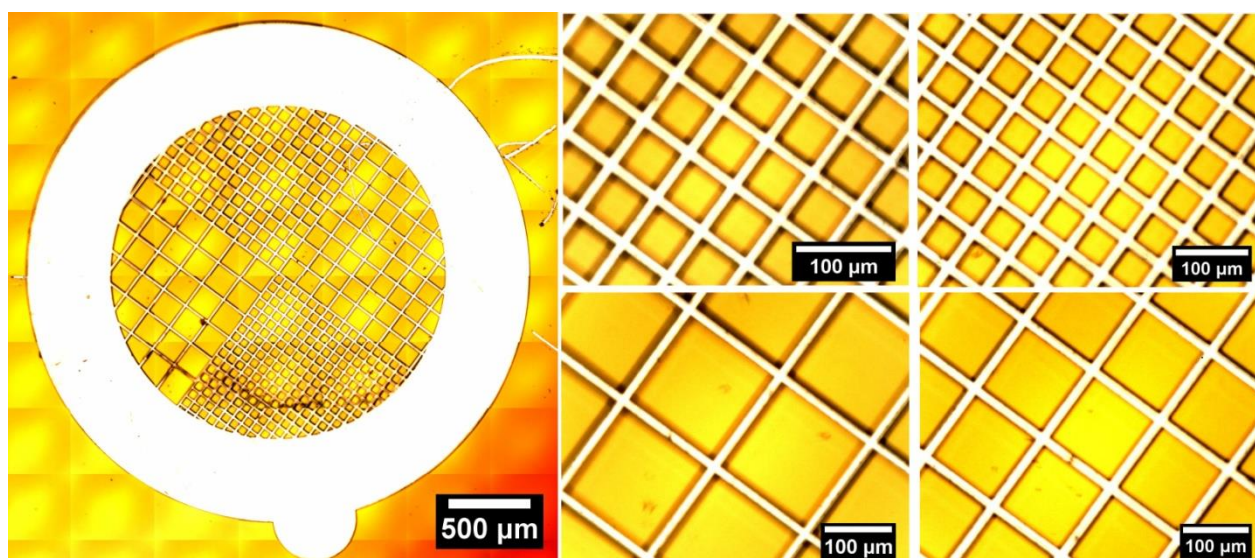
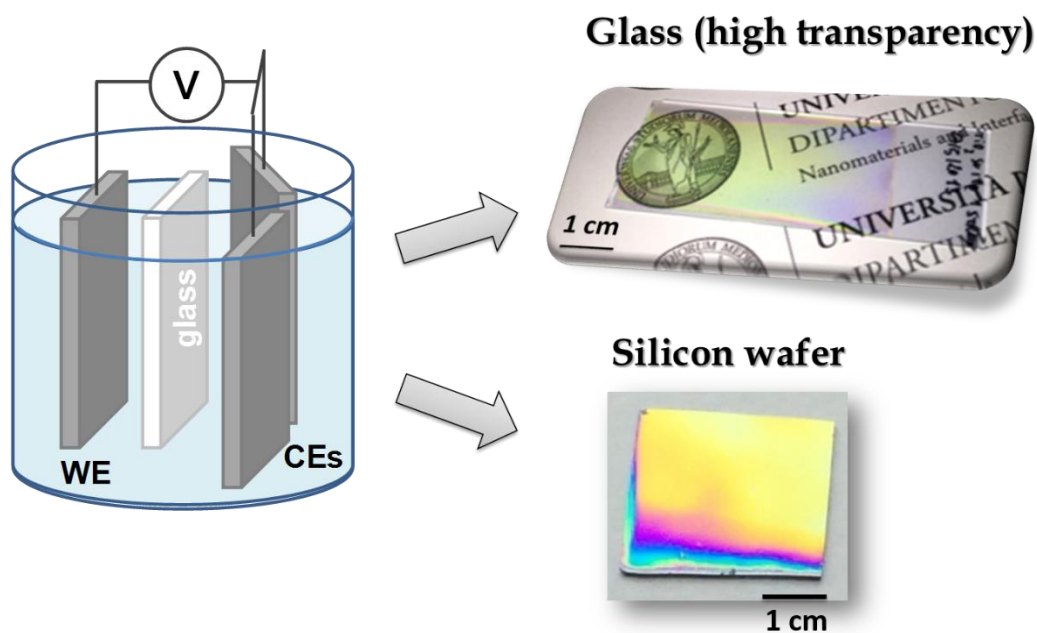


Figure C.2 Optical microscopy of the TEM grid (imaged on titania film) used to obtain grid patterns by photocatalytic lithography.

SYNTHESIS OF THE TITANIA SOL AND ITS USE FOR THE DEPOSITION OF TITANIUM DIOXIDE FILMS

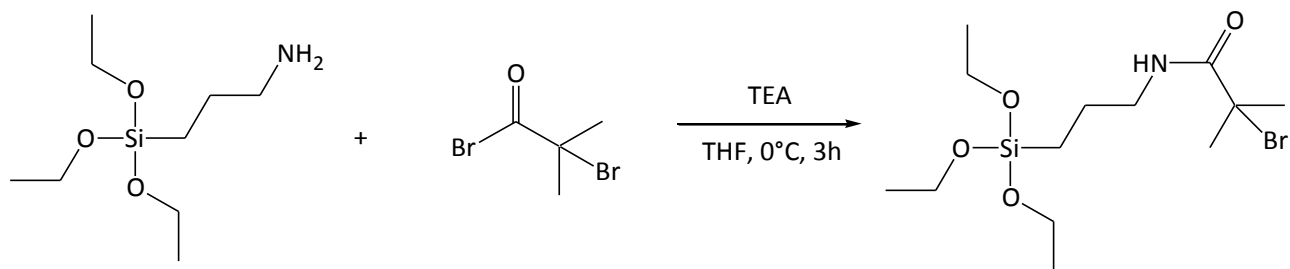
The titania sol has been developed in our group and was previously reported. Briefly, 0.9 mL of HCl 37 % was added to a solution of $\text{Ti}(\text{OC}_3\text{H}_7)_4$ in ethanol (0.1 mol in 100 mL) under stirring. Then, 0.47 g of Lutensol ON70 (BASF) was added to the sol after being dissolved in 100 mL of ethanol. Prior to the TiO_2 deposition the silicon or glass surface was cleaned by immersion for 1 h in a 3:1 v/v mixture of 98% sulphuric acid and 30% hydrogen peroxide (“piranha solution”) at 100°C , then rinsed with MilliQ water and dried with a nitrogen stream. (*Caution: piranha solution reacts violently with organic matter!*). The substrate is then immersed in the sol contained in an electrochemical cell equipped with three titanium electrodes arranged in a triangular fashion. The substrate is in the centre of the triangle described by the three electrodes (Scheme C.1). A 2 V-constant potential is then applied and deposition is carried out for 1 min or more, depending on the thickness to be reached. The substrate is then calcined at 400°C under nitrogen.



Scheme C.1 The electrochemical cell used for the electrochemically-assisted deposition of titania films along with representative samples obtained on glass and silicon substrates.

SYNTHESIS OF THE ATRP INITIATOR (BIB-APTES)

7 mL (30 mmol) 3-aminopropyltriethoxysilane (APTES) and 5 mL (36 mmol) triethylamine were dissolved in 50 mL anhydrous THF in a three-necked 100 mL round bottom flask, equipped with a dropping funnel, a nitrogen inlet and a mechanical stirrer, immersed in an ice bath. 4.45 mL (36 mmol) 2-bromoisobutyrylbromide (BIBB) were added dropwise under stirring and the reaction was allowed to continue at room temperature for 3 h. The white solid (triethylammonium bromide) was filtered off and the volatiles removed at 50 °C using rotavapor. The product was dissolved in anhydrous THF, filtered through silica gel to separate a brown impurity. After evaporation of the solvent, a quantitative yield of a viscous, colorless liquid was obtained (Scheme C.1) and stored at +4 °C. Density: 1.17 (g mL⁻¹). ¹HNMR (CDCl₃, 400 MHz, ppm): 0.64 (t, 2H, SiCH₂), 1.22 (br, 9H, CH₃), 1.65 (q, 2H, CH₂), 2.02 (s, 6H, CH₃), 3.26 (t, 2H, CH₂NH), 3.83 (q, 6H, CH₃CH₂OSi), 6.85 (s br, 1H, NH).



Scheme C.1. Synthesis of BIB-APTES.

GRAFTING OF THE BIB-APTES INITIATOR To improve grafting of initiator molecules, the substrates are subjected to a cleaning treatment before functionalization. TiO₂ surfaces are activated by irradiation with 254 nm UV (0.25 J cm⁻²), while silicon and glass substrates are piranha-cleaned. These treatments are useful to remove organic contamination and increase the surface hydroxyl groups. The substrates are then immersed in a 10 mM BIB-APTES solution in anhydrous toluene for 4 h at 55 °C, left overnight at 30 °C, washed and gently sonicated with toluene, acetone and ethanol and dried with a nitrogen stream. The functionalized substrates can be stored at room temperature in the dark until use.

CHEMICAL VAPOR DEPOSITION OF SILRES BS 1701

SILRES BS 1701 is produced and commercialized by Wacker Chemie AG. It is a mixture of isomeric octyltriethoxysilanes with iso-octyltriethoxysilane as the main component.

To perform chemical vapor deposition, the substrate to be functionalized with SILRES is placed in a glass container (Petri dish) together with a Teflon® cup filled with some drops of SILRES. The container is placed in an oven at 100 °C for 3 hours to vaporize the siloxane and to promote its chemisorption. Eventually, the substrate is sonicated in toluene and dried.

In case of titania substrates they are irradiated for 1 h using 365 nm-UV light, while in case of silicon substrates they are previously piranha-cleaned.

SYNTHESIS OF SPHERICAL SILVER NANOPARTICLES (AgNPs)

To synthesize spherical silver nanoparticles, first 0.15 g (0.88 mmol) of silver nitrate are dissolved in 25 mL of water and this solution is added under stirring to a solution of 0.50 g (1.7 mmol) of trisodium citrate and 0.25 g of poly(vinylpyrrolidone) (PVP10, $M_w \sim 10000 \text{ g mol}^{-1}$) in 125 mL of water. The resulting solution is poured in a three-necked, round-bottomed 250 mL flask equipped with a mechanical stirrer and a dropping funnel. The solution is cooled in an ice bath and an ice-cooled solution of sodium borohydride, obtained by dissolving 12 mg (0.32 mmol) of solid in 30 mL of water, is added dropwise under stirring. The resulting dark brown suspension is left under stirring for 5 minutes after the addition, aged at + 4 °C for 24 hours before use and stored in the dark at that temperature. The aqueous particle suspension displays the characteristic surface plasmon resonance peak at around 400 nm associated with silver nanoparticles of dimensions lower than 30 nm. Zeta potential measurements confirm that the particle surface was negatively charged ($-30 \pm 3 \text{ mV}$) due to strong adsorption of citrate molecules. HR-TEM shows particles with an average diameter of $11 \pm 1 \text{ nm}$ with high crystallinity and sharp size distribution.

Collaborations

The work presented in this Thesis is highly interdisciplinary. That means that each result is the product of intense collaborations with skilled Experts from different fields. Without their contributions, this Thesis would never have been written.

The experiments on photocatalytic lithography described in Chapters 1 and 2 were performed in collaboration with Prof. Silvia Ardizzone and Guido Soliveri from Università degli Studi di Milano.

The electrochemical analyses on polymer brushes described in Chapter 3 were performed by Dr. Valentina Pifferi from Università degli Studi di Milano.

Positron Annihilation Spectroscopy experiments (Chapter 4) were conducted by Prof. Rafael Ferragut and Dr. Stefano Aghion from LNESS in Como (Politecnico di Milano) and by Prof. Giovanni Consolati (Politecnico di Milano).

The electrochemical Device described in Chapters 5 – 7 was developed and characterized by a joint collaboration with the Group of Prof. Silvia Ardizzone and the Group of Prof. Luigi Falciola (Università degli Studi di Milano).

Last but not least, the fundamental contribution of many Researchers of the ENI Donegani Research Centre for Renewable Energies and Environment (Novara) has to be highlighted. Dr. Gianluigi Marra performed all the XRD, XRR, SEM and TEM analyses. Dr. Laura Meda performed XPS measurements. Dr. Alberto Savoini performed AFM measurements. Dr. Mario Salvalaggio performed SERS experiments.

Acknowledgments

To ANYONE who helped, supported and encouraged me during these three years,
eventually making possible for me to accomplish this Thesis, from the deep of my heart

I say:

THANK YOU!

Copyright note

Part of the work described in this Thesis including graphs, diagrams and figures, has already been published and is used and reproduced with permission.

Chapter 1

Panzarasa, G.; Soliveri, G.; Sparnacci, K.; Ardizzone, S. **Patterning of Polymer Brushes Made Easy Using Titanium Dioxide: Direct and Remote Photocatalytic Lithography** *Chem. Commun.* **2015**, *51*, 7313–7316 (Reproduced with permission from the Royal Society of Chemistry).

Panzarasa, G.; Soliveri, G.; Ardizzone, S.; Sparnacci, K. **Photocatalytic lithography: an innovative approach to obtain patterned pH-responsive polymer brushes** *Mater. Today Proc.* **2015**, *2*, 4183–4189 (Reproduced with permission from Elsevier).

Chapter 3

Panzarasa, G.; Soliveri, G.; Pifferi, V. **Tuning the electrochemical properties of silicon wafer by grafted-from micropatterned polymer brushes** *J. Mater. Chem. C* **2016**, *4*, 340–347 (Reproduced with permission from the Royal Society of Chemistry).

Chapter 4

Panzarasa, G.; Aghion, S.; Soliveri, G.; Consolati, G.; Ferragut, R. **Positron Annihilation Spectroscopy: A New Frontier for Understanding Nanoparticle-Loaded Polymer Brushes** *Nanotechnology* **2016**, *27*, 02LT03 [*Press coverage*: featured in the *Nanotechnology LabTalk* (14 December 2015) as **Antimatter matters! especially for polymer brushes** (link: <http://iopscience.iop.org/0957-4484/labtalk-article/63531>)] (Reproduced with permission from IOP).

Chapter 5

Soliveri, G.; Pifferi, V.; Panzarasa, G.; Ardizzone, S.; Cappelletti, G.; Meroni, D.; Sparnacci, K.; Falciola, L. **Self-cleaning properties in engineered sensors for dopamine electroanalytical detection** *Analyst* **2015**, *140*, 1486–1494. [*Press coverage*: featured in *Chemistry World* (23 January 2015) as: **Self-cleaning sensors see the light** by Simon Neil (link: <http://www.rsc.org/chemistryworld/2015/01/self-cleaning-electrochemical-sensor-ultraviolet-light>) and in *Scientific American* (27 January 2015) as: **Sensors Cleaned by Light Could Drop Costs of Detecting Pollution or Disease** (link: <http://www.scientificamerican.com/article/sensors-cleaned-by-light-could-drop-costs-of-detecting-pollution-or-disease>); selected as a Hot Article by *Analyst* (24 March 2015)] (Reproduced with permission from the Royal Society of Chemistry).

Chapter 7

Pifferi, V.; Soliveri, G.; Panzarasa, G.; Ardizzone, S.; Cappelletti, G.; Meroni, D.; Falciola, L. **Electrochemical sensors cleaned by light: a proof of concept for on site applications towards integrated monitoring systems** *RSC Adv.* **2015**, *5*, 71210–71214 (Reproduced with permission from the Royal Society of Chemistry).